



Probing the Sources of Gravitational Waves

A Search for UHE Photons Induced by Compact Binary Mergers
at the Pierre Auger Observatory

DISSERTATION
zur Erlangung des akademischen Grades eines
Doktors der Naturwissenschaften
(Dr. rer. nat.)

vorgelegt von
M. Sc. Philip Rühl

eingereicht bei der
Naturwissenschaftlich-Technischen Fakultät
der Universität Siegen

Siegen, September 2020

Probing the Sources of Gravitational Waves

**A Search for UHE Photons Induced by Compact Binary Mergers
at the Pierre Auger Observatory**

DISSERTATION

zur Erlangung des akademischen Grades eines

Doktors der Naturwissenschaften

(Dr. rer. nat.)

vorgelegt von

M. Sc. Philip Rühl

eingereicht bei der

Naturwissenschaftlich-Technischen Fakultät

der Universität Siegen

Siegen, September 2020



Betreuer und erster Gutachter	Prof. Dr. Markus Risse Universität Siegen
Zweiter Gutachter	Prof. Dr. Ivor Fleck Universität Siegen
Tag der Disputation	16.12.2020

Abstract

Since almost 60 years, physicists have been puzzled about the origin of ultra-high-energy (UHE) cosmic rays (CRs). In 2015, the first direct measurement of gravitational waves (GWs) shed light on a new promising type of source candidate: the merging processes of compact binary systems (compact binary mergers, CBMs).

Since charged CRs are considerably deflected by extragalactic magnetic fields, one has to rely on neutral messenger particles like photons or neutrinos if correlations between GWs and CRs shall be analyzed. The technique of observing a single astronomical object in the light of multiple messenger signals is called “multimessenger astronomy” (MMA) and witnessed a major breakthrough with the observation of a binary neutron star merger in 2017. The analysis presented in this work shall open a new window in the field of MMA by searching for photons with energies beyond 10 EeV from transient point sources.

For the first time, constraints on UHE photons from CBMs are derived using data collected by the Pierre Auger Observatory and public data on GWs from the LIGO and Virgo detectors. Air shower events that have been found to be coincident with a GW are analyzed separately and the sensitivity of the Auger Observatory surface detector to a potential photon signal is evaluated. In preparation for future GW observations, a dedicated analysis strategy is developed aiming to optimize the physics results within the capabilities of Auger. Furthermore, also the atypical blazar TXS 0506+056 is analyzed for UHE photons during two periods of enhanced high-energy neutrino emission.

Finally and as an addition to this thesis, a first step is taken to lower the energy threshold of the Auger surface detector for the search for photons from transient point sources. For this purpose a new photon-discriminating air shower observable is being developed and analyzed in a simulation study.

Zusammenfassung

Seit fast 60 Jahren beschäftigen sich Wissenschaftler mit der Frage nach dem Ursprung der ultra-hochenergetischen (UHE) kosmischen Strahlung (KS). Der direkte Nachweis von Gravitationswellen (GW) im Jahr 2015 warf zum ersten Mal Licht auf die Verschmelzungsprozesse kompakter Binärsysteme (compact binary mergers, CBMs), welche als vielversprechende Kandidaten für die Beschleunigung höchstenergetischer KS gelten.

Da geladene KS starke Ablenkung in den extragalaktischen Magnetfeldern erfährt, muss bei der Untersuchung einer Korrelation zwischen GW und KS auf neutrale Botschafterteilchen wie Photonen und Neutrinos zurückgegriffen werden. Die Beobachtung eines Objekts im Lichte verschiedener Botschaftersignale, genannt "Multimessenger-Astronomie" (MMA), feierte einen bedeutenden Durchbruch mit der Beobachtung der Verschmelzung eines binären Neutronensternsystems im Jahr 2017. Die Analyse, die in der vorliegenden Arbeit präsentiert wird, öffnet durch die Suche nach Photonen mit Energien jenseits von 10 EeV ausgehend von transienten Punktquellen ein neues Fenster im Forschungsfeld der MMA.

Zum ersten Mal werden obere Schranken auf den Fluss von UHE Photonen ausgehend von CBMs hergeleitet durch die Analyse der Daten, die am Pierre Auger Observatorium genommen wurden und der veröffentlichten Daten der GW Detektoren LIGO und Virgo. Luftschauerereignisse, die in Koinzidenz mit einer GW gemessen wurden, werden gesondert untersucht und die Sensitivität des Auger Oberflächendetektors gegenüber einem möglichen Photonsignal ausgewertet. Vorbereitend für zukünftige GW Messungen werden außerdem weiterführende Analysemethoden entwickelt, die die Möglichkeiten von Auger maximal ausschöpfen sollen. Neben den CBMs wird auch der atypische Blazar TXS 0506+056 im Hinblick auf UHE Photonen während zwei Phasen erhöhter Neutrinoemission untersucht.

Abschließend wird dieser Arbeit eine zusätzliche Studie angehängt, in der ein erster Schritt unternommen wird, die Energieschwelle des Auger Oberflächendetektors für die Suche nach Photonen von CBMs zu senken. Zu diesem Zweck wird eine neue Luftschauerobservable entwickelt und auf ihre systematischen Eigenschaften untersucht.

Contents

1	The cosmos and humanity	3
1.1	Ancient myth and natural philosophers	3
1.2	The dawn of modern astronomy	6
2	Astroparticle physics	9
2.1	Early discoveries of the 20th century	9
2.2	Progenitors of particle physics	13
2.3	The beginning of astroparticle physics	15
3	Cosmic rays and extensive air showers	19
3.1	The cosmic ray energy spectrum	19
3.2	Sources and acceleration mechanisms	23
3.3	Composition	27
3.4	Extensive air showers	29
3.5	Photons as primary particles	36
3.6	Multimessenger astronomy	42
4	General relativity and gravitational waves	45
4.1	GWs as solutions of Einstein's field equations	45
4.2	Basic properties of GWs	47
4.3	Compact binary mergers	49
4.4	Detection of GWs	50
5	The Pierre Auger Observatory	55
5.1	Hybrid design	57
5.2	The fluorescence detector (FD)	59
5.2.1	Event reconstruction with the FD	61
5.3	The surface detector (SD)	66
5.3.1	The water Cherenkov detector	66
5.3.2	Calibration	68
5.3.3	The SD trigger hierarchy	69
5.3.4	Geometry reconstruction	71
5.3.5	Energy reconstruction	74
5.4	Other facilities of Auger	75
5.4.1	The low-energy extensions of Auger	75
5.4.2	AERA	77
5.4.3	Laser facilities CLF and XLF	78
5.4.4	The Auger Prime upgrade	78

6	Data, simulations and software	81
6.1	Air shower simulations	81
6.1.1	Simulation set <i>A</i> : photon spectrum	82
6.1.2	Simulation set <i>B</i> : photons and protons at fixed energies	82
6.2	Detector simulation and reconstruction	83
6.2.1	Simulation sets <i>A</i> and <i>B</i>	83
6.2.2	Air shower data	84
6.3	Public gravitational wave data	85
6.4	Further software	85
7	Separation between primary photons and hadronic background	87
7.1	Photon energy	88
7.2	Event selection	90
7.3	Observables	91
7.4	Principal component analysis	94
7.5	Angular resolution	95
7.6	Background estimation and photon detection efficiency	97
8	A search for photons above 10 EeV induced by GW events	103
8.1	Definition of quantities	104
8.2	Follow-up analysis of GW150914	108
8.2.1	Localization	109
8.2.2	Observation time windows	111
8.2.3	Exposure	112
8.2.4	Data unblinding and estimation of background	113
8.2.5	Upper limits on k_γ	114
8.2.6	Upper limits on \mathcal{F} and F	115
8.2.7	Upper limits on E_{tot}	118
8.2.8	Expected number of photons	119
8.3	Results for all GW events from LIGO/Virgo runs O1 and O2	121
8.3.1	Exposure	122
8.3.2	Upper limits	122
8.3.3	Constraints on the BNS merger GW170817	125
8.3.4	Coincident air shower events	126
8.4	Significance in case of a photon candidate detection	128
8.5	Discussion of systematical uncertainties	129
8.5.1	Variation of the spectral index α	131
8.5.2	Bias due to the finite angular resolution of the SD	131
8.5.3	Uncertainty of the photon significance	132
8.5.4	Anisotropic emission	133
8.5.5	Cosmological redshift	134
9	Improving the GW event selection for future follow-up searches	135
9.1	The problem of time dependent penalization	136
9.2	Reevaluation of the photon significance	138

9.3	Options for a GW event selection	140
9.4	Tuning of the analysis parameters	142
9.4.1	Choice of directional search area Ω_{CL}	142
9.4.2	Cut on source localization $\Omega_{50\%}$	145
9.4.3	Cut on source distance D_L	146
9.4.4	Cross-dependent event selection based on source distance and localization	147
9.4.5	Summary of proposed selection criteria	149
9.5	Constraining GW sources with the stacking method	150
10	A search for UHE photons from the blazar TXS 0506+056	155
10.1	UHE neutrinos from the blazar TXS 0506+056	156
10.2	Photon search analysis	156
10.3	Results	157
11	Lowering the energy threshold of the SD photon search	159
11.1	Definition of R_{MoPS}	159
11.1.1	MoPS-veto counts	160
11.1.2	ToTd counts	161
11.2	R_{MoPS} event selection	163
11.3	Performance of R_{MoPS}	164
11.4	Conclusion and further steps	168
12	Summary and outlook	171
Appendix		175
13.1	Appendix of Chapter 6	175
13.2	Appendix of Chapter 7	178
13.3	Appendix of Chapter 8	187
13.4	Appendix of Chapter 9	202
13.5	Appendix of Chapter 11	203
Bibliography		207
List of abbreviations and acronyms		231

Preface

The experimental discovery of gravitational waves in 2015 opened a new window to the universe. Along with an unprecedented validation of Einstein's theory of general relativity the first measurements of gravitational waves also revealed new types of transient astronomical sources – compact binary mergers. Such mergers combine extreme physical conditions in various aspects. Highly compact objects like neutron stars or stellar-mass black holes have dimensions of only a few tens of kilometers and revolve each other with orbital periods of microseconds and velocities close to the speed of light right before they merge into a single compact remnant. Moreover, compact objects like pulsars or magnetars are known to be accompanied by the strongest magnetic fields that are known in the Universe. Given their unique properties, the sources of gravitational waves might also be suitable sites for the acceleration of ultra-high-energy (UHE) cosmic rays. Due to the distance and transient nature of these sources, this hypothesis can only be tested through the measurement of neutral messenger particles like photons or neutrinos since they travel through the universe on straight lines at the speed of light. The Pierre Auger Observatory in Malargüe, Argentina has a unique exposure to UHE photons and neutrinos and is thus ideally suited to complement the global effort in multimessenger astronomy in the UHE regime.

In this thesis the first search for photons above 10 EeV from compact binary mergers is presented using data collected by the Pierre Auger Observatory. The first chapter shall give an overview of the historical development of classical astronomy and cosmology with a focus on western Europe and the emergence of modern scientific methodology. In Chapter 2 the path-finding discoveries of the 20th century for the fields of particle and astroparticle physics are outlined. A scientific overview of cosmic rays and the phenomenon of extensive air showers in the atmosphere is given in Chapter 3 with an emphasis on primary photons and their role in multimessenger astronomy followed by a short introduction into gravitational waves and their recent successful measurement in Chapter 4. The introductory chapters conclude with a description of the Pierre Auger Observatory and its data taking routines in Chapter 5. The technical description of the software and configurations used for the simulation of air showers and their interactions in the detector is described in Chapter 6 along with the air shower and gravitational wave data that is relevant for the analyses presented thereafter. In the following chapters, the follow-up search for UHE photons from transient astronomical sources is developed, starting with the description of the procedure used for photon-hadron discrimination in Chapter 7. The application of the analysis to gravitational wave events measured during the LIGO/Virgo observation runs O1 and O2 and its results are presented in Chapter 8. In Chapter 9, further improvements of the analysis for future applications are elaborated. In a similar approach

as in Chapter 8, the analysis is also applied in order to search for UHE photons from the blazar TXS 0506+056 during two periods of enhanced high-energy neutrino emission. The results of this study are presented in Chapter 10. As an extension to this thesis, in Chapter 11 a first study on a new criterion for photon-hadron separation below the current energy threshold is shown with a focus on the application to follow-up analyses of transient sources. The thesis concludes in Chapter 12 with a summary of the presented work, the scientific results and the possibilities for future extensions and further improvements of the analysis.

The cosmos and humanity

SINCE record of human history was taken, one subject has always been of primary interest as it still is upon the present day. The “fixed” nature of the stars and the milky way as opposed to the movements of the planets, the sun and the moon, the irregular occurrences of lunar and solar eclipses or the sudden flashing of shooting stars. All these phenomena have been sources for endless discussions over the past millennia. Feeling the inherent urge to grasp and understand his surroundings, man started to construct models in order to explain these intriguing observations.

1.1. Ancient myth and natural philosophers

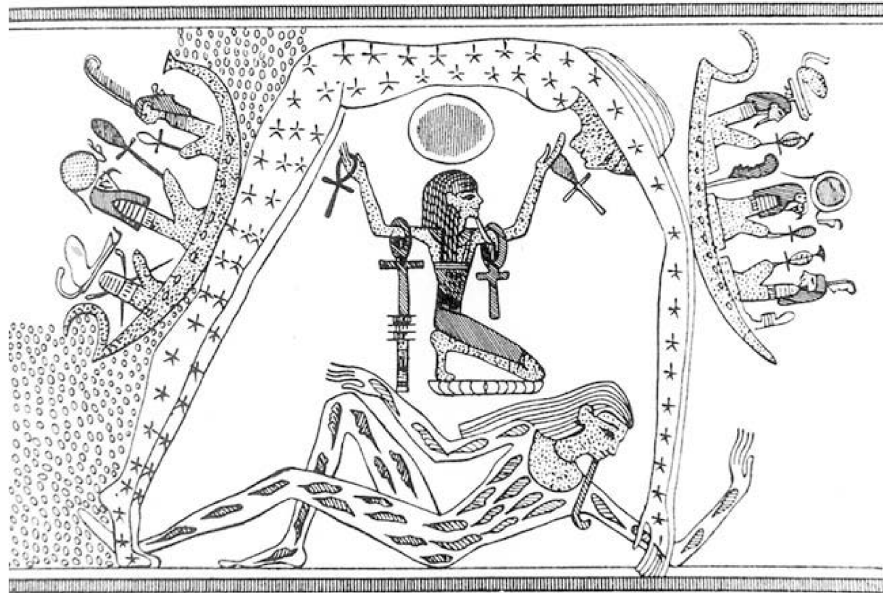


Figure 1.1: The ancient Egyptians’ view of the world [LO93]: the sky-goddess Nut, depicted with stars on her body, bends over the earth-god Geb who is lying on the ground while Shu, the god of air, separates the two. The sun-god Ra, sitting in a barque, is sailing the body of Nut from east to west resembling the cycle of a day.

The first models passed on from ancient civilizations involved many elements from experiences people encountered in their every-day life. The ancient Egyptians

of the 3rd and 2nd millennia BCE pictured the sky as a heavenly version of the Nile, often depicted as an elongated woman – the sky-goddess Nut, on which the sun-god Ra sailed every day from east to west on a barque (see Fig. 1.1). As the sun sets in the evening, it was thought to be swallowed by Nut just to be reborn again in the following morning [TJ04]. A great deal of resemblance also exists between the myths of genesis of the different ancient cultures. In the Egyptian and Mesopotamian lore, the sky and the earth once were one and the same entity combined in something that was described as a great ocean before they were separated by a driving force, which in the Egyptian case is the god Shu, the god of wind and air and father of Nut, to prevent her from engaging with the earth-god Geb [HA51, TJ04].

Until the 6th century BCE cosmology and myth were strongly connected. The first cosmological models only based on astronomical observations without relying on divine intervention goes back to the Ionian-Greek philosophers Thales, Anaximander and Anaximenes. The latter was most likely the first one who recorded the distinction between the “fixed” stars and the planets due to their relative movements. The first time that the earth was considered equal to the other planets in the solar system goes back to the Pythagorean model which is commonly attributed to Philolaus of Crotona who lived in the second half of the 5th century BCE. While this model already correctly described the shape of the planets as spheres moving on concentric orbits, it still did not recognize the stars as individual bodies but rather as a texture on a sphere enveloping the planets and the sun and rotating around their common center – which was not the sun in that model but a place named the “central fire” [TJ04].

Correct explanations for lunar and solar eclipses were already given by Anaxagoras who was born around 500 BCE and rather modern concepts like an eternally expanding universe and the existence of elementary and inseparable instances named “atoms” as the building blocks of all matter in the universe (dated back to Leucippus) existed among the Athenian scholars. However, it was the geocentric model of Aristotle (c. 384-322 BCE) that was adopted until the 17th century among universities of western Europe (see Fig. 1.2). The Aristotelian cosmology treated the earth as fundamentally different in nature than the celestial objects which are not composed of the four elements water, earth, air and fire but made of a fifth element named “ether.” In his view, the earth should be at the center of all motions in the cosmos. Believing that only perfect circles revolved in uniform motion could be allowed trajectories for all celestial objects, the varying angular velocities that were observed from the planets were later brought into consistence with Aristotle’s model by the mathematician Apollonius of Perga (c. 240-170 BCE) and the astronomer Hipparchus (c. 190-120 BCE) through the construct of epicycles centered on the earth. Heliocentric views also already exist during antiquity as proclaimed by e.g. Aristarchus of Samos (c. 310-230 BCE) but due a lack of scientific methodology and technical tools none of these different models could be either validated or rejected [TJ04].

Apart from the controversial debates about the correct interpretations of the

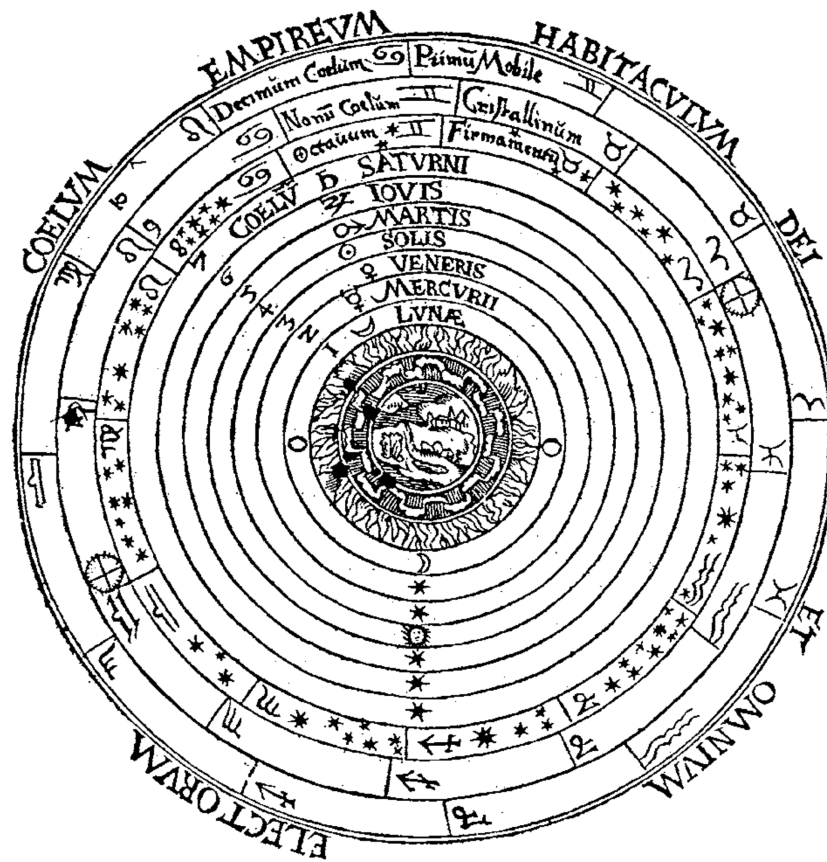


Figure 1.2: The world model of Aristotle as depicted by Petrus Apianus around 1530. The earth which is decomposed into the four elements is in the center. Around the earth there are seven celestial spheres, one for each of the six planets including the moon and one for the sun. The three outer spheres contain the fixed stars and impose their own movements on the lesser spheres. As an addition to Aristotle’s model, the void outside the “tenth heaven” is depicted as the realm of God that spans into eternity. Figure taken from [TJ04], originally from [HS77].

celestial bodies’ movements, the first scientific measurements of the size of the earth and the relative distances between earth, sun and moon go back to the Greek natural philosophers Aristarchus, Hipparchus and Eratosthenes of Cyrene (c. 276-194 BCE). Invoking a simple, but at this point sufficient model of the solar system they were able to conduct geometrical calculations that were purely based on measurements. While the results of the relative distances of sun and moon were off by about one order of magnitude, due to large uncertainties in the measurements and the lack of tools provided by trigonometry, the first estimate of the size of the earth had a deviation of less than 2% from the correct value. The greatest achievements of ancient Greek astronomy have been compiled in a treatise, later known as the *Almagest*, which also contained a catalog of 1022 stars along with their corresponding coordinates and magnitudes [TJ04].

After the fall of the Roman empire, the intellectual center of astronomy moved to the Arabic world. The *Almagest* had been translated into Arabic and served

as a guide and reference for astronomical observations for centuries. Many astronomical observatories have been built in western Asia during the end of the first millennium and the beginning of the second and more precise measurements of the positions and magnitudes of stars have been summarized in astronomical and mathematical tables like the *Hakemite Tables* (around c. 1000 CE) and the *Ilkhanik Tables* (c. 1271 CE) [TJ04].

It was not until the second decade of the 16th century that the geocentric cosmology of Aristotle was questioned again by Nicolaus Copernicus (1473-1543) who revived the heliocentric hypothesis of Aristarchus. Following up on Copernicus' hypothesis, Thomas Digges (1546-1595) and Giordano Bruno (1548-1600) added the proposal of the stars being self-illuminated and in their nature equal to our sun while being distributed over varying distances in infinite space rather than being attached to celestial spheres at fixed distances. On top of this break with the traditional Aristotelian model, Bruno also suggested, that even the sun itself is not the center of the cosmos but is, like the earth, in constant motion. And since he thought of the stars not being different from the sun, he also speculated about an infinite number of worlds equal to the earth. These claims however, were not based on scientific observations but rather on fiction and personal beliefs [TJ04, PR14].

1.2. The dawn of modern astronomy

Almost two millennia after the first scientific deductions of the distances of sun and moon and the size of the earth by the ancient Greek, it were Tycho Brahe (1546-1601) and Galileo Galilei (1564-1642) who made the next step forward in observational astronomy. They deduced the distances of the planets by measuring their parallax and spotting time variations beyond the sublunar region like the emergence of new stars in 1572 and 1602 and variations on the surface of the sun. Tycho Brahe's observations on the motions of celestial bodies served as the basis for his student Johannes Kepler's (1571-1630) discovery of the three empirical laws of planetary motion nowadays known as "Kepler's laws." Though quite accurately describing the planetary motion, Kepler's laws were still lacking a theory of the driving force behind those motions until Isaac Newton (1642-1727) formulated his law of gravity in his famous treatise *Philosophiae naturalis principia mathematica* in 1687. Therein he related the nature of earthly and celestial motions and identified the driving force behind them as the attraction between two massive bodies which is proportional to the product of the two masses and inverse to the square of their distances [TJ04].

Now not only supported by observations but also by a conclusive underlying theory, the heliocentric model with the infinite number of sun-like, self-illuminated stars began to flourish and geocentrism lost all credibility. However, the distances of the stars were still subject of speculation since no parallax could be measured from the earth's orbit around the sun until the 1830s. It was the mathematician and astronomer Christiaan Huygens (1629-1695) who first used a conceptually completely different approach to determine the distance of the star Sirius. Starting

from the assumption that all stars, including Sirius, are compatible to the sun in nature, he compared the diameter of the sun and Sirius by pointing his telescope at the sun and covering one side of its tube with an opaque plate that had a hole of variable size. He then reduced the diameter of the hole until the sun appeared to have about the same brightness as Sirius. Huygens found, that he had to reduce the diameter to the 27664th part of the angular diameter of the sun and hence claimed a distance of Sirius to be 27664 times the distance of the sun, i.e. 27664 au (astronomical units¹). Despite its actual distance being about 20 times larger as known nowadays [LF07], there was no flaw in his methodology but only in his assumption of uniformity of the stars of which no better record had been held at his time. This measurement is illustrative for the change in scientific methodology and the scientific revolution going on during the late 17th century [TJ04].

With the first usage of refracting telescopes at the time of Galilei, and later also reflecting telescopes going back to Newton, new tools were at the hands of astronomers and astrophysicists to study the universe in more detail. Also the mathematical development of the differential calculus by Newton and Gottfried Wilhelm Leibnitz (1646-1716) helped theorists to provide their models in the form of precise mathematical expressions. Among the greatest astronomical achievements of that time was the first evaluation of the speed of light by the Danish astronomer Ole Rømer (1644-1710) by making use of the time delay of Jupiter moon eclipses along the orbit of the earth. With the higher angular resolution of the telescopes as compared to the naked eye also the first proper motions of close-by stars were discovered during the 18th century falsifying the picture of “fixed” stars. It took until the early 19th century until Newton’s discovery of the spectral decomposition of light was used by Joseph Fraunhofer (1787-1826) to discover about six hundred dark lines in the spectrum of the sun (see Fig. 1.3). Initially a mystery, the lines were soon after reproduced in laboratory experiments and identified as unique fingerprints of the elements traversed by the light. As such, these spectral lines or *Fraunhofer lines* provided a completely new well of information about the celestial objects and for the first time a method to determine their chemical composition has been found. Also, knowing about the finite speed of light, deductions about relative motions of stars and – using the thermodynamical laws of Josef Stefan (1835-1893), Ludwig Boltzmann (1844-1906) and Wilhelm Wien (1864-1928) – their surface temperature could later be made by measuring relative shifts and the broadening of spectral lines due to the Doppler effect (Johann Christian Doppler, 1803-1853) [TJ04].

The gradual improvement of optical devices made it also possible to observe the annual parallactic motion of close stars for the first time in 1838 by Friedrich Wilhelm Bessel (1748-1846). This was the first direct experimental proof of the motion of earth and thus of the heliocentric model. Also the distance of those

¹The distance measure of one astronomical unit (au), which corresponds to the average distance between the center of masses of sun and earth has not been defined at the time Huygens drew his conclusions about the distance of Sirius. In 2012 the astronomical unit has been redefined to be exactly 149 597 870 700 m [IAU12].

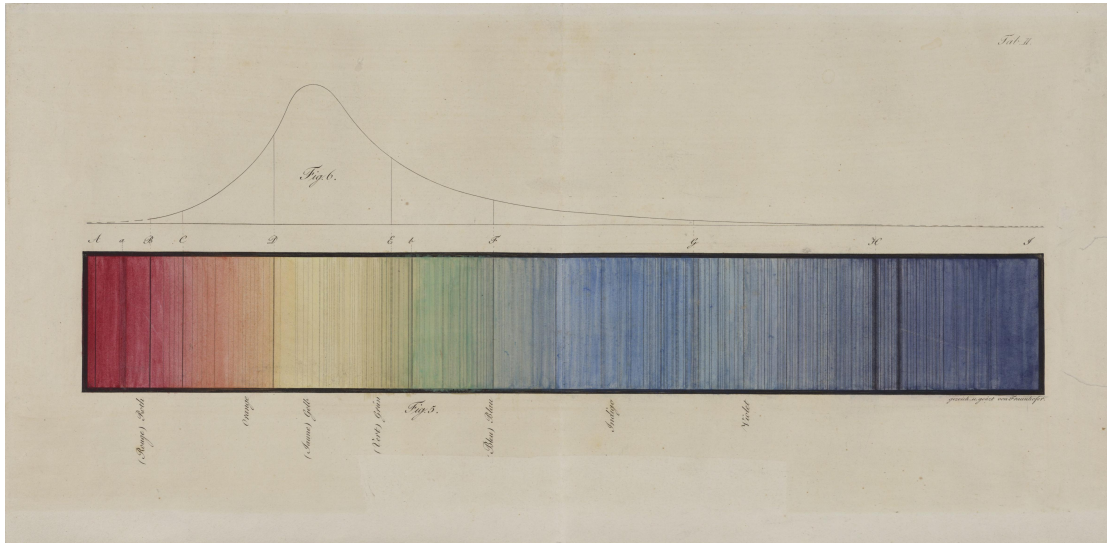


Figure 1.3: The dark lines in the spectrum of the sun as recorded by Joseph Fraunhofer [FJ17]. The upper curve depicts the spectral distribution of sunlight.

stars with a measurable parallax could be determined with good precision through simple geometric deduction. Knowing the distance of the sun, a new measure of distance d , the *parsec* (pc), has been defined in these terms as the inverse of the angular diameter of the parallactic motion in arcseconds p'' :

$$d = \frac{1}{p''} \text{ pc.} \quad (1.1)$$

The distance measurement of close stars using annual parallactic motion was the first step towards the geometrical mensuration of the universe that we today know as the *cosmological distance ladder*. This mensuration involves different techniques to measure the distances of astronomic objects which are successively farther away allowing for cross-calibration of each technique with the preceding one. Thus it nowadays allows us to identify some objects even up to the distance range of Gigaparsecs. With a first glance of the distance of the closest stars, ideas arose proclaiming a universe that extends well beyond the visible stars. Those ideas were driven by observations of cloud-like structures among the stars, named *nebulae*. Early on they were interpreted by Christopher Wren (1632-1723) as something he called “island universes.” Later this hypothesis got elaborated by the German philosopher Immanuel Kant (1724-1804) who suggested that those nebulae might actually be systems of distant stars much like the star system we are living in – the *Milky Way*. The resolution of those nebulae into clusters of stars by William Herschel (1738-1822) and his studies of the structure of the Milky Way finally lead to the picture of the *galaxies* that correctly identifies the Milky Way as only one system of stars among countless others. [RM85]

Astroparticle physics

PARALLEL to the rapid evolution of our understanding of cosmology and the enormous distances associated to it, great discoveries were also made in the field of the smallest structures accessible through science: the physics of elementary particles. Though the idea of matter being composed of atoms dates back at least until the 5th century BCE, it was due to John Dalton (1766-1844) that the atomic theory was brought into modern science [RA05]. First indications for the existence of a subatomic structure were found during the end of the 19th century: the discovery of the *electron* by Joseph John Thomson (1846-1950) during his experimentation on cathode rays [TJ97], *X-rays* by Wilhelm Röntgen (1845-1923) [RW95] and *radioactivity* by Henri Becquerel (1852-1908) [BH96], Marie Skłodowska Curie (1867-1934) and Pierre Curie (1859-1906) [SM04]. The latter was identified as a type of radiation that directly came from the atomic nuclei of some heavy ores like Uranium, Polonium, and Radium. In association to radioactivity Marie Curie also found elemental transitions among the aforementioned ores [CP98]. Those transitions were named *radioactive decays* and proved that atoms are indeed alterable [CP11, GC05].

2.1. Early discoveries of the 20th century

The remnant conductivity of air has already been known since Charles-Augustin de Coulomb (1736-1806) [CC85] discovered a spontaneous discharge of electroscopes that could not be related to defective isolation or air humidity. However, this phenomenon remained without proper explanation until the discovery of radioactivity more than one century later. The radiation emitted from radioactive ores has been found to be capable of ionizing the air thus allowing for a remnant conductivity even in absence of any humidity. Hence, the new type of radiation was dubbed *ionizing radiation*. A component of ionizing radiation of extraterrestrial origin was early discussed by Charles Thomson Rees Wilson (1869-1959) but subsequent investigations found no support for his assumption [WC01]. In the first decade of the 20th century, scientists were trying to comprehend the true nature of the ionizing radiation that was responsible for discharging electroscopes in any experiment that was performed. Radioactive ores as the source of this radiation (*terrestrial radiation*) seemed plausible at first. With time however there were more and more experimental results that could not easily be explained with terrestrial radiation alone. In 1903, Ernest Rutherford (1871-1937) found a strongly

penetrating component of ionizing radiation when he shielded the enclosed vessel of an electroscope with highly pure metal. Though the measured ionization was indeed reduced, the shielding could not prevent the discharge completely and the discharge rate could only partly be explained by the remaining radioactivity of the vessel itself. Thus the source of the ionization had to reside outside of the metal shielding either in the crust of the earth, in the air itself or even in extra-terrestrial space [CP11].

Since it was generally assumed that all ionizing radiation originates from radioactive ores in the crust, calculations were made on how the ionization should decrease with altitude [EA11a]. It was the German scientist and Jesuit priest Theodor Wulf (1868-1946) who made the effort to test the hypothesis by measuring the atmospheric ionization as a function of altitude using the improved and more mobile Wulf electroscope (see Fig. 2.1) [WT09]. In 1909, Wulf climbed the Eiffel Tower in Paris, 300 m above ground, and indeed found a reduction of ionization with altitude. However, at the top of the Eiffel Tower he found that the ionization is merely reduced to a half compared to his measurements on the ground. His findings were in tension with calculations invoking pure terrestrial radiation since these predicted a reduction to the order of only a few percent. Not having enough evidence to propose a different origin of ionizing radiation than terrestrial ores, with his measurements he could also not exclude a radiation component from outer space or from the atmosphere itself [CP11].

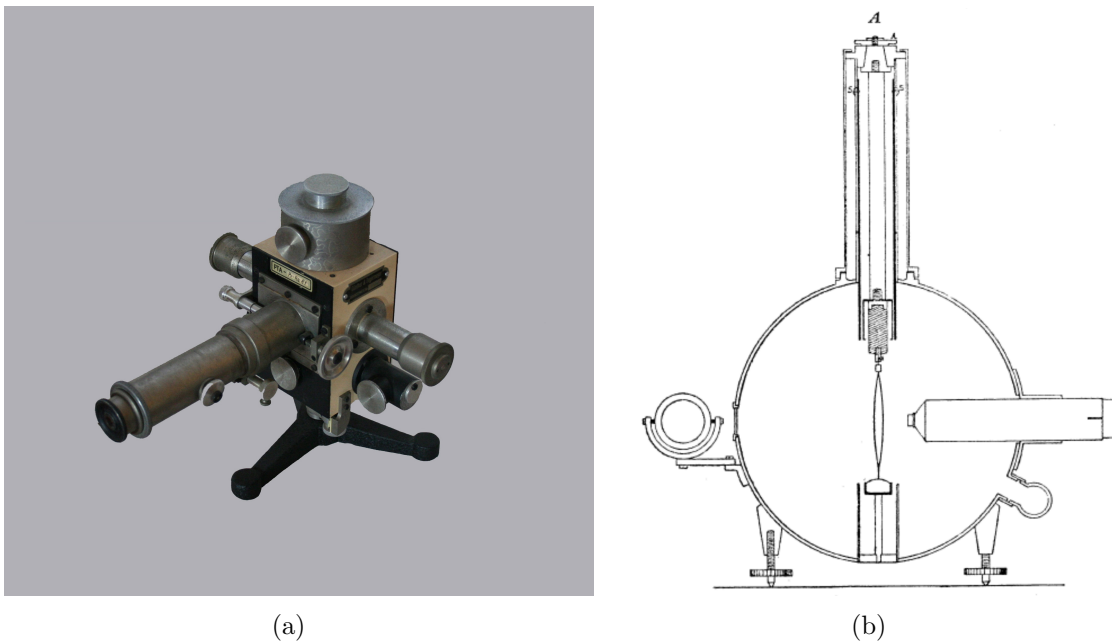


Figure 2.1: (a) The original Wulf electroscope used by Theodor Wulf around 1912 [AA12]. (b) A sketch of the Wulf electroscope that has been designed and used by Theodor Wulf in order to measure the attenuation of ionizing radiation with altitude on top of the Eiffel Tower. Image taken from [CP11], originally from [WT09].

The question about the origin of ionizing radiation was tackled again from 1909

to 1911 by the Italian physicist Domenico Pacini (1878-1934) who – following the recommendation of Theodor Wulf [WT09] – conducted measurements on a variety of places: on mountains, over lakes and over the sea [MM11, PD09, PD10, PD12]. Pacini was the first one to state that his own and many other experimental results could not be explained solely by terrestrial radiation. He found that the ionization at the ground was compatible to that measured a few kilometers off the shore over the sea in the Gulf of Genova (see Fig. 2.2). In contrary, when conducting measurements under water he realized a significant decrease already at a depth of 3 m. Perceiving the absence of a sufficient amount of radioactivity in water Pacini concluded that his measurements were consistent with the expected attenuation of radiation coming from above [PD12]. Rejecting the hypothesis of pure terrestrial radiation, Pacini was analyzing possibilities for extraterrestrial sources. In 1910 he attempted to correlate a possible increase in ionization with the passage of the Halley’s comet but found no effect. [CP11]

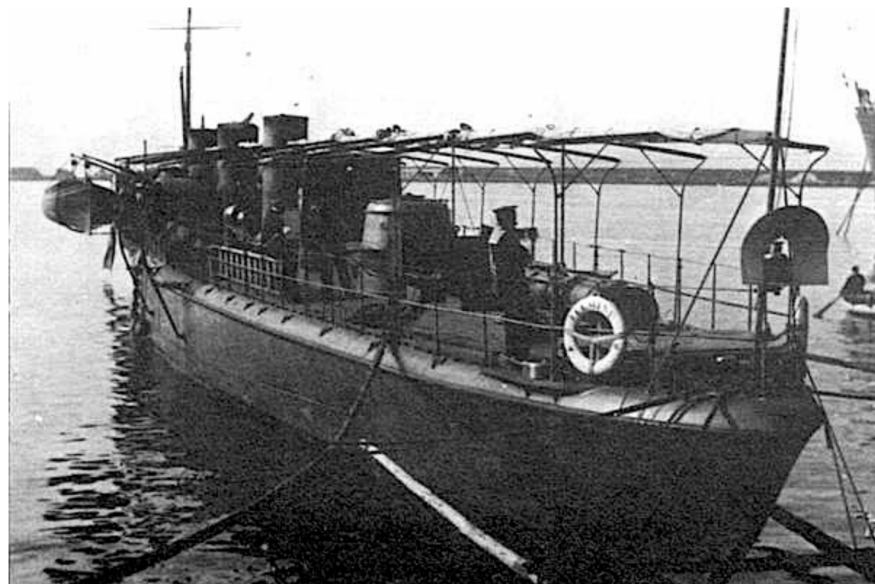


Figure 2.2: The Italian military ship “cacciatorpediniere ‘Fulmine’” from which Domenico Pacini conducted his oversea measurements of atmospheric ionization in 1910 [CP11] (courtesy of the Marina Militare Italiana).

In an attempt to further investigate the altitude effect found by Wulf, Alfred Gockel (1860-1927) undertook a series of three successive balloon flights in 1909 at which he made measurements in altitudes up to 4500 m above sea level (a.s.l.). As he could not find a further decrease in ionizing radiation compared to Wulf’s measurements, he also rejected the hypothesis of pure terrestrial radiation and suggested a large contribution of radiation not coming from the earth’s crust.

The origin of the abundance of ionizing radiation was still unsettled in the early second decade of the 20th century and scientists were struggling to match the results of Wulf, Pacini and Gockel with the prevailing hypothesis of terrestrial

radiation. It was thus that between 1911 and 1912 Victor Franz Hess (1883-1964) commenced another series of balloon flights to even higher altitudes up to 5200 m a.s.l.. After a small decrease immediately above ground Hess noticed an increase in radiation above 1000 m and found that between 4000 m and 5200 m his measurements exceeded even the radiation on ground (see Fig. 2.3(a)). He subsequently concluded that the origin of the radiation had to be extraterrestrial and excluded the sun as a source due to a lack of day-night modulation. His results were confirmed by Werner Kolhörster who later extended Hess' measurements to altitudes up to 9200 m (see Fig. 2.3(b)).

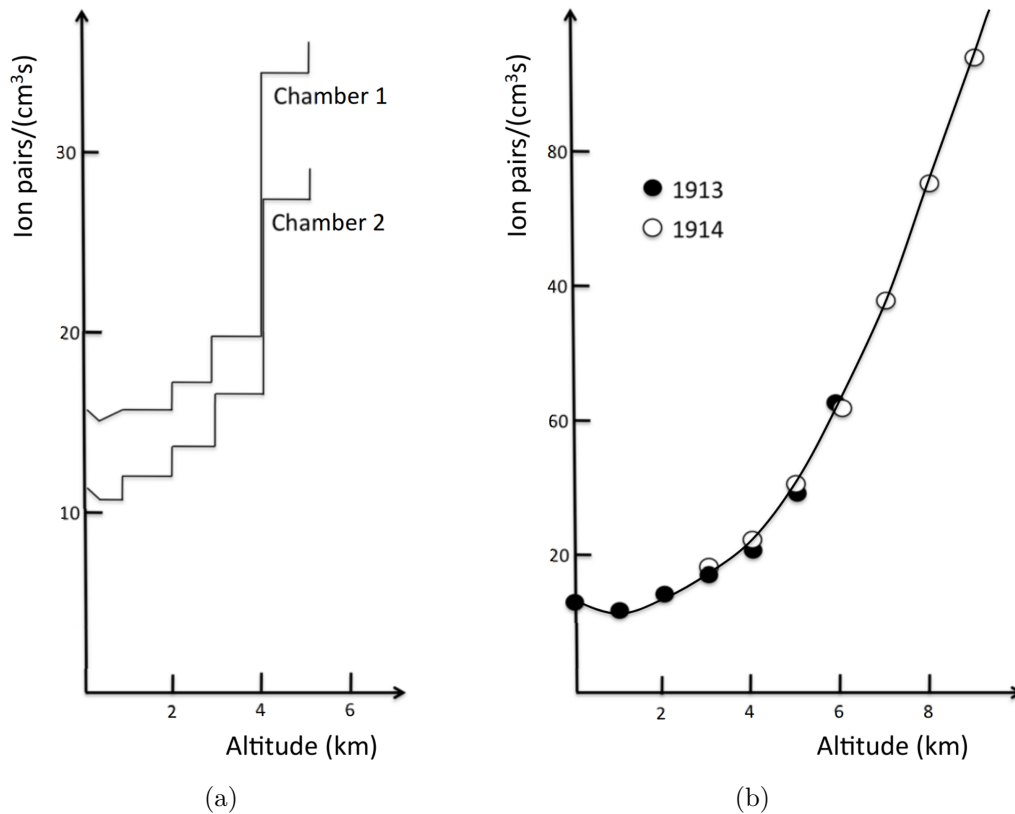


Figure 2.3: (a) The dependence of atmospheric ionization as measured by Hess during his last balloon ascent in 1912. The two curves correspond to two different Wulf-type electroscopes he used during this flight to analyze systematic uncertainties. The measurement of the third electroscopes mentioned in [HV12] is not shown here since it was designed to measure β -radiation rather than penetrating γ -radiation. Image taken from [CP11], depicting the numerical values originally given in [HV12]. (b) Werner Kolhörster's results on air ionization with altitude confirming his predecessor Victor Hess' results and extending them to higher altitudes. Image taken from [CP11], depicting the numerical values originally given in [KW13] and [KW14, HV18].

The term *cosmic rays* has first been advertised by Robert Andrews Millikan (1868-1953) in 1926 who claimed that those cosmic rays have to be γ -rays due to their penetrating properties known from radium decays [MR26a, MR26b, MR26c].

Thereafter, different experiments were performed by Jakob Clay (1882-1955) [CJ27, CJ28] measuring the geomagnetic latitude dependence of cosmic rays and Walther Bothe (1891-1957) and Kolhörster [BW29] performing coincidence counting with the newly developed Geiger-Müller counters. Those experiments suggested a corpuscular and charged nature of cosmic rays as opposed to Millikan's conviction. That dispute about the true nature of cosmic rays was only settled when Arthur Holly Compton (1892-1962) confirmed the previous results of Clay, Bothe and Kolhörster in 1933 in a series of independent experiments [CA32, CA33]. The correct identification of the predominant component of cosmic rays as protons was due to Marcel Schein (1902-1960) in 1941 [SM41].

2.2. Progenitors of particle physics

The invention of the cloud chamber by Wilson in 1912 [WC12] enabled the observation of tracks produced by through-going cosmic ray particles (see Fig. 2.4). Through application of external electric and magnetic fields it was possible to analyze the properties of those particles and classify them. It was thus that with the beginning of the 1930s new types of particles were being discovered starting with the discovery of the *positron* in 1932 by the American physicist Carl David Anderson (1905-1991) [AC32, AC33]. The positron, as the positively charged counterpart of the electron, was also the first piece of anti-matter to be detected. Its existence had been predicted by Paul Adrien Maurice Dirac (1902-1984) four years earlier in 1928 as a solution of his famous Dirac equation which describes the free propagation of an electron and, necessarily, its anti-particle [DP28].

In the same year as the positron, also the neutron has been discovered conclusively by James Chadwick (1891-1974) [CJ32] based on a series of preceding experiments by Bothe and Irène Joliot-Curie (1897-1956) and Frédéric Joliot-Curie (1900-1958) on a phenomenon formerly named "Beryllium radiation." Only shortly after the announcement of the discovery of the *neutron*, the Russian physicist Lew Dawidowitsch Landau (1908-1968) published his calculations and predictions about the existence of stars mainly composed of neutrons (*neutron stars*) which he was working on already prior to the discovery of the neutron [LL32]. The stability of neutrons in a neutron star, as opposed to the finite lifetime of free neutrons, is based on the Pauli exclusion principle theorized in 1925 by Wolfgang Ernst Pauli (1900-1958) [PW25]. Following the exclusion principle neutrons cannot decay into occupied electron states. The electron states inside a neutron star however should already be occupied up to energies levels well above the 0.77 MeV, which is the maximum energy of electrons from neutron decays. Hence, the stability of neutrons within the conglomerate of a neutron star.

With the exclusion principle Pauli also introduced a new two-state quantum number which was shortly after revealed as the electron spin by George Eugene Uhlenbeck (1900-1988) and Samuel Abraham Goudsmit (1902-1978) [UG25, UG26]. To preserve energy, momentum and angular momentum in nuclear β -decay Pauli postulated the existence of the *electron neutrino* ν_e in 1930 [PW30]. Experimental

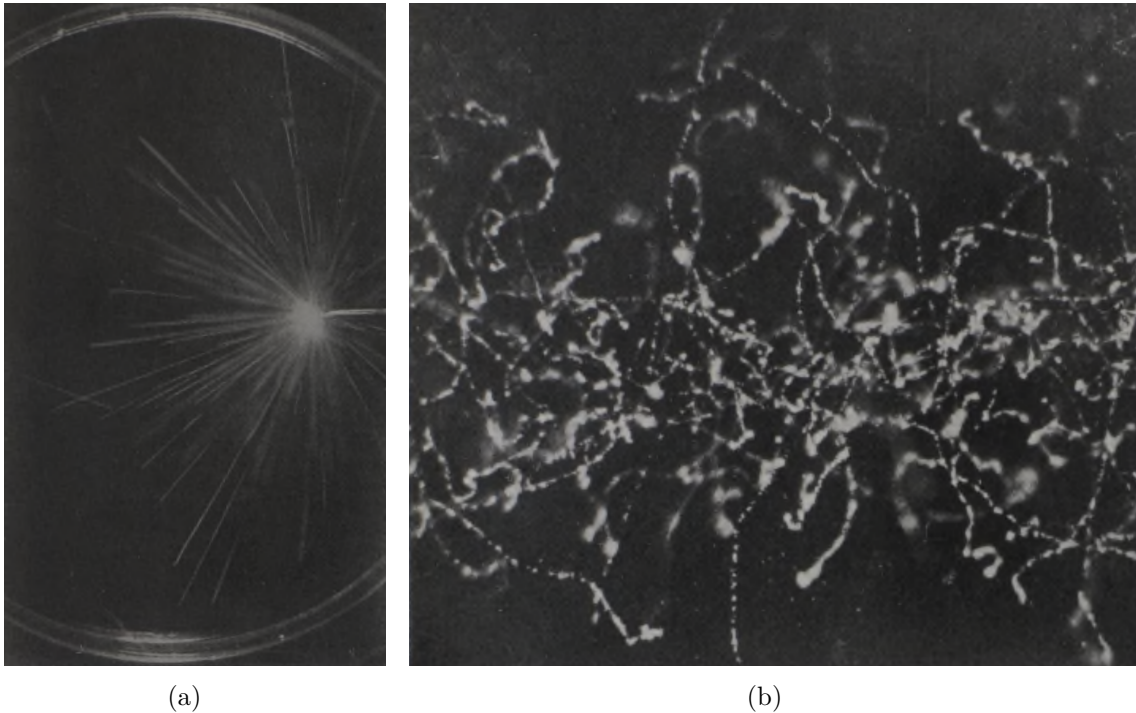


Figure 2.4: Two images of particle tracks visualized through a cloud chamber as they were originally published by Wilson in 1912 [WC12]. (a) α -rays from a radium source. (b) ions produced in air by a cylindrical x-ray beam of 2 mm radius passing from right to left.

evidence for the existence of the neutrino was not found until 1956 [RF56].

The next particle from cosmic radiation to be discovered in a cloud chamber was the *muon* μ in 1937 by Anderson and Seth Henry Neddermeyer (1907-1988) [AC36]. The muon was initially mistaken for the previously theorized Yukawa particle (Hideki Yukawa, 1907-1981, [YH35]) due to its mass and charge. But its lack of strong interactions made it evident that it did not fulfill Yukawa's requirements of a particle that mediates nuclear bonding. The latter has been found with the discovery of the charged *pions* π^\pm in 1947 by the group around Cecil Frank Powell (1903-1969) who used photographic emulsion plates instead of cloud chambers to image particle tracks from cosmic radiation [OG47]. The discovery of the neutral pion π^0 took place in 1950 at the cyclotron of the University of California and was the first new particle that has been found using a dedicated earth-bound accelerator experiment rather than cosmic rays [BR50].

Further particles kept showing up in cosmic ray experiments like: the neutral and charged *kaons* $K^{0,\pm}$ in the late 1940s and the Λ^0 , Ξ and Σ hyperons with the beginning of the 1950s [GC05]. The urge for a deeper understanding of elementary particles and their underlying mechanics separated the branch of elementary particle physics from cosmic ray physics to some extent. Earth-bound particle accelerators aiming for higher and higher energies were built throughout the following decades to study the behavior of elementary particles in high energy colli-

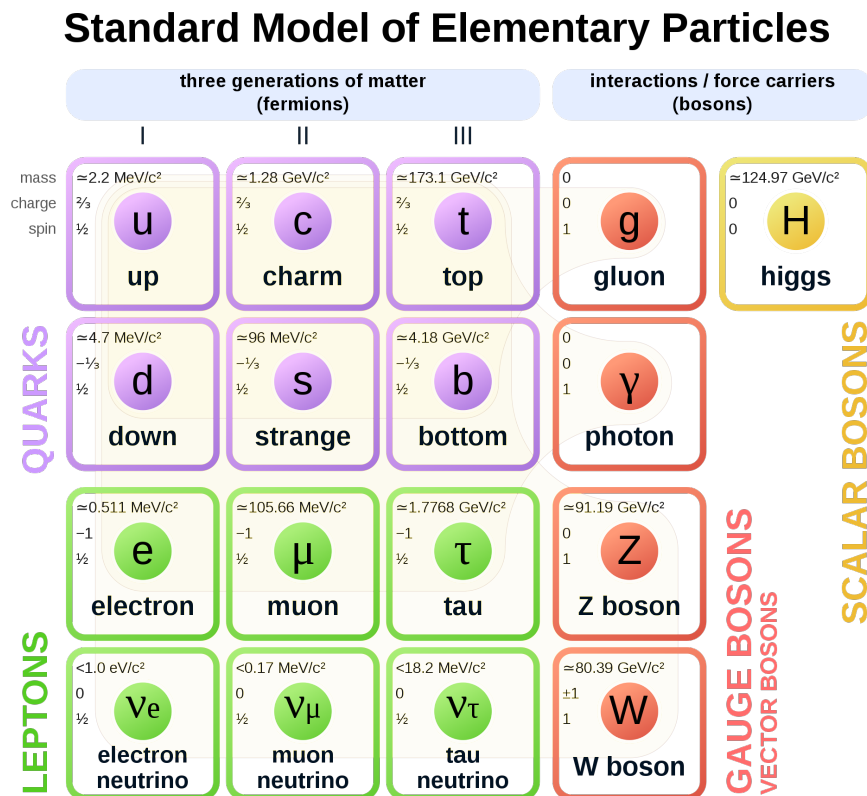


Figure 2.5: A schematic view of the Standard Model of Elementary Particles as of the year 2020 [URL5]. The elementary particles of the matter that is described by the model is entirely composed of six *quarks* and six *leptons* which are each divided into three *flavours* or *families* and their corresponding anti-particles. The forces between those particles are mediated by the four types of vector gauge bosons with the W-boson splitting up into a negative and a positive charged version and the *gluon* comprising actually eight types of different color-anticolor combinations. The *Higgs* boson is an excitation of the Higgs field through which the massive particles obtain their mass [GD08].

sions. Those experiments revealed further types of particles and interactions and eventually lead to the development of the so called “standard model of elementary particles” (term first coined by Abraham Pais and Sam Treiman in 1975 [CT98]). The standard model describes the physics of all ordinary matter in the visible universe and its dynamics as it is known to us at the present day (see Fig. 2.5). While the analysis of the variety of newly discovered particles defined the new discipline of *elementary particle physics*, the study of the primary cosmic radiation itself established its own research field, named *astroparticle physics* [GC05].

2.3. The beginning of astroparticle physics

In the 1930s the contribution of a significant fraction of cosmic rays to the overall atmospheric ionization was a commonly accepted fact. Still veiled in mystery

however was the nature of that radiation. The problem of disentangling cosmic rays from background effects like terrestrial radiation, remnant radioactivity in the air and even in the material of the measurement devices itself was tackled by Erich Regener (1881-1955). His measurements on the isotropic flux of radiation as a function of altitude were transferred into predictions on the vertical flux by Bernhard Gross (1905-2002) [RE33, GB33] (see Fig. 2.6(a)). Using a threefold coincidence counting technique involving three Geiger-Müller counting tubes, Regener together with his student Johann Georg Pfozter (1909-1981) accomplished to measure the flux of incident cosmic rays from zenith angles less than 20° and experimentally confirmed the existence of a maximum in the ionization curve at an altitude of about 20 km [RE35] (see Fig. 2.6 (b)). This maximum was expected in the case that the cosmic radiation measured in the atmosphere was actually only the product of collisions of primary cosmic rays with atomic nuclei high in the atmosphere. The phenomenon of high energy radiation causing particle avalanches (“showers”) in lead plates was already known from experiments by Bruno Benedetto Rossi (1905-1993) [RB33] and was now also found for cosmic radiation in the atmosphere.

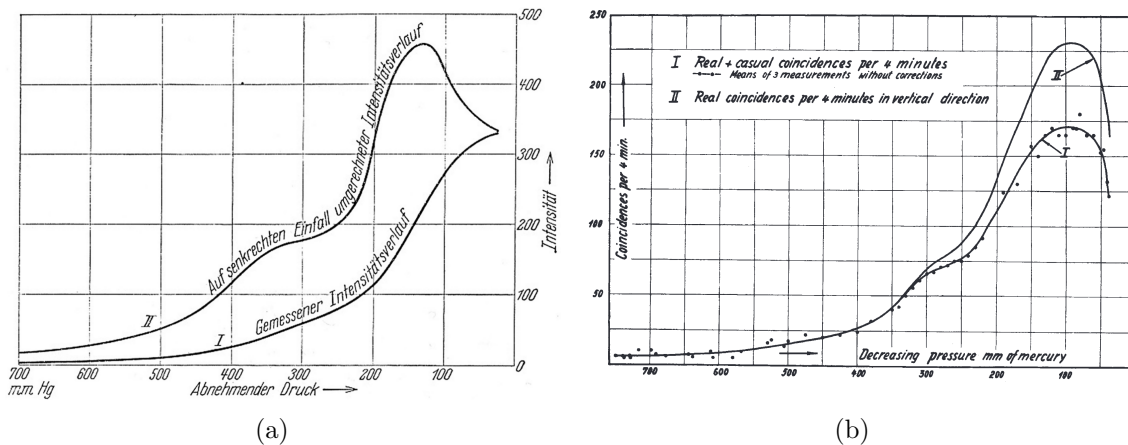


Figure 2.6: (a) The lower curve shows the measured isotropic intensity of primary cosmic rays as a function of decreasing atmospheric pressure with altitude [GB33]. The upper curve displays the therewith derived vertical component of the flux. (b) The flux of cosmic rays from zenith angles less than 20° as measured by Regener and Pfozter in 1935 [RE35].

The particle showers in the atmosphere were directly observed in 1938 by the group of Pierre Victor Auger (1899-1993) [AP38a, AP38b]. Expecting a similar shower development in the air as Rossi found in lead plates, Auger conducted measurements with spatially separated particle counters. With an improved resolving time of $5 \mu\text{s}$ [MR28] Auger registered coincident particle arrival times that clearly exceeded the expectations from chance coincidences. He compared measurements at sea level and at high altitudes at the Pic du Midi (2900 m a.s.l.) and the Jungfrauoch (3500 m a.s.l.) and was able to measure coincidences with detector separation distances up to 300 m (see Fig. 2.7). Auger extrapolated the

particle counts in his detectors to a total number of 10^6 particles per shower and consequently labeled the phenomenon “extensive cosmic-ray showers” (later *extensive air showers*). From his measurements he derived primary particle energies in the order of 10^{15} eV which was by far more than any man-made experiment could accomplish at that time [AP39].

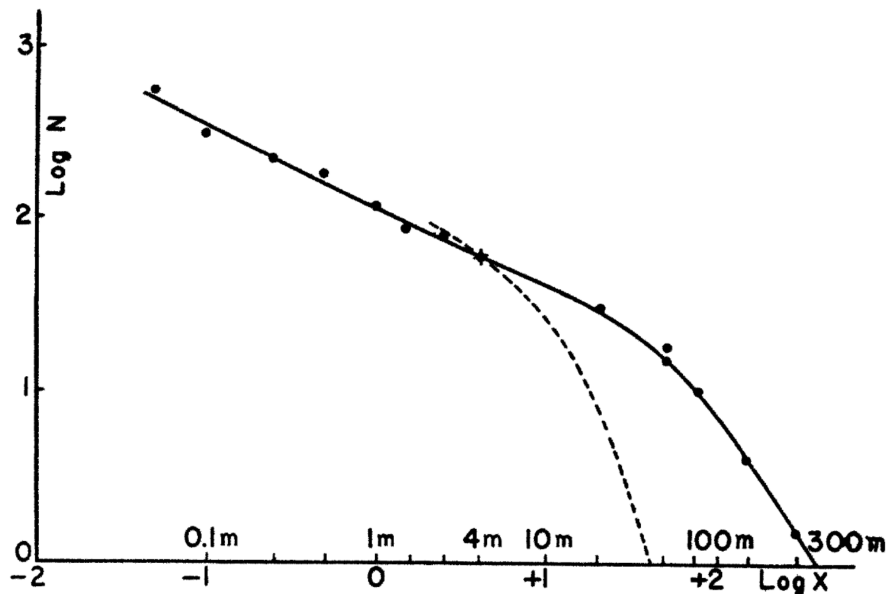


Figure 2.7: The coincidence rate measured by Auger with two horizontal and parallel counters as a function of increasing distance between them [AP39]. The detection of coincident particles separated by up to 300m was the first direct proof of extensive air showers. The dashed line shows a calculation from Hans Euler predicting the coincidence rate with cascade equations derived from particle showers in lead. Auger assumed the discrepancy between the predictions and the data to come from an enhanced production of weakly interacting particles of medium mass (“mesotrons”) in air showers compared to showers in lead.

An impression of the true extent of the cosmic ray energy spectrum was obtained in 1962 when John Linsley (1925-2002) measured an air shower with a primary energy of $\sim 10^{20}$ eV with an array of 19 plastic scintillation detectors at Volcano Ranch near Albuquerque New Mexico [LJ63]. The existence of cosmic rays of such extreme energies was confirmed by different experiments in the following decades [LM91, TM03]. The most energetic particle that has ever been measured had a reconstructed energy of $(3.2 \pm 0.9) \times 10^{20}$ eV and was detected in 1991 at the Fly’s Eye air shower detector in Utah [BD95]. The detection of a cosmic ray particle at that energy was and still is especially puzzling since a strong flux-suppression is expected above $\sim 6 \times 10^{19}$ eV due to interactions of primary protons or nuclei with the cosmic microwave background (CMB). Hence the detection of particles beyond that threshold suggests a relatively close source [GK66, ZG66].

The bulk of primary cosmic rays at moderate energies could be measured more and more precisely since the first satellite-based experiments were launched in

1957 and 1958 (attached to the Sputnik 1 and the Explorer 1 satellites). Type and arrival direction of the primary particles were then directly accessible before any particle interaction in the atmosphere. Another generation of satellite-based experiments measuring extraterrestrial γ - and X-rays were to follow in the late 1960s and the first point sources of high energy extraterrestrial radiation could be identified in – among others – the Crab Nebula, and the binary star systems Vela X-1 and Cygnus X-3 [GC05].

With the directional reconstruction of primary cosmic rays, be it with the reconstruction of air showers or with direct measurements at satellite-based experiments, a new discipline within the field of astroparticle physics arose, namely *particle astrophysics*: in addition to optical observations of astronomical objects or measurements in the infrared or radio regimes, these objects could now also be analyzed “in the light of” high energy cosmic rays. Given the extreme conditions that are necessary to accelerate cosmic rays to the highest energies, these messenger particles provide important insights into the physics of their sources.

The content of this particular thesis shall be a continuation of the long line of work done in this field and as such probe a just recently discovered type of astronomical source: the merging processes of compact binary systems (compact binary mergers, CBMs) with measurements of an associated flux of photons among the highest energy cosmic rays.

Cosmic rays and extensive air showers

MUCH progress has been made in the field of astroparticle physics since the discovery of cosmic rays more than a hundred years ago. The energy spectrum of the incident particle flux has been measured over several orders of magnitude and its chemical composition has been unveiled for a large fraction of the spectrum. The experimentation methods have been evolving continuously during that time in order to tackle the most fundamental questions related to cosmic rays like their origin or the different acceleration and interaction mechanisms that produce their spectral shape as known to us today. Some sources of high energy cosmic rays have already been identified, and numerous models exist that describe the acceleration capabilities of the most violent astrophysical sites to explain the observations of cosmic ray particles at the very highest energies. In this chapter, the current state of knowledge revolving around the field of cosmic rays and its unsettled questions are summarized in Sec. 3.1 to 3.3. Extensive air showers, which were first measured by Pierre Auger in the 1930s, are nowadays a common tool to measure the properties of primary cosmic ray particles at the highest energies. The physics behind those phenomena are described thereafter in Sec. 3.4.

One peculiar task is the identification of neutral particles, like primary photons or neutrinos, among the highest energy cosmic rays. Specifically those neutral messenger particles would not only pinpoint their sources since they are not deflected by magnetic fields, but could also be correlated with transient astrophysical sources at large distances from earth as they travel virtually at the speed of light. An identification of neutral messengers among the cosmic ray flux can also give important insights into the physics of their production sites. Primary photons at ultra-high energies (UHE), i.e. above $\sim 10^{18}$ eV, and the currently ongoing search for those messengers are tackled in Sec. 3.5. Implications of UHE photon searches on the field of multimessenger astronomy are discussed in Sec. 3.6.

3.1. The cosmic ray energy spectrum

The all-particle energy spectrum of primary cosmic rays extends from energies below 1 GeV to energies beyond 100 EeV ($1 \text{ EeV} = 10^{18} \text{ eV}$) covering more than eleven orders of magnitude. The associated particle flux follows a steep profile that can roughly be described by a power law $d\Phi/dE \propto E^\alpha$ with an approximate spectral index $\alpha \simeq -3$. As a consequence, the fluxes that have been measured

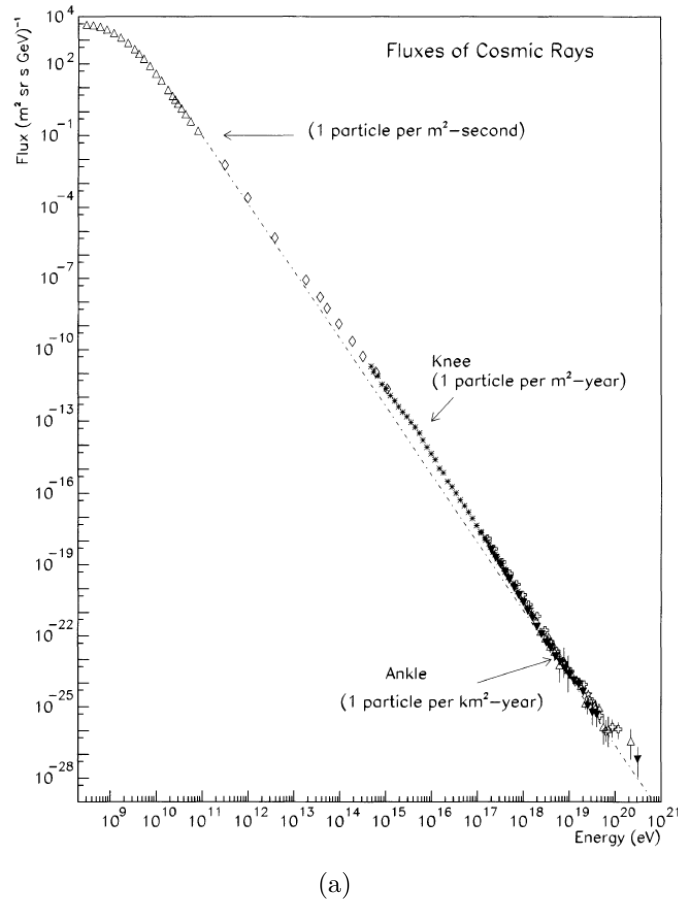


Figure 3.1: (a) The differential all-particle energy spectrum of primary cosmic rays [SS01].

over the whole energy spectrum span over more than 30 orders of magnitude (see Fig. 3.1). At the low end of the energy spectrum the integral flux is as high as several thousand particles per square meter and second. The cosmic ray flux is suppressed by solar activity generating a magnetic field that deflects particles from outside the solar system with energies below the GeV-range. The sun itself however contributes to the low energy cosmic ray flux (up to GeV) in the form of electrons, protons and a small fraction of heavier nuclei [TJ04]. Up to energies of a few PeV where the flux is in the order of one particle per square meter and year, direct measurements of the primary cosmic ray particles are possible via balloon or satellite experiments. Some more recent balloon-based experiments are ATIC [IJ95], TRACER [MD07] or CREAM [AH07] and of the satellite based experiments PAMELA [PP07] or, attached to the International Space Station (ISS), AMS [BR98] and ISS-CREAM [SE14].

The direct detection method however runs out of statistics at energies above the PeV-range. Due to the rapidly decreasing particle flux it becomes technically and financially more and more challenging to build sufficiently large detectors to compensate the low particle flux. Hence, the measurement of primary cosmic rays

with energies in excess of a few PeV have to be measured indirectly with ground-based detectors. These detectors make use of the effect of extensive air showers which were first analyzed by Auger in his coincidence measurements in the Swiss Alps. They measure the secondary particles that are produced within those air showers to draw conclusions about the initial primary cosmic rays on top of the atmosphere. Though, a reconstruction of the direction of incidence or the energy of the primary particle is more involved from the data analysis point of view, the active detector area is not limited to the size of a balloon or a satellite. The detection of secondary cosmic rays can be done in a variety of ways like the sampling of shower particles at the ground level. This technique has been used in the past at the Haverah Park experiment [TR67], AGASA [TM86], KASCADE [AT03] and KASCADE-Grande [AW10] but also in recent experiments at IceTop [AR13], the Telescope Array (TA) [AT12] and the surface detector of the Pierre Auger Observatory [AA15a]. Another way to measure air showers is the detection of air-Cherenkov radiation as it is being done at H.E.S.S. [FS04] or the future Cherenkov Telescope Array [AB13]. The isotropically emitted air-fluorescence light, which is created when air shower particles excite nitrogen atoms in the air, has been utilized for instance by the Fly’s Eye experiment and is currently being measured by TA and the Auger fluorescence detector. Air showers can also be analyzed through measurements of radio signals generated by geomagnetic charge separation and the Askaryan effect [HT13] (Tunka-Rex [BP15], AERA [KJ11]). At the very highest energies above 10^{20} eV the particle flux is so low that on average less than one particle per square kilometer and century arrive at earth. Giant ground-based detector arrays like the Telescope Array or the Pierre Auger Observatory which cover hundreds or even thousands of square kilometers are needed to accumulate a sufficient amount of data for a statistical analysis of these rare events [MS18].

Though at first glimpse the energy spectrum of cosmic rays seems to follow a simple power law distribution, a closer look reveals a variety of spectral features which express themselves through transitions in the spectral index. When multiplying the energy spectrum with a power of the primary particle energy, these features become more prominent and can even be seen by the naked eye (see Fig. 3.2). The first significant feature is visible around 4 PeV, commonly called the cosmic ray “knee.” At this point, the spectral index steepens from $\alpha \simeq -2.7$ below the knee to $\alpha \simeq -3$ above. A second steepening, called the “second knee”, follows at around 100 PeV leading to a spectral index of $\alpha \simeq -3.3$. A less prominent transition is also visible between the first and the second knee around 20 PeV which leads to a hardening of the spectrum from spectral indices somewhat below -3 to values slightly above. Between 100 PeV and 5 EeV the spectral index stays rather constant. At the “ankle” around 5 EeV the spectrum hardens towards a spectral index of $\alpha \simeq -2.6$. Above 40 EeV a strong suppression becomes apparent and the existence of a final cutoff with an exponential flux suppression above 200 EeV is indicated by recent results. Though, the statistics in this energy region is still too low to give a conclusive picture of the particle flux at those energies. A comprehensive picture from various measurements of the energy spectrum above

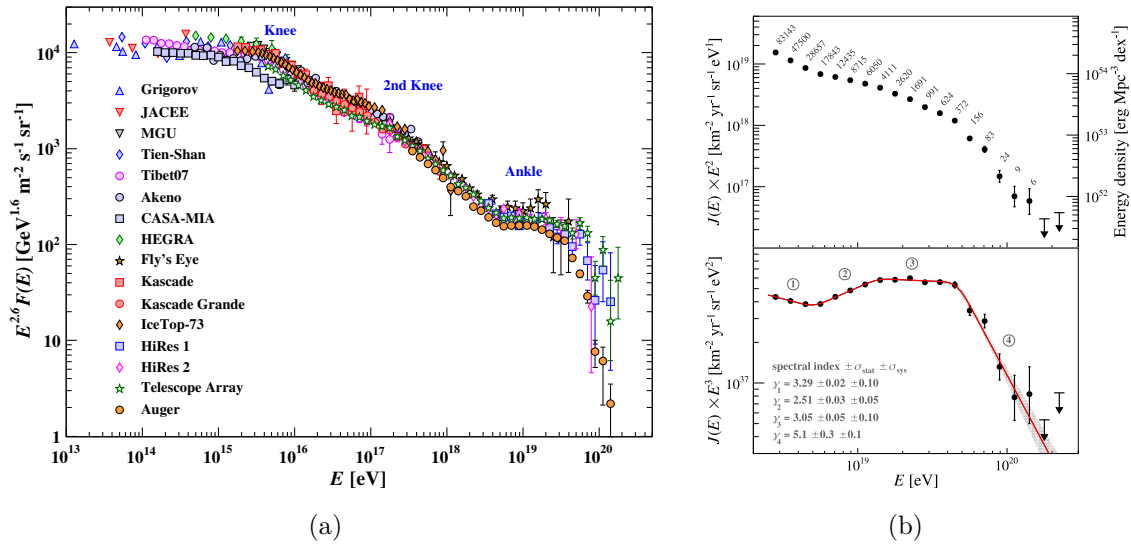


Figure 3.2: (a) The energy spectrum above 10 TeV as measured by multiple experiments [MS18]. The ordinate is multiplied by $E^{2.6}$ to highlight the energy dependent features of the spectral index. (b) The energy spectrum above 3 EeV as measured by the Pierre Auger Observatory [AA20b]. The upper figure shows the spectrum scaled by E^2 which provides an estimate for the energy density per decade. The number each to next point denotes the number of detected events in each energy bin. The lower figure shows the spectrum scaled by E^3 to highlight the changes in the spectral index. The shaded area indicates the uncertainty of the fit.

10 TeV is given in Fig. 3.2(a). Recent results from the Pierre Auger Observatory expose two further significant features of the spectrum in the UHE regime. At about 13 EeV, the spectrum changes from $\alpha \simeq -2.51$ to $\alpha \simeq -3.1$ and softens further with $\alpha \simeq -5.1$ beyond 50 EeV (see Fig. 3.2(b)) [MS18, AA20b].

The origins of the many features along the energy spectrum are related to the sources of cosmic rays, their production mechanisms, interactions and propagation through the interstellar medium and to their chemical composition. Hence, the shape of the spectrum is an indicator for various aspects of astrophysics and elementary particle physics. The origins of the knee and the second knee, though not fully explained yet, are likely due to a rigidity²-dependent process. As such, the second knee follows the spectrum of primary iron (Fe) ions and reflects the first knee as a feature of the proton spectrum at about $1/26$ -th of the energy of the second knee. The steepening of the spectrum could be caused by a rigidity-dependent maximum energy that can be obtained from galactic sources [PB61] or due to a diffusion and drift effect causing cosmic rays to escape the galaxy above a certain energy threshold [PV93]. The flattening of the spectrum at 5 EeV can be explained by a transition between galactic and extra-galactic cosmic rays which happens in the region between the second knee and the ankle. Showing no correlations with

²Rigidity $R = |\vec{p}|/eZ$, with the absolute value of the momentum $|\vec{p}|$, the elementary charge e and the nuclear charge number Z , e.g. $Z = 1$ for protons and $Z = 26$ for iron nuclei.

the galactic plane or the galactic center, cosmic rays with energies above the ankle are commonly believed to have extra-galactic origin [MS18]. The strong suppression starting at 40 EeV has been predicted already in 1966 by Greisen [GK66], Zatsepin and Kuzmin [ZG66] shortly after the discovery of the cosmic microwave background (CMB). They proposed an interaction of primary cosmic ray protons at ultra-high energies with photons from the CMB as

$$p + \gamma_{CMB} \rightarrow \Delta^+(1232) \rightarrow \begin{cases} p + \pi^0 \\ n + \pi^+ \end{cases}, \quad (3.1)$$

later named the Greisen-Zatsepin-Kuzmin (GZK) effect. Such an interaction with a resonance energy of 1232 MeV and the temperature of the CMB ($T_{CMB} = 2.7260 \pm 0.0013$ K [FD09]) would lead to an energy-cutoff of the cosmic ray proton spectrum around 50-60 EeV (and for heavier nuclei at respectively higher energies). However, apart from the steepening of the spectrum no evidence for this process has been found so far. Thus, the question if the flux suppression is caused by the GZK effect or is due to the limitations of the acceleration mechanisms, which by coincidence result in similar spectral features as the GZK effect, is still unsettled [MS18].

3.2. Sources and acceleration mechanisms

At the low end of the energy spectrum, the sun is an efficient accelerator of cosmic rays. The dynamics of the electromagnetic fields generated by sunspots pose suitable sites for the acceleration of charged particles up to a few GeV [GC05]. Cosmic rays of higher energies evidently originate from outside the solar system as their arrival directions do not show any correlation with the sun. The identification of extra-solar sources of cosmic rays however is more complicated since charged particles are being deflected by galactic magnetic fields and do thus not point back to their site of production or acceleration. From the spectral shape one can tell that cosmic ray acceleration is a non-thermal process that requires an active acceleration mechanism in order maintain a power law dependency over several orders of magnitude [LM01].

Promising candidate sources within the galaxy are the remnants of supernovae (SNRs). At the shock fronts of SNRs, which can expand over timescales of 10,000 years, cosmic ray particles may get scattered back and forth between the medium of the expanding supernova ejecta and the interstellar medium each time gaining or losing a statistical amount of energy. This mechanism, called first order Fermi acceleration, is in theory capable of accelerating cosmic rays up to energies of the EeV-scale while providing a spectral distribution similar to that observed in cosmic ray measurements [BA78]. A similar mechanism proposes magnetized molecular clouds as possible acceleration sites. Charged particles in such molecular clouds could successively gain energy by repeatedly being reflected between randomly moving magnetic mirrors. Since this mechanism is technically similar but less efficient than the acceleration at SNRs, it is named second order Fermi

acceleration [FE49]. First direct evidence for cosmic ray acceleration in a SNR was the discovery of photons with energies beyond 100 TeV from the Crab Nebula (see Fig. 3.3(a)) measured with the Tibet air shower array in 2019 [AM19]. Photons of such energies are expected to be produced when primary cosmic rays interact with matter surrounding the SNR like the solar wind of the progenitor star.

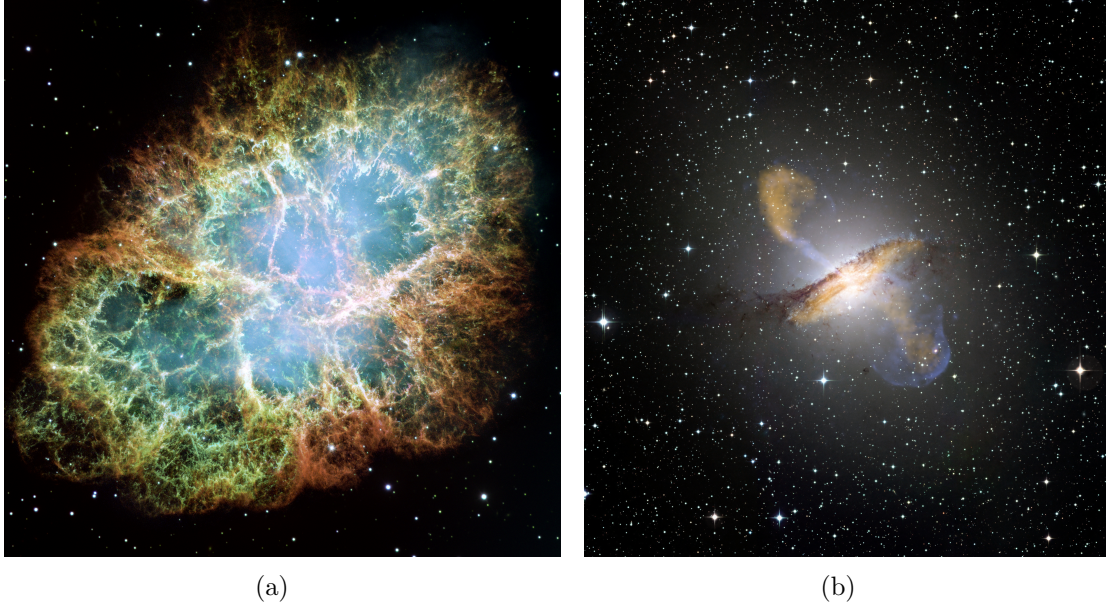


Figure 3.3: (a) A mosaic image taken by the NASA’s Hubble Space Telescope of the Crab Nebula [NA05]. The structure is the remnant of a supernova that took place in 1054 CE and was at its time observed and recorded by Chinese astronomers. At its center is a rapidly spinning neutron star, a *pulsar*, which powers the luminous blue color of the inner region by confining highly energetic electrons in its magnetic field. The expanding shock fronts of the SNR are suitable sites for the acceleration of galactic cosmic rays up to the EeV range via first order Fermi acceleration. (b) The radio galaxy Centaurus A [ES09]. The colors shown in the picture depict a wide range of wavelengths obtained from different measurements in the X-ray (blue), sub-millimeter (orange) and optical bands (dust lane in the galactic disk and background stars).

The acceleration of cosmic rays to energies above the ankle is typically attributed to extra-galactic sources. This claim has found additional support in the recent discovery of a dipole structure of UHE cosmic rays by the Pierre Auger Observatory (see Fig. 3.4) [RE19, AA18]. It became evident that this dipole, which has an amplitude of $0.066^{+0.012}_{-0.009}$ above 8 EeV, points about 125° away from the galactic center. Taking into account deflections in the galactic magnetic field, the alignment of the dipole is more consistent with the direction of the outer spiral arm of the galaxy or the flux-weighted dipole of close galaxies (closer than 100 Mpc) listed in the 2MRS catalog [RE19]. The mechanisms that are capable of generating such large amounts of energy however are still not entirely clear. Some contribution to the flux above 3 EeV might be attributed to radio galaxies (see Fig. 3.3(b)). Having galactic nuclei that are emitting an extraordinary amount of matter in the

form of giant jets (active galactic nuclei, AGN), the compact nuclei as well as the giant radio lobes provide an environment that should be able to accelerate cosmic rays up to energies beyond 10^{20} eV in cases of very powerful radio galaxies like M87. The isotropy of UHE cosmic rays on the other hand cannot be explained by radio sources alone as only relatively close sources are expected to contribute to the flux at the highest energies due to the GZK suppression. The number of close-by radio galaxies, however, is limited to only a few suitable candidates from which an excess of UHE cosmic rays should be measurable [LM01].

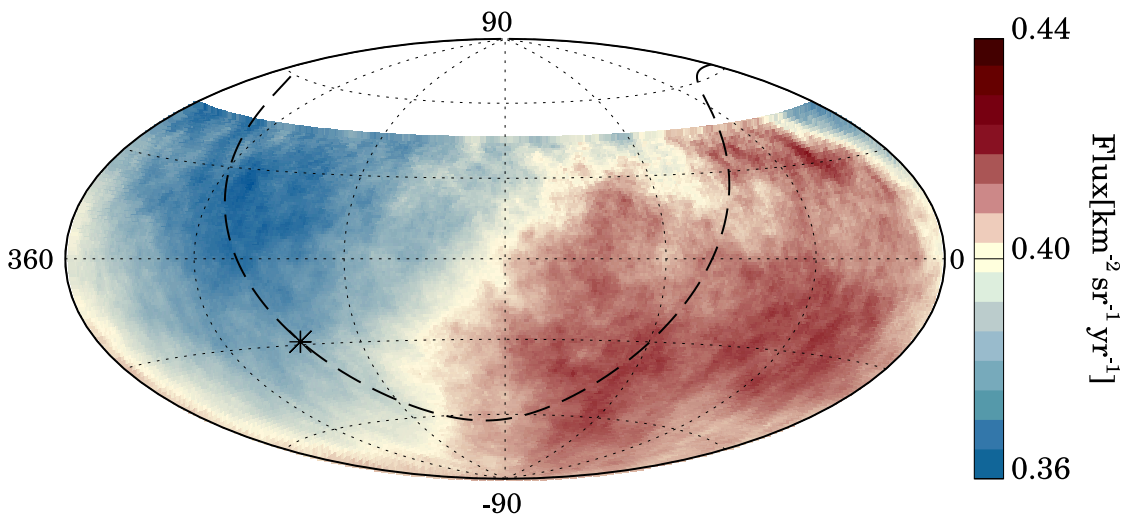


Figure 3.4: The cosmic ray flux above 8 EeV in equatorial coordinates averaged over top-hat windows of 45° radius [RE19]. The dashed line represents the galactic plane and the asterisk marks the direction of the galactic center.

In general, the capability of an astronomical site to accelerate charged particles can roughly be classified by two parameters: its elongation L and its average magnetic field B . For the acceleration process, a cosmic ray particle has to be confined to its source. With increasing energy, also its Larmor radius increases until the particle at some point leaks out of the magnetic confinement of the acceleration site. Also stronger magnetic fields lead to smaller Larmor radii and hence to particles being confined inside smaller volumes. The relation between L , B and the corresponding maximum attainable energy E_{\max} can be expressed by the formula

$$E_{\max} \simeq \Gamma e Z B L, \quad (3.2)$$

which depends on the charge eZ of the nucleus that is being accelerated. The Lorentz boost factor Γ accounts for sources that move with respect to the rest frame of the observer. A classification of astronomical sites by Z and B has first been compiled by Hillas in 1984 [HA84]. Such a Hillas-plot is shown in Fig. 3.5. The diagonal lines in Fig. 3.5 represent the exclusion criteria below which a potential source candidate is not expected to accelerate protons (or respectively iron) to energies above 100 EeV since the particles would escape the magnetic field before

reaching that energy. For boosted sources these lines are shifted downwards (blue lines in Fig. 3.5 as an example for $\Gamma = 100$). Corresponding lines for lower energies of the same particle types would also enter the plot as downward shifted parallel lines.

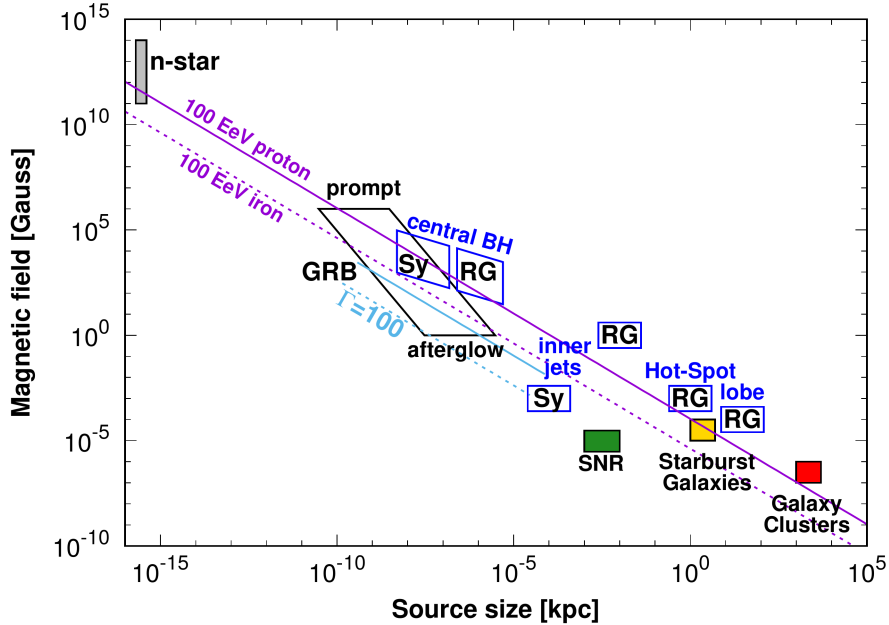


Figure 3.5: The Hillas plot shows different possible acceleration sites for cosmic rays categorized by their typical size and magnetic field [MS18]. The diagonal lines indicate the threshold for the capability of a source to accelerate particles of a given charge (here proton and iron) to energies above 100 EeV. For lower energies as well as for boosted sources ($\Gamma > 1$) these lines are shifted downwards. The acceleration sites shown in the plot are neutron stars (n-star), gamma-ray bursts (GRB), the central black holes (BH) of Seyfert (Sy) and radio galaxies (RG) and their respective inner jets, lobes and hot-spots, supernova remnants (SNR), starburst galaxies and galaxy clusters.

Another possible type of source for UHE cosmic rays are the merging processes of binary neutron star (BNS) systems. Though the existence of neutron stars and BNS systems has been known for quite some time [HR75], a direct observation of the final merging process has not been accomplished until the detection of a gravitational wave signal from a BNS in 2017 by the Advanced LIGO and Virgo detectors [AB17a]. These processes can produce highly turbulent magnetic fields and result in the birth of magnetars – young neutron stars hosting a particularly strong magnetic field [KV17]. During the merging process and shortly after, particle acceleration up to the EeV scale and possibly even beyond has been predicted [PA16, KS19a, DV19a]. Also the merging processes of binary systems of stellar mass black holes are speculated to be capable of accelerating cosmic rays to high energies given appropriate boundary conditions. Though, these events are expected to be less efficient than BNS mergers [KK16]. Due to the transient nature of these events and the short observational history, the acceleration hypotheses

could not be tested thoroughly so far.

3.3. Composition

The most abundant particles in the spectrum of primary cosmic rays are protons ($\sim 85\%$) and helium nuclei ($\sim 12\%$). Heavier elements also exist among the cosmic rays but they only pose a small fraction. The flux of electrons is in the order of 1% of the fraction of primary protons and mostly contributed by the solar wind. Electrons thus occupy the lower end of the energy spectrum. Antiparticles (anti-protons and positrons) have also been found among the cosmic rays but are extremely rare compared to the particle fluxes. The abundance of anti-particles is well consistent with the expectations of anti-particles generated in collisions of cosmic rays with interstellar dust and rules against the hypothesis that there might be large amounts of anti-matter in the observable universe [GC05].

The overall chemical composition of primary cosmic rays resembles many features of the elemental abundances in the solar system (see Fig. 3.6). In general, atomic nuclei which contain even numbers of protons or neutrons are more stable and thus more abundant than those which contain odd numbers. This behavior can be understood in the picture of the shell model of the atomic nucleus which attributes more binding energy to pairs of nucleons with a net spin of zero. Nuclei in which one or both nucleon numbers are a “magic number” (i.e. 2, 8, 20, 28, 50, 82 and 126) are especially stable since they have only fully filled up orbital shells which is also reflected in cosmic rays. Also iron (Fe) is especially abundant in the solar system as well as in cosmic rays since it is the heaviest element which can be generated in exothermal stellar fusion processes. Heavier elements which can be produced in supernova explosions or BNS merger [VF15] do also exist among the cosmic rays but are less abundant compared to iron by a factor of $\sim 10^{-4}$ to 10^{-5} [GC05].

The deviations between the cosmic ray composition and the elemental composition of the solar system as they are visible in Fig. 3.6 for the elements lithium (Li), beryllium (Be) and boron (B) can readily be explained by the spallation of the elements of the CNO-group (carbon, nitrogen and oxygen) in collisions with the gas in the interstellar medium. The same holds for the elements just below iron, produced in the spallation of primary iron particles, which also show a larger abundance in cosmic rays than in the solar system. The under-abundance of hydrogen (H) and helium (He) might reflect the chemical composition of their respective sources. Also, the large ionization energy of those elements could pose an obstacle for their injection into the initial acceleration mechanism [MS18].

The chemical composition of cosmic rays strongly depends on the energy of the primary particles (see Fig. 3.7). While at the lowest energies around 1 GeV there is predominantly hydrogen (i.e. protons), the spectrum of primary particles contains increasingly heavier components at higher energies. The hardening of the spectrum that starts around 100 GeV is more pronounced for heavier nuclei. Thus, at around 1 PeV He is more abundant than H and at energies beyond the

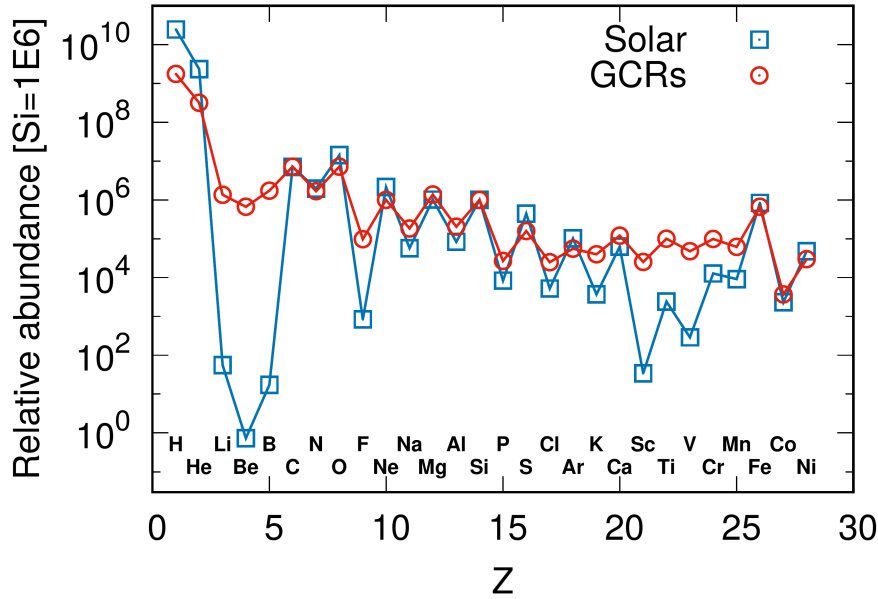


Figure 3.6: The relative abundances of elements in the solar system and in cosmic rays (up to nickel, Ni). The numbers are normalized to a value of 10^6 for silicon (Si). Image taken from [MS18] referencing data from [LK03, LK13, SD85].

cosmic ray knee, heavy elements in the mass range of Fe dominate the cosmic ray spectrum [MS18].

The composition around the ankle region and beyond is still subject of ongoing research. Due to the extremely low particle flux at those energies only indirect measurements are possible. Detectors with large apertures are necessary to gather a sufficient amount of statistics for analyzing the mass spectrum. Recent results from the Pierre Auger Observatory clearly show a trend towards a lighter composition when approaching $10^{18.3}$ eV and again towards a heavier composition above (see Fig. 3.8(a)) [YA19]. A pure composition around the ankle region is already excluded at high significance as deduced in [AA16d] and [YA19] from measurements of the atmospheric depth of air shower maxima X_{\max} (see Sec. 3.4) and its correlation with the ground signal. Combined fits to the X_{\max} -distributions using predictions from air shower simulations give a first picture of the chemical composition up to energies above 2×10^{19} eV (see Fig. 3.8(b)) [AA14] and even beyond 10^{20} eV taking also sources and propagation effects into account [AA17d]. These studies suggest that the predominant particle type of the primary cosmic rays shifts towards successively heavier elements with increasing energy. Pure compositions and mixtures of H and He are disfavored at energies below 10^{19} eV and excluded with high significance between $10^{18.5}$ eV and $10^{18.7}$ eV while with increasing energy, the picture is more consistent with a less mixed composition [YA19]. As well, a significant contribution of primary iron-like particles is not expected at energies below 10^{19} EeV. However, the combined fit analysis of the cosmic ray spectrum and the composition [AA17d] suggests a dominant contribution of iron-like particles at the high end of the observed energy spectrum above 10^{20} eV.

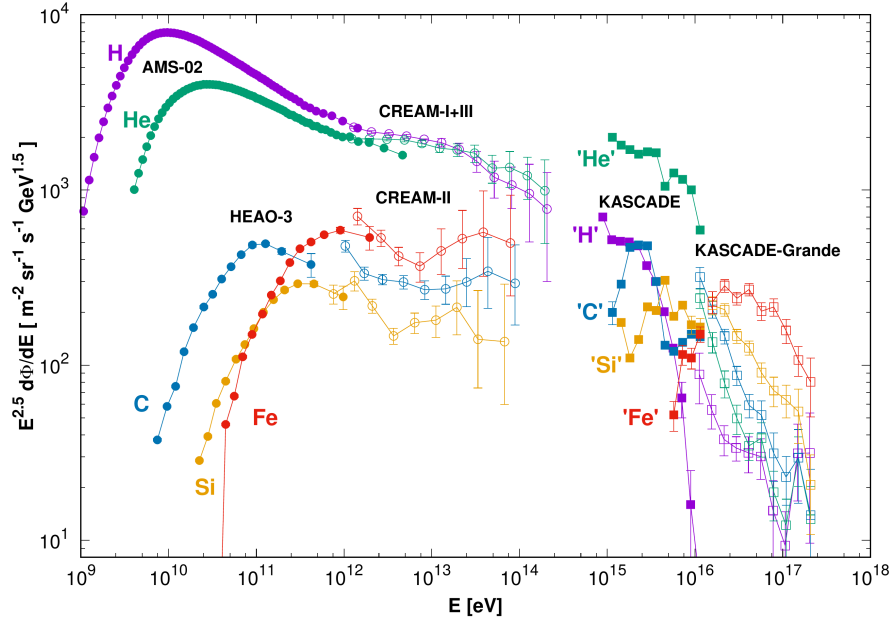


Figure 3.7: The cosmic ray spectra for individual primary particle types as measured by AMS, HEAO and CREAM for energies up to the cosmic ray knee [MS18]. The measurements above the knee taken with KASCADE and KASCADE-Grande refer to mass ranges labeled after a representative particle type from each group rather than individual elements since an identification of the primary particle could not be done with the indirect detection method of using air showers. Their measurements further inherit the uncertainties of the hadronic interaction models that were used to perform the simulations on which the analysis is based. For references on the individual measurements shown in the plot, see the references within [MS18].

3.4. Extensive air showers

When cosmic rays approach earth they first enter the geomagnetic field before they reach the atmosphere. While cosmic rays with energies $E \gtrsim 1$ GeV are only being deflected by the magnetic field leading to a latitude-dependent apparent anisotropy in arrival directions, particles of lower energy can get magnetically trapped before reaching the top of the atmosphere. Those trapped particles, mostly electrons and protons, are reflected between the earth's magnetic poles multiple times before they get either absorbed in the atmosphere close to the poles – visible on earth as northern lights – or escape again into outer space. The magnetic confinement of low-energy cosmic rays inside the magnetosphere manifests as an enhancement in ionizing radiation at altitudes between ~ 2000 km and 25000 km. Those regions are known as the Van-Allen belts [GC05].

Cosmic rays that are energetic enough to traverse the geomagnetic field will interact with nuclei of atmospheric molecules (mostly N_2 , O_2 , Ar). The atmosphere has a total column density of about 1030 g cm^{-2} at sea level which corresponds to several interaction lengths and is thus opaque to high energy radiation. The atmosphere of the earth does not start suddenly at some altitude but its density

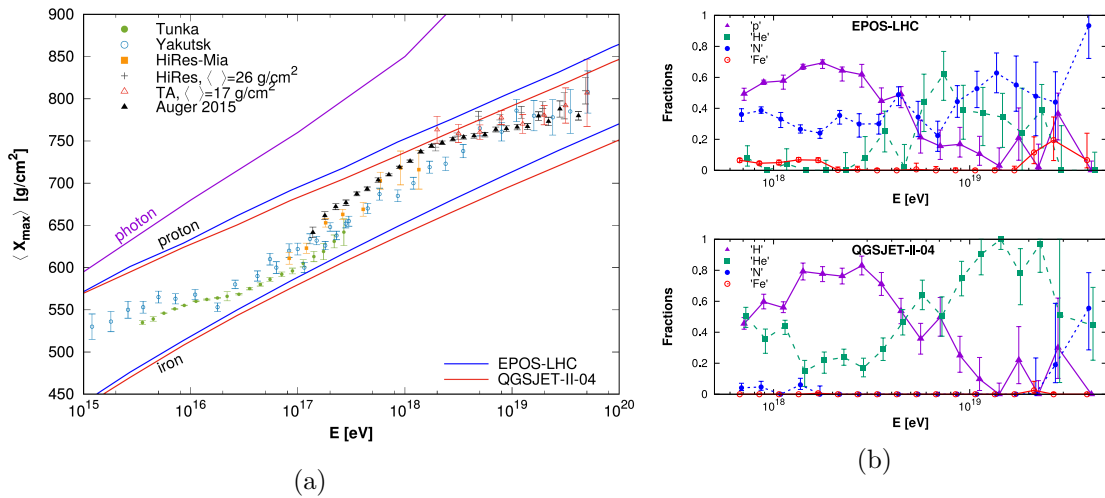


Figure 3.8: (a) Measurements of the average values of the air shower observable X_{\max} as a function of the primary particle energy [MS18]. The solid lines show expected average values for pure compositions of primary protons and iron nuclei using two different models, EPOS-LHC and QGSJET-II-04, for hadronic interactions. In addition, the expected X_{\max} values for primary photons are also indicated. The results shown in the plot refer to those given in [AA14]. (b) The reconstructed fractions of primary particle types as a function of energy as obtained by the Pierre Auger Observatory based on two different hadronic interaction models [MS18]. Pure H-He mixtures up to 10^{19} eV as suggested by the fractions obtained from QGSJET-II-04 (lower plot) are disfavored by more recent results as stated in [YA19].

rather follows an exponential form as described by the barometer formula:

$$X(h) = X(h = 0) \exp(-h/h_s) \quad (3.3)$$

where $X(h)$ is the column density at altitude h and h_s is the scale height of the atmosphere which depends on various altitude-dependent parameters like local pressure, temperature and air humidity, but can be approximated as a constant ($h_s \approx 8.5$ km [WR20]) for simple considerations. With increasing density, the interaction probability between cosmic rays and air nuclei rises as well. The first interactions between primary cosmic rays and the atmosphere typically take place at altitudes between 15 km and 20 km [GC05, GP10].

Primary hadrons, which constitute by far the largest fraction of primary cosmic rays, typically undergo inelastic scattering via strong interaction with atmospheric nuclei upon their first interaction with the atmosphere. Though in principle any hadron could be generated in such a collision (as far as it is energetically allowed), the most copiously produced particles are pions (π^+ , π^- and π^0) since they are the lightest of all hadrons. With a relative probability of about 10% compared to pions also kaons are frequently produced. If the secondary particles are also produced with a sufficient amount of kinetic energy they again can initiate further particle production in collisions with atomic nuclei. Hence, a cascade of secondary hadrons (hadronic shower) evolves through the atmosphere. Also secondary muons

(muonic shower) and neutrinos are produced through the decays of charged pions. While the neutrinos practically decouple from the particle cascade due to their stability and weak interaction, the path length of muons is mainly limited by their finite lifetime of $\tau(\mu) \approx 2.2 \mu\text{s}$ within their rest frame. Muons that are generated at high altitude can carry away large amounts of energy. Through relativistic time dilation, the lifetime of these muons is in most cases sufficient to reach the ground level before they decay. Since almost all muons are produced via pion decay, the muonic cascade is closely linked to the hadronic shower component. The decay of the neutral pions, which can be considered to be almost instantaneous (mean lifetime $\tau(\pi^0) = (8.52 \pm 0.18) \times 10^{-17} \text{ s}$ [TM18]), produces high energy photons which initiate electromagnetic cascades (electromagnetic shower). Electromagnetic showers are largely self-contained through alternating processes of electron-positron pair production and bremsstrahlung. Mainly due to the shorter radiation length of electromagnetic particles in air compared to the interaction length of hadrons (37 g cm^{-2} vs. 90 g cm^{-2} [GC05]) and a constant energy transfer from the hadronic cascade via the decay of neutral pions, the electromagnetic cascade is dominant in terms of number of particles. The bulk of all secondary particles that are produced from the same cosmic ray primary are called an *extensive air shower* or simply *air shower*. The evolution of such an air shower is depicted in Fig. 3.9 schematically and as the result of a Monte Carlo simulation. The duplication of secondary particles is stopped as soon as there is not enough energy in a collision to produce further secondary particles. Eventually, particles below that energy threshold get absorbed in the atmosphere until the whole energy of the air shower is converted into calorimetric energy. Overall, most particles that reach the ground level are muons from low energy showers with a fraction of 80% since other particle types in these showers are typically absorbed in the atmosphere before reaching the ground. Neutrinos are often disregarded in terms of air showers and treated as “lost” since they do practically not interact at all after their production and escape into deep space after traversing the earth. Thus, they are also “invisible” for most detectors [GC05, GP10].

Since the energy spectrum of primary cosmic rays follows a steep power law, the bulk of secondary particles that can be measured in the atmosphere pronounces features of predominantly low energy cascades. Primary particles with energies above the cosmic ray knee ($E \gtrsim 4 \text{ PeV}$) induce large hadronic cascades which constantly supply the electromagnetic component with energy. With every interaction, a statistically distributed amount of transverse momentum is introduced into the air shower. Hence, high energy primaries can generate large numbers of secondary particles which are distributed over several square kilometers and traverse the atmosphere in a thin layer that propagates close to the speed of light [GC05, GP10].

The number of particles N in an air shower at a given point in time is called the *size* of a shower. Since the shower size depends on the slant depth X traversed by the shower rather than on altitude it can be conveniently parameterized as a function of X which removes the dependence on the incident zenith angle to some

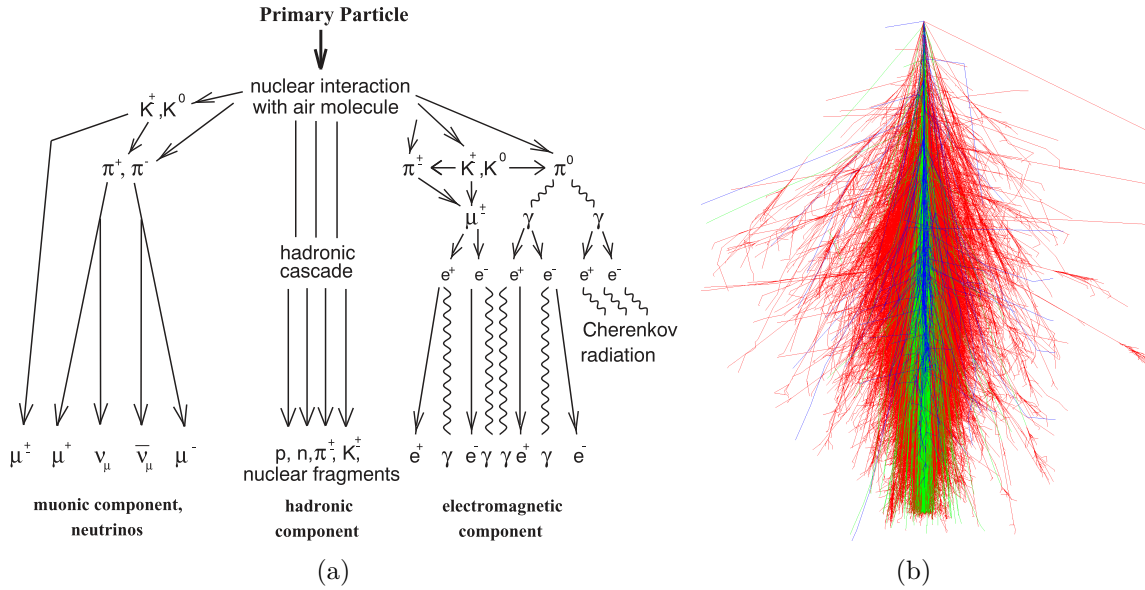


Figure 3.9: (a) A schematic view of an extensive air shower. Separately shown are the muonic, hadronic and electromagnetic components along with the predominant particle types in each of them [KB04]. (b) A visualization of a simulated air shower initiated by a vertically incident primary proton of 10 TeV. The electromagnetic shower component is illustrated in red, the muonic component in green and hadrons in blue. The graphic shows a time-integrated profile of the air shower rather than a snapshot of an instant in time. The physics simulation was performed with CORSIKA [HD98]. The visualization of the simulation output has been done with AirShower3D [KE20].

extent.³ The longitudinal development of the total shower is mainly determined by the size of its electromagnetic component (upper curve in Fig. 3.10(a)) which can be parameterized with a Gaisser-Hillas function [GT77] of the form

$$N(X) = N_{max} \left(\frac{X - X_0}{X_{max} - X_0} \right)^{\frac{X_{max} - X_0}{\lambda}} \exp \left(-\frac{X_{max} - X}{\lambda} \right). \quad (3.4)$$

X_{max} is the atmospheric depth at which the shower size reaches its maximum value N_{max} . The depth of the first interaction X_0 and the effective interaction length λ ($\simeq 70 \text{ g cm}^{-2}$) are parameters that depend on the primary particle type [MS18].

The atmospheric depth of the shower maximum X_{max} increases logarithmically with the energy of the primary particle (see Fig. 3.10(b)). This behavior can be understood qualitatively using the simple model of electromagnetic cascades proposed by Heitler (see Fig. 3.11) [HW70]. In this model, every electromagnetic particle (i.e. electrons, positrons and photons) interacts after exactly one radiation length λ with an atomic nucleus and splits up into two particles each carrying

³Very inclined showers spend a considerable amount of time in rare parts of atmosphere where charged pions are more likely to decay before undergoing nuclear interactions. This shifts the atmospheric depth at which muons are produced to lower values as compared to vertical shower.

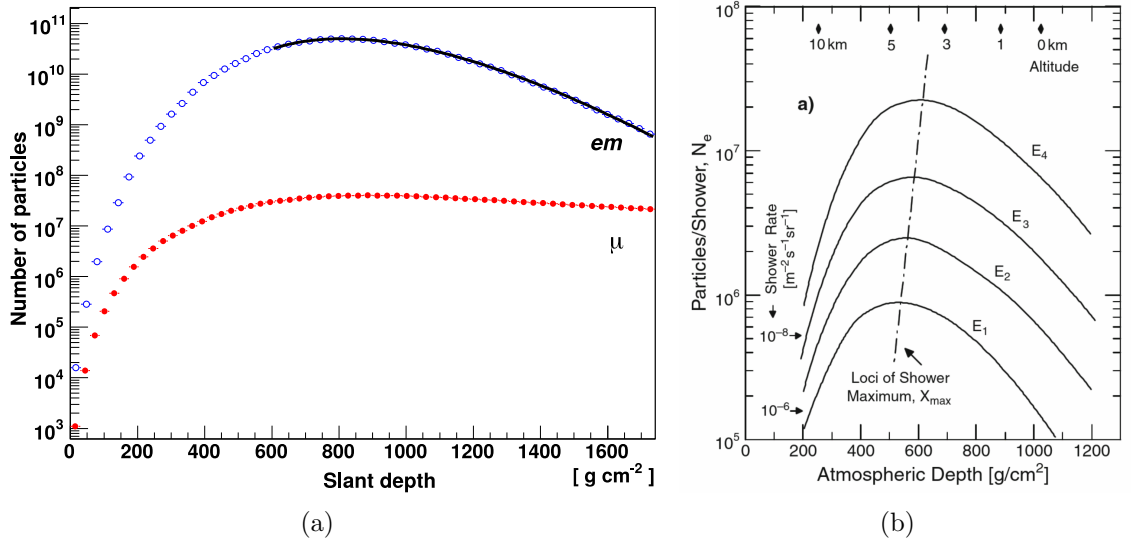


Figure 3.10: (a) Simulated longitudinal profiles of the electromagnetic (em) and muonic (μ) shower components induced by a primary proton of $E = 10 \text{ EeV}$ [MS18]. (b) Longitudinal shower profiles for four different primary particle energies $E_1 < E_2 < E_3 < E_4$ [GP10]. The maxima are connected by a dashed line to illustrate the logarithmic dependence of the shower maximum with energy, which in turn scales linearly with the maximum shower size.

away half of the initial particle energy. This splitting is motivated by electron-positron pair production in the case of photons and the emission of a photon via bremsstrahlung in the case of electrons and positrons (see Fig. 3.11). Hence, the number of particles after n interaction lengths is $N = 2^n$ at an atmospheric depth $n\lambda$. The energy of each particle of the n -th generation is E_0/N , with E_0 being the energy of the primary particle. The whole cascade is finally stopped when the particle energy drops below a critical energy E_c at which collisional energy losses exceed radiative losses and the particles get absorbed in the atmosphere. At this point, the shower in this simple model is at its maximum size. The dependence of the shower maximum on E_0 is then given by $E_0 = \lambda \log_2(E_0/E_c)$ reproducing the logarithmic relation observed in nature [MJ05, MS18].

Since muons barely interact with the atmosphere (apart from radiation losses which are still negligible even at high energies) the size of the muon shower stays almost constant after it reaches its maximum (c.f. lower curve in Fig. 3.10(a)). In high energy air showers, the energy of the charged pions produced in the first interactions is typically so high that their lifetime $\gamma\tau_\pi$ outweighs the mean time between two interactions due to a large boost factor γ . Since these pions typically interact before they can decay, muon production is suppressed and more energy is transferred into the electromagnetic shower via the decay of the much shorter-lived neutral pions. Muon production starts as soon as the pion energy falls below an energy threshold that allows the majority of charged pions to decay before undergoing further interaction. Since air showers induced by heavier nuclei with

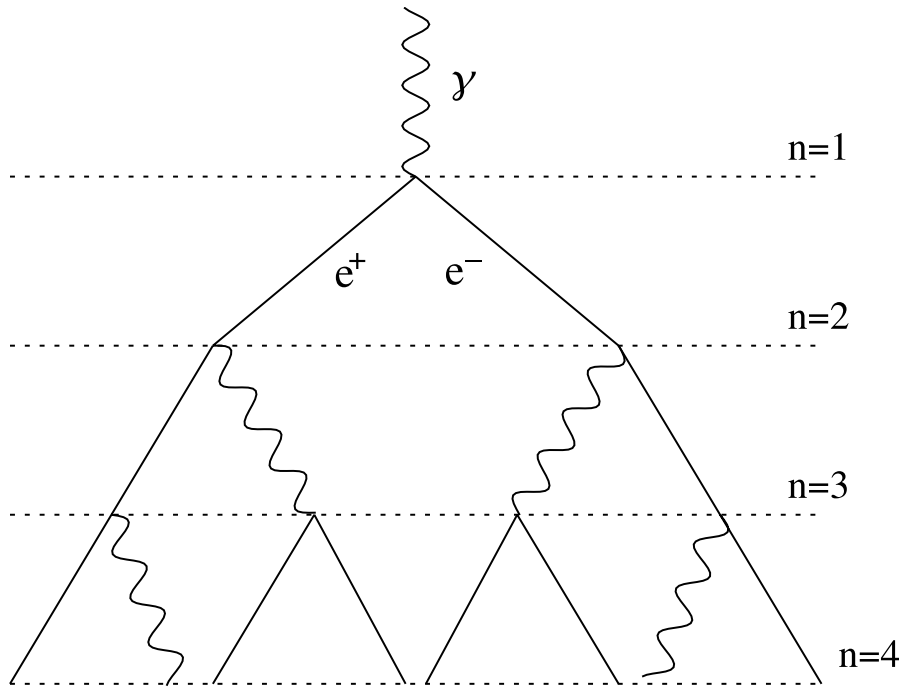


Figure 3.11: A sketch of the Heitler model used to describe basic properties of electromagnetic showers. A more detailed description of the model is given in the text. Image modified from [MJ05].

nucleon number A can be approximated by A superimposed proton showers of energy E/A , muon production starts earlier for those showers than for proton induced showers. Hence, more energy is transferred into the muon shower and the ratio between electromagnetic and muonic shower sizes can be used as an indicator for the primary particle mass [MS18].

The density of particles inside the *shower plane*, which is the plane that spans perpendicular to the direction of the incident primary particle, i.e. the *shower axis*, can approximately be described by the Nishimura-Kamata-Greisen (NKG) function [KK58, GK56] given by

$$\frac{dN_e}{dr^2} = \frac{N_e}{r_M^2} \frac{\Gamma(4.5 - s)}{2\pi\Gamma(s)\Gamma(4.5 - 2s)} \left(\frac{r}{r_M}\right)^{s-2} \left(1 + \frac{r}{r_M}\right)^{s-4.5} \quad (3.5)$$

for the case of purely electromagnetic showers and *shower age* parameters $0.5 < s < 1.5$ (see also [AT01]). The formula relates the surface density $\frac{dN_e}{dr^2}$ of electromagnetic particles at a perpendicular distance r to the shower axis to the shower age $s = 3X/(X + 2X_{\max})$. The parameter $r_M \simeq 90 \text{ m} \times (10^{-3} \text{ g cm}^{-3}/\rho_{\text{air}})$ is the Molière radius which depends on the density of the air ρ_{air} and accounts for the scaling of the lateral spread of the function and Γ denotes the gamma function. The lateral shower profile of the electromagnetic shower component is shown in Fig. 3.12 along with profiles of other shower components [MS18].

To account for both the electromagnetic and muonic shower components which can be measured by ground-based air shower detectors, a modified version of the

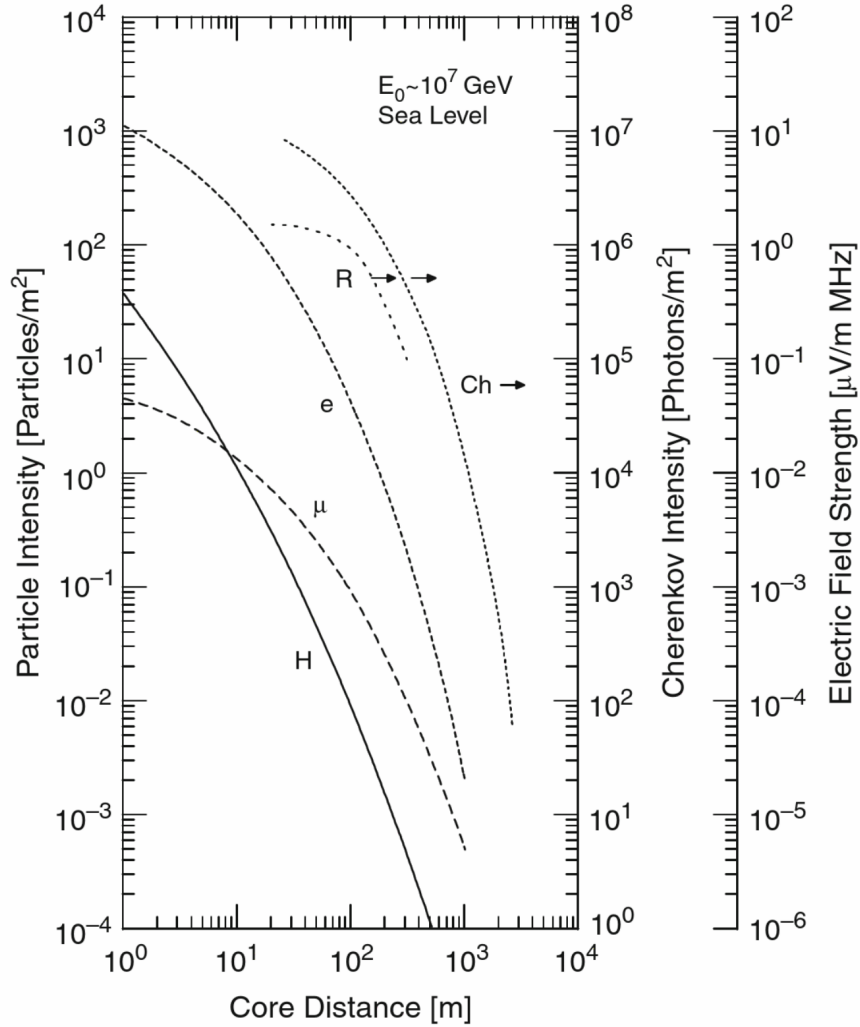


Figure 3.12: The average lateral profiles of different shower components at sea level for simulated air showers initiated by primary protons of 10 PeV [GP10]. Shown are the particle densities of hadrons (H) and muons (μ) above 1 GeV and electrons and positrons (e) above 10 GeV. Also shown as an overlay are the photon density of Cherenkov radiation (Ch) and magnetic field strength of the radio pulse (R) associated to the shower with their respective separate ordinates.

NKG function is typically used, expressing the lateral shower profile in terms of an expected amount of signal S in the detector rather than a particle density:

$$S(r) \simeq S(r_{\text{opt}}) \left(\frac{r}{r_{\text{opt}}} \right)^\beta \left(\frac{r + r_c}{r_{\text{opt}} + r_c} \right)^{\beta+\gamma}. \quad (3.6)$$

In this form of the NKG function, the Molière radius is replaced by an effective radius $r_c \simeq 700$ m and an other parameter r_{opt} which depends on the respective detector geometry for which the signal $S(r)$ is being parameterized (e.g. $r_{\text{opt}} = 800$ m for TA and $r_{\text{opt}} = 1000$ m for the Auger surface detector). The exponents

β and γ are free parameters of the lateral density distribution that depend on the energy and the zenith angle of the incident primary particle and have to be determined by a fit to the measured signal [MS18].

3.5. Photons as primary particles

Though, the bulk of primary cosmic radiation is of hadronic origin, also high-energy gamma rays are being observed. Extraterrestrial photons cover a wide range of wavelengths as shown in Fig. 3.13. Their spectrum reaches from MHz radio waves as observed from e.g. the solar system with the UTR-2 and URAN telescopes [ZV14], throughout the optical regime that has been explored for centuries by optical astronomy and goes further deep into the ultra violet (UV), the X-ray regime and even up to gamma rays beyond the GeV-range as they are observed from gamma ray bursts. The highest energy photon that has ever been detected had an energy of ~ 450 TeV and was recorded in 2019 by the Tibet Air Shower Array along with 23 other photon-like events above 100 TeV [AM19]. Their source has been identified to be the Crab nebula (see Fig. 3.3(a)). A photon of ~ 450 TeV corresponds to a wavelength of $\sim 3 \times 10^{-21}$ m which exceeds the scale shown in Fig. 3.13 to lower wavelengths by about four orders of magnitude.

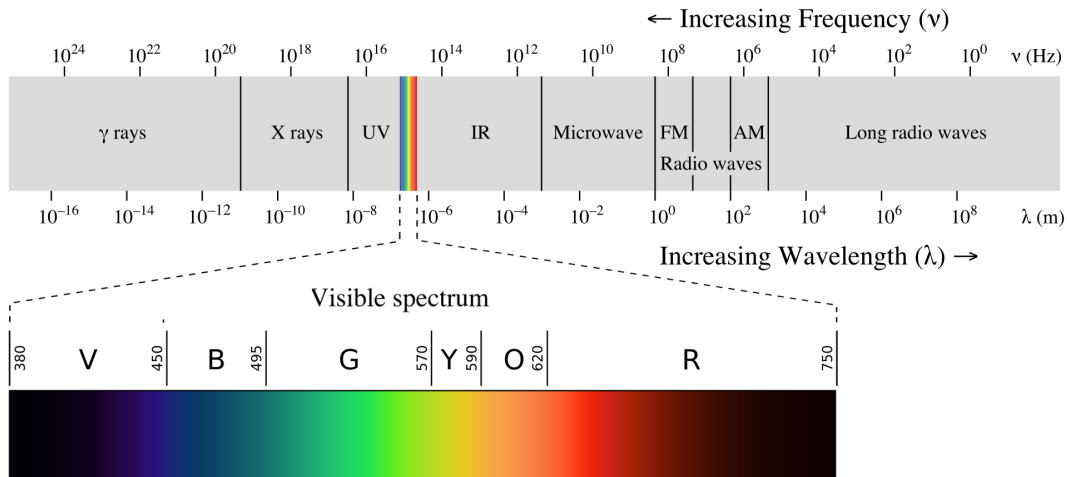


Figure 3.13: The spectrum of electromagnetic radiation ordered from left to right by increasing wavelength λ (decreasing frequency ν) [GP13]. The spectrum starts in the gamma ray regime at a wavelength $\lambda = 10^{-16}$ m which corresponds to a photon energy of $E \approx 12$ GeV and goes deep into the radio regime. The part of the spectrum between $\lambda = 380$ nm and 750 nm corresponds to the range of visible light (shown in the magnification).

Above PeV energies no extraterrestrial photons have been identified so far. Various air shower experiments have analyzed their data for characteristics of photon-induced events but no statistically significant excess has been found above the

hadronic cosmic ray background [RJ19, AW17, FY17]. Hence, from the non-observation of photon-induced air showers the overall flux of primary photons at the highest energies could be constrained. Current limits on the diffuse flux of primary photons of energies above 6×10^{16} eV are shown in Fig. 3.14. However, various theories and models predict the existence of photons beyond the cosmic ray knee and even up to the UHE regime above the ankle. These models can generally be divided into two categories: the so called “bottom-up” or “acceleration” models and the “top-down” or “non-acceleration” models. For a comprehensive reference on these models see [BP00]. Here only a brief summary of the basic ideas shall be given.

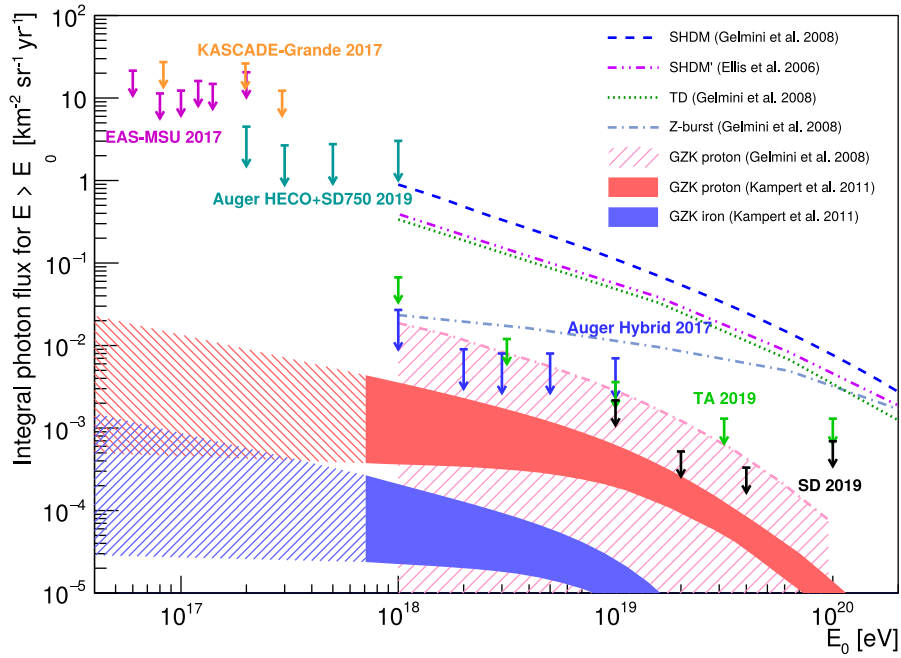


Figure 3.14: Upper limits to the integral photon flux above the energy E_0 at 90% confidence level (CL) placed by TA [AR19] and the Pierre Auger Observatory [RJ19] and at 95% CL by KASCADE-Grande [AW17] and EAS-MSU [FY17]. Predicted photon fluxes according to different top-down models [EJ06, GG08] and expected fluxes from GZK-interactions of pure proton and pure iron cosmic ray compositions [GG07, GG08, SB11] are shown for comparison. Image taken from [RJ19].

Bottom-up models describe the production of UHE photons at astrophysical sites (astrophysical photons) as secondary particles that are produced when UHE protons (or other charged particles) interact with surrounding matter, or with strong magnetic fields via the pB -process, [YY19]. The generation of cosmogenic photons via the GZK process (see Eq. 3.1) is yet another example of UHE photon production in a bottom-up process. The models are called “acceleration models” because they also need to describe how charged particles can obtain the energies necessary to produce UHE photons in the first place. The acceleration of charged particles is typically described by modelling astrophysical sites with classical, well studied physics processes and interactions or extrapolations of these towards higher

energies or strong magnetic fields. Quantifying UHE photon predictions from astrophysical sources is not an easy task since the expected fluxes may depend on many source parameters that are still inaccessible through modern science. However, the acceleration models have in common that they predict the fluxes of UHE photons and neutrinos to be comparable as they are expected to be produced in equal numbers as the decay products of neutral and charged pions.

Top-down models predict photons to be directly produced at UHE in singular events that typically involve new physics. Examples for such events are the decay of hypothetical particles like super heavy dark matter (SHDM) or topological defects like magnetic monopoles or cosmic strings which are theorized to be relics that have formed during the early universe at energy densities of the GUT (grand unified theory)-scale. Also interactions of hypothetical UHE neutrinos with the relic neutrino background (Z-burst scenario) are expected to produce UHE photons in the process.

Some of the photon fluxes that are predicted by the different models are shown in Fig. 3.14 for comparison with recent constraints from experimental results. The limits placed by TA and the Pierre Auger Observatory above 1 EeV already pose stringent constraints on several top-down models. The non-observation of photons at UHE can thus guide the ongoing search for dark matter and exotic particles by ruling out those models that would inherently lead to a large flux of UHE photons. Due to the lower expected flux, cosmogenic GZK photon predictions could so far not be strongly constrained. More exposure together with future hardware upgrades of both TA and the Pierre Auger Observatory and refined analysis methods to improve the background suppression will eventually improve the sensitivities of both detectors in order to directly probe the models of GZK photons for the first time.

Unlike charged particles, photons are not deflected by magnetic fields which are present in interstellar space within the galaxy of the order of 10^{-5} Gauss (G) [JR12] as well as in extragalactic space where the magnetic fields are in the order of $\sim 10^{-9}$ G within filaments ($\sim 10^{-12}$ G within voids) [DK05]. A primary UHE photon among the cosmic rays could thus easily be related to its source (in the case of an astrophysical photon) just by reconstructing the axis of the air shower it produced in the atmosphere. Due to the background radiation fields, which are the infrared background light (IRB), the CMB, and the universal radio background (URB), the universe at large scales is opaque to UHE photons. UHE photons can interact with low energy photons from the background radiation fields and produce electron-positron pairs in a similar process as electron-pair production in the vicinity of atomic nuclei [RM07]. The cross section for this process depends on the photon energy and the wavelength of the radiation field and is shown in Fig. 3.15 in terms of an attenuation length which corresponds to the track length after which an average fraction $\frac{1}{e} \approx 0.37$ of all photons of a given energy has not undergone an interaction. For photons above 1 EeV this implies that potential sources must not be farther away than a few tens of Mpc for photons to possibly reach the earth. However, one has to keep in mind, that these highly asymmet-

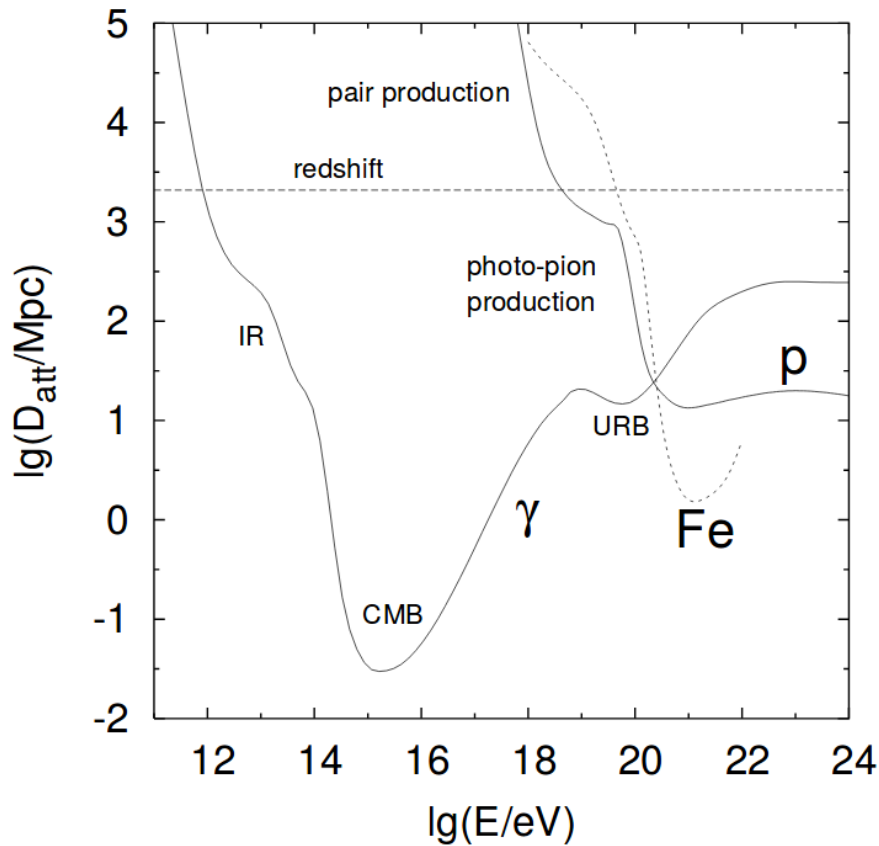


Figure 3.15: The photon attenuation length due to electron-pair production and photo-pion production as a function of photon energy [RM07]. The background radiation fields IRB (IR), CMB and URB label those parts of the energy spectrum where they contribute the dominant part to the attenuation. Also shown are the attenuation lengths for primary proton and iron cosmic rays.

ric interactions between photons have not been studied yet directly in laboratory experiments. Possible deviations from special relativity or other effects involving new physics could potentially alter the photon attenuation at the highest energies. Also the possibility of a conversion of UHE photons into axions or axion-like particles (ALPs) within the strong magnetic fields of their sources has been proposed in [GD01, FM11]. Such a conversion would enable the particles to propagate over cosmological distances since all possible interactions of axions in the extragalactic medium are negligible. If those UHE axions or ALPs interact again with the galactic or geomagnetic field they might eventually end up again as UHE photons on top of the earth's atmosphere and initiate an air shower that is measurable with ground-based detectors. The existence of ALPs that would enable such an interaction with sufficiently high cross-section is limited to a parameter space that is not yet ruled out by experimental results but within the reach of experiments like CAST [AE08] or the new generation axion helioscope [II11].

Air showers that are initiated by primary photons evolve fundamentally different

from those initiated by hadrons. Being electromagnetic particles themselves, photons directly initiate an electromagnetic cascade with the first interaction. Hadrons that might be produced during the first interactions as well carry typically only a minor fraction of the total energy. Due to the close connection between muonic and hadronic shower components, photon initiated air showers are poor of muons and rich of electromagnetic particles. Since electromagnetic particles are stronger confined around the shower axis they expose a steeper lateral density distribution than muons, which inherit the large transverse momenta that hadrons obtain in nucleon interactions. Also the expected X_{\max} of photon-induced air showers is deeper in the atmosphere than that of hadron-induced showers. This is mainly due to the higher multiplicity of secondary particles in hadronic interactions and the, on average, deeper point of the first interaction of primary photons [RM07, GP10].

At energies above $\sim 10^{19}$ eV the Landau-Pomeranchuk-Migdal (LPM) effect [LL53, MA56] starts to affect the development of electromagnetic cascades and leads to even deeper values of X_{\max} due to a reduction of the cross sections of bremsstrahlung and pair production. At higher photon energies $E \sim 5 \times 10^{19}$ eV, a reduction of X_{\max} is expected which is caused by the interaction of primary photons with the geomagnetic field. These interactions can lead to electron-pair production and subsequent synchrotron radiation already well above the atmosphere – starting an electromagnetic cascade, called *preshower* [MB81].

The distinctive traits of photon-induced air showers are shown for 1 PeV photons in Fig. 3.16 where the electromagnetic, muonic and hadronic shower components are visualized using computer simulations and compared to those of proton and iron induced showers. From that figure one can see that in photon-induced showers all shower components – especially the electromagnetic component – are strongly confined around the shower axis. The different electromagnetic showers shown in the first row are actually of comparable sizes but are significantly wider spread in the hadron-induced showers. Also visible is the delayed start of the muonic and hadronic components of the photon-induced shower as compared to its electromagnetic component. While primary hadrons typically start the hadronic cascade directly with the first interaction, primary photons first initiate an electromagnetic cascade. Since in hadron-induced showers the muonic and electromagnetic components are closely linked to the hadronic component via the decays of charged and neutral pions respectively, all three shower components are fueled early in the shower development.⁴ The start of muonic and hadronic shower components from electromagnetic primaries, on the other hand, is typically induced by comparably rare processes like muon pair production later along the shower development [ST85].

⁴As discussed earlier in Sec. 3.4, for high energy showers the development of the muon component can be significantly delayed due to the suppression of muon decay in favor for muon-hadron interactions. This effect is not clearly visible at the 1 PeV showers displayed in Fig. 3.16.

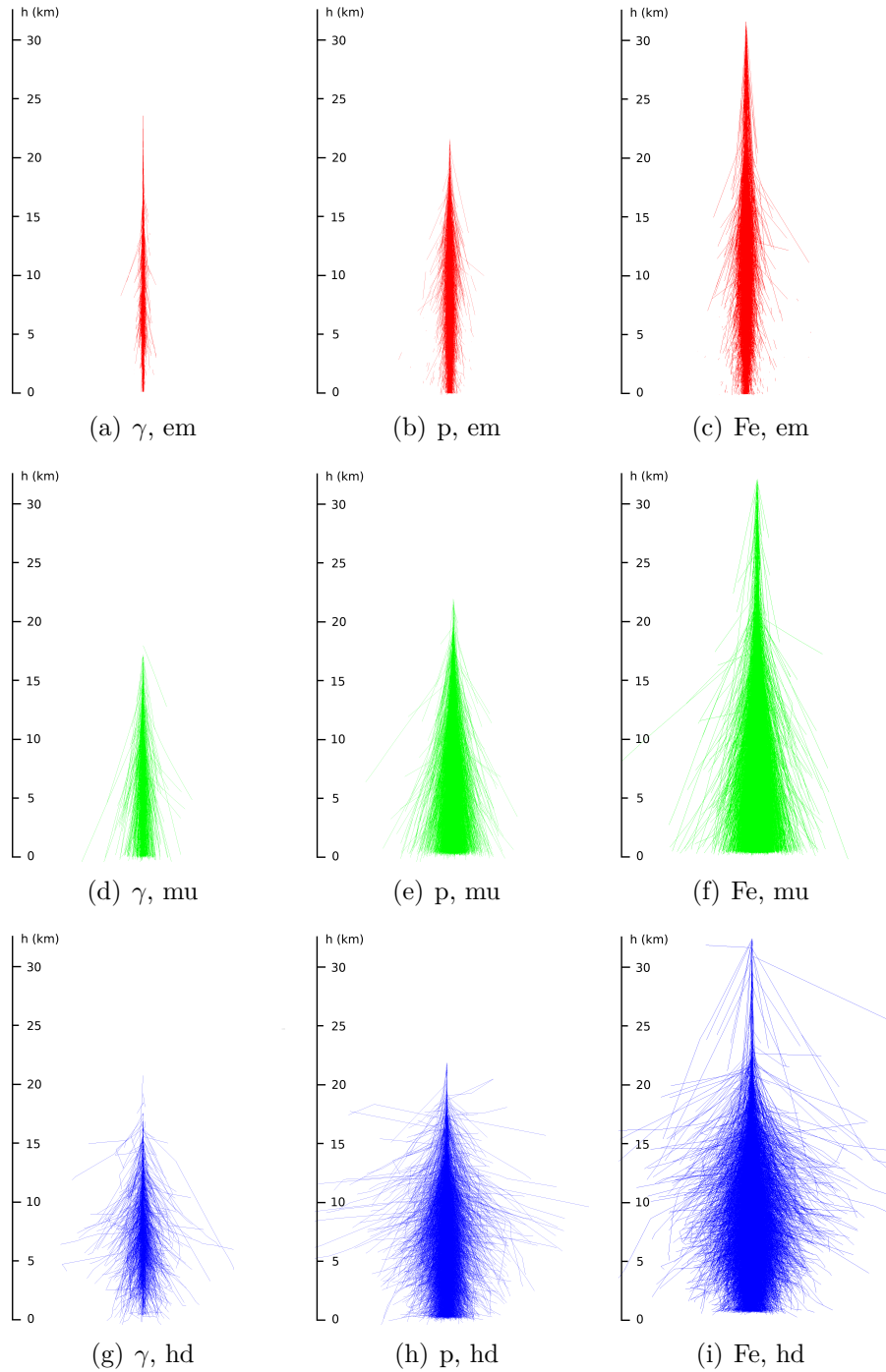


Figure 3.16: The different air shower components shown separately for a primary photon (γ), proton (p) and an iron nucleus (^{56}Fe). The top row shows the electromagnetic component (em) for a (a) photon (b) proton and (c) iron shower. The middle row, (d), (e) and (f), shows the muonic components (mu) in the same order from left to right and the bottom row, (g), (h) and (i), shows the corresponding hadronic components (hd). Each primary particle was simulated with an initial energy of $E = 1 \text{ PeV}$ and only those particle tracks with an energy above 1 GeV are displayed. The physics simulation was performed with CORSIKA [HD98]. The visualization of the simulation output has been done with AirShower3D [KE20].

3.6. Multimessenger astronomy

Multimessenger astronomy can be defined as “*the exploration of the universe through combining information from a multitude of cosmic messengers: electromagnetic radiation, gravitational waves, neutrinos and cosmic rays*” [BI17].

Optical light has been the only source of information about extraterrestrial physics for a long time and still is the richest source for astronomical observations. With the discovery of radio waves, X-rays and gamma rays and the development of instruments to detect such radiation originating from outer space, the electromagnetic spectrum through which the universe was accessible was vastly broadened. Multiwavelength observations of distinct astronomical objects like e.g. the galactic center [EA11b] help understanding the physics of these objects and also provide insights in physical scenarios that can not be reproduced on earth. Fig. 3.17 shows images of the full 4π -sky across the whole electromagnetic spectrum from microwaves up to gamma rays. New features and details become apparent within each wavelength band which cannot be observed from the others.

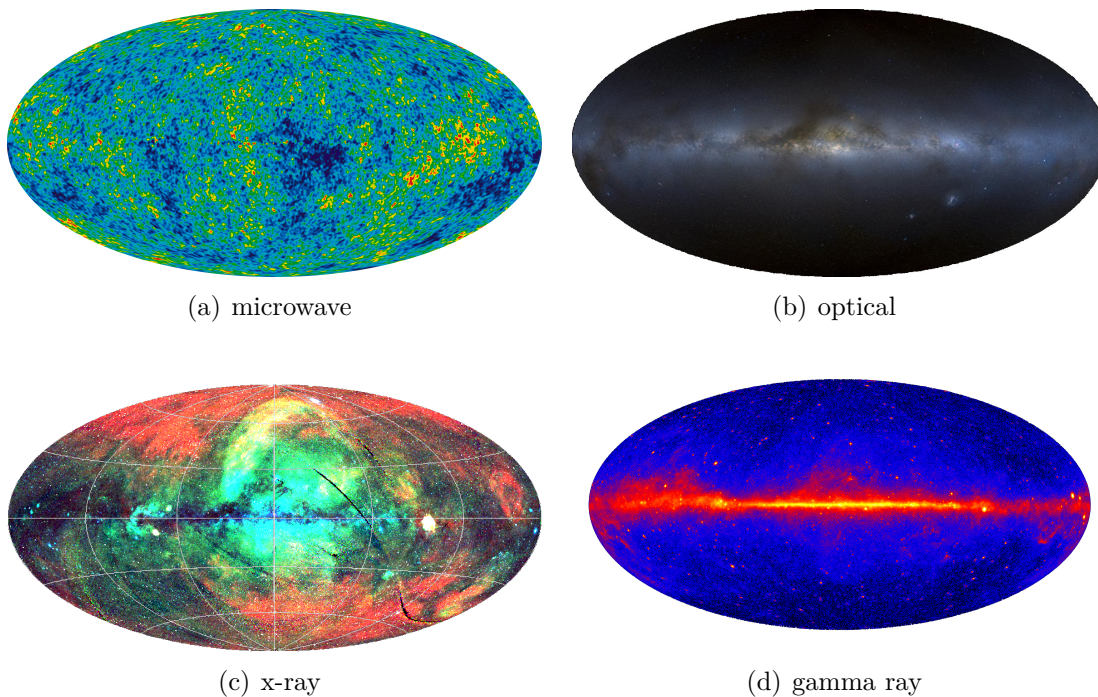


Figure 3.17: Maps of the full 4π -sky in galactic coordinates in the light of (a) micro- and radio waves [NA20a], (b) infrared and visible light [MA09], (c) x-rays [MPI19] and (d) gamma rays [NA20b]. The coordinate system is chosen such, that the galactic center is at the center of each plot.

Further complementary information can be provided by cosmic rays. Analyzing specific sources in the light of cosmic rays however is rather challenging since cosmic rays are mainly charged particles which are deflected by magnetic fields and do not point back to their origin. Therefore, during the last decades great effort has been put into the detection of neutral messengers like high energy neutrinos. Those

messenger particles indirectly probe the capability of the sources to accelerate cosmic rays since neutrinos are expected to be produced in the decay of pions which themselves can be produced in interactions of cosmic rays with surrounding matter.

In September 2015 a completely new type of messenger was observed for the first time in history. The detection of a signal from a gravitational wave (GW) emitted by a binary black hole (BBH) merger event with the Laser Interferometer Gravitational-Wave Observatory (LIGO) opened a new window in the field of multimessenger astronomy. Until then, black holes were largely inaccessible by direct observations since no radiation – neither particles nor electromagnetic – can escape the event horizon. Consequently the detection of a GW was the first signal ever recorded from the merging process of two black holes. Furthermore, GWs carry information that would be inaccessible by the means of electromagnetic observations, like the magnitude and distribution of mass at the source as a function of time. Even an independent measurement of the Hubble constant is possible using GWs from BBH mergers [AB16, AB19a].

Less than two years later, in August 2017, the first successful multimessenger observation was made with the combined observation of a binary neutron star (BNS) merger in the light of GWs and an associated short gamma ray burst shortly after (see Fig. 3.18). The ringdown process of the compact object in the final state lasted for several months and could be observed in a broad frequency range from X-ray emissions down to radio waves [AB17a].

Only shortly after the first multimessenger observation of a BNS merger the first detection of a high-energy neutrino from a known astrophysical source, a blazar known as TXS 0506+056, had been reported by the IceCube Collaboration together with an earlier period of enhanced neutrino activity from the same direction in 2014 as found in a posterior data analysis [AM18a] (the multimessenger observation of TXS 0506+056 is discussed in more detail in Chapter 10). These ground-breaking observations during the past decade marked the prelude to a new era of multimessenger astronomy.

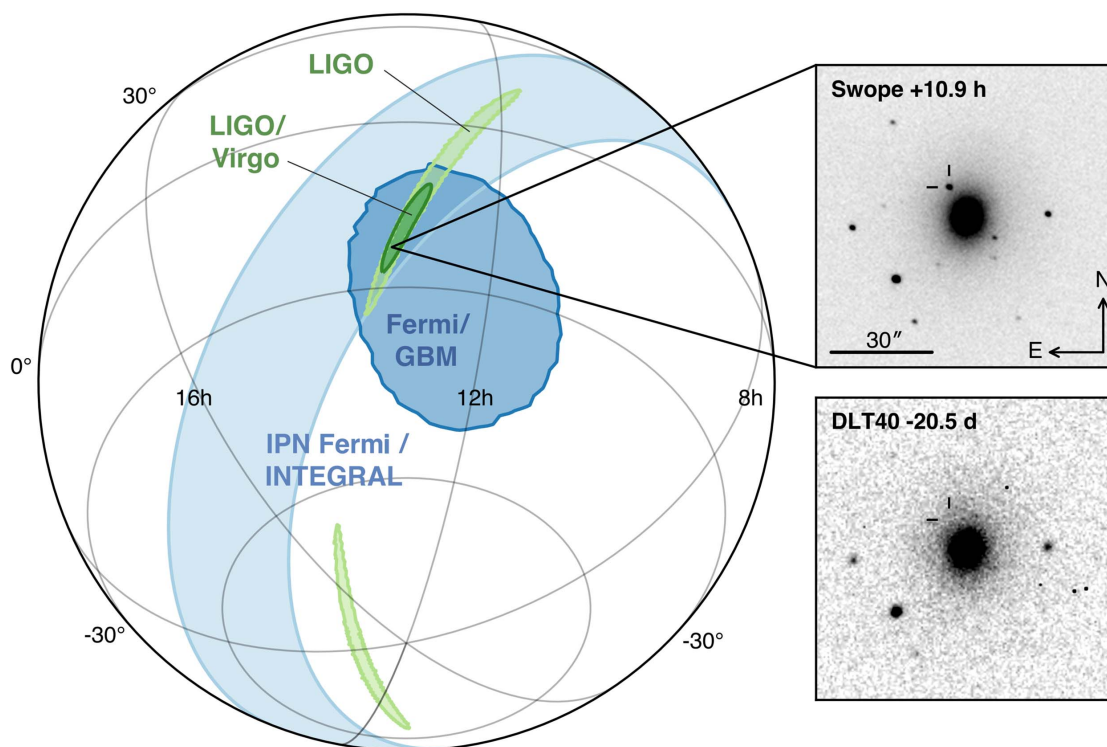


Figure 3.18: Localizations of the source of GW178017 (a BNS merger) in the light of GWs, gamma rays and optical signals [AB17a]. The green areas are the 90% contours of the sky localization by LIGO (light green) and LIGO+Virgo (dark green). The shaded blue regions are obtained from an IPN triangulation of the time delay between signals at Fermi-GBM and INTEGRAL (light blue) and the localization of Fermi-GBM (dark blue). The pictures to the right show images 20.5 days before (lower right, by DLT40) and 10.9 h after (upper right, by Swope) the merger time in the optical band. The direction of the transient event is indicated by the reticle in both pictures.

General relativity and gravitational waves

GRAVITATIONAL waves (GWs) had been a construct of theory for almost 100 years. Their existence was first proposed by Albert Einstein (1879-1955) in 1916 [EA16, EA18] shortly after the publication of his relativistic theory of gravity in 1915 [EA15]. In 2015 these waves were detected for the first time directly in an earth-bound experiment, the Advanced LIGO detectors [AB16], confirming the validity of Einstein's theory in great detail. However, the first experimental evidence for the existence of gravitational waves was already provided by the discovery of the Hulse-Taylor binary as early as 1974 with the Arecibo radio telescope [HR75]. The Hulse-Taylor binary system is a system of two neutron stars, one of which is a pulsar. The binary which today has an orbital period of 7.75 h was found to be gradually contracting. That contraction had been interpreted as being due to the energy loss caused by the radiation of GWs.

Since the main focus of this work is the experimental analysis of GW sources, the main concepts and properties of GWs in the framework of general relativity shall be summarized in this chapter and a rough sketch of the detection principle of the latest generation GW detectors is given. The formulas and derivations shown in this chapter follow those given in [KK02] and [SH88].

4.1. GWs as solutions of Einstein's field equations

Of the four fundamental forces of nature, gravity is by far the weakest. Its relative coupling strength is about 25 orders of magnitude weaker than the coupling of the weak interaction and about 36 orders of magnitude weaker than the electromagnetic force. It couples to mass in a similar way as electromagnetism couples to electric charge with the force acting between two massive bodies decreasing with distance like $\propto r^{-2}$. In contrast to the electric charge however, the mass has no equivalent of oppositional charge signs. For that reason and since macroscopic structures of matter have a net charge of zero, gravity is the dominant force in the universe on large scales. Moderate gravitational forces as they are exerted by planets or average stellar objects can well be described by Newton's laws of classical mechanics. The accuracy of Kepler's descriptions of planetary orbits which were incorporated in the Newtonian theory proves the wide range of validity of classical mechanics. Strong gravitational fields on the other hand, as they are present in the vicinity of massive objects like highly massive stars or black holes,

expose the limitations of Newton's theory of gravity. Another limitation of classical mechanics is the description of time-varying gravitational fields acting on a remote observer. Since the finite speed of light is not accounted for, gravity acts instantaneously in classical mechanics. This behavior contradicts the fundamental principle of special relativity since it does not conserve causality.

In 1915, Einstein published a corrected version of the theory of gravity which is valid for strong gravitational fields and accounts for causal connection by introducing retarded gravity potentials while incorporating the Newtonian dynamics in the limits of classical mechanics. This *general theory of relativity* models the gravitational action as a result of curvatures in the four-dimensional manifold of space-time. A particle that feels no force except gravity moves along geodesics of that curved space-time. In the mathematical framework of general relativity the curvature is encoded in the metric tensor $g_{\mu\nu}$. Any deviation of $g_{\mu\nu}$ from the Minkowski metric $\eta_{\mu\nu} = \text{diag}(-1, 1, 1, 1)$ refers to a non-vanishing curvature. The sources of curvature are any distribution of mass or energy density and can be described by the stress-energy tensor $T^{\mu\nu}(x^\lambda)$ at the 4-coordinate⁵ x^λ . Curvature and energy density are connected in a way that is described by Einstein's *gravitational field equations*

$$G_{\mu\nu} := R_{\mu\nu} - \frac{1}{2}g_{\mu\nu}R = kT_{\mu\nu} \quad (4.1)$$

with $G_{\mu\nu}$ being the *Einstein tensor* which can be expressed through the *Ricci tensor* $R_{\mu\nu}$ and the *scalar curvature* R . The quantity $k = 8\pi G/c^4$ is the coupling constant of the theory with $G \approx 6.67 \times 10^{-11} \text{ m}^3 \text{ kg}^{-1} \text{ s}^{-2}$ being the gravitational constant and c being the speed of light in vacuum. $R_{\mu\nu}$ and R are derived by contractions of the *Riemann tensor* $R_{\kappa\lambda\mu\nu}$ which itself is a function of $g_{\mu\nu}$ and its first and second derivatives and thus a measure of the curvature of space-time. The Ricci tensor vanishes in regions where no matter distribution is present. This however does not imply a vanishing Riemann tensor and means that even though curvature is generated by energy and mass distributions, the existence of curvature is possible even in empty space.

The existence of GWs within this theory can be shown by introducing small time-dependent perturbations $h_{\mu\nu}$ to the metric tensor $g_{\mu\nu}$ of a static matter distribution, hence the perturbed metric is

$$\tilde{g}_{\mu\nu} = g_{\mu\nu} + h_{\mu\nu}. \quad (4.2)$$

For the case of small perturbations ($|h_{\mu\nu}| \ll 1$) and for observers that are far away from the static mass distribution, the field equations can be linearized in terms of $h_{\mu\nu}$. Using the linearized equations it can be shown that the *trace reverse* of $h_{\mu\nu}$, defined as

$$\tilde{h}_{\mu\nu} := h_{\mu\nu} - \frac{1}{2}\eta_{\mu\nu}h^\alpha{}_\alpha, \quad (4.3)$$

⁵Lowercase Greek indices (μ, ν, λ, \dots) label 4-vector components and run from 0 to 3.

is governed by a wave equation of the form

$$\left(-\frac{\partial^2}{\partial t^2} + \nabla^2\right)\tilde{h}^{\mu\nu} = 0. \quad (4.4)$$

The simplest solution of this wave equation is that of a plane wave and can be written as

$$\tilde{h}^{\mu\nu} = A^{\mu\nu} e^{ik_\alpha x^\alpha}, \quad (4.5)$$

where the wave vector k_α is a *lightlike* vector (i.e. $k_\mu k^\mu = 0$) which implies that gravitational waves propagate at the speed of light. The amplitude $A^{\mu\nu}$ has two free dimensionless parameters h_+ and h_\times and can be written as

$$A^{\mu\nu} = h_+ \epsilon_+^{\mu\nu} + h_\times \epsilon_\times^{\mu\nu}. \quad (4.6)$$

The *unit polarization tensors* $\epsilon_+^{\mu\nu}$ and $\epsilon_\times^{\mu\nu}$ represent two possible orthogonal polarization states. For a GW propagating in z -direction the unit polarization tensors are given by

$$\epsilon_+^{\mu\nu} = \begin{pmatrix} 0 & 0 & 0 & 0 \\ 0 & 1 & 0 & 0 \\ 0 & 0 & -1 & 0 \\ 0 & 0 & 0 & 0 \end{pmatrix} \quad \text{and} \quad \epsilon_\times^{\mu\nu} = \begin{pmatrix} 0 & 0 & 0 & 0 \\ 0 & 0 & 1 & 0 \\ 0 & 1 & 0 & 0 \\ 0 & 0 & 0 & 0 \end{pmatrix}. \quad (4.7)$$

A distribution of test masses in the x - y -plane that gets struck by a GW polarized in $\epsilon_+^{\mu\nu}$ -direction experiences tidal forces that alternate between the x - and y -direction. A GW polarized along $\epsilon_\times^{\mu\nu}$ leads to tidal forces that are rotated by 45° with respect to the other polarization. In Fig. 4.1 the effect of a perpendicularly traversing GW on a set of test masses is shown for the two polarization states. In analogy to electromagnetic waves, these are the linear polarized states. Arbitrary superpositions of these states are possible and also elliptical and circular polarized states can be achieved by introducing a phase difference between the linear polarized components.

4.2. Basic properties of GWs

Though any change⁶ in any given mass distribution does in principle produce GWs, the amplitudes of these waves are typically so small that it is practically impossible to measure them. The most luminous sources of GWs in the universe comprise compact mass distributions on length scales in the order of their Schwarzschild radii that move at velocities close to the speed of light. Following the order-of-magnitude estimate in [KK02], the luminosity L_{GW} of an arbitrary GW source

⁶Actually, only changes of mass quadrupoles or higher multipoles can produce GWs since monopolar and dipolar changes are excluded due to the lack of negative mass and reasons involving the conservation of energy and angular momentum.

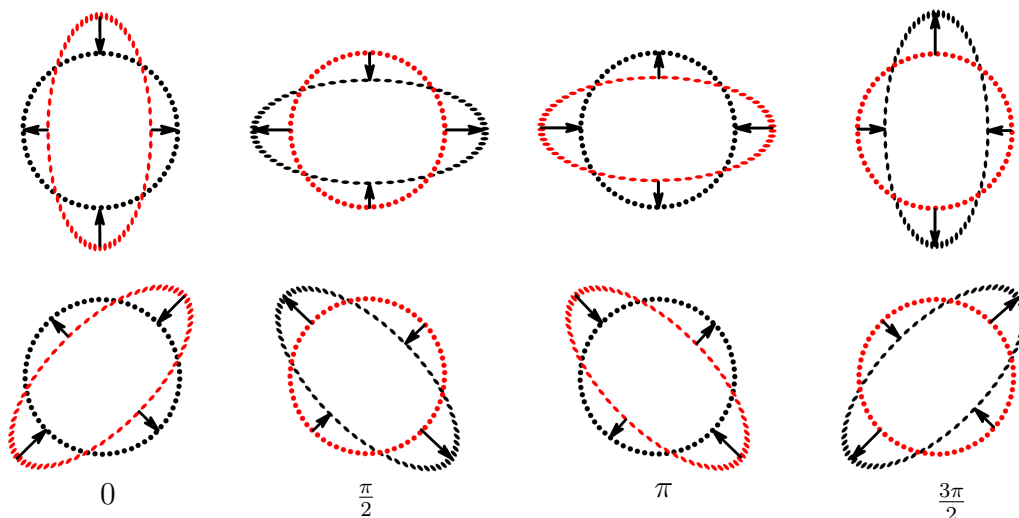


Figure 4.1: The movements of a ring of test masses (black dots) during the perpendicular transition of a linearly polarized GW. The upper row corresponds to the $\epsilon_+^{\mu\nu}$ polarization state while the lower row corresponds to the $\epsilon_x^{\mu\nu}$ state. The four columns show snapshots of the wave at different phases. The red dots illustrate the state of the system at an earlier phase $\varphi - \frac{\pi}{2}$ to visualize the relative movements between the snapshots which are indicated by the arrows.

depends on the size R of the source, its Schwarzschild radius $R_{\text{Sch}} = \frac{2GM}{c^2}$, which is a function of source mass M and the velocity v at which its mass distribution changes as

$$L_{\text{GW}} \sim \frac{c^5}{G} \left(\frac{R_{\text{Sch}}}{R} \right)^2 \left(\frac{v}{c} \right)^6. \quad (4.8)$$

The most efficient sites for the generation of GWs are thus objects like compact binary systems right before their merger or the implosion of a star during a supernova.

Once generated, GWs can propagate over cosmological distances without suffering any significant attenuation apart from a geometrical attenuation of the amplitude $\propto r^{-1}$ of a spherical wave front and the impact of the cosmological redshift. Their absorption by surrounding matter is expected to be even weaker than that of neutrinos. In a similar way as electromagnetic radiation, GWs can be diffracted and focused by strong gravitational fields through gravitational lensing. The solution of the field equations shown above were obtained by neglecting higher orders of the perturbation field $h_{\mu\nu}$. In general GWs have a non-linear nature, that can lead to exotic effects like non-linear self interaction, scattering on the background curvature or the formation of *geons* which are bundles of GWs stuck together by their self-generated curvature. However, for the small amplitudes of even the strongest GWs that are observed on earth, those non-linear effects are completely negligible [KK02].

4.3. Compact binary mergers

The merging processes of two coalescing compact objects (compact binary mergers, CBMs) are probably the most luminous sources of GWs in the universe. A binary star system gradually loses energy in the form of gravitational waves. This energy loss leads to a decreasing orbital radius and an increasing orbital frequency $\nu(t)$. Using a post-Newtonian expansion (i.e. an expansion in some parameter that quantifies the deviation from Newton's classical theory of gravity) the change in orbital frequency $\dot{\nu} = \frac{d\nu}{dt}$ can be expressed as a function of orbital frequency ν . The leading term of the expansion is

$$\dot{\nu} = \frac{96}{5} \pi^{8/3} \left(\frac{G\mathcal{M}}{c^3} \right)^{3/5} \nu^{11/3}, \quad (4.9)$$

where the parameter \mathcal{M} is called the *chirp mass* of the system and depends on the masses M_1 and M_2 of the constituents of the binary system as

$$\mathcal{M} = \frac{(M_1 M_2)^{3/5}}{(M_1 + M_2)^{1/5}}. \quad (4.10)$$

Hence, by measuring the orbital frequency as well as its time derivative one can determine the chirp mass of the system. Taking into account higher orders of the post-Newtonian expansion parameter, more details like the individual constituent masses and spins can be resolved [CC94]. Once knowing M_1 and M_2 one can distinguish between different types of compact objects. While masses below $3 M_\odot$ ($1 M_\odot =$ one solar mass) are attributed to neutron stars, masses higher than $4.5 M_\odot$ are attributed to black holes [FW11]. The mass region in between is referred to as the *mass gap* region where the nature of the compact objects is unclear [AB20b]. A chart of possible evolution scenarios for CBMs is shown in Fig. 4.2

Given the distance a_0 between two orbiting objects, their total mass M and their reduced mass $\mu = \frac{M_1 M_2}{M_1 + M_2}$, the time left until the merger, i.e. until the two objects fuse into a single compact remnant, is given by

$$\tau = \frac{5}{256} \frac{c^5}{G^3} \frac{a_0^4}{\mu M^4}. \quad (4.11)$$

For the case of the Hulse-Taylor binary, which presently has a separation of 1.1 solar radii at periastron and 4.8 solar radii at apastron [WJ81], the expected time until the merger is $\tau \sim 3.5 \times 10^8$ yr. Though the formulas given above are derived for circular orbits, the highly elliptical orbit of the Hulse-Taylor binary is expected to become circular long before the merger due to the radiation of GWs.

For the amplitude of a GW that is emitted by a CBM as a function of distance r to the source, the relation

$$h = 5 \times 10^{-22} \left(\frac{M}{2.8 M_\odot} \right)^{2/3} \left(\frac{\mu}{0.7 M_\odot} \right) \left(\frac{\nu}{100 \text{ Hz}} \right)^{2/3} \left(\frac{15 \text{ Mpc}}{r} \right) \quad (4.12)$$

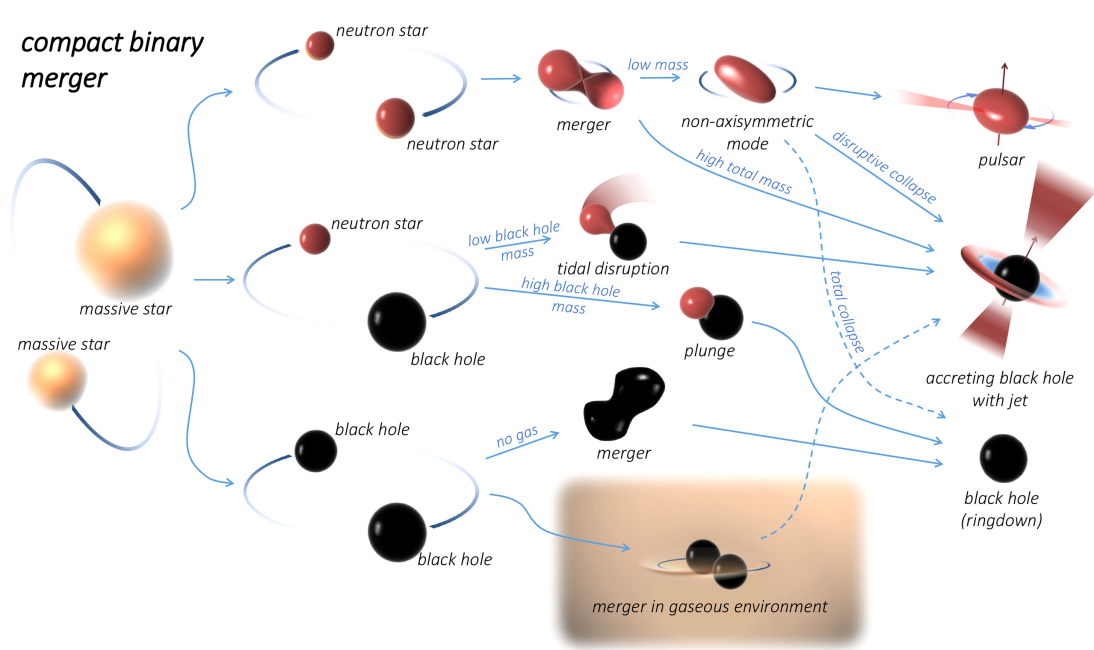


Figure 4.2: A chart of possible evolution scenarios of CBMs depending on their masses and different initial states [BI17].

holds [KK02]. Given a typical GW event as routinely observed by LIGO and Virgo from BBH mergers of stellar-mass black holes at distances of a few 100 Mpc and peak frequencies of a few 100 Hz [AB17a], typical amplitudes at earth are of the order of $h \sim 10^{-21} \dots 10^{-22}$. Hence, the relative movement of two test particles separated by 1 km would be of the order of 10^{-18} m during the transit of a GW. This makes obvious the experimental challenges associated to the detection of GWs and why it took more than 40 years from the first experimental evidence until their direct observation in an earth-bound detector.

4.4. Detection of GWs

The detection of GWs is in principle as simple as measuring the variation of the distance between two objects. However, the amplitudes of even the strongest GWs are so small (see Sec. 4.3) that their impact is not measurable with conventional tools. The Advanced LIGO [AB09, AA15d, URL6] (Fig. 4.3(a)) and Advanced Virgo detectors [AF15, URL7] (Fig. 4.3(b)) are the first GW detectors that were capable of actually measuring those tiny variations. Their basic concept is that of a Michelson interferometer (see Fig. 4.4). A laser beam of near-infrared light is generated at the central facility and sent through the central beam splitter. One part of the beam traverses the beam splitter and enters the interferometer arm on the opposite side while the other part is reflected perpendicularly into the other arm. The arms, also called the “antennas” of the detector, have a length of 4 km (3 km for Virgo) and contain an ultra-high vacuum of 10^{-9} Torr inside a volume of $\sim 10^4$ m³. The vacuum is necessary to prevent diffusion of the laser beam by



Figure 4.3: Aerial pictures of (a) the LIGO detector in Hanford, Washington [URL6] and (b) the Virgo detector in Italy [URL7].

scattering and diffraction and to minimize noise effects like sound waves and winds due to temperature gradients between the opposing sides of the beam pipe. The tubes inside the antennas are built like Fabry-Perot cavities with mirrors on both ends. The inner mirrors have a higher transmission than the outer mirrors since they have to be traversed twice by the laser beam, once when entering the cavity and a second time on exit. The beams are reflected multiple times between the two mirrors to increase the optical path of the interferometer arms. When the two parts of the beam join again at the central intersection, they interfere such that their phases completely cancel each other in the direction of the photo-detector.

If now a GW traverses the detector such that its propagation is perpendicular to the detector plane and its polarization along the axes of the antennas is non-zero, the antennas are alternately stretched and squeezed by the action of the wave. This relative change of the arm length, the so called *strain* $\frac{\Delta l}{l}$, leads to a difference in the optical path between the two interferometer arms. Upon interference at the central beam splitter the two beam parts will have a relative phase that perturbs the interferometric extinction. Hence, the photo detector records a signal that is proportional to the strain. The wavelength of the laser is altered as well, however, this effect is negligible compared to the difference in light-travel time since the speed of light is the same in both arms.

To be sensitive to such small variations in distance, much thought has been put into the reduction of all possible sources of background. The beam pipes are passively and actively isolated against seismic action, the mirrors are mounted on 4-segment pendulum suspensions and are even corrected for tidal forces created by the moon and the sun to name only a few measures that are taken to reduce variations of the optical path due to other sources than GWs. Fig. 4.5 shows an example of strain data measured by the two LIGO detectors on the same GW event.

A single GW detector of the type described above is only sensitive to one polarization and to sky directions that have a significant elevation with respect to

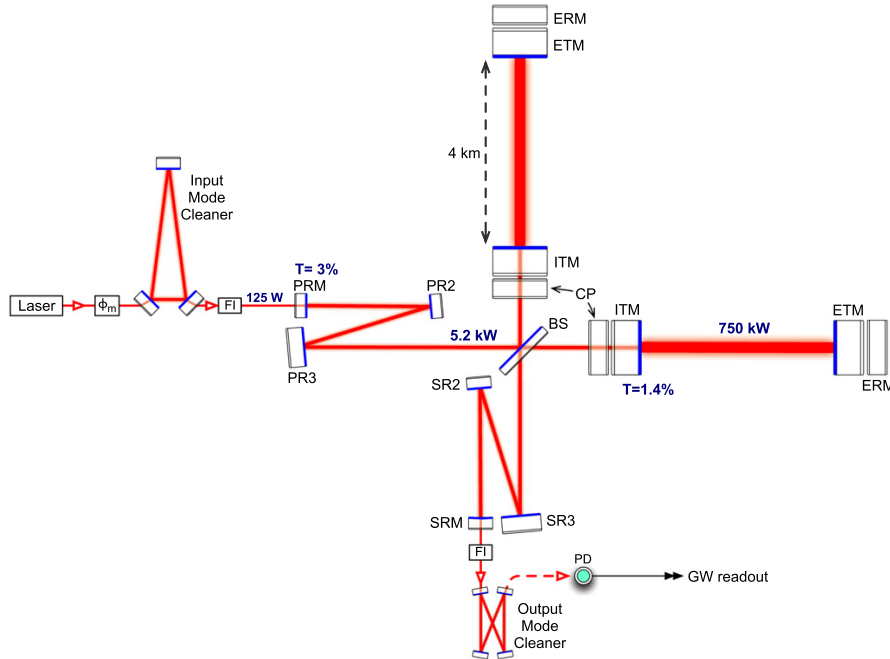


Figure 4.4: A schematic picture of the optical system of LIGO [AA15d]. Its base concept is that of a Michelson type interferometer with Fabry-Perot cavities along the beam arms. The additional mirrors in each arm reflect the laser beam multiple times along the 4 km arms of the interferometer to increase the effective path of the beam.

the detector plane. For that reason LIGO comprises two observation sites, one in Hanford, Washington and one in Livingston, Louisiana. A third detector, Virgo in Santo Stefano a Macerata, Italy complements the search for GWs by largely increasing the baseline of the GW detector network across the globe. The joint measurement provides a much better angular resolution to GW sources through triangulation of the signal arrival time giving rise to GW astronomy. The best source localizations are currently in the order of 10 deg^2 (at 90% CL) and the sensitivity to a diversity of polarization states and source directions is expected to be further increased with more detectors all over the world (like KAGRA [AT18a] and LIGO-India [UC13]) reaching the sensitivity to efficiently detect GWs in the near future.

A detector design as implemented with the advanced LIGO and Virgo detectors has its peak efficiency in the 100 Hz frequency regime. GWs in this regime are expected to originate predominantly in the inspiral and subsequent mergers of compact binary systems of solar mass objects. Also nearby core-collapse supernovae are expected to produce GW signals that are measurable with those detectors [AB20c]. The detection of GWs from mergers of massive black holes ($\sim 10^6 M_\odot$) which have frequencies in the order of a few mHz requires larger antennae. A detector capable of measuring these events is currently in development with the Laser Interferometer Space Antenna (LISA) [DK17] which is designed as three identical spacecrafts that are arranged in a triangular formation separated by 2.5 million km located in an earth-trailing orbit. To measure even lower frequency GWs down to the nHz

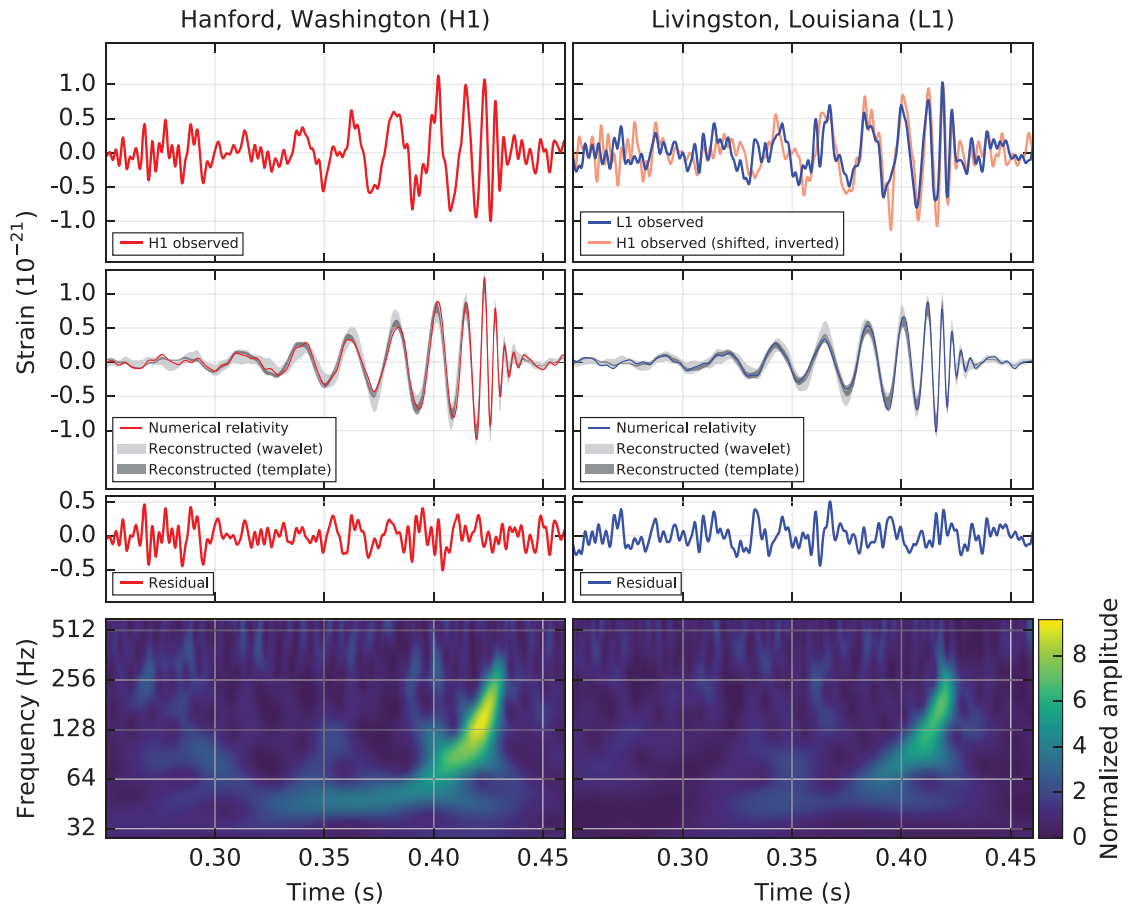


Figure 4.5: The strain data of GW150914 as measured by LIGO Hanford (left) and LIGO Livingston (right) [AB16]. The panels show the strain data after application of frequency filters to eliminate well known noise effects (first row), the reconstructed wave forms using different reconstruction approaches (second row), the residual between the wave form numerical relativity calculations and the filtered strain data (third row) and a time-frequency representation of the strain data (fourth row).

regime as they are expected from merging supermassive black holes ($\sim 10^9 M_{\odot}$) or the stochastic GW background from the early universe, a different measurement technique is deployed with the International Pulsar Timing Array (IPTA) [HG10]. Instead of laser interferometers, timing information from an ensemble of millisecond pulsars all over the galaxy is used to reach a galactic-scale detector baseline. These pulsars are analyzed by three consortia which are the European Pulsar Timing Array (EPTA), the North American Nanohertz Observatory for Gravitational Waves (NANOGrav) and the Parkes Pulsar Timing Array (PPTA) using data from a multitude of different radio telescopes on both hemispheres. A chart giving an overview of the frequency bands of GWs and detection efficiencies of the different detection methods is given in Fig. 4.6.

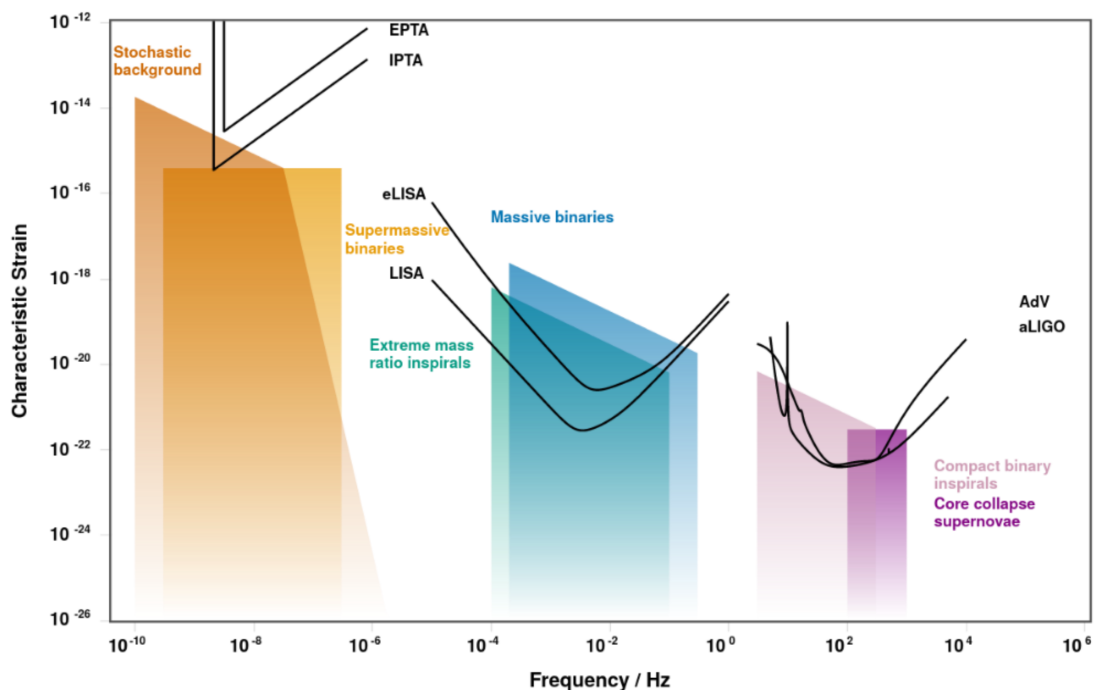


Figure 4.6: The characteristic strain plotted against frequency for different sources of GWs [MC14] (figure composed with [MC19]). The black curves show the design sensitivities of different GW detectors. The abbreviations Adv and aLIGO stand for advanced Virgo and advanced LIGO respectively. As a down-scaled version of LISA, eLISA has been proposed in 2013 with an arm length of 10^6 km [WG13].

The Pierre Auger Observatory

To investigate the origin and the nature of cosmic rays above 10^{20} eV which were first discovered by John Linsley in 1963 [LJ63] and confirmed by further observations in the following decades (see Chapter 2), a detector dedicated to measure cosmic rays at the highest energies was needed. The extremely low particle flux (c.f. Fig. 3.1) at these energies had to be compensated by a large effective detector area. Hence, in 1991, the idea of the Pierre Auger Observatory was developed by James Cronin and Alan Watson at the International Cosmic Ray Conference (ICRC '91) in Dublin. The design of the Observatory was specified in the following years to be a hybrid detector comprised of a large baseline surface detector (SD) to detect the secondary particles of air showers and a fluorescence detector (FD) that measures the fluorescence light produced by air showers when they propagate through the atmosphere. In 1999, the Pierre Auger Collaboration was officially founded as an international science collaboration of scientists from 18 different countries. After an engineering and testing period, the construction following the finalized detector design started in 2002 at the remote countryside of the city of Malargüe, Argentina at the elevated plane of Pampa Amarilla. First data taking started in 2004 while the detector was still under construction. The deployment of the baseline detector was completed in 2008 [AA15a].

The finalized SD array consists of 1660 water Cherenkov detectors (WCDs) distributed on a hexagonal grid with a spacing of 1.5 km between two neighboring stations, covering a total area of ~ 3000 km² – about 50 km to 70 km in diameter. To the west, part of the SD array is populated with additional detector stations in between the stations of the regular SD forming a dense sub-array with a reduced next-neighbor spacing of 750 m. The plane on which the SD is located has an average altitude of ~ 1420 m above sea level with individual detector stations placed at altitudes between 1340 m and 1610 m giving a generally flat geometry to the SD array [AI08]. The geographic location of the SD lies between latitudes 35.0°S and 35.3°S and between longitudes 69.0° and 69.4° [AA15a].

In total 27 fluorescence detector elements, called “bays” form the finalized FD and are located at four opposing sites on the edge of the SD plane. The four FD sites are called *Los Leones* to the south, *Los Morados* to the east, *Loma Amarilla* to the north and *Coicueco* to the west of the SD plane. The bays are arranged in groups of six at each of the four sites with an additional set of three bays, called HEAT (High Elevation Auger Telescopes) close to the site of Coihueco. Each bay

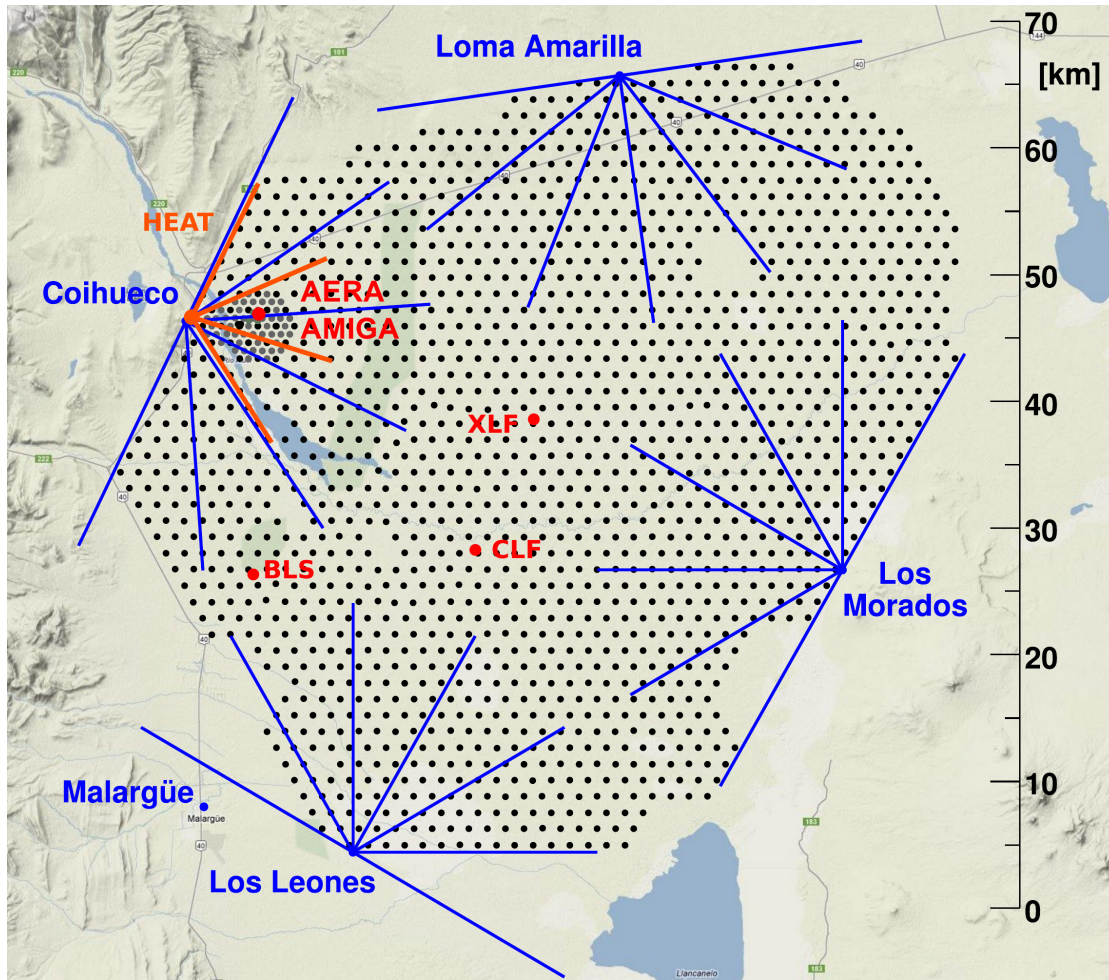


Figure 5.1: On the map showing the countryside region of the city of Malargüe, the locations of the 1660 SD stations are marked by the red dots [VD13]. The four FD buildings are marked along with blue lines indicating the fields of view of each telescope. Additionally, the locations of the laser facilities CLF and XLF, the balloon launching station (BLS) and the extensions AERA and AMIGA (see Sec. 5.4) are marked on the map.

hosts an autonomous FD telescope with a field of view of $30^\circ \times 30^\circ$. The six telescopes inside each FD building are arranged such that they add up to a combined field of view of 180° in azimuth and from 1.5° to 31.5° in elevation. All telescopes face towards the interior of the SD plane observing the sky above the SD. The three bays of HEAT are mounted in a way that allows for vertical tilting in order to cover elevations between 30° and 60° right above the field of view of Coihueco. HEAT aims to complement the field of view of the Coihueco telescopes to observe air showers of lower energy that develop high in the atmosphere [AA15a]. Fig. 5.1 shows an overview of the whole Pierre Auger Observatory with the positions of all SD stations marked on a map of the region around Malargüe together with the four FD sites.

This chapter aims to give an overview of the Pierre Auger Observatory as a

whole and of the operation of the main detector components. The general concept of the hybrid design, i.e. the simultaneous measurement with SD and FD will be discussed in Sec. 5.1. Sec. 5.2 gives a brief introduction into the operation of the FD and the associated data taking and event reconstruction. Since the work presented in this thesis is based only on data taken by the SD, the focus of this chapter will be the detailed description of that detector in Sec. 5.3. To give a more complete picture of the whole experiment, further facilities that are operated in parallel to the SD and the FD and aim to complement the data taken by the two main detector components are described in Sec. 5.4.

5.1. Hybrid design

As stated above, the Pierre Auger Observatory features two main baseline detectors, the SD and the FD. The detectors are arranged such that they can measure the same air shower events simultaneously and fully independent of each other while each measurement technique has its own advantages. Thus, important crosschecks and measurement redundancy are ensured by the hybrid design. Using the complementary data collected by both detector types, the energy spectrum and the arrival directions of primary cosmic rays at the highest energies can be determined with an accuracy of which one detector component alone is not capable [SP95, DB96].

The SD is designed to reach full detection efficiency for primary cosmic ray energies of 3×10^{18} eV making the calculation of the exposure vastly independent of energy above that energy threshold. The SD stations are unaffected by weather conditions and daylight and can thus be operated during day the same as in the night without interruption. Hence, the duty cycle of the SD is close to 100% [AJ10a]. For the FD to be operational it requires clear nights poor of moon light. Right after the construction phase, the average duty cycle of the FD was about 12% [AP11] while nowadays it is at a level of about 15% after improvements to the nightly startup of the running procedure [AA15a]. Aerosols in the atmosphere can obscure the fluorescence light profile of an air shower through scattering processes of the ultraviolet (UV) fluorescence light itself and by scattering of the Cherenkov light created by charged shower particles into the FD telescopes. On the other hand, clouds can obscure the longitudinal profile of an air shower as well since they are opaque to the fluorescence light. A shower piercing through a cloud could only partially be observed by the FD. Therefore, continuous monitoring of the aerosol density in the atmosphere and the cloud coverage above the SD plane is done using the laser facilities CLF and XLF, lidar systems and infra red (IR) cloud cameras at each FD site (for a further description of the laser facilities, see Sec. 5.4). To measure the density of aerosols and clouds above the FD buildings there is one lidar station installed at each FD site. A lidar is able to measure the atmospheric parameters relevant for a precise reconstruction of an air shower with the FD as a function of altitude. The laser of the lidar system has a wavelength of 351 nm matching the peak of the nitrogen fluorescence spectrum. The

backscattered light is focused with a mirror of 80 cm in diameter and detected with a PMT [BS07]. The FD has been constructed such that full detection efficiency is achieved for all showers with shower cores (i.e. the point of intersection between the shower axis and the ground level) inside the SD array beginning with energies of 10^{19} eV. Showers with lower energy can still be efficiently measured with the FD but the maximum distance up to which the FD is fully efficient decreases with energy [AP11].

Despite aiming to measure the same properties of the primary cosmic rays like energy spectrum, arrival directions and mass of the primary particle, the measurement techniques implemented by the SD and the FD are intrinsically different. They are designed such that they provide a maximum of complementary information about the nature of the air showers they measure. The SD observes a slice through an air shower typically right below its maximum by measuring the particle density as a 2-dimensional distribution in the detector plane, called the “footprint” of the shower. The signal start time in each SD station gives information about the direction while the total amount of signal provides an estimator for the energy of the incident primary particle [AA15a]. The FD is used to image the longitudinal profile of an air shower. The intensity of the fluorescence light emitted from a certain point along the path of air shower is proportional to the differential calorimetric energy deposited in the atmosphere in that part of the shower. The FD samples the fluorescence light as a function of viewing angle and time and projects it on an 2-dimensional array of pixels. Thus, it is able to reconstruct the development of the shower in the atmosphere giving a direct measurement of X_{\max} . The total energy can be reconstructed by integrating the calorimetric energy over the whole longitudinal profile and a 3-dimensional reconstruction of the shower axis can be achieved by combining the 2-dimensional projection of the profile with the timing information of the signal in each pixel [AJ10b].

While standalone-applications of both detectors are in principle possible, a combined event reconstruction, using data from both SD and FD improves the directional reconstruction significantly: timing information and position of only one triggered SD stations together with the FD data allows for a geometrical reconstruction with typical uncertainties less than 0.5° [BC09]. The calorimetric deduction of the shower energy with the FD gives the most direct estimator for the primary particle energy and only has to be compensated for missing energy ($\sim 10\%$) transferred into neutrinos and high energy muons which do practically not interact with the atmosphere [AA15a]. Events which are reconstructed using information from both detector types are called “hybrid events.”

Since the duty cycle for measuring hybrid events is limited by the operation time of the FD, the high-quality events which allow for both, a hybrid event reconstruction and a reconstruction with the SD in stand-alone mode can be used to cross-validate the directional and energy reconstruction of the SD in standalone mode (see Sec. 5.3). With that, a higher fidelity in the SD event reconstruction can be obtained during times when no hybrid data is available and thus the high duty cycle of the SD can be utilized.

5.2. The fluorescence detector (FD)



Figure 5.2: A photography of the FD building Coihueco taken during daytime, hence the closed shutters in front of each bay. The white building in the background to the right of the FD building is the lidar station at the site of Coihueco.

Charged particles as they are produced within air showers lose energy in collisions with atmospheric particles. Part of that energy is lost by excitation of nitrogen atoms which in turn emit fluorescence light in the UV range between ~ 300 nm and 430 nm. The number of fluorescence light photons generated within an atmospheric volume is proportional to the total amount of energy deposited within. By measuring the fluorescence light emission along the air shower as a function of slant depth X , the profile of the longitudinal energy deposit $\frac{dE}{dX}(X)$ (longitudinal shower profile) of an air shower is accessible. By integrating the longitudinal shower profile along the shower axis one can obtain the total calorimetric energy after compensating for missing energy ($\sim 10\%$) carried away by muons and neutrinos [AJ10b, AA15a]. The nitrogen fluorescence yield in air as a function of wavelength and its dependencies on air temperature and pressure has been measured and analyzed e.g. in [NM04, AM07a, AM13]. For instance, the fluorescence yield in air at 1013 hPa and 20° C of the 337 nm band is $5.61 \pm 0.06_{stat} \pm 0.22_{sys}$ photons per MeV as stated in [AM13]. Thus, atmospheric monitoring is of high importance for precise measurements with the FD. Temperature, pressure and air humidity are monitored using a weather station at each FD building. To keep track of the aerosol density in the atmosphere above the SD plane, four lidar stations are additionally installed at the FD sites (see Sec. 5.4). Measurements with weather balloons that were commenced at the balloon launching station (BLS) are used to build an atmospheric model that can be calibrated with ground-based measurements at the weather stations. The data collected during the balloon ascends was later used to validate the satellite data from the Global Data Assimilation System (GDAS) which then replaced the balloon data [AA15a].

The fluorescence light is collected by the 27 FD telescopes each located in its

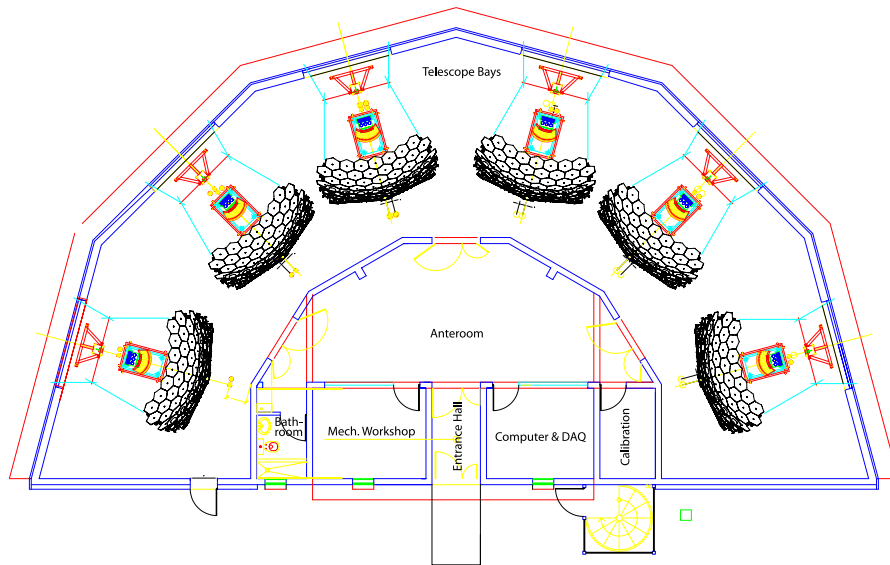


Figure 5.3: A sketch of the interior layout of an FD building [AJ10b]. The six fluorescence telescopes – each located in its own bay – are separated by opaque curtains (not shown in the image) to avoid light scattering between the telescopes. The six telescopes cover an azimuthal field of view of 180° and elevations between 1.5° and 31.5° .

own bay. Each of the four FD building contains six bays and three additional bays form the HEAT (see Sec. 5.4) located in visual range of Coihueco. The arrangement of the bays within an FD building is illustrated in Fig. 5.3. The UV nitrogen fluorescence light enters the FD bay through an entrance window followed by a circular aperture of 1.1 m radius with a corrector ring and a UV filter. The corrector ring is installed to reduce spherical and comatic aberration. The UV filter is made of Schott MUG-6 glass [URL3] and its transmission is limited to light in the UV wavelength regime: above 50% for light between 310 nm and 390 nm and above 80% between 330 nm and 380 nm to keep the light pollution and noise from background light sources at a minimum [AA15a]. Fig. 5.4 shows the interior layout of a single bay and a ray tracing simulation of the optical system.

Each FD comprises a large mirror with an area of $\sim 13\text{m}^2$. The mirrors are segmented into smaller pieces for easier transportation and to reduce the overall manufacturing costs. Two different mirror designs were installed in the field. The mirrors at the sites of Los Leones and Los Morados are segmented into 36 rectangular anodized aluminum mirrors. For the mirrors at Coihueco and Loma Amarilla a hexagonal segmentation into 60 glass mirrors has been chosen. All telescopes have spherical inner radii of 3400 mm allowing with deviations radii up to 3420 mm for individual segments. A laser is used to maintain the spherical alignment of the mirror segments and the alignment of the center of curvature with the optical axis of the FD telescope [AJ10b].

The mirrors reflect the incident UV light onto a camera – the central part of the FD telescope. It is composed of a matrix of 440 pixels (22 rows \times 20 columns)

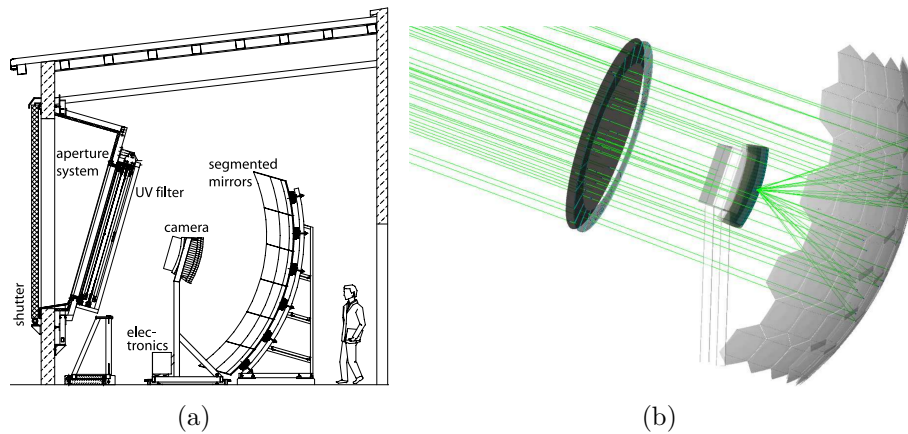


Figure 5.4: (a) A sketch of the arrangement of optical devices inside an FD bay [AJ10b]. (b) A ray tracing simulation of UV light from a distant source calculated with Geant4 [AS03]. The light passes the aperture system, gets reflected by the mirror and focused onto a single point at the PMT camera.

and located on the focal surface of the telescope which is a sphere with a radius of 1.743 m (Fig. 5.5(a)). Each pixel is realized by a photomultiplier tube (PMT) with an enframing light collector. The field of view covered by a single pixel has an angular diameter of 1.5° which is the limit of the angular resolution of the FD to UV point sources. When an air shower traverses the field of view of an FD telescope, the fluorescence light is reflected at the camera in a way that a track across the pixel matrix is created. An illustration of such a track from an air shower is shown in Fig. 5.5(b). The amount of signal recorded at a pixel is proportional to the amount of fluorescence light incident from field of view of that pixel and thus a direct measure for $\frac{dE}{dX}(X)$. The trigger timing information of the pixels can be used to obtain additional information about the shower axis as described in the next section. Since the PMTs of the camera are easily damaged by bright light during operation, the entrance window can be covered with a mechanical shutter system (visible in Fig. 5.2) during daytime. The shutter also closes automatically when a light source, like a bright star, enters the field of view of the respective telescope. Additionally, a fail-safe curtain is mounted at each entrance window in case of a technical failure of the shutter system [AJ10b, AA15a].

5.2.1. Event reconstruction with the FD

Geometry reconstruction. The reconstruction of the air shower geometry with the FD is done in two steps. First, the shower-detector plane (SDP) that contains the shower axis is reconstructed using the track information from the FD camera. Then, the precise location of the axis within the SDP is determined using the timing information from the camera pixels.

The SDP is the plane that contains both, the shower axis and the FD building that observed the shower. Hence, multiple SDPs are possible if a shower is observed at more than one FD site. The SDP is found by fitting a straight line to the

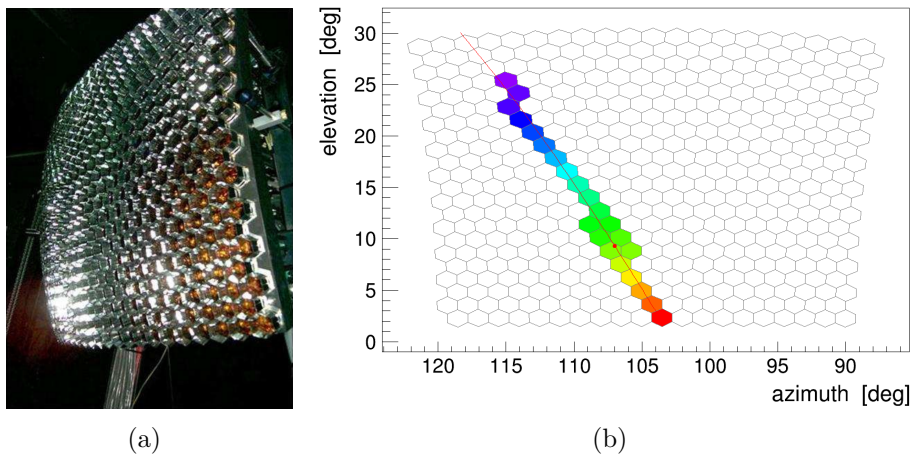


Figure 5.5: (a) The photograph shows the 440 pixels (PMTs) arranged in a hexagonal pattern on a spherical surface that form the camera unit of the FD telescope [AJ10b]. (b) The pattern of an air shower recorded with an FD telescope at Coihueco and displayed via the `Offline` EventBrowser. The projection of the shower axis as reconstructed from the pixel data is indicated by the red line. The color code of the pixels in this image contains timing information – from purple (early signal) to red (late signal).

triggered FD camera pixels (or more precisely a great circle since the pixel array of the FD camera is spherical). An example of such a fit is shown in Fig. 5.5(b) by the red line. Since every pixel points towards a direction in the sky, the fitted line spans a plane containing the FD building and the best fit for the projected shower axis – the SDP. Using laser shots from the central laser facility (CLF) to emulate artificial shower axes, the uncertainty on the SDP reconstruction has been found to be in the order of a few 10ths of a degree depending on the length of the observed track.

The precise determination of the shower axis is more involved than the derivation of the SDP. The shower axis inside the SDP is fully described by two parameters: the minimum distance R_p of the axis to the FD telescope and the angle χ_0 between the axis and the ground on the opposite side of the FD inside the SDP. An illustration of the whole geometry involved in the FD event reconstruction is shown in Fig. 5.6. For the shower axis to be reconstructed with the FD, there has to be a measurable change in the timing difference in the camera pixels. The change in timing is caused by the varying angular velocity of the shower front combined with a relativistic distortion of the angular velocity as the shower front passes the FD. The signal start time t_i of a camera pixel i pointing in the direction with angle χ_i to the ground in the SDP is thus described by

$$t_i = t_0 + \frac{R_p}{c} \tan\left(\frac{\chi_0 - \chi_i}{2}\right) \quad (5.1)$$

where t_0 is the time at which the shower front passes the closest point at the distance R_p and c is the speed of light. The parameters R_p and χ_0 are found

through a χ^2 minimization of the deviations between the measured PMT signal times and the expected values calculated under a set of trial parameters. The individual uncertainties on the signal time measurements are estimated from the width of the signal distributions and taken into account in the fitting procedure as weights.

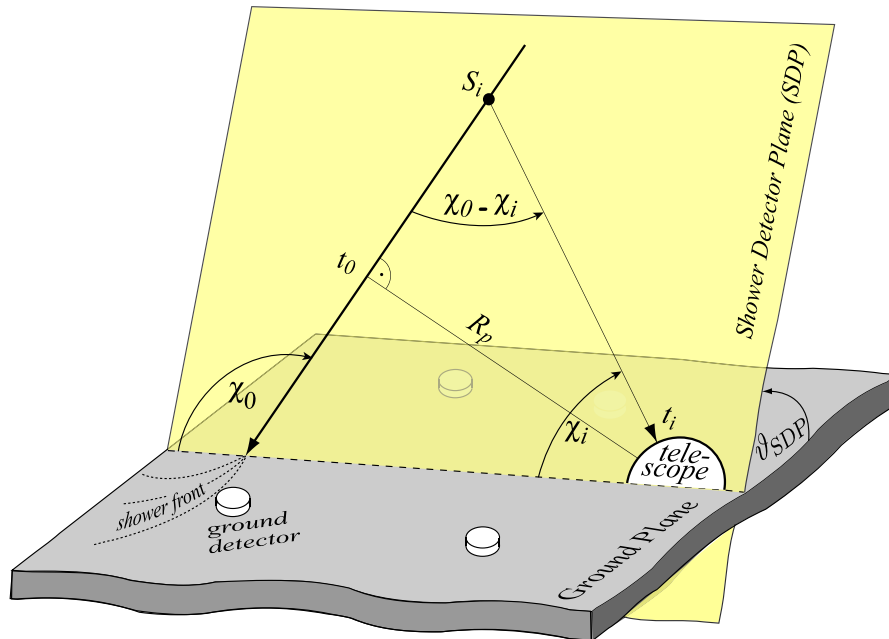


Figure 5.6: An illustration of the geometry reconstruction of an air shower axis with the FD. The yellow plane is the SDP in which all quantities are sketched that are used to fit the shower axis [AJ10b]. For details on the reconstruction procedure see the text.

This reconstruction procedure suffers heavily from short observed track lengths or from shower geometries that do not provide a measurable change in timing difference. Thus, geometry reconstructions with the FD alone, so called “mono events”, can be afflicted with large uncertainties. These uncertainties would then be propagated further into other shower observables like the reconstructed energy. Therefore, additional timing information from the SD is included into the χ^2 minimization to achieve a much better constraint on the free parameters of the shower axis. With this hybrid event reconstruction technique typical uncertainties on the shower axis and thus on the direction of incidence of the initial primary particle in the order of $\sim 0.5^\circ$ are routinely achieved. The shower core is typically reconstructed with an uncertainty of ~ 50 m. Fig. 5.7 shows the difference in reconstruction quality between mono and hybrid reconstruction of the shower axis. The mono reconstruction fixes the curve only at large angles χ and therefore allows for a variety of different possible shower axes within the error margin. The additional data provided by the SD removes that degeneracy by adding timing information close to the ground and helps determining the axis with high precision. [AJ10b, AA15a]

Profile and energy reconstruction. Once the shower axis has been successfully

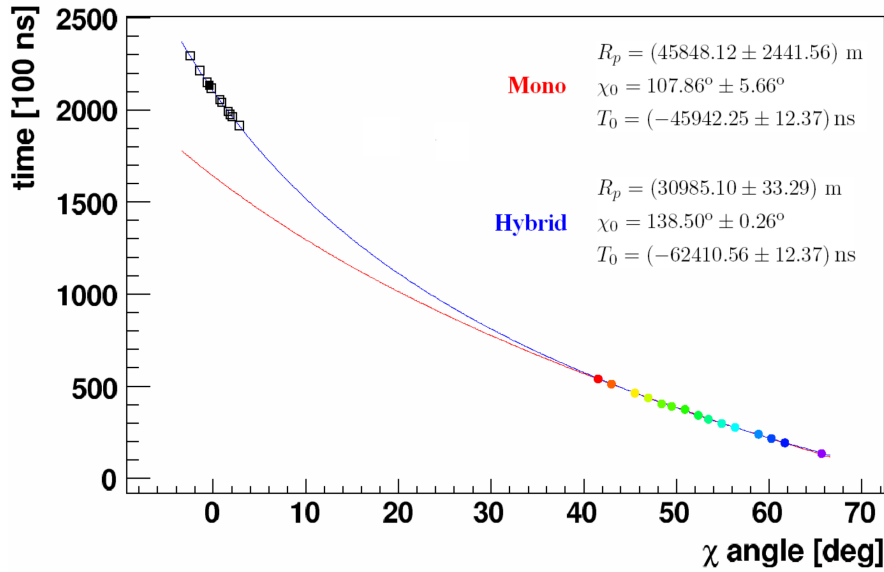


Figure 5.7: The signal time of the FD camera pixels and the triggered SD stations as a function of the angle χ that parameterizes the shower axis inside the SDP (c.f. Fig. 5.6) [AJ10b]. The red curve shows a fit of Eq. 5.1 to the FD data points which have a large degeneracy due to the small curvature of the fit function around the data points. The fit result is significantly improved by including the signal times of the SD stations into the fit resulting in the blue curve.

reconstructed, the signal recorded at the FD camera as a function of time can be converted into a calorimetric energy deposit along the shower axis as a function of slant depth. First, the conversion of PMT signal to the initial amount of light at the aperture has to be known. For this purpose, two different calibration methods are performed on a regular bases.

The absolute calibration is done via an external light source, a pulsed UV LED placed inside a “drum” – a cylindrical apparatus of 2.5 m in diameter that can be mounted at the aperture from the outside. The drum simulates a diffuse light source with known intensity. Since the drum is mounted on the outside of the FD building the relation between light intensity and the associated detector response includes all systematic effects of the optical system from the light entering the aperture to the digital signal output of the flash analog-to-digital converter (FADC) that processes the analog signal output of the camera PMTs. An independent crosscheck of the drum calibration is done via a portable Rayleigh calibration system that emits a laser vertically at a distance from the FD. The light from Rayleigh scattering of the laser beam with atmospheric molecules is then used to calibrate the FD [AJ10b]. Together with the AugerPrime upgrade (see Sec. 5.4) a new method for the absolute calibration of the FD is currently being implemented with the “XY-Scanner” that shall replace the drum calibration procedure in the future [DJ20].

A relative calibration is performed before and after each night of operation to monitor the long and short term performance of the FD telescopes. The relative

calibration is done with three LED light sources by measuring the transmission of the filter and the reflectivity of the mirror components [AJ10b].

With knowledge about the relation between the amount of light at the aperture and the detector response, the light intensity has to be traced back to the shower axis. Multiple effects including scattering on atmospheric particles and aerosols attenuate the fluorescence light during its propagation to the FD telescope while other light sources, direct and scattered Cherenkov light and multiply-scattered light contribute background noise to the data. Those effects have to be disentangled first before the detector signal can be converted into a calorimetric energy deposit profile [UM08].

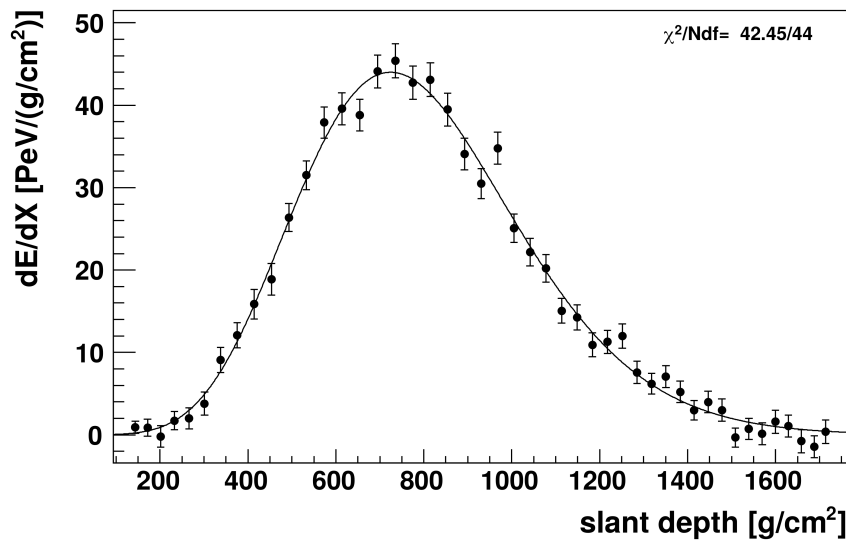


Figure 5.8: The longitudinal profile of an air shower as measured by the FD [AJ10b]. The fitted curve has the functional form of a Gaisser-Hillas function (see Eq. 3.4) and has been used to reconstruct the energy of the primary particle to be $3.0 \pm 0.2 \times 10^{19}$ eV following the procedure described in the text.

The total calorimetric energy of the shower is found by fitting a Gaisser-Hillas function (see Eq. 3.4) to the shower profile and integrating it. The initial energy of the primary particle is then estimated as the total calorimetric energy plus a fraction of about 10% to compensate for energy transferred into muons and neutrinos for which the atmosphere has low cross section. From the fitted Gaisser-Hillas function also the value of the shower maximum X_{\max} can directly be obtained. The typical resolution in terms of statistical uncertainty on the primary particle energy is typically in the order of 10% while the average deviation of X_{\max} has been found to be $\sim 20 \text{ g cm}^{-2}$ [DB07]. An example of a fitted shower profile is shown in Fig. 5.8.

5.3. The surface detector (SD)



Figure 5.9: A panorama picture of the elevated plane on which the SD is located gives an impression of the level terrain. The photograph is taken from the top of the FD building at the site of Coihueco that lies on a small hill at the western edge of the SD. Only a minor fraction of the whole area is overlooked by the picture since the SD spans well beyond the horizon in each direction shown here. The white buildings that are visible in the foreground are the enclosures of the HEAT telescopes.

While the FD observes the longitudinal development of air showers as a function of time, the SD measures the lateral particle density distribution within a horizontal slice through an air shower. The information about the air shower obtained from the SD is complementary to the data taken by the FD and inaccessible by the means of fluorescence light detection. The SD consists of an array of 1660 autonomous WCD stations arranged on a hexagonal grid that covers an area of $\sim 3000 \text{ km}^2$. The SD array is located on an elevated plane with an average altitude of 1420 m above sea level. The elevated location of the SD array was chosen in order to measure the lateral shower profile of air showers with energies $> 10^{19} \text{ eV}$ just below their shower maximum. The elevations of single SD stations lie between 1340 m and 1610 m while the deviation between neighboring stations is typically only in the order of a few meters. The distance between two neighboring stations is 1500 m. However, due to practical reasons small deviations from the ideal spacing had to be taken into account during deployment. The median displacement with respect to the ideal grid is 12 m while only 4% (0.4%) of all stations have a displacement more than 50 m (100 m). The array as a whole can be considered remarkably plane and regular. Fig. 5.9 shows a photograph of a small part of the SD plane taken from the rooftop of the FD building at Coihueco and gives an impression of the terrain.

5.3.1. The water Cherenkov detector

The operation of the SD started in January 2004 after the deployment of the first SD stations in the field. The deployment phase lasted about four years until in 2008 a total number of 1660 WCD stations were operational. Each SD station (Fig. 5.10(a)) works autonomously and completely independent of the other stations and the other parts of the detector. It consists of a cylindrical shaped water tank with a water surface of 10 m^2 and a height of 1.2 m. The outer layer of the tanks is made of polyethylene and colored in a light beige tone to fit into the natural surroundings of the environment. The cavity on its inside is filled with

12 t of highly purified water to serve as a Cherenkov radiator. When charged particles from the secondary cosmic radiation at high energies penetrate the wall of an SD station, they produce a Cherenkov light cone that is beamed in forward direction with respect to the trajectory of the particle. The Cherenkov light can be detected with the three PMTs that are located in three symmetrically arranged hatches in the top wall of the station, each at a distance of 1.2 m from its central axis (see Fig. 5.10(b)). To avoid direct exposure to Cherenkov light, the PMTs are facing downward. The Cherenkov light that is produced by air shower particles that are typically propagating in downward direction is diffusively reflected by the inner Tyvek layer of the station walls before being detected by the PMTs [AA15a, SH01, AI08].

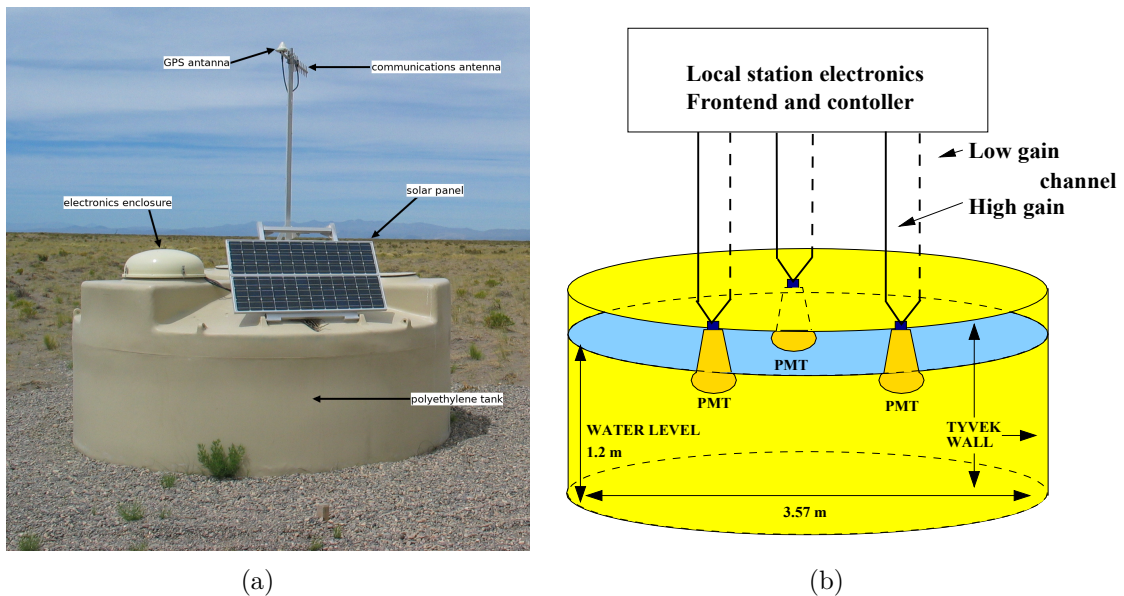


Figure 5.10: (a) A photograph of an SD station as deployed in the field. The hardware components that are visible from the outside are labeled except for the battery box which is located on the backside of the station. Image modified from [URL4]. (b) A schematic view of an SD station and its connection to the front-end electronics [SH01]. Not shown on the drawing are the solar panel, the electronics and battery enclosures and the GPS and communications antenna.

The PMTs are connected to the front-end electronics via a high-gain (HG) and a low-gain (LG) channel. The LG is connected to the anode of the PMT while the HG is connected to the last dynode. The signal of the HG is inverted and amplified by the base electronics of the PMT to provide a signal with 32 times the charge gain of the anode [AA15a]. The analog signal from the PMT is digitised by a 10 bit FADC which operates at a 40 MHz sampling rate [AJ10a]. An exemplary set of time traces recorded by the three PMTs is shown in Fig. 5.11. As a consequence of the FADC sampling rate, the width of a single time bin of a signal trace corresponds to 25 ns.

The electronic components of the WCD are powered by a photovoltaic system

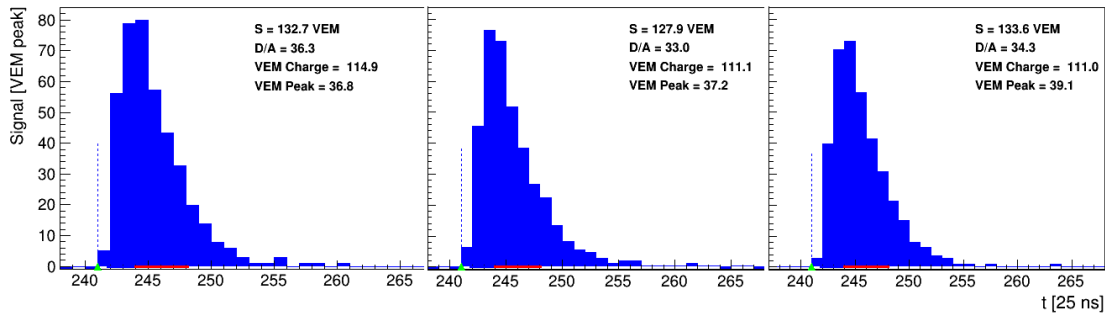


Figure 5.11: An exemplary set of signal traces recorded with the three PMTs measuring the same air shower signal. The width of a single time bin is 25 ns and is given by the sampling rate of the FADC. The bin content has already been rescaled from the 10 bit FADC count to the physical signal unit VEM (see Sec. 5.3.2)

that provides the required average power of 10 W. The power produced by the system is consumed by the local station front-end electronics, the PMTs and the wireless communication system that connects the SD stations to the main campus. It is designed such, that a constant supply of power is provided during 99% of the time and expected to drop only by a few percent after long-term operation. The system includes a solar panel mounted on top of each station that charges a lead-acid battery. The enclosure of the battery is always located on the ground to the south side of each station to keep the exposure to direct sun light at a minimum. The exact timing and positioning information which are important for the physics event reconstruction are obtained from a GPS module located next to the communications antenna on top of the station [AI08]. A picture labeling all the components of an SD stations as visible from the outside is given in Fig. 5.10(a).

5.3.2. Calibration

The SD array is exposed to a constant rate of atmospheric muons produced high in the atmosphere by low energy primary particles. Those muons are typically of low energy and cannot be associated to an air shower event. However, their abundance leads to a continuous counting rate of ~ 3 kHz in each station. For comparison, signal counts due to air shower events are expected to only occur once per hour. Transmission of all recorded data to the central data acquisition system (CDAS) for an offline analysis is not possible due to the bandwidth limitations of the wireless communication system that has a power of 1 W available for transmission over a distance up to 40 km. This limits the total bandwidth at the CDAS to 1200 bit/s [AJ10a]. As a consequence, the calibration of the SD has to be done locally and automatized for each station. The flux of atmospheric muons is therefore used as a source for calibration. A single muon that traverses an SD station vertically and centrally is expected to generate a well-defined pulse in the PMT time trace corresponding to a charge of Q_{VEM} . The background of atmospheric muons produces a peak $Q_{VEM}^{peak} =: 1$ VEM (vertical equivalent muon) in the charge distribution and a peak in the distribution of pulse heights I_{VEM}^{peak} that are

proportional to the charge Q_{VEM} . The reference values of Q_{VEM}^{peak} and I_{VEM}^{peak} are then used for an absolute calibration of the PMT charge gain in regular intervals of 60 s [BX06].

5.3.3. The SD trigger hierarchy

Also limited by wireless transmission bandwidth is the amount of data that can be transmitted to the CDAS by the SD. Hence, data possibly relevant for physics event reconstruction has to be separated from the background rate locally at each SD station by the front-end electronics. The separation of air shower data from background muons and random coincidences is realized by a hierarchical order of trigger levels. Each trigger level induces a stricter condition on the recorded signal and thus sorts out more background than the previous one [AJ10a].

The first two trigger levels T1 and T2 are single station triggers and are installed at the local front-end electronics at each SD station. A measured signal is considered a T1 if it fulfills at least one of the two conditions: either a single time bin exceeds a threshold value of $1.75I_{VEM}^{peak}$ (T1-Threshold, TH-T1 or Th1) or a series of at least 13 bins above a threshold of $0.2I_{VEM}^{peak}$ is found within a time window of 120 bins (Time over Threshold, ToT-T1 or ToT1, or just ToT). The ToT triggers are directly promoted to the second trigger level T2 (ToT-T2 or ToT2), while a Th1 trigger is only considered to be a T2 if at least one bin exceeds a charge value of $3.2I_{VEM}^{peak}$ (T2-Threshold, TH-T2 or Th2). Events that are promoted to a T2 are then sent via the wireless communicator to the CDAS for application of global event triggers while all events that pass the T1 level are stored locally at the SD stations for 10s for the case of a possible request by the CDAS to supplement a global event reconstruction. With the hierarchical ordering of the local triggers, the rate at which data is sent via the wireless communicator is reduced from an initial counting rate of 3kHz to 20 Hz for the Th2 and 2 Hz for the ToT triggers [AJ10a].

In 2013, two additional T2-trigger algorithms have been installed at the SD stations, the MoPS (Multiplicity of Positive Steps) and the ToTd (Time over Threshold deconvolved) [SM13]. These trigger algorithms are designed to be more sensitive to the electromagnetic shower component and thus increase the exposure to light cosmic ray particles and primary photons. The algorithm behind the MoPS trigger scans the raw, uncalibrated time trace of the FADC for certain patterns inherent to signals from the electromagnetic component of air showers while rejecting signals from through-going muons. The ToTd uses a deconvolution of the VEM signal trace to identify single particles in the WCD. An event that passes either the MoPS or the ToTd trigger is directly considered a T2 without the necessity to fulfill one of the other threshold or time-over-threshold triggers [BP09, BP11]. A more detailed description of the trigger algorithms can be found in [BP09, BP11] and in Sec. 11 where the algorithms are utilized for the construction of a new air shower observable.

Every T2 is sent to the CDAS, which is located in the remote control room at the main campus of the Observatory in Malargüe. There, the T2 events are

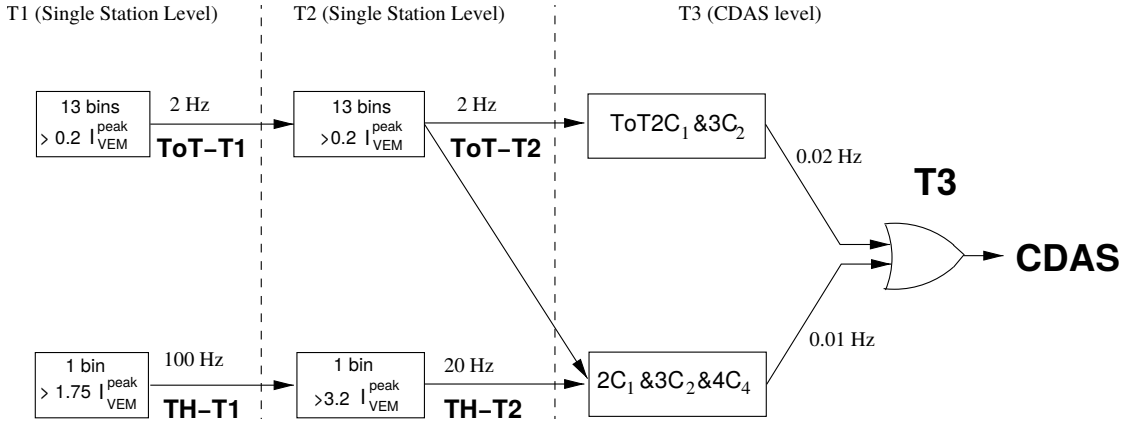


Figure 5.12: A schema of the station trigger logic of the SD array [AJ10a]. The general trigger structure is hierarchical which means that as a necessary condition for an event to pass the trigger level T_N it must pass all $T_1 \dots T_{N-1}$ preceding trigger levels (with $N \leq 5$, c.f. Fig. 5.14). The T1 and T2 trigger levels shown here are local station triggers while the T3 is the first level that takes into account the global trigger information from the SD array. The algorithms behind the different T1 and T2 types which are also indicated in this schema are explained in the text and a description of the array trigger T3 is given in the caption of Fig. 5.13.

checked for spatial and temporal coincidence. A ToT-T2 is promoted to the T3 level, if it fulfills one of two spatial compactness criteria while a Th2 has to fulfill the stricter one of the criteria to pass the T3 level. The definitions of the two compactness criteria are given in the caption of Fig. 5.13. Additionally, a criterion on temporal coincidence is placed that requires only those T2 events are to be taken into account that are within $(6 + 5n) \mu\text{s}$ with respect to the first T2. Here, n is the distance to the first T2 station in terms of “crowns” C_n which are defined as concentric hexagons around the first T2, e.g. the first crown C_1 contains six stations, the second crown C_2 contains twelve stations and so on. When a T3 has been activated, all signal traces that at least pass the T1 level and are thus buffered locally at the SD stations are requested by the CDAS and stored along with the T3 data if the trigger times are within $30 \mu\text{s}$ of the T3 [AJ10a].

The next step in the trigger hierarchy is the T4 level, which applies physics constraints to the stored T3 data. An event passes the T4 if it contains either three neighboring stations in a triangular pattern with ToT-T2 status (3ToT) or 4 neighboring stations without any condition on T2 type or pattern (4C1) (see Fig. 5.14). In addition, the station trigger times have to be consistent with a flat shower front propagating at the speed of light in order to pass either of the two T4 conditions. To reject stations which just by chance are coincident with the physics event, they are marked as “accidental” if they are not consistent with a “first-estimate” shower front or are spatially isolated as closer described in [AJ10a]. The event selection efficiency of the 3ToT (4C1) is $> 98\%$ ($\sim 100\%$) for air showers with zenith angle below 60° and 99.9% of all T4 events allow for a full event reconstruction [AJ10a].

The last trigger level T5 is a fiducial trigger that rejects air shower events which

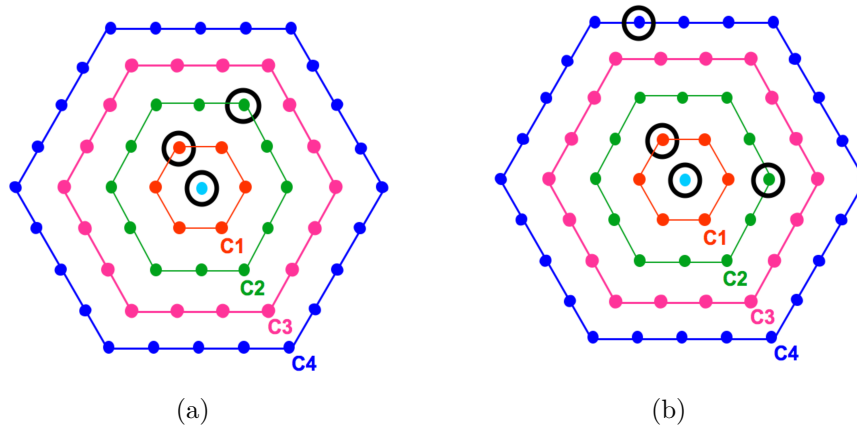


Figure 5.13: This figure is meant to illustrate the two selection criteria of the array trigger level T3 [AJ10a]. (a) the $ToT2C_1\&3C_2$ condition (c.f. Fig. 5.12) requires at least two stations with a ToT-T2 status as close as the first crown C_1 and a third one not farther away than the second crown C_2 . (b) Independent of the T2-type, every configuration of T2 events that passes the $2C_1\&3C_2\&4C_3$ (c.f. Fig. 5.12) condition is promoted to the T3 level. This condition requires two stations with an arbitrary T2 status within the first crown, three stations within the second crown and a fourth station within the third crown.

are only partially observed. This happens when the shower core is close to the edge of the SD array or close to missing or malfunctioning (“black”) stations. Such a detector geometry can lead to poorly reconstructed shower cores and as a consequence to a bias in the reconstructed energy. The T5 is applied offline before the event reconstruction and requires a complete working hexagon around the “hottest” station, i.e. the station with the largest signal (6T5). This condition reduces the effective area of the array on average about 10% and makes sure that the effective area saturates to the geometrical one above a certain energy threshold but also ensures a robust event reconstruction [AJ10a]. There are also other, more relaxed versions of the T5 trigger that require less than 6 active station on the first crown around the hottest station labeled $NT5$, with $N \leq 6$ being the number of required active stations on the first crown. The usage of those less strict T5 versions like in [AA17a] can increase the event statistics and ultimately depends on the goals of the physics analysis that is applied to the data [BP08].

5.3.4. Geometry reconstruction

A rough estimate for the arrival direction of the primary particle can be obtained by fitting a flat shower front to the signal start times of the triggered SD stations. If an air shower event has at least 4 triggered stations, the shower axis can be reconstructed more precisely by determining two critical points along the shower axis: the shower core and a point called the “virtual origin” of the air shower. Instead of a plain shape, the shower front is approximated by a concentric sphere expanding at the speed of light c . The virtual origin \vec{x}_{sh} which is the center of that

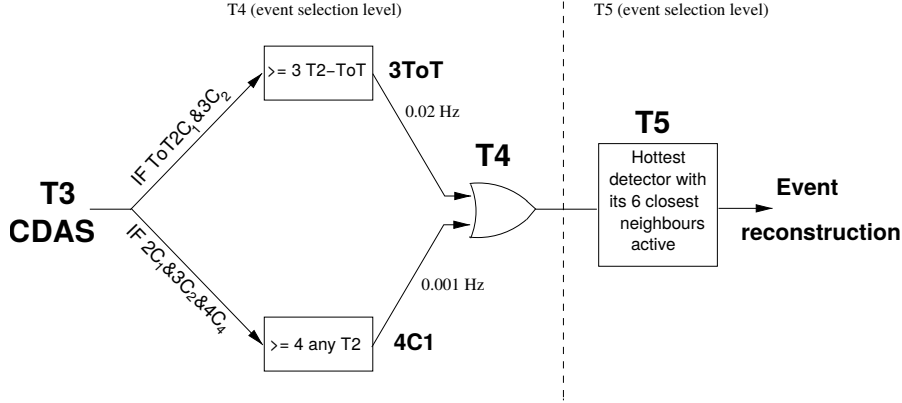


Figure 5.14: The continuation of the SD trigger schema shown in Fig. 5.12 [AJ10a]. After the array trigger level T3, the events are checked for a physically plausible spatial and temporal station trigger distribution to pass the T4 level. Finally the T5 selection is applied as a fiducial trigger to ensure a consistent event reconstruction.

sphere is found by fitting a 4-parameter equation to the signal start times t_i and corresponding station positions \vec{x}_i :

$$c(t_i - t_0) = (\vec{x}_i - \vec{x}_{\text{sh}}). \quad (5.2)$$

The parameter t_0 is the fourth fit-parameter and represents the virtual start time of the shower corresponding to the virtual origin [AA15a].

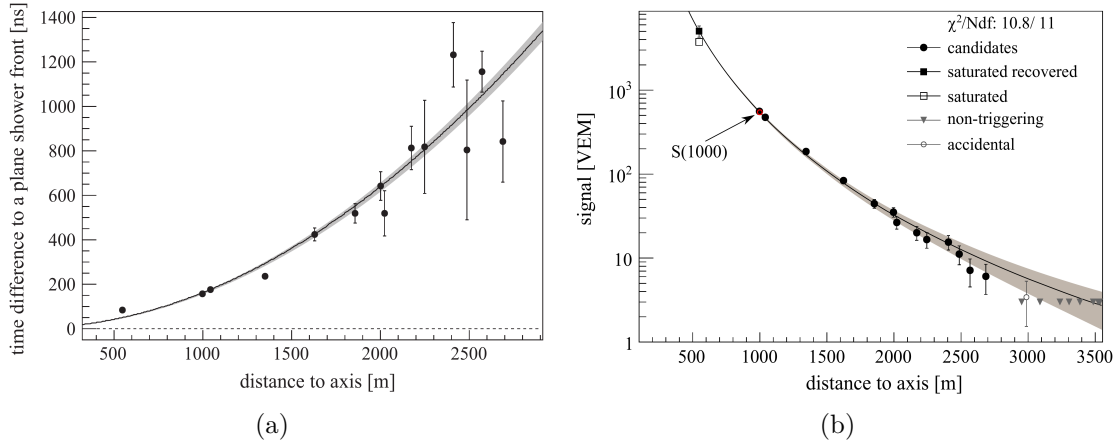


Figure 5.15: (a) The deviation of signal start times with respect to a plane shower front and (b) the integrated VEM signal as a function of distance to the shower axis [AJ10a]. In (b), the fitted value of the shower size estimator $S(1000)$ is indicated.

The shower core \vec{x}_{gr} is found by fitting a lateral distribution function (LDF) to the signals measured by the SD. The function that is used to describe the lateral density distribution of an air shower is a modified NKG function (see Eq. 3.6), which parameterizes the expected signal S at an orthogonal distance r from the shower axis. The optimal distance r_{opt} depends on the geometry of the detector

array and is $r_{\text{opt}} = 1000$ m for the 1500 m spacing of the hexagonal SD grid [ND07]. Hence, the scaling parameter is $S(1000\text{m})$ or just $S(1000)$ and is a measure for the total shower size at ground level. $S(1000)$ and the parameters β and γ are fitted to the signals of the SD stations using a maximum likelihood fit that also takes into account “silent” stations (stations without a trigger) and stations with a large signal that saturates the dynamic range of the PMTs. For events with only 3 triggered stations the fitting procedure is done with fixed values for β and γ which are determined from a parametrization using events with at least 5 triggered stations. With this procedure the shower core \vec{x}_{gr} is found as the position of $r = 0$ of the best fit [AA15a]. The uncertainty on the shower size $S(1000)$ depends on the primary energy and is typically in the order of $\sim 10\% - 20\%$ [AM07b]. Finally, the shower axis \hat{a} is determined by interpolating between \vec{x}_{sh} and \vec{x}_{gr} like

$$\hat{a} = \frac{\vec{x}_{\text{sh}} - \vec{x}_{\text{gr}}}{|\vec{x}_{\text{sh}} - \vec{x}_{\text{gr}}|}. \quad (5.3)$$

To determine the uncertainty on the angular reconstruction of the shower axis with the SD as a standalone detector, a signal time variance model has been developed [BC09]. The angular resolution of events with 3 triggered stations turns out to be typically better than 1.6° and better than 0.9° for events with 6 or more stations [BC09]. The angular resolution of the SD as a function of zenith angle and the number of triggered stations is shown in Fig. 5.16.

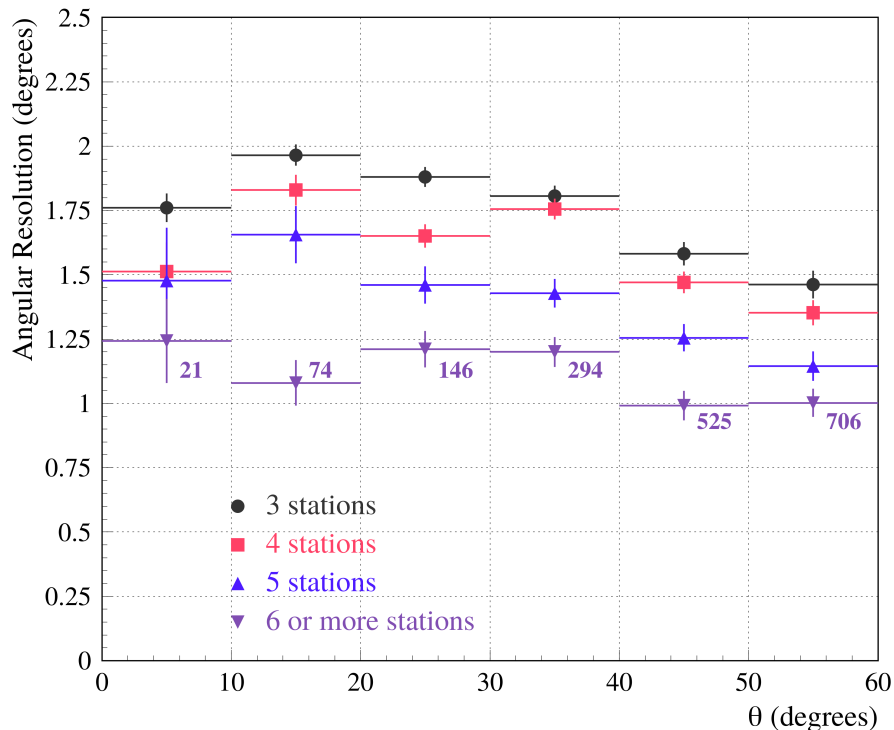


Figure 5.16: The angular resolution of the SD as a function of zenith angle and the number of triggered stations as derived using the signal time variance model [BC09].

5.3.5. Energy reconstruction

The energy reconstruction with the SD alone relies on a cross-calibration with the near-calorimetric energy measurement of the FD and is a two-step process. First the zenith angle dependent shower size estimator $S(1000)$ has to be transferred into the zenith independent quantity S_{38} . The shower size depends on the age of the air shower and decreases after the shower has passed its maximum. Since inclined showers are older than vertical showers when they reach the ground level, $S(1000)$ also depends on the zenith angle of the shower axis as shown in Fig. 5.17(a). That zenith angle dependency can be fitted using the constant intensity cut (CIC) method [HJ61] which makes use of the highly isotropic flux of primary cosmic rays. The CIC function $f_{\text{CIC}}(\theta)$ used to fit the $S(1000)$ dependency on the zenith angle θ is a 3rd order polynomial in $x(\theta) = \cos^2(\theta) - \cos^2(\bar{\theta})$ with the reference zenith angle $\bar{\theta} = 38^\circ$:

$$S(1000) = S_{38} f_{\text{CIC}}$$

$$\text{with } f_{\text{CIC}} = 1 + ax + bx^2 + cx^3. \quad (5.4)$$

The coefficients a , b and c are found by fitting the CIC function to data events at $S_{38} = 50 \text{ VEM}$ [AA15a]. The mean values of the coefficients that are used throughout this work are fixed at $a = 0.956$, $b = -1.625$ and $c = -1.210$ corresponding to those used in [VI15] as documented in the source code of the `Offline` software framework (see Sec. 6.2) in the revision r31920. Fig. 5.17(a) shows a more recent version of the CIC parametrization taking into account the energy dependence of the parameters that can be modeled as second order polynomials in $\log(S_{38}/40 \text{ VEM})$. The value of S_{38} that can thus be derived from the reconstructed values of $S(1000)$ and θ is directly an estimator for the energy of the primary particle.

Using especially well measured hybrid events that allow for both, a full SD reconstruction and a precise measurement of the calorimetric energy with the FD, the zenith angle independent energy estimator S_{38} can then be calibrated with E_{FD} (i.e. the calorimetric energy after compensation for missing energy). The correlation of S_{38} and E_{FD} can be described by a simple power law

$$E_{\text{FD}} = A(S_{38}/\text{VEM})^B \quad (5.5)$$

as shown in Fig. 5.17(b). Eq. 5.5 is fitted to data events with $E_{\text{FD}} > 3 \text{ EeV}$ using a maximum likelihood fit that takes into account different types of uncertainties [VV19]. The resulting mean values of the fit parameters that are used here are $A = 0.187 \text{ EeV}$ and $B = 1.023$ in coherence with [VI15] as implemented in `Offline` r31920. A and B define the energy scale of the SD array and are used to estimate the shower energy for the bulk of data with a systematic uncertainty in the order of $\sim 14\%$ mainly originating in the uncertainty of the absolute calibration of the FD [VV19, VV13]. For primary particles like photons which produce significantly different air showers than the bulk of data, this energy reconstruction method introduces an additional bias that leads to an underestimation of the

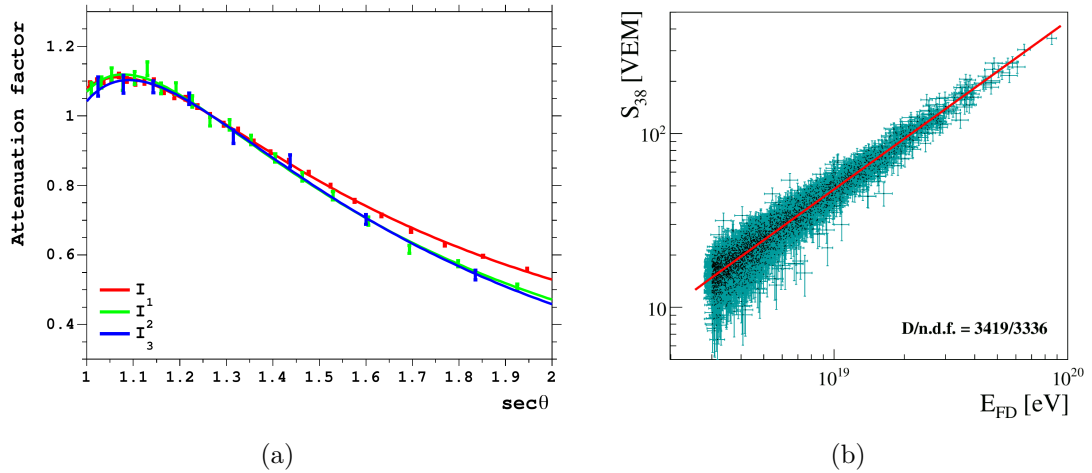


Figure 5.17: (a) The shower size as a function of zenith angle θ normalized to the size $S(1000)$ at $\theta = 38^\circ$ for three different intensity thresholds corresponding to the energies 3 EeV (I_1), 8 EeV (I_2) and 20 EeV (I_3) [VV19]. The fitted functions are described by f_{CIC} (Eq. 5.4) with parameters that depend on the respective S_{38} as described in the text. (b) The correlation of the zenith independent shower size estimator S_{38} and the energy estimator of the FD for 3338 well measured hybrid events recorded between January 1st 2004 and December 31st 2017 [VV19]. The best fit shown by the straight line is the calibration curve for the SD energy scale.

energy. Therefore, in Sec. 7 an alternative method to reconstruct the energy of primary photons is described.

5.4. Other facilities of Auger

Besides the SD and the FD which are the main detector components, the Pierre Auger Observatory comprises a variety of extensions and additional detectors. Some of those which are related to the analysis presented in this thesis or might be relevant for future improvements of the same will be shortly described in the following. Also a major upgrade of the whole detector dubbed ‘‘Auger Prime’’ is currently under deployment and will supplement the whole SD array with hardware enhancements to measure the secondary muons and the radio footprint of air showers at the ground level. This upgrade might also provide useful tools to improve and extend the physics analysis of this thesis in the future and shall therefore also be addressed here briefly.

5.4.1. The low-energy extensions of Auger

The standard hybrid detector of Auger has an energy threshold of $\sim 10^{18}$ eV, at which the detection efficiency for vertical ($\theta < 60^\circ$) cosmic rays is already reduced to $\sim 50\%$, while it only starts to be fully efficient at energies above $\sim 3 \times 10^{18}$ eV [AJ10a, AA15a]. To lower this threshold in order to analyze the transition region in the cosmic ray spectrum from galactic to extragalactic cosmic

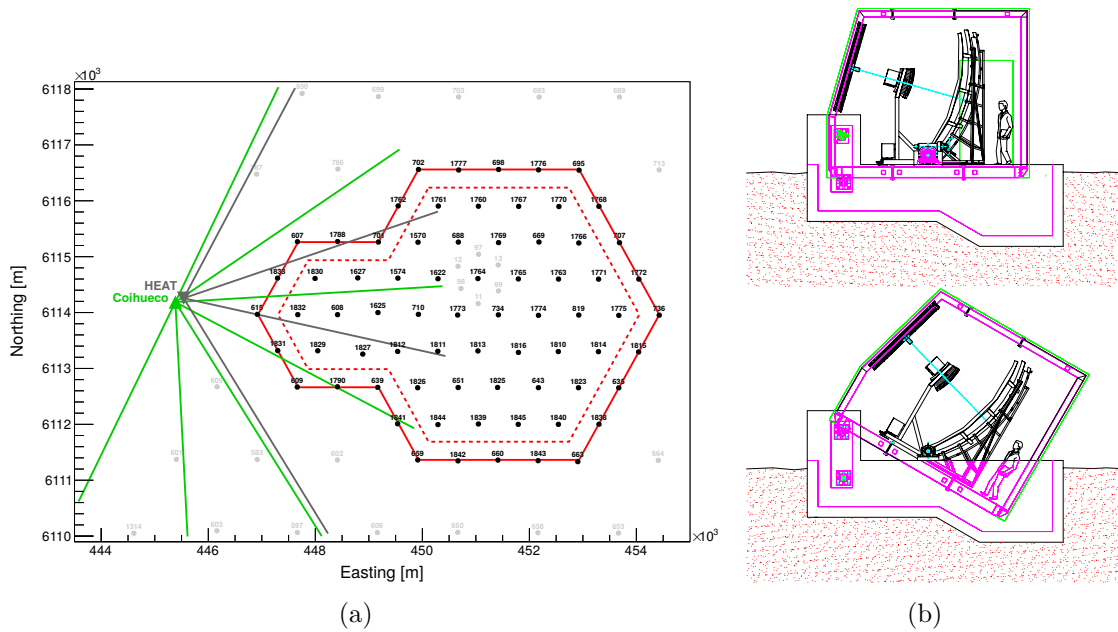


Figure 5.18: (a) A schema of the low energy enhancements of Auger [RJ19]. The red dots mark the positions of the infilled WCDs between the WCDs of the regular SD array (black dots). The horizontal fields of view of the three HEAT telescope along with the fields of view of the six telescopes of Coihueco are indicated as well. (b) The layout of the interior of a HEAT bay which can be tilted about 29° to extend the field of view of Coihueco to higher altitudes [MH11].

rays, low-energy enhancements have been installed along with the main detector components.

To lower the energy threshold of the FD, the High Elevation Auger Telescopes (HEAT) [MH11] have been installed next to the main FD building of Coihueco. Those telescopes are technically identical to those used for the standard FD but are supplemented with an electrically driven hydraulic system that makes it possible to tilt each of the three bays individually about 29° in upward direction (see Fig. 5.18(b)). Thus, it is possible to measure low energy air showers that die out in the atmosphere before traversing the field of view of Coihueco. When HEAT is operated in low-elevation mode, its field of view is completely covered by Coihueco (c.f. Fig. 5.18(a)) allowing for a cross-calibration of the two detectors. The event reconstruction for Coihueco and HEAT does work independently but an additional reconstruction procedure has been developed to improve the measurement of air showers that are observed by both detectors. Since they observe complementary regions of the sky, an additional, “virtual” FD dubbed “HECO” has been defined that combines the fields of view of Coihueco and HEAT to cover a larger solid angle [AA15a, MH11].

In conjunction with HEAT, an area of about 27.5 km^2 of the SD has been upgraded with additional WCDs in between the already existing ones of the standard SD. The additional detectors are placed such, that they form a hexagonal grid with

a next-neighbor spacing of 750 m, the SD-750 m array. The area of the SD-750 m array is chosen such, that it is overlooked by HEAT following up on the hybrid design concept of the Observatory [MM06, AJ10a].

In order to have a handle for a direct measurement of the muon content of air showers and hence to determine the composition of primary cosmic rays, scintillation detectors have been buried next to the WCD stations of the SD-750 m array at a depth that corresponds to $\sim 540 \text{ g cm}^{-2}$. While currently only installed within a hexagonal unitary cell for engineering purposes, the finalized muon detector (MD) array shall be installed beneath at least 61 WCDs of the SD-750 m array. The full installation of the SD-750 m and MD array is named AMIGA (Auger Muons and Infill for the Ground Array) [AA16c]. The low-energy enhancements of Auger extend the energy threshold about one order of magnitude towards lower energies such that a full detection efficiency is reached already at $3 \times 10^{17} \text{ eV}$ [AA15a].

5.4.2. AERA

To explore and understand the radio emission processes of extensive air showers, the Auger Engineering Radio Array (AERA) is situated in the field of the SD-750 m array below the fields of view of Coihueco and HEAT. AERA currently comprises 153 radio antennas distributed over an area of $\sim 17 \text{ km}^2$. The antennas are of two different types, i.e. LPDA (logarithmic-periodic dipole antenna) and butterfly antennas, with different spacing between neighboring antennas (see Fig. 5.19). AERA has been constructed to evaluate the advantages of different radio detection techniques and to demonstrate the capabilities of the radio technique to measure air shower properties like arrival direction, energy and primary particle mass [KJ11, AA15a, GM19].

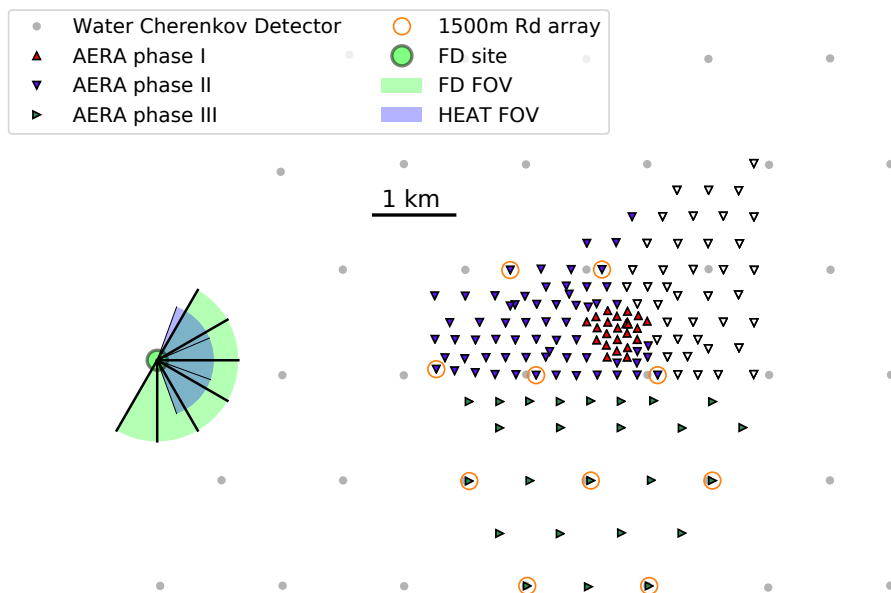


Figure 5.19: A map showing the positions of the AERA radio antennas in the field of the SD-750 m array [GM19].

5.4.3. Laser facilities CLF and XLF

For the calibration of the FD and measurements of atmospheric conditions, two laser facilities are installed in the field at the locations indicated on the map in Fig. 5.1, the Central Laser Facility (CLF) and the extreme laser facility (XLF). The laser facilities operate at a wavelength of 355 nm in between the two nitrogen fluorescence bands at 337 nm and 357 nm at a high spectral purity. The laser pulses of 6.5 mJ are aimed in upward direction and the fluorescence yield, which can be measured by the FD, compares to that of an extensive air shower at 5×10^{19} eV at a distance of 16 km from the FD telescope. With every laser shot, also a nearby SD station is triggered using light from the same laser shot to emulate a hybrid event. Since the power of the laser shots is well known, they serve as an absolute calibration source for the FD and the hybrid measurement technique. The laser shots are performed in sets of 50 pulses every 15 min to track the aerosol content of the atmospheric volume between the laser facilities and the FD telescopes [BS07, VL13].

5.4.4. The Auger Prime upgrade

A major upgrade of the whole Pierre Auger Observatory, dubbed “Auger Prime” is presently in the state of deployment. The upgrade is intended to extend the physics capabilities of the Observatory and expected to give deeper insights into the open questions around UHE cosmic rays, especially about the composition above the cosmic ray ankle region. The upgrade comprises a surface scintillation detector (SSD) and a radio detector (RD) on top of each of the 1660 WCDs in addition to an extension of the dynamic range of the WCD with a fourth, small PMT (sPMT) and an upgrade of the SD station electronics that enables a higher sampling rate of 120 MHz compared to 40 MHz. Also the AMIGA enhancement shall be finalized with underground scintillation detectors next to 61 WCDs of the SD-750 m array and the duty cycle of the FD shall be extended about 50% by reducing the supplied high voltage of the camera PMTs [AA15c, CA19].

The SSD unit is a thin layer of $3.8 \text{ m} \times 1.3 \text{ m}$ containing two scintillator modules with an active detector area of 3.8 m^2 . The scintillators are enclosed in a light-tight and waterproof aluminum box. The light that is produced when ionizing radiation scatters inside the scintillator is bundled with wavelength shifting fibers and conducted to a PMT that translates the amount of scintillation light into an electric signal read out by the SD station electronics. One SSD unit will be mounted horizontally on top of each WCD of the SD array like shown in Fig. 5.20. The detection methods of the SSD and the WCD are fundamentally different and so are their response to the different air shower components. The sensitivity of the SSD to the electromagnetic component relative to the muonic component is more than twice as large compared to the WCD. As a consequence the WCD-SSD tandem is bound to provide a precise measurement of the muon density of individual air showers giving high-quality information about the primary particle on an event-to-event basis [SR17, CA19].

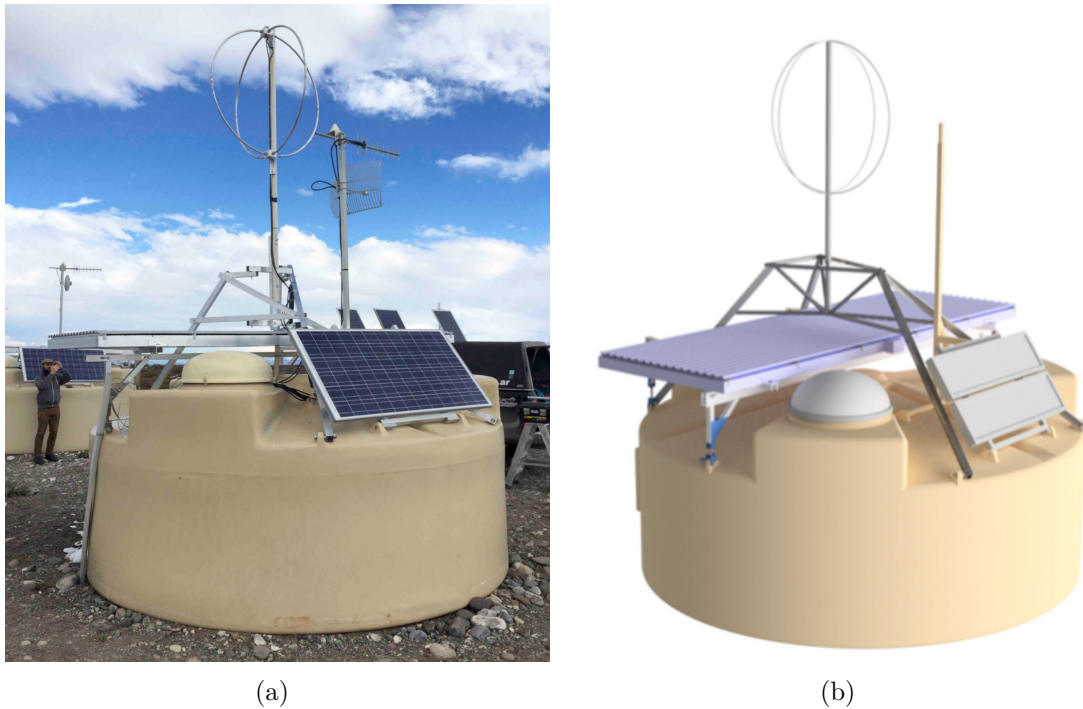


Figure 5.20: (a) A photograph and (b) a computer-generated graphic of an upgraded SD station [CA19]. Visible are the SSD unit as the horizontally attached panel on top of the WCD and the SALLA antenna above the SSD as it is directly attached to the enclosure of the WCD via a mechanical structure that avoids touching the SSD.

In addition to the WCD and the SSD, a third detector type shall be deployed along with the SSD on top of every SD station: the RD. As it has been evaluated using the radio antennas installed in the engineering array AREA, the radio detection method allows for a reliable reconstruction of the electromagnetic component of horizontal air showers. Similar to the tandem measurement technique involving WCD and SSD, a measurement of the electromagnetic shower component complements the muon-dominated signal in the WCD for inclined showers providing not only measurement redundancy but also a tool for the identification of the primary particle mass. The antenna type that has been chosen for the array-wide upgrade is a short aperiodic loaded loop antenna (SALLA) with a dipole loop diameter of 1.2 m and a resonance frequency range between 30 Mhz and 80 MHz [PB19].

The upgrade of the traditional WCD – the installation of an additional sPMT – is aimed to increase its dynamic range. The active area of the sPMT which is only 1/80 of the already installed PMTs increases the maximum detectable signal to 2×10^4 VEM. The sPMT enables the measurement of unsaturated signal traces as close as 250 m to the core of an air shower at 6×10^{19} eV. This allows for an even better reconstruction of air showers at the very highest energies and might provide important insights in the nature of those rare events [CA17, CA19].

Data, simulations and software

THE analyses presented in the following chapters are based on simulations of extensive air showers as well as measured data from the Pierre Auger Observatory and public data on gravitational waves from the Advanced LIGO and Virgo detectors. The technical tools used for simulations, processing of measured data and for analyzing the results build the very basis of every modern work of scientific data analysis. This chapter shall therefore give a brief summary of the software, the software configurations and the data formats that were used to derive the physics results elaborated throughout this thesis.

6.1. Air shower simulations

For all simulations of extensive air showers, the CORSIKA (COsmic Ray Simulations for KAScade) [HD98, HD16] code has been used in the version 7.5600, compiled with the gfortran compiler of the GNU Compiler Collection (GCC) version 4.9.1. CORSIKA, which is mainly written in Fortran77, is being developed at the Karlsruher Institut für Technologie (KIT) and designed to compute detailed Monte Carlo (MC) simulations of extensive air showers initiated by high energy primary particles of various types. While originally written to perform air shower simulations for the KASCADE experiment, it has been continuously revised and extended for other applications and is now a common tool for many groups in astroparticle physics.

CORSIKA tracks individual particles during their propagation through the atmosphere and takes into account their interactions and their decays. For the high and low energy hadronic interactions, different models of cross sections and scattering amplitudes are implemented and can be invoked by the user during compilation. Also, for the simulation of the electromagnetic shower component different numerical realizations may be picked by the user depending on the requirements on output precision and computation time. In particle decays all decay branches down to branching ratios of 1% are taken into account. While different modules like the interaction models or the geometry of the detector which is meant to detect the simulated air showers have to be included during the compilation of the code, many options like direction, energy or type of the primary particle can be controlled by the user via ASCII files in the format of CORSIKA steering cards, an example of which is shown in Fig. 13.1 in the appendix.

6.1.1. Simulation set A: photon spectrum

For the analysis of Chapter 7, a set of 5000 air showers has been simulated with photons as primary particles (simulation set A). The initial particles were simulated continuously between energies of $10^{18.5}$ eV and $10^{20.5}$ eV following a power law spectrum with spectral index $\alpha = -1$ to achieve a logarithmically flat distribution. The distribution in zenith angle θ was simulated proportional to $\sin(\theta) \cos(\theta)$ to account for a geometrical weighting of higher zenith angles with $\sin(\theta)$ and the decreasing effective aperture of a flat detector plane to inclined events due to projection onto the shower plane with $\cos(\theta)$. For the simulation of hadron interactions, the high-energy hadronic interaction model EPOS LHC v3400 [PT15] and the low-energy model FLUKA 2011.2c [FA05] have been used. The electromagnetic showers are simulated with the EGS4 package [NW85] which offers a full MC simulation of all electromagnetic particles. The full MC treatment of air showers beyond the EeV-range however needs immense computation time and the simulation output storing every single particle that reaches the ground level may consume several terabytes of disk space for a single air shower. Therefore, an algorithm named “air shower thinning” has been implemented in CORSIKA (options THIN and THINH). This thinning option enables the user to set a threshold energy as a fraction of the primary particle energy below which not all particles are tracked individually anymore. Instead, in the final state of an interaction only one particle is chosen as “representative” and assigned a weighting factor that accounts for all other particles in the interaction, which are then omitted from further processing. In a later step, these thinned showers are again un-thinned within the Offline framework prior to the simulation of the detector response. The particle energy threshold at which thinning algorithms start to affect the shower development has been set to a fraction of 10^{-6} of the primary particle energy for all simulations in this work. A maximum allowed weight for both hadronic and electromagnetic particles has been chosen according to the optimum thinning relations given in [HD16]. The distance to the shower core up to which an additional thinning at the detector level is applied is set to 300 m. An exemplary CORSIKA steering card (configuration file) of an air shower from this set of simulations is shown in the appendix in Fig. 13.1. Since this simulation set consists of photon-induced air showers at high energies, the preshower effect has to be considered. This effect has also been taken into account in the simulation within CORSIKA.

6.1.2. Simulation set B: photons and protons at fixed energies

In Chapter 11 two different sets of air shower simulations are used to analyze the properties of the newly developed air shower observable R_{MoPS} . One set consists of primary photons (simulation set B_γ) and the other one of primary protons (simulation set B_p). Instead of a continuous energy spectrum, the primary particles of B_γ (B_p) have been simulated at fixed energies between $10^{18.4}$ eV and $10^{19.0}$ eV (between $10^{18.0}$ eV and $10^{19.0}$ eV) with a step size of 0.2 in $\log_{10}(E/\text{eV})$. For each particle type and energy 2000 air showers have been simulated yielding in total 8000 photon showers and 12000 proton showers. The software versions of CORSIKA and

its external dependencies for both sets are the same as for set *A*. The CORSIKA steering cards differ from the one in Fig. 13.1 only by the energy range (ERANGE) which is set to a fixed energy for each energy-subset and, in case of primary protons, by the primary particle ID (PRMPAR). Also the maximum weight for air shower thinning has been adjusted according to the optimum thinning relation for each energy. Finally, for the simulation of the proton subset the optional preshower plugin has been omitted.

6.2. Detector simulation and reconstruction

After finishing the air shower simulation step, the particle distribution at ground level is used to simulate the response of the Auger SD to each shower. The simulation of the detector as well as the standard event reconstruction have been done using the `Offline` software framework [AS02] in the Apache Subversion (SVN) revision r31920 for all detector simulations and event reconstructions as well as data reconstructions in this thesis. Compilation of the `Offline` framework as well as all C++-based analysis code has been done with the g++ compiler of the GCC version 4.9.1. `Offline` is being developed by the Pierre Auger Collaboration and written in the programming language C++. It has a modular design which allows for a variety of applications around the simulation and reconstruction of events at the Pierre Auger Observatory and its many different detector types. The response of the WCDs of the SD array is simulated within the `Offline` framework using the functionality of the Geant4 (GEometry ANd Tracking) framework [AS03]. `Offline` has a number of external dependencies which are not distributed along with `Offline` but have to be installed separately or via the APE (Auger Package Environment) tool. A list of all external packages with their version tag as used in this thesis is given in Tab. 6.1. The configuration of the `Offline` runtime is done via configuration files in the XML format. The basic simulation setup which determines the modules that are invoked during an `Offline` run are defined within a *ModuleSequence* file while individual parameters of each module can be overridden with a *bootstrap* file allowing for a high degree of customization of the runtime behavior.

6.2.1. Simulation sets *A* and *B*

The simulation and reconstruction of both simulation sets *A* and *B* have been done within the same run for each shower using the `Offline` module sequence shown in Fig. 13.2 in the appendix. Apart from the usual modules that are commonly used in the standard application of simulation and reconstruction of SD events, the modules *SdCompositionParameters* and *RiseTime1000LLL* have been included for the calculation of the air shower observables used in Chapter 7. Moreover, each shower has been used 5 times with different randomized shower cores inside the plane of the SD. The logic of the event reconstruction follows the procedure described in Sec. 5.3. Only for the photon simulations of set *A*, the SD stations that were triggered solely by one of the new trigger types MoPS or ToTd were rejected during the reconstruction step for consistency with the prevailing photon

package name	version tag
AERARootio	v00r16
aevread	v02r00p04
AIRES	2-8-4a
boost	1.67.0
CDAS	v6r0p1
CLHEP	2.4.0.4
CPPUNIT	1.13.2
Eigen	3.1.2
fdeventlib	4.1.9
FFTW	3.3.3
Geant4	10.04.p01
HDF5	1.10.1
ROOT	5.34.38
Xerces-C++	3.1.3

Table 6.1: A list of the external dependencies of Offline and their corresponding version tags as used in this thesis.

search analyses. This rejection has not been made for the simulations of set *B*. The fully simulated and reconstructed air shower events are finally stored in the form of ADST (Advanced Data Summary Tree) data files which allow for efficient access to high level properties like shower energy or axis through a collection of C++ libraries distributed together with Offline.

6.2.2. Air shower data

The data that are used as *training data* in this thesis are a subset of the whole Auger SD data. It comprises 2% of the data collected between UTC 2004-01-01T12:00:00 and UTC 2018-07-01T11:59:59. The training data until UTC 2013-05-14T23:59:59 have first been selected randomly in [KN17] and later adopted in [RJ19]. Data events with later time stamps are selected as part of the training data if their SD event ID is a multiple of 50.

The reconstruction of raw data from the Auger SD basically follows the same steps as the reconstruction of simulated events. Additional steps that have to be taken for data reconstruction are for instance further checks on the quality of the signal traces, the status of individual stations of the array which might have been irresponsive at the event time due to hardware issues and a rejection of events that were induced by lightning or laser shots rather than cosmic rays. The module *SdPMTSignalShapeQualityChecker* [PP15, PP18b, URL1] has been used in addition to the standard module sequence to reject stations with PMTs exhibiting certain features that would have malicious effects on the photon search analysis (see Chapter 7).

6.3. Public gravitational wave data

The GW data that is used for the multimessenger studies of this thesis have been measured by the Advanced LIGO and Virgo detectors and are distributed via the publicly available Gravitational-Wave Candidate Event Database (GraceDB) [URL2] in the form of the Flexible Image Transport System (FITS) data format [WE79]. In addition to a key-value map containing information about e.g. the GW event time, the source distance for the most likely source direction and the corresponding uncertainty, each FITS file contains a 2-dimensional probability density distribution on the celestial sphere describing the directional localization of the GW source. The distribution is encoded in a pixelized sky map using the HEALPix (Hierarchical Equal Area isoLatitude Pixelisation) [GK05] format. Depending on the order k , HEALPix allows for a rasterization of the sphere into $N_{pix} = 12 \times 2^{2k}$ pixel of equal area $\Omega_{pix} = \frac{\pi}{3 \times 2^{2k}}$ with their geometrical centers aligned on rings of constant latitude and being equidistant in azimuth [GK05]. An example of a HEALPix grid imposed on a spherical surface is shown in Fig. 6.1 for $k = 0, 1, 2, 3$. The resolutions of the sky maps that are provided by LIGO/Virgo vary between events and depend on the overall resolution quality. Typical resolutions currently lie between $k = 6$ for poorly localized events and up to $k = 11$ for the best localizations. For each pixel there is not only information about the directional source probability in the FITS files, but also an individual estimate for the source distance and the corresponding uncertainty assigned to that respective pixel. For most applications, however, only the “best-fit” source distance has been used which is the distance that is assigned to the most likely source direction and is explicitly given in the key-value map.

Reading and processing of the FITS files and their embedded HEALPix maps has been done using the HEALPix C++ libraries which provide a file handle for the FITS format and routines to convert the recursive pixel numbering scheme of HEALPix into human readable spherical coordinates.

6.4. Further software

Beside the aforementioned tools for simulation and data reconstruction, further software for computing and data analysis has been used in this thesis. The computing platform that has been used for simulations and data reconstruction is the HPC (High Performance Computing) cluster SiMPLE (Siegen Multi Processor Linux Environment) provided by the group for experimental particle and astroparticle physics of the University of Siegen running Debian 8 (“jessie”, testing, kernel version 3.16.0-4-amd64) as its operating system. The analysis code, which is written mainly in C++14 with parts written in python 3.6.9 and GNU bash (versions 4.4.20 and 4.3.33), has been developed partly on Debian 8 and on Ubuntu 18.04 LTS (“Bionic Beaver”, kernel version 4.15.0-111-generic). For plotting, the C++ libraries of the ROOT Data Analysis Framework [BR97] (version 5.34.38) developed at the European Organization for Nuclear Research (Organisation Européenne pour la Recherche Nucléaire, CERN) [URL8] have been used. This thesis

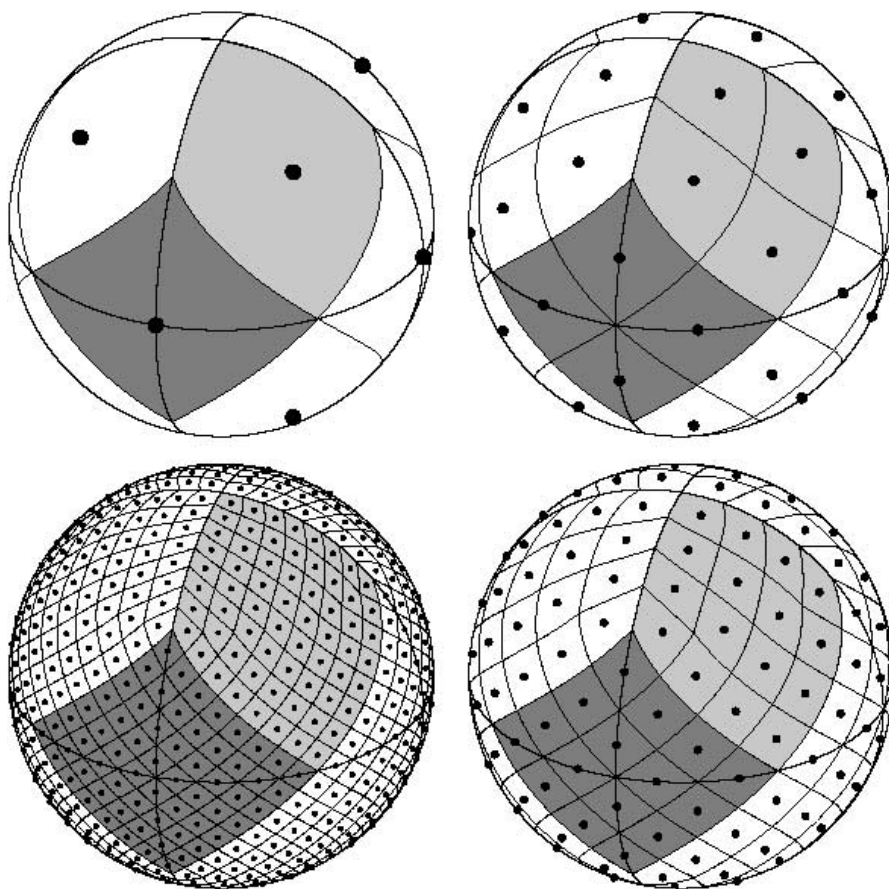



Figure 6.1: The HEALPix rasterization of a sphere for four different resolution parameters $k = 0, 1, 2, 3$ [GK05].

itself is written in \LaTeX and compiled with pdfTeX (version 3.14159265-2.6-1.40.15 as distributed with the TeX Live 2015/dev/Debian package).

Separation between primary photons and hadronic background

 ONE difficulty that comes with the indirect measurement of cosmic rays is the reconstruction of the primary particle from air shower properties. While it is comparably easy to reconstruct the direction of incidence from the air shower geometry, the deduction of the primary particle type is more challenging as discussed in Chapter 3. Statements about primary particle types and masses are typically only made on a statistical basis rather than about individual events. This approach is not possible when searching for rare particles like primary UHE photons. Different techniques have been elaborated at the Pierre Auger Observatory that make use of the distinctive features of photon-induced air showers (see Sec. 3.5) in order to separate a possible component of primary photons from the background of hadronic cosmic rays [AA16a, AA17a, RJ19]. Finding a set of air shower observables that have a good separation power between photons and hadrons is the key for the discovery of a possible photon component. The Auger hybrid detector allows for high separation power due to the complementary measurement techniques of SD and FD, and its energy threshold for photon discrimination is about 1 EeV. The hybrid measurement using the low-energy extensions HECO and the SD-750 m array, though at the cost of having less exposure, enables an extension of the photon energy range down to 0.2 EeV. However, while hybrid measurements provide good separation power, their duty cycle is limited to the operation time of the FD which is only about 15% (see Sec. 5.2). When analyzing the diffuse flux of primary photons, the reduced duty cycle only leads to a reduction of the exposure by the same factor. For a follow-up search for photons from transient sources like CBMs it means that on average less than one out of six sources will be covered by the up-time of the FD. For that reason the SD as a standalone detector is more suited to study the sources of GWs in a first approach since these are still rather limited in number.

The method that is used in this thesis to identify photon-induced air showers among the bulk of hadronic events measured with the SD has been adopted from previous studies. The basic concept of the method including the derivation of the photon energy, the photon discriminating air shower observables and the combination of those observables in a principal component analysis (PCA) has been developed in [KN17]. Further improvements to the event selection method have been proposed in [PP15, PP18b, URL1] and an application of the method to

SD data has been presented in [RJ19]. In this chapter, the method that has been applied in [RJ19] to identify photon-induced air showers is documented covering all details that are necessary for a successful reproduction of the photon search analysis presented therein. In addition to the reproduction of the analysis, the photon discrimination method is analyzed here in more detail in preparation for the analyses in Chapters 8, 9 and 10.

In Sec. 7.1, the determination of the photon energy scale is described and its associated statistical and systematical uncertainties are further analyzed and discussed. The selection of the basic data set is described in Sec. 7.2. The photon discriminating air shower observables and the final photon candidate selection cut are defined in Sec. 7.3 and Sec. 7.4. The results of the reproduced analysis using a training data set are also shown. Furthermore, the angular resolution of the SD to primary photons that pass the event selection cuts is analyzed in Sec. 7.5. In Sec. 7.6, the photon detection efficiency of the event selection is derived as a function of energy and zenith angle and an estimation of the isotropic background rate associated to that analysis is given.

7.1. Photon energy

The water Cherenkov detectors of the SD are mostly sensitive to the muon component of air showers. Photon-induced showers which are poor of muons produce less signal in the SD stations and consequently the energy of primary photons is underestimated by the standard energy reconstruction of hadronic primaries as described in Sec 5.3. For photon energies above 10 EeV the factor between the reconstructed hadronic energy and the true MC energy is on average about 2.5 and has only a small energy dependence. The bias of the reconstructed energy using the standard energy reconstruction is shown in Fig. 7.1(a) as the residual between reconstructed and MC energy for simulated photon showers in the energy range between $10^{19.0}$ eV and $10^{20.5}$ eV (corresponding plots for narrower energy bins can be found in the appendix in Fig. 13.4). The bias is due to the energy calibration of the SD which uses hybrid data to make use of the precise determination of the calorimetric energy with the FD. Since the bulk of data consists of hadron-induced air showers with a large muon component, this energy calibration naturally does not provide correct results for primary photons.

In order to have a more accurate estimate of the energy of an air shower that has been induced by a primary photon, an alternative method to reconstruct the photon energy has been developed in [KN17] (and applied in [RJ19]). This method makes use of an iterative approach that converges to the best-guess value for the shower energy under the assumption that the primary particle was a photon rather than a hadron. The first step of the algorithm is an estimation of the shower maximum $X_{\max,1}$ from the first-guess value of the photon energy $E_{\gamma,0} = 2E_{\text{hd}}$ by using the empirical formula

$$X_{\max,i}(E_{\gamma,i-1}) = q_0 + q_1 \log_{10}(E_{\gamma,i-1}/\text{EeV}) + q_3 \log_{10}^2(E_{\gamma,i-1}/\text{EeV}) \quad (7.1)$$

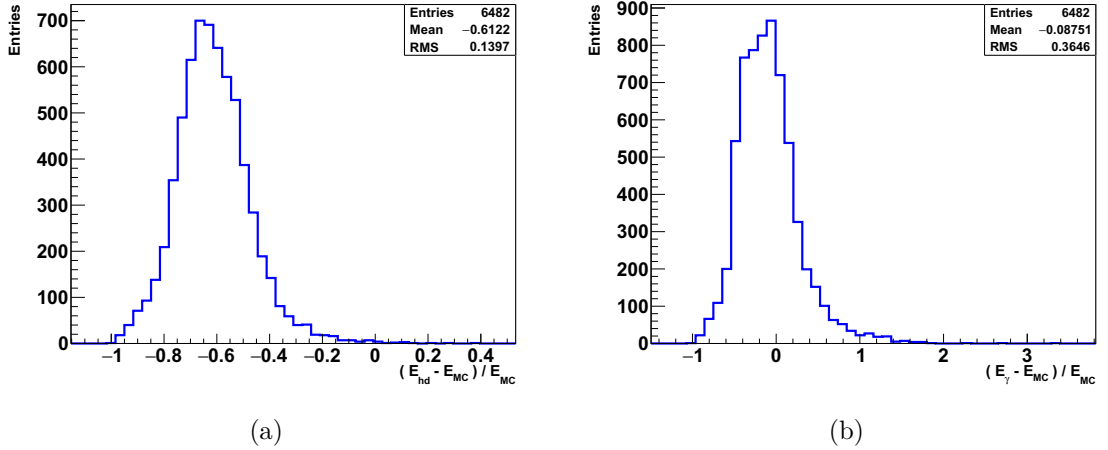


Figure 7.1: (a) The residual between the MC energy E_{MC} and the reconstructed hadron energy E_{hd} using the standard energy reconstruction of the SD. (b) The residual between E_{MC} and the reconstructed photon energy E_γ following the reconstruction algorithm described in the text. The plots show the distributions for the photon simulation set A described in Sec 6.1.1.

for the elongation rate (i.e. the change of X_{max} with energy) of primary photons. The parameters $q_0 = (871 \pm 18) \text{ g cm}^{-2}$, $q_1 = (64 \pm 31) \text{ g cm}^{-2}$ and $q_2 = (37 \pm 12) \text{ g cm}^{-2}$ have been fitted in [KN17] to non-preshowering photon showers in the energy range from $10^{18.5} \text{ eV}$ to $10^{20.5} \text{ eV}$. Compared to hadron primaries the elongation rate for photons in this energy range is described better by a quadratic function than by a linear one due to the LPM effect (c.f. Fig. 3.8(a)).

In the next step, the universal profile of electromagnetic cascades (c.f. Sec. 3.4) is used to obtain the next iteration value for the photon energy, $E_{\gamma,1}$. The longitudinal profile is represented by a Gaisser-Hillas-shaped function

$$\frac{S(1000)}{(E_{\gamma,i}/\text{EeV})^\alpha} = p_0 \left(1 + \frac{\Delta X_{gr} - p_2}{p_1} \right)^{p_1/\Lambda} \exp \left(-\frac{\Delta X_{gr} - p_2}{\Lambda} \right) \quad (7.2)$$

with

$$\alpha = \alpha_0 + \alpha_1 \Delta X_{gr} \quad (7.3)$$

correcting for the energy dependence of the universal profile, $\Delta X_{gr} = X_{max,i} - X_{gr}$ and $X_{gr} = X_{gr,vertical} / \cos \theta$ being the vertical atmospheric depth of the detector ($X_{gr,vertical} \approx 880 \text{ g cm}^{-2}$ for Auger) divided by the cosine of the zenith angle θ . The parameters are $p_0 = (3.04 \pm 0.01) \text{ VEM}$, $p_1 = (592 \pm 13) \text{ g cm}^{-2}$, $p_2 = (152 \pm 2) \text{ g cm}^{-2}$, $\alpha_0 = 0.83 \pm 0.01$ and $\alpha_1 = (2.3 \pm 0.3) \times 10^{-4} (\text{g cm}^{-2})^{-1}$ of which only the central values are used for the iterative procedure⁷ (the same is true for

⁷In the revision r31920 of the `Offline` software framework that has been used for the reconstruction of the photon energy, the central values of the parameters q_0 and p_0 have been slightly changed to $q_0 = 872 \text{ g cm}^{-2}$ and $p_0 = 3.03 \text{ VEM}$.

Eq. 7.1). For the attenuation length Λ a value of $\Lambda \approx 100 \text{ g cm}^{-2}$ is used. The next step $E_{\gamma,1}$ in the approximation of the photon energy is obtained by inserting the reconstructed $S(1000)$ and θ together with $X_{\max,1}$ from Eq. 7.1 into Eq. 7.2. The procedure is repeated iteratively to obtain higher order approximations of E_{γ} until the algorithm converges, i.e. two successive iterations of E_{γ} differ by less than 10 TeV. The convergence happens on average after 8 iterations as stated in [KN17]. The photon energy estimator that is returned by this algorithm reduces the bias in the energy reconstruction to $\sim 9\%$ averaged over the energy range $10^{19.0} \text{ eV} \leq E_{\gamma} < 10^{20.5} \text{ eV}$ with a spectral distribution $\propto E^{-1}$ (see Fig. 7.1(b)). The remaining bias exposes an energy dependence reaching from $\sim 1.8\%$ for $10^{19.0} \text{ eV} \leq E_{\gamma} < 10^{19.5} \text{ eV}$ to $\sim 21\%$ for $10^{20.0} \text{ eV} \leq E_{\gamma} < 10^{20.5} \text{ eV}$ as visible from the right column of plots in Fig. 13.4 in the appendix. In all energy bins the bias on E_{γ} is dominated by its statistical uncertainties due to shower-to-shower fluctuations. These uncertainties are in the order of 36% for the whole energy range while reaching from 33% in the lowest energy bin to 38% in the highest energy bin.

7.2. Event selection

To clean the data set of non-well reconstructed events, a number of selection criteria has been introduced in the analysis presented in [RJ19] and further described in [URL1]. The selected events are required to have reconstructed energy, shower axis and LDF and have to fulfill the 6T5 trigger criterion (6 active SD stations around the station with the highest signal). For the calculation of the discriminating air shower observables Δ and L_{LDF} (introduced in more detail in Sec. 7.3) events with reconstructed hadronic energy $E_{\text{hd}} < 10^{18} \text{ eV}$ (Δ -flag) and events without triggered stations (excluding LG saturated stations) more than 1000 m away from the shower axis (LDF-flag) are rejected. Furthermore, also events were rejected for which the routine to determine the photon energy converged to an X_{\max} value less than 50 g cm^{-2} below ground level or did not converge at all (E_{γ} -flag). To avoid biases on the observables L_{LDF} and Δ , malfunctioning SD PMTs are identified and excluded in the `Offline` module `SdPMTSignalShapeQualityChecker` described in [PP15], [PP18b] and [URL1]. As mentioned before, a cut on the zenith angle and the reconstructed photon energy was placed to allow only for reconstructed showers with $30^\circ \leq \theta \leq 60^\circ$ and photon energy $10^{19.0} \text{ eV} \leq E_{\gamma} < 10^{20.5} \text{ eV}$. Finally, events with a time stamp within a “bad period” (i.e. a period of known issues related to data taking with the SD) and stations that were triggered by lightning⁸ rather than cosmic rays are also rejected. The impact of the different cuts on a simulated spectrum of primary photons is shown in Fig. 7.2. The integrated detection efficiency for photons above $10^{19.0} \text{ eV}$ following a (reweighted) spectral distribution $\propto E^{-2}$ after application of all cuts is $\epsilon_{\text{SD}} = 0.483 \pm 0.008$ (statistical

⁸The electromagnetic pulse of a lightning strike induces high frequency noise in the electronics of nearby SD stations which can activate the local SD station triggers [BX09]. Such stations which are triggered by lightning are filtered during the air shower reconstruction within the `Offline` module `SdEventSelector` via the algorithm `IsLightning()` of the `sevt` namespace.

error margin at 68% CL derived from the Clopper-Pearson confidence interval of binomial distributed random numbers [CC34]).

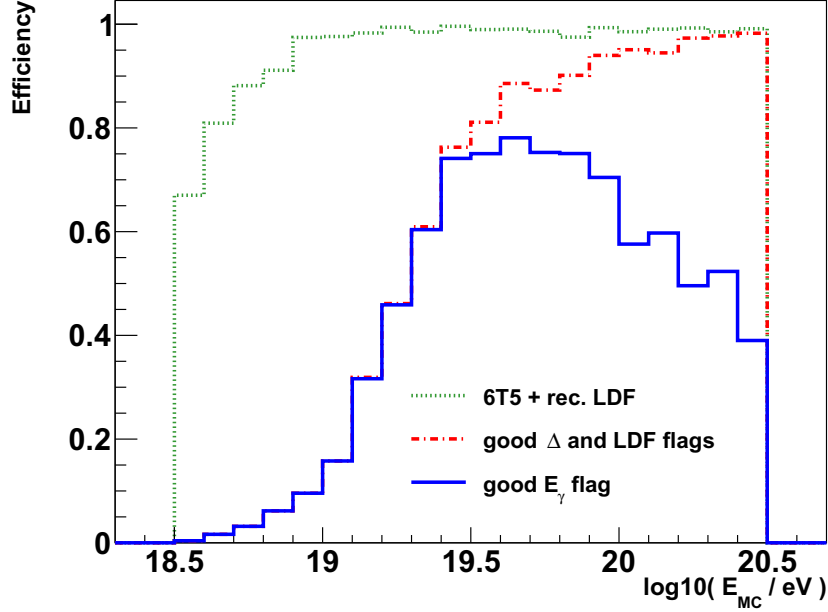


Figure 7.2: The photon detection efficiency as a function of the MC energy after the successive application of selection cuts. The green dotted line shows the fraction of events that have a reconstructed energy, shower axis and LDF and pass the 6T5 trigger. The red dash-dotted line shows the efficiency after application of the selection cuts necessary for the calculation of the observables Δ (“good Δ flag”) and L_{LDF} (“good LDF flag”), and the blue solid line shows the net photon detection efficiency after application of the final quality cut needed for the reconstruction of the photon energy (“good E_γ flag”). The plot shows the distribution for the photon simulation set *A* described in Sec 6.1.1.

7.3. Observables

After applying all selection cuts as described in Sec. 7.2 the remaining set of air shower events is scanned for possible *photon candidate* events. This analysis uses two observables to discriminate between air showers that are induced by photons and those induced by hadronic primaries. The first observable, L_{LDF} (originally named R_{NKG} in [KN17], later renamed in [RJ19]) is given by

$$L_{\text{LDF}} := \log_{10} \left(\frac{1}{N} \sum_i \frac{S_i}{LDF(r_i)} \right) \quad (7.4)$$

where the sum goes from $i = 1$ to $i = N$ with N being the number of triggered SD stations, S_i is the signal (in VEM) of station i which has an orthogonal distance r_i to the shower axis and $LDF(r_i)$ is the average signal of a station at distance r_i . $LDF(r_i)$ is obtained by fitting the lateral signal distribution of the shower with

a parameterized LDF obtained from the bulk of data events. Air showers with a small muonic component on average have a steeper LDF compared to showers with a larger muonic component. For an average data event, the observable L_{LDF} is expected to be close to zero. Thus, L_{LDF} for photon-induced showers is expected to be negative. The second observable Δ is given by

$$\Delta := \frac{1}{N} \sum_i \delta_i, \quad \text{with } \delta_i = \frac{t_{1/2}^i - t_{1/2}^{\text{Bench}}}{\sigma_{t_{1/2}}^i}. \quad (7.5)$$

Here, the sum runs again over all triggered SD stations. δ_i is the residual of the signal risetime $t_{1/2}^i$ of station i and $t_{1/2}^{\text{Bench}}(r_i)$ is a parameterized “data benchmark” for the risetime of a station at distance r_i that has been corrected for the expected asymmetry in the azimuth angle with respect to the shower axis. The signal risetime is defined as the time difference between the 10% and the 50% quantiles of the PMT signal traces. $\sigma_{t_{1/2}}^i$ is the expected width of the distribution of $t_{1/2}$ caused by sampling fluctuations and has been estimated using doublet stations (two stations deployed with a spacing of a few meters for systematical studies of which one station belongs to the standard 1500 m grid and the other station is considered off-grid) and stations in the same event which have a similar signal and distance to the shower axis. A detailed description of both air shower observables can be found in [KN17]. Δ is sensitive to both the ratio between the electromagnetic and the muonic shower component at ground level and the distance of the shower maximum X_{max} to the observation plane. Producing larger risetimes due to a smaller muonic component and deeper X_{max} , photon-induced air showers are expected to have larger values of Δ compared to the average (hadronic) data event. Further, both observables L_{LDF} and Δ are normalized (normalized quantities gL_{LDF} and $g\Delta$) such that a sample of non-preshowering primary photons would have a median at zero and a root-mean-square (RMS) deviation of one. The normalization is done separately in five bins in energy and six bins in zenith angle to reduce the energy dependence of the observables. The exact values used for the normalization are taken from histograms shown in [KN17] and are compiled here in Tab. 13.1. The distributions of gL_{LDF} and $g\Delta$ are shown in Fig. 7.3 for simulated photon showers (including preshowering events) and for a set of training data (photon simulation set A and training data described in Chapter 6).

The separation power of these observables can be quantified using the merit factor η which is defined as

$$\eta = \frac{|\mu_d - \mu_\gamma|}{\sqrt{\sigma_d^2 + \sigma_\gamma^2}}, \quad (7.6)$$

where $\mu_{d/\gamma}$ is the mean value of the data/photon distribution and $\sigma_{d/\gamma}$ is the corresponding the root-mean-square deviation. The merit factor is a general measure for the resolvability of two symmetric distributions and quantifies their separation by relating the distance between their medians to their combined width. For the

distributions shown in Fig. 7.3 the merit factors of the two observables evaluate to

$$\eta(gL_{\text{LDF}}) = 1.06, \quad (7.7)$$

$$\eta(g\Delta) = 1.75. \quad (7.8)$$

Though the merit factor allows for a relative comparison of the separation power of the two observables, their distributions are not perfectly symmetric hence introducing a small bias to η . Another measure of the separation power which is more tailored-made for the present analysis is ρ_{50} . ρ_{50} is the relative amount of background (i.e. data) which is rejected when placing a cut at the median of the signal (i.e. photon) distribution. Hence, it is the evaluation of the receiver operating characteristic (ROC) at a signal efficiency of 0.5. For the distributions shown in Fig. 7.3 the values of ρ_{50} are

$$\rho_{50}(gL_{\text{LDF}}) = \frac{730}{767} \approx 95.12\% \quad (7.9)$$

$$\rho_{50}(g\Delta) = \frac{766}{767} \approx 99.87\% \quad (7.10)$$

and the full ROC curves are shown in Fig. 13.7 in the appendix. However, due to the limited set of 767 events in the training data sample the values of ρ_{50} are afflicted with large statistical uncertainties, especially in the case of $g\Delta$ where only one event from the training data passes the cut at the median of the photon distribution.

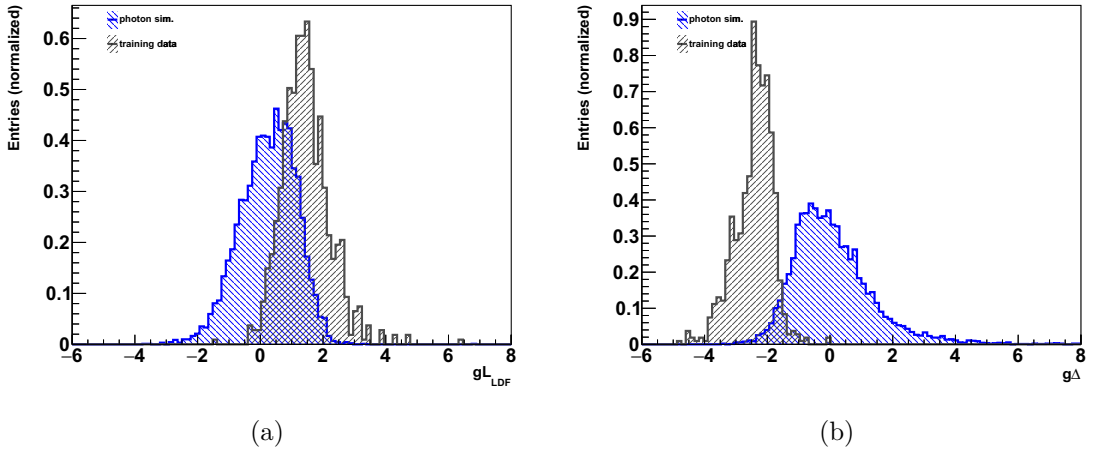


Figure 7.3: The distributions of the normalized observables (a) gL_{LDF} and (b) $g\Delta$ for simulated photon showers in blue (simulation set A) and a training set of 767 data events in gray (training data described in Sec. 6.2.2). Both sets only contain events with reconstructed photon energy between $10^{19.0}$ eV and $10^{20.5}$ eV and reconstructed zenith angles between 30° and 60° . More detailed information on the individual distributions is given in Fig. 13.5 in the appendix. The plots are reproducing the results shown in [RJ19].

7.4. Principal component analysis

In the next step, the normalized observables gL_{LDF} and $g\Delta$ are projected onto their common principal component (PC) axis in order to find a parameter that combines their separation power (principal component analysis, PCA). The PC axis of a 2-dimensional distribution is the axis which contains the mean value of the distribution and is aligned in the direction of maximum variance. For a given distribution it can be derived by calculating the eigenvector of the covariance matrix that belongs to the largest eigenvalue. The PC axis has been found in [RJ19] using the combined distribution of 458 data events (which are a sub-sample of the training data set used here) and a set of simulated non-preshowering photon events in the ratio of 1:1.653 which has been found in [KN17] to give good results in terms of separation power. The resulting angle of the PC axis is $\alpha = 22.2^\circ$ and the principal components PC_0 and PC_1 are given by a rotation in the space of the normalized observables

$$\begin{pmatrix} \text{PC}_0 \\ \text{PC}_1 \end{pmatrix} = \begin{pmatrix} \cos(\alpha) & -\sin(\alpha) \\ \sin(\alpha) & \cos(\alpha) \end{pmatrix} \begin{pmatrix} g\Delta \\ gL_{\text{LDF}} \end{pmatrix} + \begin{pmatrix} b_1 \\ b_2 \end{pmatrix}. \quad (7.11)$$

The additional translation accounts for rotating around the center of the observable space coordinate system rather than around the geometrical center of the two distributions. The translation parameter is $b_1 = 0.902$ while the value of b_2 is irrelevant since PC_1 is a redundant degree of freedom which is not considered any further in the analysis. Thus, PC_0 is further simply referred to as PC. Fig. 7.4(a) shows the distributions of training data and simulated photon events in the space of $g\Delta$ and gL_{LDF} . Both distributions are largely uncorrelated with correlation coefficients of -0.085 for photons and -0.14 for data. The final photon candidate cut is defined at the PC value of the photon distribution median (including preshowering photons) and is $\text{PC} > 0.87(50656135)$. The distributions of the PC values for the 767 data events of the training data set and the simulated photons from simulation set *A* are shown in Fig. 7.4(b). The value of the photon candidate cut is indicated by the vertical line.

The largest amount of the separation power of the PC is contributed by $g\Delta$ which is not only noticeable at the higher separation power of $g\Delta$ as compared to gL_{LDF} but also on the distributions of the observables in the scatter plot in Fig. 7.4(a). With the combination of the two photon-discriminating air shower observables in a PCA, their combined separation power exceeds the separation power of the individual observables. The resulting merit factor of the PC distribution is

$$\eta(\text{PC}) = 1.95. \quad (7.12)$$

and the background rejection ρ_{50} reaches 100% since no event of the training data set passes the final photon candidate cut. The full ROC curve is shown in Fig. 13.7 in the appendix. Further details on the separation between primary photons and hadrons with the SD 1500 m array can be found in [KN17, RJ19], and on the Auger Wiki page for the search for photons with the SD [URL1].

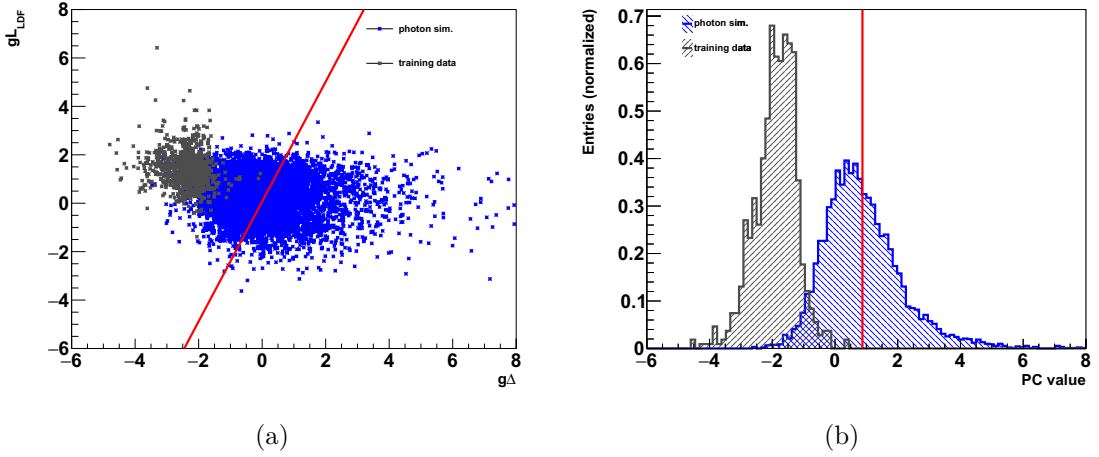


Figure 7.4: (a) The distributions of the normalized photon observables $g\Delta$ and gL_{LDF} combined in a scatter plot for a set of simulated photon showers in blue (simulation set A) and a set of training data in gray (training data described in Sec. 6.2.2). (b) The principal component, i.e. the projection of the distributions of $g\Delta$ and gL_{LDF} onto the principal component axis, of the photon simulations (blue) and the training data (gray). In both plots the red lines indicate the photon candidate cut. The plots are reproducing the results shown in [RJ19] with an independently simulated set of photon air showers. Further information on the individual distributions of (b) are given in Fig. 13.6 in the appendix.

7.5. Angular resolution

When searching for astronomical sources of UHE photons, the angular resolution of the SD to their direction of incidence is of special interest. The angular deviation ψ between the reconstructed direction of an air shower and the true MC direction of the initial particle are given on a great circle of the celestial sphere by

$$\sin\left(\frac{\psi}{2}\right) = \sqrt{\frac{1}{2}(1 - \sin\theta_{MC} \sin\theta_{\gamma} \cos(\phi_{MC} - \phi_{\gamma}) - \cos\theta_{MC} \cos\theta_{\gamma})}. \quad (7.13)$$

The spherical coordinates (ϕ_{MC}, θ_{MC}) denote the true MC direction (azimuth, zenith) while $(\phi_{\gamma}, \theta_{\gamma})$ are the reconstructed direction. The distribution of angular deviations of simulated photons between $10^{19.0}$ eV and $10^{20.5}$ eV (simulation set A) after application of all cuts described in Sec. 7.2 is shown in Fig. 7.5(a). The value of the cumulative distribution function (shown in Fig. 7.5(b)) can be interpreted as the confidence level (CL) at which a primary photon from a given direction will be reconstructed within a circle⁹ of angular diameter ψ .

Assuming the angular deviations to be approximately normal distributed (which is in reasonable agreement with the distribution shown in Fig. 7.5) the error dis-

⁹An exactly circular contour line implies that the directional uncertainties in declination and right ascension are uncorrelated and independent of the direction of incidence which in general is not necessarily true. In the considered zenith range, this dependency however is expected to be small and its impact on the analysis in this work is negligible.

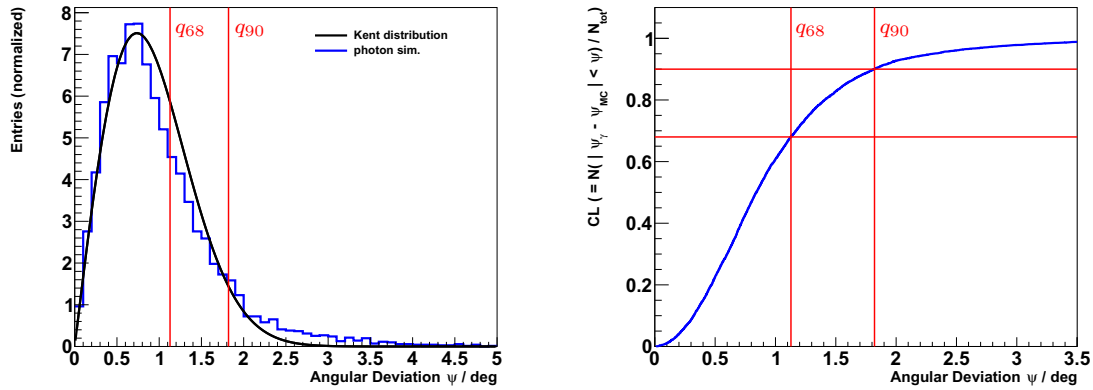


Figure 7.5: (a) The distribution of angular deviations ψ between reconstructed and simulated shower axes for the photon showers of simulation set *A* (described in Sec. 6.1.1). The vertical lines represent the 68% and 90% quantiles of the distribution. The black curve shows the Kent distribution with its 68% quantile coinciding with the simulated distribution. (b) The cumulative distribution of angular deviations. The 68% quantile $q_{68} = 1.128^{+0.011}_{-0.013}$ deg used for fitting the Kent distribution and the 90% quantile $q_{90} = 1.821^{+0.019}_{-0.021}$ deg, which is the radius of the search region used in Chapter 10, are again highlighted by the red lines.

tribution function on a sphere can be described by a symmetric Kent distribution [KT82]

$$K(\psi) = \frac{\kappa \sin \psi \exp(\kappa \cos \psi)}{4\pi \sinh \kappa}. \quad (7.14)$$

The additional $\sin(\psi)$ -term comes from the transformation of the distribution into polar coordinates on a spherical surface. The concentration parameter κ describes the spread of the distribution and corresponds to the inverse of the variance in the limit of a 2-dimensional Gaussian distribution (limit for large κ and small ψ). Performing a fit of $K(\psi)$ to the distribution of simulated photon events by forcing the reconstructed 68% quantile of $K(\psi)$ to coincide with the quantile of the photon distribution ($q_{68} = 1.128^{+0.011}_{-0.013}$ deg) results in $\kappa = 5880^{+140}_{-110}$. A χ^2 fit of the Kent distribution results in $\kappa = 6100 \pm 800$. The fit result is well consistent with the result from the simpler approach of fixing the quantile which is why $\kappa = 5880$ is adopted in the following. The resulting Kent distribution is shown by the smooth curve in Fig. 7.5(a).

The fitted function does not perfectly describe the simulations. The deviation from the Kent distribution originates partly in the remaining dependence of the angular resolution on the energy of the primary photon which reaches from $q_{68} \approx 0.8^\circ$ between $10^{20.0}$ eV and $10^{20.5}$ eV to $q_{68} \approx 1.4^\circ$ between $10^{19.0}$ eV and $10^{19.5}$ eV (see Fig. 13.8 in the appendix). Considering typical numbers of triggered SD stations in each energy bin, these values are in good agreement with the results in [BC09] (shown here in Fig. 5.16). However, this dependence has only little impact on the analyses shown in the following chapters since the angular resolution

is only used to define search regions in the sky for photons from astronomical point sources. These search regions are defined independently of the photon energy. The remaining effect of the energy dependent directional resolution of the SD to UHE photons on the central results of this thesis is further discussed in Sec. 8.5.2.

7.6. Background estimation and photon detection efficiency

Using the photon candidate selection criterion described above, in total $N_{\gamma,\text{diff}}^{\text{cand}} = 11$ photon candidate events have been found among the diffuse flux of cosmic rays during the whole period between January 2004 and June 2018 as reported in [RJ19]. The number of photon candidate events has been found to be compatible with the expectations from the hadronic background. Hence, that number can be used to obtain an estimate of the rate of diffuse background events in the signal region

$$\beta_{\text{diff}} = \frac{N_{\gamma,\text{diff}}^{\text{cand}}}{\int_{E_0}^{E_1} dE_\gamma k E_\gamma^\alpha \mathcal{E}_{\text{diff}}(E_\gamma)}, \quad [L^{-2} \Omega^{-1} T^{-1}] \quad (7.15)$$

with

$$k = \left(\int_{E_0}^{E_1} dE_\gamma E_\gamma^\alpha \right)^{-1} \quad (7.16)$$

being the normalization factor for the spectral shape of the photon flux which is here assumed to be a power law with spectral index α and $\mathcal{E}_{\text{diff}}(E_\gamma)$ is the energy dependent exposure to a diffuse flux of photons between $E_0 = 10^{19.0}$ eV and $E_1 = 10^{20.5}$ eV averaged over the field of view $30^\circ < \theta < 60^\circ$.¹⁰ The exposure $\mathcal{E}_{\text{diff}}$ inherits the energy dependence of the SD photon detection efficiency ϵ_{SD} and is given by

$$\mathcal{E}_{\text{diff}}(E_\gamma) = \int_{t_0}^{t_1} \iint_{\Omega} dt d\Omega A(t) \cos \theta \epsilon_{\text{SD}}(E_\gamma) \quad [L^2 \Omega T] \quad (7.17)$$

$$= \epsilon_{\text{SD}}(E_\gamma) \frac{\pi}{2} \int_{t_0}^{t_1} dt A(t) \quad (7.18)$$

$$\approx \epsilon_{\text{SD}}(E_\gamma) 1.32 \times 10^{22} \text{ cm}^2 \text{ s sr}. \quad (7.19)$$

¹⁰Note that the exposure to photon candidate events from the hadronic background is unknown and does not necessarily follow the same energy dependence as the exposure to primary photons. However, this dependence cancels out when the background rate is multiplied with another photon exposure integrated over the same energy interval. Multiplying β_{diff} with a photon exposure integrated over a different energy interval could introduce a bias to the expected number of photon candidate events. For such a purpose β_{diff} should be recalculated first.

The aperture $A(t)$ of the SD depends on the time-varying number of active stations (i.e. active station hexagons) in the SD array as further described in Sec 8.1. The evaluation of the time integral over $A(t)$ has been done numerically in time-steps of 60s as the status of the SD is reported once every 60s to the CDAS. The integration over the solid angle Ω covers the field of view of the analysis and runs over zenith angles $30^\circ \leq \theta \leq 60^\circ$ and azimuth angles $0 \leq \varphi < 360^\circ$.

The energy dependence of ϵ_{SD} has been shown in Fig. 7.2 (blue solid line). In order to carry out the energy integral in Eq. 7.15 independently of the bin size of the histogram, $\epsilon_{\text{SD}}(E_\gamma)$ has been approximated with an analytic function. Therefore, the impact of the two consecutive quality cuts on the observable flags (Δ - and LDF-flag) and the photon energy (E_γ -flag) were fitted separately in a first step. It turns out that the efficiencies of both, the cut on the observable flags $\epsilon_{\Delta, \text{LDF}}$ and the cut on the photon energy flag ϵ_{E_γ} can be well described by hyperbolic tangent functions:

$$\epsilon_{\Delta, \text{LDF}}(E_\gamma) = \frac{a_0}{2} (\tanh(a_1(\log(E_\gamma/\text{eV}) - a_2)) + 1) \quad (7.20)$$

$$\epsilon_{E_\gamma}(E_\gamma) = \frac{b_0}{2} (1 - \tanh(b_1(\log(E_\gamma/\text{eV}) - b_2))). \quad (7.21)$$

The fitted functions (using a χ^2 -minimization) are shown in Fig. 7.6(a) and (b) and the fit parameters a_i and b_i , $i \in \{0, 1, 2\}$, are listed in Tab. 7.1. The shape of the total efficiency $\epsilon_{\text{SD}} = \epsilon_{\Delta, \text{LDF}} \times \epsilon_{E_\gamma}$ has been fitted in two different ways: first by simply multiplying Eq. 7.20 and Eq. 7.21 and keeping the parameters fixed to the values obtained previously in the separate fits (red dotted line in Fig. 7.6(c)) and a second time by performing a free fit of the combined function

$$\epsilon_{\text{SD}}(E_\gamma) = \frac{c_0}{4} (\tanh(c_1(\log(E_\gamma/\text{eV}) - c_2)) + 1) (1 - \tanh(c_3(\log(E_\gamma/\text{eV}) - c_4))) \quad (7.22)$$

to the efficiency histogram keeping all 5 remaining parameters c_i , $i \in \{0, 1, 2, 3, 4\}$, variable. The results of the fitted parameters c_i are also given in Tab. 7.1 and the corresponding curve is shown in Fig. 7.6(c) as the black solid line. Though, both fit results seem to be reasonable approximations to the energy dependence of the efficiency,¹¹ the free fit of Eq. 7.22 has only five instead of six parameters since the scaling parameters a_0 and b_0 are absorbed into c_0 in Eq. 7.22. For that reason Eq. 7.22 is favored over the multiplication of Eqs. 7.20 and 7.21 for a description of $\epsilon_{\text{SD}}(E_\gamma)$.

In addition to its energy dependence, the efficiency also shows a variation with the zenith angle θ , i.e. $\epsilon_{\text{SD}} = \epsilon_{\text{SD}}(E_\gamma, \theta)$. This dependence has been analyzed additionally in three bins $30^\circ \leq \theta < 40^\circ$, $40^\circ \leq \theta < 50^\circ$ and $50^\circ \leq \theta < 60^\circ$ which have a similar geometrical exposure to an incident isotropic flux. In each zenith bin the energy dependence of the efficiency has been fitted with the same function

¹¹The goodness of fit criterion χ^2/ndf is 0.020/10 for the free fit of Eq. 7.22 and 0.027/9 for the fit of the product of Eqs. 7.20 and 7.21.

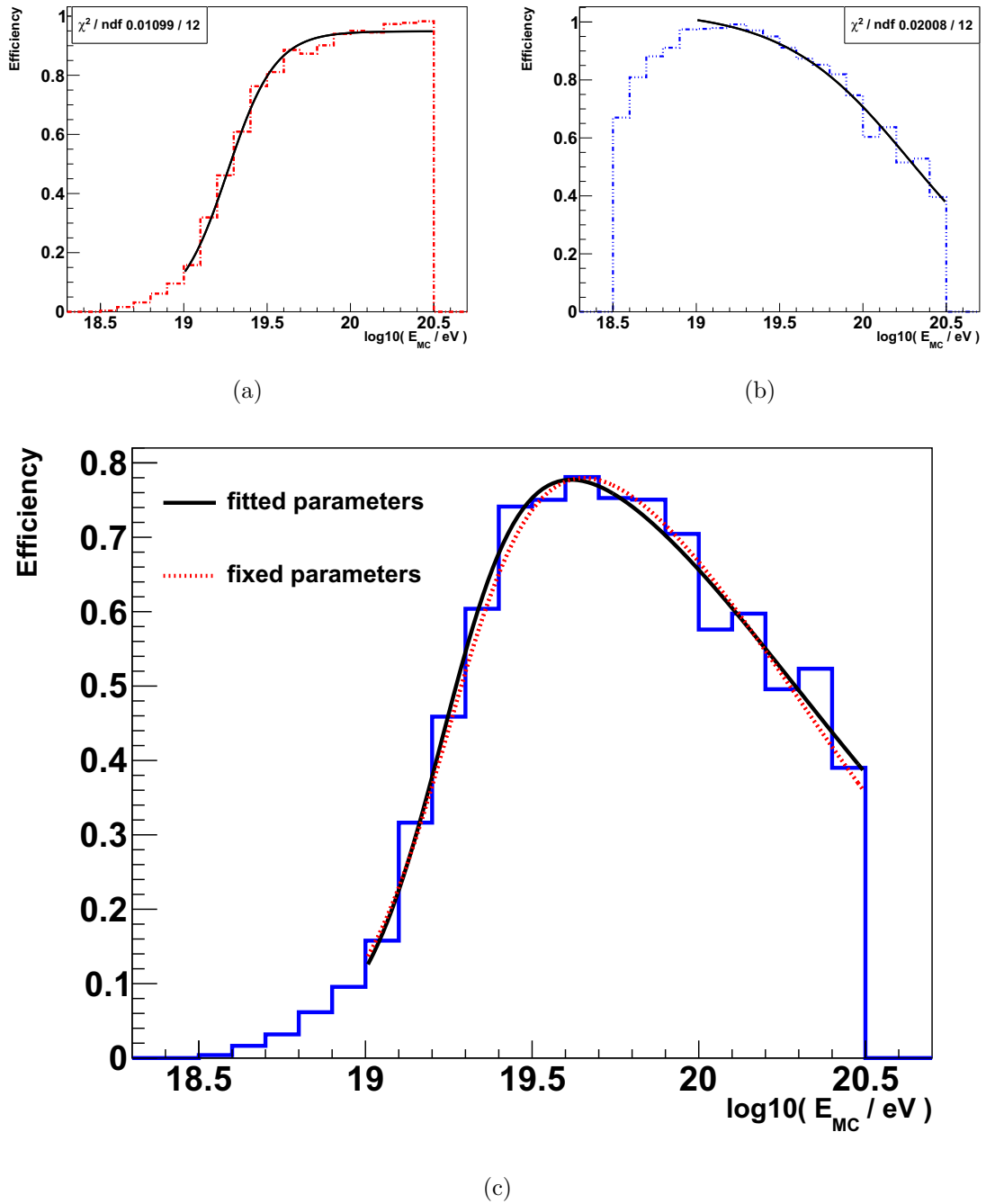


Figure 7.6: (a) A fit of Eq. 7.20 to the photon detection efficiency after application of the selection criteria imposed by the observables Δ and L_{LDF} (labeled Δ -flag and LDF-flag). (b) A fit of Eq. 7.21 to the photon detection efficiency after application of the selection criterion imposed by the reconstruction of the photon energy (labeled E_γ -flag). (c) The photon detection efficiency after application of all cuts fitted by the product of Eqs. 7.20 and 7.21 (red dotted line) and a free fit of Eq. 7.22 (black solid line). The numerical values of all parameters are given in Tab. 7.1. All efficiencies shown here also include the 6T5 criterion and have successfully reconstructed hadronic energy, shower axis and LDF. The impact of these latter conditions however is negligible above 10^{19} eV (c.f. Fig. 7.2).

templates as the whole zenith range, i.e. Eqs. 7.20, 7.21 and 7.22. The fitted distributions for each zenith bin are shown in Figs. 13.9 and 13.10 in the appendix and the corresponding fit parameters are given in Tab. 7.1. In order to construct a smooth transition between the fit parameters c_i (obtained in free fits of Eq. 7.22 to the corresponding distribution in each zenith bin), the parameters have been interpolated with quadratic splines following the Catmull-Rom construction¹² [CE74]. The constructed polynomials for all five parameters $c_i(\theta)$ are listed in Eqs. 7.23 and are illustrated in Fig. 13.11 in the appendix.

$$\begin{aligned}
c_0(\theta) &= -1.806 \times 10^{-3} (\theta/\text{deg})^2 + 0.1831 (\theta/\text{deg}) - 3.619 \\
c_1(\theta) &= 0.7600 \times 10^{-3} (\theta/\text{deg})^2 - 0.0225 (\theta/\text{deg}) + 3.612 \\
c_2(\theta) &= 0.4000 \times 10^{-3} (\theta/\text{deg})^2 - 0.03900 (\theta/\text{deg}) + 20.15 \\
c_3(\theta) &= 8.395 \times 10^{-3} (\theta/\text{deg})^2 - 0.7355 (\theta/\text{deg}) + 19.05 \\
c_4(\theta) &= 5.150 \times 10^{-3} (\theta/\text{deg})^2 - 0.3620 (\theta/\text{deg}) + 26.18
\end{aligned} \tag{7.23}$$

For a spectral index $\alpha = -2$ and an energy dependent efficiency as given in Eq. 7.22, the *spectrum-averaged photon exposure* $\tilde{\mathcal{E}}_{\text{diff}}$ in the denominator of Eq. 7.15 has been computed numerically to be

$$\tilde{\mathcal{E}}_{\text{diff}} := \int_{E_0}^{E_1} dE_\gamma k E_\gamma^\alpha \mathcal{E}_{\text{diff}}(E_\gamma) \stackrel{\alpha=-2}{\approx} 6.34 \times 10^{21} \text{ cm}^2 \text{ sr s}, \tag{7.24}$$

hence the diffuse background rate is

$$\beta_{\text{diff}} \simeq (1.74_{-0.51}^{+0.70}) \times 10^{-21} \text{ cm}^{-2} \text{ sr}^{-1} \text{ s}^{-1}. \tag{7.25}$$

The statistical error margin at 68% CL corresponds to the uncertainty inherited from the observed number of eleven photon candidate events out of a total number of 40570 air shower events analysed in the diffuse photon search analysis.

The values given in Eqs. 7.24 and 7.25 represent zenith angle averaged values and are valid for a diffuse flux of UHE photons. For the search for photons from point sources, the zenith angle dependence of the photon detection efficiency has to be taken into account explicitly. Omitting the implicit averaging over the field of view, the spectrum-averaged photon exposure to a fixed direction in the horizontal coordinate system as a function of zenith angle is

$$\tilde{\mathcal{E}}(\theta) := \int_{E_0}^{E_1} dE_\gamma k E_\gamma^\alpha \mathcal{E}(E_\gamma, \theta) \quad [L^2 T] \tag{7.26}$$

$$= \int_{E_0}^{E_1} dE_\gamma \left(k E_\gamma^\alpha \int_{t_0}^{t_1} dt A(t) \cos(\theta) \epsilon_{\text{SD}}(E_\gamma, \theta) \right), \tag{7.27}$$

¹²The resulting parabolic shape of $c_i(\theta)$, which in the special case of three control points coincides with a simple parabolic fit, is consistently expandable for arbitrary numbers of controls points (i.e. zenith angle bins) in an analytic approach.

	$30^\circ \leq \theta < 60^\circ$	$30^\circ \leq \theta < 40^\circ$	$40^\circ \leq \theta < 50^\circ$	$50^\circ \leq \theta < 60^\circ$
a_0	0.9486	0.9167	0.9713	0.9914
a_1	3.497	2.642	3.986	4.671
a_2	19.26	19.42	19.20	19.21
b_0	1.041	1.014	1.005	0.990
b_1	1.321	2.725	2.966	3.638
b_2	20.28	19.77	20.31	21.72
c_0	0.9944	0.5786	0.9655	0.9913
c_1	3.033	3.755	4.138	4.673
c_2	19.25	19.27	19.20	19.21
c_3	1.137	3.589	2.950	3.990
c_4	20.29	19.82	20.32	21.85

Table 7.1: The fitted parameters of the efficiency curves in Eqs. 7.20, 7.21 and 7.22.

and with the time-integral running over the search period used in [RJ19]:

$$\approx 8.41 \times 10^{21} \text{ cm}^2 \text{ s} \cos(\theta) \int_{E_0}^{E_1} dE_\gamma k E_\gamma^\alpha \epsilon_{\text{SD}}(E_\gamma, \theta). \quad (7.28)$$

When analyzing a certain solid angle region Ω_{source} in the sky, the number of expected background events b from that direction can thus be obtained by multiplying the expected diffuse background rate β_{diff} with $\tilde{\mathcal{E}}(\theta)$ integrated over the solid angle region of interest:

$$b = \beta_{\text{diff}} \iint_{\Omega_{\text{source}}} d\Omega \tilde{\mathcal{E}}(\theta). \quad (7.29)$$

Since the energy integral in Eq. 7.28 is not easily solvable, a numerical solution for $\tilde{\mathcal{E}}(\theta)$ for a spectral index $\alpha = -2$ is given in Fig. 7.7 and the impact of a variation of the spectral index is discussed in Sec. 8.5.1. For the application of Eq. 7.29 in Chapters 8 and 9 a more general case is considered in which the zenith angle θ corresponds to the direction of an astronomical object, i.e. the source of a gravitational wave, and is thus time-dependent due to the rotation of the earth. The calculation of the spectrum-averaged exposure to a source in a fixed direction of the equatorial coordinate system is discussed later in Sec. 8.1 (see Eq. 8.6).

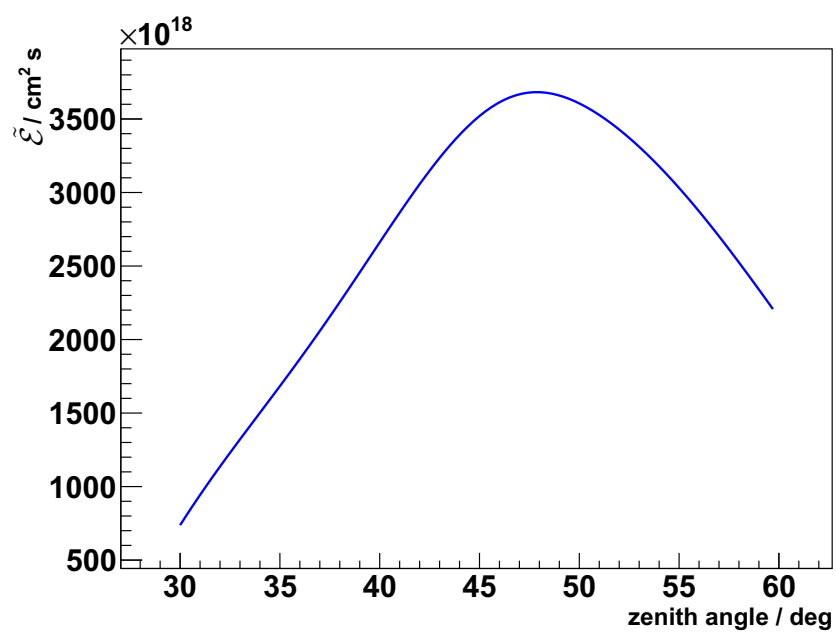


Figure 7.7: The dependence of the spectrum-averaged photon exposure $\tilde{\mathcal{E}}(\theta)$ to a fixed direction in the search period from January 2004 to June 2018 as a function of zenith angle. The curve represents a numerical solution of Eq. 7.28 for a spectral index $\alpha = -2$.

A search for photons above 10 EeV induced by GW events

WITH the first gravitational waves measured by the Advanced LIGO and Virgo detectors in 2015, not only a new window to the universe has been opened, but also a completely new type of transient astronomical object has been observed for the first time in history: the merging process of two compact stellar mass objects (compact binary merger, CBM). Due to the characteristic shape of their GW signals, these CBMs can be identified at a high significance and even be located through their GW emission. The nature of two highly compact objects engulfed in extreme magnetic fields – as they are typical for neutron stars – orbiting each other at velocities close to the speed of light makes the conclusion almost inevitable, that these sites are not only the sources of GWs but pose also suitable production sites for various kinds of radiation and high energy particles. Since the physical conditions at CBMs by far exceed anything that can yet be reproduced within laboratory experiments, these sources might very well host new and unknown physical processes. Consequently, analyzing these exotic events thoroughly with all means available on earth could provide intriguing insights into rare physics phenomena. Conclusions about the physics of CBMs would not only expand the horizon of our knowledge in astrophysics but could potentially also provide important information for the research in particle and astroparticle physics, fundamental physics and cosmology. Therefore multiple follow-up searches for electromagnetic and neutrino counterparts of the GWs have been established at different physics experiments like MAGIC, H.E.S.S., Fermi-LAT, IceCube, Antares, the Pierre Auger Observatory and many others [AS16b, AA16b, AB17a, AA17b].

The Pierre Auger Observatory has a unique exposure to UHE neutrinos as well as UHE photons thanks to the size of its SD array. Moreover, the sky fraction that is covered by Auger complements the field of view of the TA experiment on the northern hemisphere, allowing for a thorough coverage of the full UHE photon sky. Thus, an important part of the photon phase space in terms of energy and direction can only be studied using the data of the Pierre Auger Observatory. First results on UHE neutrinos from GW sources have already been published by the Pierre Auger Collaboration [AA16b, AA17b, SM19]. In the following sections (Sec. 8.1 and 8.2) a first follow-up search for UHE photons from GW sources is introduced and described in detail using the example of GW150914 which was the historically

first GW that has been measured. Moreover, a comprehensive summary of the follow-up photon searches after all GW events observed during LIGO/Virgo runs O1 and O2 and a dedicated analysis of the neutron star merger event GW170817 are to follow in Sec. 8.3. The sensitivity of the analysis procedure and its capability to identify photons from transient sources is evaluated in Sec. 8.4, and Sec. 8.5 concludes this chapter with a discussion about the main sources of systematical uncertainties and their impact on the analysis results.

8.1. Definition of quantities

The measured quantity N_γ^{cand} is the number of extensive air shower events in an energy interval $[E_0, E_1)$ which are coincident with the GW source direction in a certain time window around the GW event time and are classified as *photon candidates* as defined by a photon candidate cut (see Sec. 7.4). In the case that no event is classified as a photon candidate ($N_\gamma^{\text{cand}} = 0$), an upper limit N_γ^{UL} on the expected number of coincident photon events is placed instead. In the case of $N_\gamma^{\text{cand}} > 0$, in addition to an upper limit, also a lower limit N_γ^{LL} could be placed which may or may not be equal to zero depending on the expected amount of background and the level of confidence at which the limits should contain the true value. N_γ^{LL} and N_γ^{UL} are derived using the Feldman-Cousins approach [FG98] which allows for a statistically consistent transition between the case where only upper limits can be placed (with lower limits equal to zero) and the other case where two-sided confidence intervals can be placed. For more details on the construction of confidence intervals see Sec. 8.4.

From the upper (lower) limits $N_\gamma^{\text{UL(LL)}}$, one can obtain limits on the corresponding *spectral photon flux* $\frac{d\Phi_\gamma^{\text{GW}}}{dE_\gamma}(E_\gamma)$, which is the number of photons at the earth from the direction of the GW source per unit time and area in the energy range $[E_\gamma, E_\gamma + dE_\gamma)$. Assuming that the spectral photon flux follows a power law with *spectral index* α it can be written as

$$\frac{d\Phi_\gamma^{\text{GW}}}{dE_\gamma}(E_\gamma) = k_\gamma E_\gamma^\alpha, \quad [E^{-1}L^{-2}T^{-1}] \quad (8.1)$$

where without deeper knowledge about the actual energy dependence, the exponent is usually set to $\alpha = -2$ to introduce a simple benchmark for consistency and comparison to other analyses [AS16b, AA16b].

With the energy dependence modeled as a simple power law, the *flux normalization factor* k_γ^{GW} is not a function of energy and can directly be derived from the number of observed photon candidate events. Corresponding upper (lower) limits on k_γ can be obtained from $N_\gamma^{\text{UL(LL)}}$ as in [AA16b] like

$$k_\gamma^{\text{UL(LL)}} = \frac{N_\gamma^{\text{UL(LL)}}}{\int_{E_0}^{E_1} dE_\gamma E_\gamma^\alpha p_{\gamma\text{-cut}} \mathcal{E}(E_\gamma, \theta_{\text{GW}}, \Delta t)}. \quad [E^{-\alpha-1}L^{-2}T^{-1}] \quad (8.2)$$

The energy integration in the denominator goes over the energy interval $[E_0, E_1)$ for which $N_\gamma^{\text{UL(LL)}}$ has been derived.

$p_{\gamma\text{-cut}}$ is the value of the cumulative photon distribution function at the $p_{\gamma\text{-cut}}$ -quantile of the photon distribution in the space of the discriminating parameter at which the final photon candidate cut is placed. In this analysis the discriminating parameter is the principal component value PC introduced in Sec. 7.4. The photon distribution function is based on a set of simulated photon showers (shown in Fig. 7.4). In coherence with [RJ19], the photon candidate cut is chosen such that $p_{\gamma\text{-cut}} = 0.5$, i.e. at the median of the photon distribution.

\mathcal{E} is the *SD photon exposure* to a point source at zenith angle θ_{GW} and depends on the photon energy E_γ and the observation time $\Delta t = t_1 - t_0$ as

$$\mathcal{E}(E_\gamma, \theta_{\text{GW}}, \Delta t) = \int_{t_0}^{t_1} dt A(t) \epsilon_{\text{SD}}(E_\gamma, \theta_{\text{GW}}(t)) \Theta_{\text{FoV}}(\theta_{\text{GW}}(t)) \cos(\theta_{\text{GW}}(t)). \quad [L^2 T] \quad (8.3)$$

Since the zenith angle θ_{GW} of the GW source is a coordinate of the horizontal coordinate system which co-rotates with the earth, θ_{GW} is here – unlike in Eq. 7.27 – not a fixed direction in the sky but a function of the sidereal time t , source right ascension α_{GW} and source declination δ_{GW} :

$$\cos(\theta_{\text{GW}}(t)) = \sin \lambda \sin \delta_{\text{GW}} + \cos \lambda \cos \delta_{\text{GW}} \sin(2\pi t/T - \alpha_{\text{GW}}), \quad (8.4)$$

with $\lambda = -35.4^\circ$ being the latitude of the Auger SD array and $T = 23 \text{ h } 56 \text{ min } 4.0905 \text{ s}$ the duration of one sidereal day.

The *step-function* Θ_{FoV} accounts for the fraction of the observation time in which the source is covered by the SD field of view (FoV) and is 1 during the time when the source is inside the field of view and 0 when it is not.

$A(t)$ is the *aperture* [PE05] of the SD array and is given by

$$A(t) = 1.95 \text{ km}^2 N_\square(t), \quad [L^2] \quad (8.5)$$

with $N_\square(t)$ being the time dependent number of hexagons of active SD stations with a side length of 1.5 km. The contribution of 1.95 km^2 of a single SD station to the overall geometrical aperture of the whole array is constructed by assigning an elementary aperture to each station. The elementary aperture is assigned such that it contains the set of all points for which the respective SD station is the closest out of all SD stations of the array. Hence, the elementary aperture itself is a hexagon centered on an SD station with its corners placed in the centers of the surrounding triangular unit cells of the hexagonal SD grid (see Fig. 8.1).

The *SD photon detection efficiency* $\epsilon_{\text{SD}}(E_\gamma, \theta)$ is the fraction of primary photons that are recorded as SD events after applying all SD selection cuts (prior to the application of the final photon candidate cut) out of all primary photons on top of the atmosphere. Using air shower simulations with photons as primary particles it has been found that the efficiency at energies above 10 EeV and zenith angles $30^\circ < \theta < 60^\circ$ does not have a strong dependence on the azimuth of the arrival direction [PE05]. The dependence of ϵ_{SD} on photon energy and zenith angle has

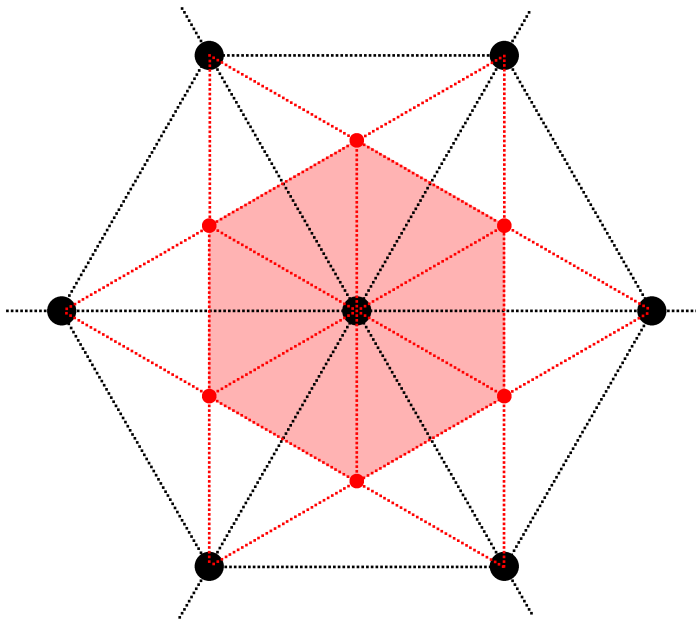


Figure 8.1: An illustration of the contribution of a single SD station within a hexagon of six fully operational neighboring stations (big black dots) to the total SD aperture. The black dots mark the positions of seven operational SD stations forming a hexagonal cell of the SD array. The contribution of the one station in the middle to the overall SD aperture is highlighted by the shaded region which has an area of 1.95 km^2 . The corners of that region are located in the centers of the six surrounding triangular unit cells of the SD grid and are marked by the small red dots.

been analyzed in Sec. 7.6 where Eq. 7.22 has been found as an analytic approximation for $\epsilon_{\text{SD}}(E_\gamma, \theta)$. Finally, the cosine factor in the expression for the exposure comes from the effective area of the SD array when projecting it on the plane orthogonal to the shower axis.

The energy dependence of the exposure is fully contained in the efficiency. Hence, by assuming an incident photon flux with spectral index α , one can construct the energy-independent quantity

$$\tilde{\mathcal{E}}(\alpha_{\text{GW}}, \delta_{\text{GW}}) = \int_{t_0}^{t_1} \int_{E_0}^{E_1} dt dE_\gamma k E_\gamma^\alpha A(t) \epsilon_{\text{SD}}(E_\gamma, \theta_{\text{GW}}(t)) \Theta_{\text{FoV}}(\theta_{\text{GW}}(t)) \cos(\theta_{\text{GW}}(t)) \quad (8.6)$$

which is the spectrum-averaged exposure to UHE photons from a source with fixed coordinates α_{GW} and δ_{GW} in the time interval between t_0 and t_1 . The factor k is the normalization factor given in Eq. 7.16 – not to be confused with the physical quantity k_γ of Eq. 8.2 which is the absolute scale of the UHE photon flux. Eq. 8.6 differs from Eq. 7.27 by the time dependence in the zenith angle. While Eq. 7.27 describes the exposure to a fixed direction in horizontal coordinates, Eq. 8.6 is the exposure to a point source which has a fixed direction in equatorial coordinates and hence time-dependent coordinates in the horizontal system.

The flux normalization k_γ is central when it comes to placing limits on physical quantities as it has been done in [AA16b] for the follow-up neutrino search at the Pierre Auger Observatory or in [AS16a] and [AS16b] at IceCube and ANTARES. From the flux normalization, a *spectral fluence* \mathcal{F} in a certain energy band can be obtained by weighting the flux with the energy and integrating over the respective energy band and time interval as

$$\mathcal{F} = \int_{t_0}^{t_1} \int_{E_0}^{E_1} dt dE_\gamma \frac{d\Phi_\gamma^{\text{GW}}}{dE_\gamma} E_\gamma. \quad [E L^{-2}] \quad (8.7)$$

\mathcal{F} represents the total amount of energy per unit area which reaches the earth's atmosphere in the form of UHE photons initiated by the GW source. When inserting Eq. 8.1 with $\alpha = -2$ and an energy interval $[E_0, E_1) = [10^{19.0} \text{ eV}, 10^{20.5} \text{ eV})$, the flux normalization can be converted into a spectral fluence in that energy interval

$$\begin{aligned} \mathcal{F}_{\alpha=-2} &= k_\gamma (t_1 - t_0) \int_{E_0}^{E_1} dE_\gamma E_\gamma^{-1} \\ &= \ln\left(\frac{E_1}{E_0}\right) k_\gamma (t_1 - t_0) \\ &= \ln(10^{1.5}) k_\gamma (t_1 - t_0). \end{aligned} \quad (8.8)$$

In this form of \mathcal{F} a constant emission of UHE photons by the source in the time between t_0 and t_1 is assumed. Hence, if the source is in the field of view only for a fraction of the time between t_0 and t_1 , the exposure is effectively reduced and \mathcal{F} correspondingly increased by that fraction due to the step-function in Eq. 8.3. \mathcal{F} becomes an estimator for the fluence in the whole time window by executing the time integral in Eq. 8.7 from t_0 to t_1 irrespective of the source being in the field of view at a given time or not. Setting the spectral index α to the benchmark value of -2 at this point has the advantage of leading to the same spectral fluence for each decade in energy making it straightforward to compare measurements and sensitivities at other energies.

The *total fluence* F is the average number of UHE photons per unit area that reaches the earth's atmosphere from the GW source and is obtained by integrating the flux over the observed energy range and observation period as

$$F = \int_{t_0}^{t_1} \int_{E_0}^{E_1} dt dE_\gamma \frac{d\Phi_\gamma^{\text{GW}}}{dE_\gamma}. \quad [L^{-2}] \quad (8.9)$$

Introducing the same simplifications as applied in the step from Eq. 8.7 to Eq. 8.8, the total fluence can directly be calculated from k_γ as

$$F_{\alpha=-2} = \frac{E_1 - E_0}{E_1 E_0} k_\gamma (t_1 - t_0). \quad (8.10)$$

Note that in Eq. 8.8 and 8.10 the simple multiplication with $t_1 - t_0$ represents the assumption of constant emission in that time period and the results are only valid for the emission during that time. If a more sophisticated emission model should be tested, one would have to do the time integration explicitly using Eq. 8.7 and Eq. 8.9 directly.

Up to this point, a possible attenuation of the photons on their way from the source to the earth has not been taken into account since only the photon flux on top of the earth's atmosphere has been considered. Taking into account photon propagation effects is necessary if one wants to constrain the photon flux close to the source. A simple attenuation model in which photons are just treated as being "lost" for the analysis after an interaction with the background radiation fields would enter the energy integral in Eq. 8.2 as an additional energy dependent factor. Given the hypothetical condition that UHE photons would (similar to neutrinos) be able to travel all the way from the GW source to earth without interacting, an estimator for the *total energy* E_{tot} radiated by the GW source in UHE photons between E_0 and E_1 can be found by extrapolating the measured value of the spectral fluence to a 4π -sphere around the source at a luminosity distance D_L , hence

$$E_{\text{tot}} = 4\pi D_L^2 \mathcal{F}. \quad [E] \quad (8.11)$$

This condition might be fulfilled if new physics is involved. For instance, a photon could be converted into an UHE axion or axion-like particle in the strong magnetic field at its distant source. Such an axion could propagate the universe practically unimpeded and has a chance to convert back into a photon within the geomagnetic field or the magnetic field of the galaxy before entering the atmosphere [GD01, FM11] (see also Sec. 3.5). In the case of \mathcal{F} being an upper limit, the corresponding value of E_{tot} may very well underestimate the realistic upper limit since it is only valid in the idealistic case of zero photon attenuation. To obtain a more realistic upper limit on the total energy radiated in UHE photons without invoking new physics, one has to track the propagation and cascading of an ensemble of primary photons from the GW source to the earth.¹³ When a lower limit $\mathcal{F}^{LL} > 0$ would be found, the resulting lower limit on E_{tot} as derived in Eq. 8.11 is a real lower limit on the total energy radiated in UHE photons since any photon attenuation during their propagation would lead to a limit that is higher.

8.2. Follow-up analysis of GW150914

During the first two observation runs O1 and O2 of the LIGO and Virgo GW detectors, in total eleven transient GW events have been found and identified as the mergers of compact binary objects. Ten of those have further been identified as binary black hole (BBH) mergers and one as a binary neutron star (BNS) merger.

¹³When taking photon propagation effects into account, the limits on the spectral fluence should also be recalculated with a correspondingly modified energy spectrum of primary photons at the earth.

In this section, the derivation of constraints to the production of UHE photons associated with such a transient source shall be illustrated using the example of the historical event GW150914.

8.2.1. Localization

For GWs observed by the LIGO/Virgo detectors, the localization accuracy of the source position depends on various parameters like the number of responsive detectors, the signal to noise ratio and direction of the incident GW relative to the detectors [AB19b]. For the eleven GW events from LIGO/Virgo runs O1 and O2, the region in the sky which contains the source at 90% CL reaches from a small spot in the sky of 16 deg^2 for the BNS merger GW170817 to large unconnected areas of more than 1500 deg^2 spanning over the whole sky (eg. GW151012, GW170823). For this reason, the sky localizations of the GW sources are communicated as probability density distributions on pixelized sky maps in HEALPix coordinates (see Sec. 6.3). For the example of GW150914 this distribution is shown in Fig. 8.2. The visualization of the full 4π -sky on a 2-dimensional plot has been realized using the equal-area Hammer-Aitoff projection of the right ascension α and declination δ angles of the equatorial coordinate system on Cartesian coordinates (x, y) . The coordinate transformation is given by

$$x = \frac{\pi \cos(\delta) \sin(\frac{\alpha}{2})}{\sqrt{1 + \cos(\delta) \cos(\frac{\alpha}{2})}} \quad (8.12)$$

$$y = \frac{\frac{\pi}{2} \sin(\delta)}{\sqrt{1 + \cos(\delta) \cos(\frac{\alpha}{2})}}. \quad (8.13)$$

From such a map, the contour which contains the true source direction at a confidence level p is extracted by ordering the pixels according to their value (i.e. the probability assigned to that pixel at which it contains the GW source) and summing up those values starting with the largest one until the sum reaches a total of p .¹⁴ Every pixel which contributes to the sum is then considered to be inside the p -CL region. Out of the theoretically infinite number of valid p -CL regions, this procedure naturally leads to a region encircled by a valid contour line of the underlying distribution and allows for possible occurrences of several disconnected regions which may pop up if multiple local probability maxima exist. For a given confidence level, a region constructed like this has the smallest possible area. For GW150914, the contours which belong to the 68%, 90%, 99% and 99.9% CL regions are shown in Fig. 8.3. Additionally, the fields of view for the different follow-up searches at Auger are illustrated by the shaded areas in equatorial coordinates at the instant of the GW detection. In horizontal coordinates, the field of view for

¹⁴In case the sum exceeds p after adding the value of pixel i which belongs to a subset of pixels all having the same value, all pixels of this subset are counted as being inside the contour. This may lead to a (typically negligible) over-coverage of the region but removes the arbitrariness from the procedure which occurs during the ordering step within subsets of pixels with numerically identical values.

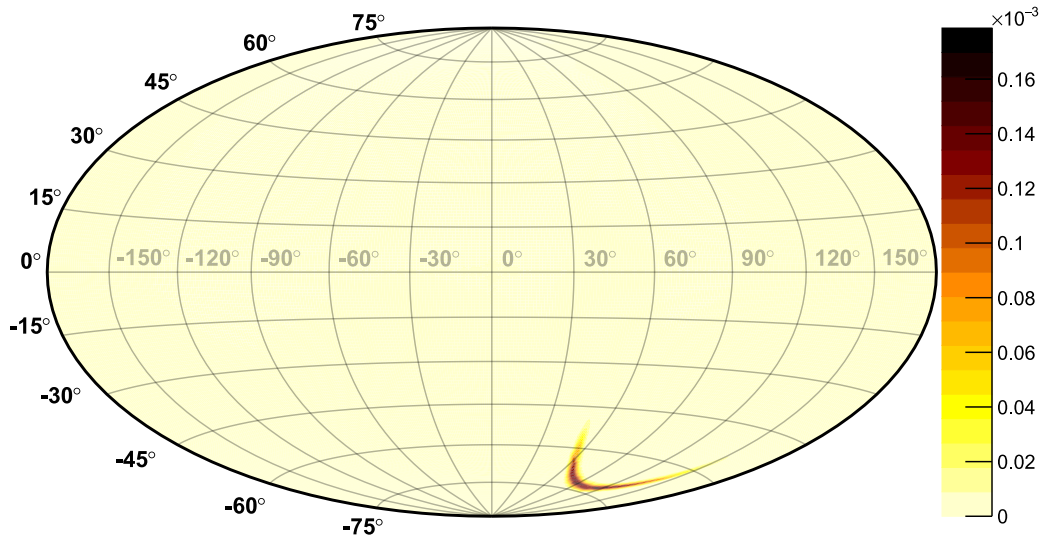


Figure 8.2: The probability density distribution for the source direction of GW150914. The skymap is given in equatorial coordinates with HEALPix rasterization and a HEALPix resolution parameter of $N_{side} = 512$ (i.e. $12 \times N_{side}^2 = 3145728$ pixels). The localization map shown here has been built (software version `ligo.skymap 0.0.16`) and distributed by the LIGO/Virgo collaborations in December 2018.

the photon search lies between zenith angles of 30° and 60° covering a solid angle of 0.732π sr (≈ 7550 deg 2). The 90% CL region of GW150914 has a size of 180 deg 2 and is covered by the instantaneous field of view of the photon search by a fraction of 78%.

However, the SD has a limited directional resolution to primary photons. To ensure that the probability at which an UHE photon at the SD coming from the GW source has a reconstructed shower axis within the unblinded sky region is at a level of 90%, the sky localization map has been convolved with the detector resolution before constructing the 90% contour. The detector resolution can roughly be described by a symmetric Kent distribution $K(\psi)$ (see Eq. 7.14) with a concentration parameter $\kappa \simeq 5880$ as discussed in Sec. 7.5. Hence, the convolved sky map is given by

$$P(\alpha, \delta) = \iint_0^{4\pi} d\Omega' P'(\alpha', \delta') K(\psi) \quad (8.14)$$

with $P'(\alpha', \delta')$ being the original sky map and ψ is the angular distance between (α', δ') and (α, δ) (see Eq. 7.13). In the case of GW150914, the convolution inflates the 90% CL region by $\sim 30\%$ to 236 deg 2 while the fraction of that region that is covered by the field of view is almost unchanged at 78%. In the following, only the 90% CL region of the convolved sky map is considered, if not explicitly stated otherwise.

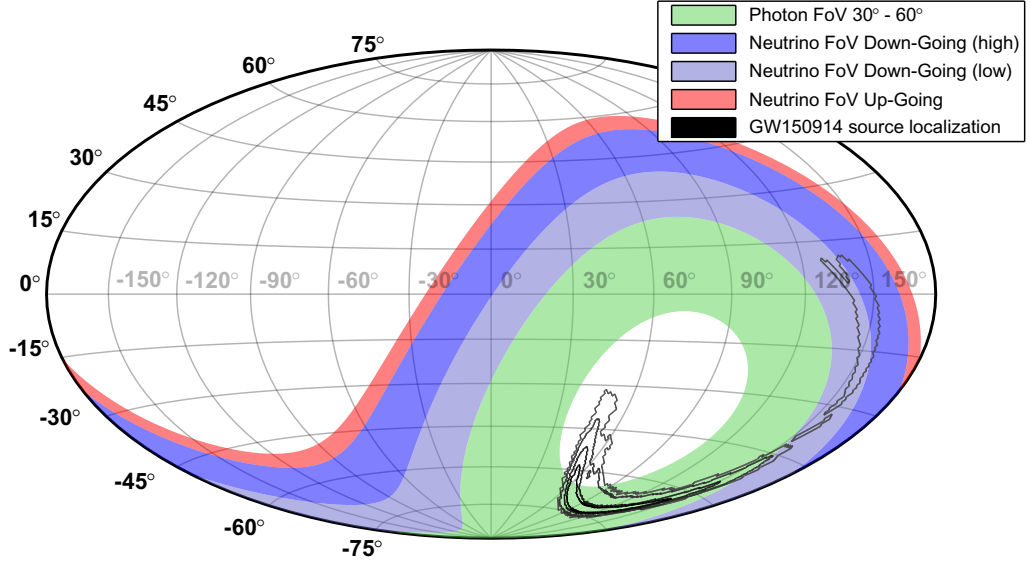


Figure 8.3: The 68%, 90%, 99% and 99.9% contours (from the innermost to the outermost contour) of the localization map, i.e. the probability density distribution of the source direction of GW150914 in equatorial coordinates shown in Fig. 8.2. The regions encircled by the contours have been derived following the ordering procedure described in the text. The shaded areas indicate the fields of view (FoV) at the instant of the GW detection for the different follow-up searches at the Pierre Auger Observatory: neutrinos up-going ($90^\circ < \theta < 95^\circ$), neutrinos down-going high ($75^\circ < \theta < 90^\circ$), neutrinos down-going low ($60^\circ < \theta < 75^\circ$) and photons ($30^\circ \leq \theta \leq 60^\circ$).

8.2.2. Observation time windows

When time moves on, the field of view in Fig. 8.3 moves towards increasing right ascension with an angular velocity of $\sim 15 \frac{\text{deg}}{\text{h}}$ and almost one hour after the event time of GW150914, the 90% contour was fully covered by the field of view of the photon search. To allow for a photon candidate detection coincident in time and direction with a high photon significance and to simultaneously cover a larger time window in which the GW source still has the potential to be a source of high energy particles (cf. [KK16, PA16]), the follow-up search has been split into two separate time windows. The first time window lasts 1000 s and is placed ± 500 s around the GW event time. The second window lasts one full sidereal day and starts +500 s after the GW event time. Given the latitude $\lambda = -35.4^\circ$ of the Auger SD, a total fraction of 0.708 of the whole sky is being covered during a sidereal day. Depending on the declination, different parts of the sky are observed for a different fraction of time (see Fig. 8.4). Around the southern pole of the sky, a circle with an angular radius of 5.4° exists which is constantly covered by the photon field of view. On the northern hemisphere, declinations up to $\delta = +24.6^\circ$ are being covered but the daily coverage fraction of declinations close to that limit is dropping rapidly as shown in Fig. 8.4(b).

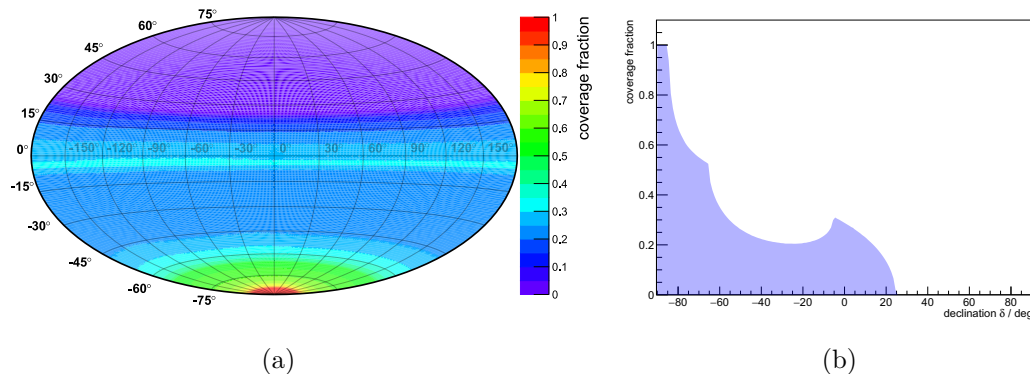


Figure 8.4: (a) The skymap in equatorial coordinates shows the fraction of a sidereal day at which a spot in the sky is being covered by field of view of the photon search, i.e. at zenith angles $30^\circ \leq \theta \leq 60^\circ$. When the observed time window is exactly one sidereal day (or multiples of that), the coverage fraction is independent of right ascension and only a function of the declination angle which is shown in (b).

8.2.3. Exposure

The calculation of the spectrum-averaged exposure $\tilde{\mathcal{E}}$ (see Eq. 8.6) to UHE photons from GW150914 in each time window has to be done individually for each direction inside the 90% contour since the source of GW150914 is actually a point source with well-defined coordinates $(\alpha_{\text{GW}}, \delta_{\text{GW}})$. The extended area in the sky which is being taken into account just comes from the limited knowledge about the true source direction. The spectrum-averaged exposure to photons above 10 EeV has no dependence on the azimuth angle. Hence, for a certain direction (α, δ) inside the 90% contour $\tilde{\mathcal{E}}$ is only a function of $\theta(\alpha, \delta)$ and the time for which the direction has been inside the field of view. For the 1d-time window, the rotation of the earth removes the dependence of the exposure on right ascension α and the relative observation time of a spot at declination δ is shown in Fig. 8.4. Thus, the exposure for the 1d-time window is only a function of δ presuming the aperture A is approximately constant during that time. The calculation of A which is needed for the calculation of $\tilde{\mathcal{E}}$ is done using the *HexagonFiles* which store the information of the number of active hexagons, i.e. hexagons of seven active SD stations, on a time grid with a spacing of 60s. When performing the time integral in Eq. 8.6, for every numerical time-step the corresponding entry in the *HexagonFile* is chosen such that the time difference between the entry and the time for which the aperture is being calculated is minimal. The integration has been performed in 1000 time-steps for both the 1000s and the 1d time window. The spectrum-averaged exposure for both time windows is shown as a function of α and δ inside the 90% contour of GW150914 in Fig. 8.5. About 48 min after the start of the 1d time window (see Fig. 8.5(b)), every direction inside the contour was being covered by the field of view leading to an exposure $\tilde{\mathcal{E}} > 0$ in the whole region. In the 1000s time window, part of the contour extends to zenith angles $\theta < 30^\circ$ which is outside the field of view of the present photon search. Thus, the

exposure is zero in that direction. The parts of the contour that move into the field of view during the time window – due to the rotation of the earth by about 4.2° – have an accordingly lower exposure than those parts which are covered during the whole period and thus lead to the rapid but continuous drop of the exposure visible in the left part of Fig. 8.5(a).

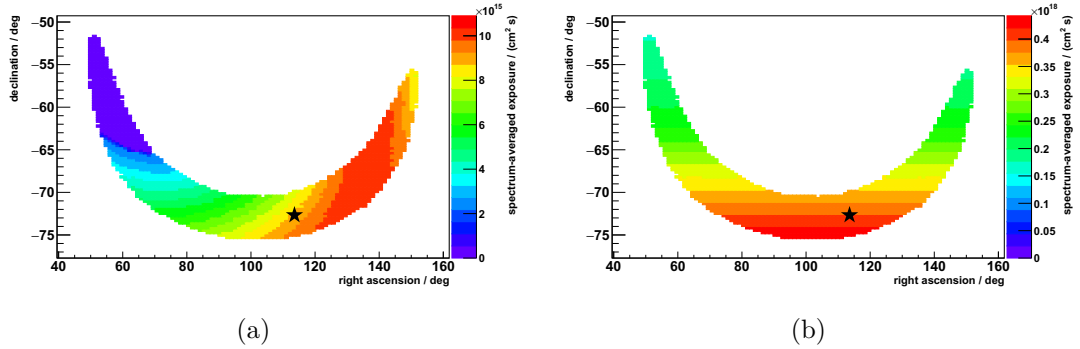


Figure 8.5: The spectrum-averaged exposure to UHE photons from all possible directions of GW150914 within the 90% CL region. In (a) the exposure is shown for the 1000 s time window and in (b) for the time window of 1 d. The rapid, but continuous drop to zero on the left part of (a) comes from the fact, that the 90% contour at the event time of GW150914 extends to zenith angles $\theta < 30^\circ$ which is outside the field of view (see Fig. 8.3). The rotation of the earth causes the contour to drift about 4.2° in right ascension during the 1000 s time window moving it slowly into the field of view. This causes some directions to be observed only for a fraction of that time.

8.2.4. Data unblinding and estimation of background

Unblinding the air shower data of the Auger SD for GW150914 in both the 1000 s and the 1 d time windows revealed no coincident event above 10 EeV. Thus, the number of photon candidate events in both time windows is $N_\gamma^{\text{cand}} = 0$. Using the Feldman-Cousins (FC) approach, upper limits on the expectation value of the number of photon candidate events were placed at 90% CL. The FC confidence intervals depend on the amount of expected background in the signal region. The larger the background, the lower are both the upper- and lower limits of the confidence interval given the same measurement result. The background in the present case is contributed by events that pass the photon candidate cut but were induced by hadronic particles or even UHE photons from a different source than the BBH merger which were just by chance coincident with the GW. So far, no photon signal has been unambiguously identified among the diffuse air shower data of the Pierre Auger Observatory. Nevertheless, photon candidate events have been found in [RJ19] and also at energies below 10 EeV using the Auger hybrid detector [AA17a]. An estimation of the diffuse background rate $\beta_{\text{diff}} \simeq (1.74_{-0.51}^{+0.70}) \times 10^{-21} \text{ cm}^{-2} \text{ sr}^{-1} \text{ s}^{-1}$ of photon candidate events measured with

the SD in the zenith and energy region of this analysis has been derived in Sec. 7.6 using the number of photon candidate events found in [RJ19] and the exposure to a diffuse flux of UHE photons. The total number of expected background events in directional and temporal coincidence with the GW is then given by Eq. 7.29. This leads to an expected background of $7.4_{-2.2}^{+3.0} \times 10^{-7}$ background showers from the 90% CL region of GW150914 that pass the photon candidate cut in the 1000 s time window and $3.91_{-1.15}^{+1.56} \times 10^{-5}$ in the 1 d time window. The given uncertainties on the background come from the statistical uncertainties on the number on $N_{\gamma,\text{diff}}^{\text{cand}}$ and are calculated using the Clopper-Pearson approach for confidence intervals on sample proportions [CC34].

However, since the expected background in the relatively short time windows analyzed here is very small, the resulting upper limits on the photon flux are not significantly different to cases with no background at all as shown in Fig.8.6. Therefore, and to get a result which is independent of systematical errors that come from the background estimation, the background is assumed to be zero for the calculation of upper limits. This introduces a tiny amount of conservatism since a confidence interval calculated that way covers slightly more than 90%. But the over-coverage is negligible in this case. If upper limits including the background estimation would be calculated, a contribution of a so far unidentified signal component could lead to an over-estimation of the background which in turn results in upper limits which are too low leading to an undercoverage of the 90% confidence interval. Though, introducing conservatism into confidence intervals is not desirable, an undercoverage should in any case be avoided [FG98]. The FC upper limit at 90% CL for a measured signal of zero events and no background is $N_{\gamma}^{\text{UL}} \approx 2.44$ (with the corresponding lower limit N_{γ}^{LL} being equal to zero).

8.2.5. Upper limits on k_{γ}

Following Eq. 8.2, the upper limit on the flux normalization k_{γ}^{UL} is obtained by dividing N_{γ}^{UL} by the energy integral over the energy-weighted exposure to photons from a certain direction (α, δ) and the photon selection efficiency $p_{\gamma\text{-cut}} = 0.5$. k_{γ}^{UL} is derived for the energy interval $[10^{19.0} \text{ eV}, 10^{20.5} \text{ eV}]$. This gives the upper and lower bounds for the integral in Eq. 8.2. Calculating k_{γ}^{UL} for all directions which lie within the 90% CL region of GW150914 and have a non-zero exposure leads to the distribution of k_{γ}^{UL} shown in Fig. 8.7(a) for the 1000 s and in Fig. 8.7(b) for the 1 d time window. For the 1000 s time window, the upper limit k_{γ}^{UL} for the direction with the highest probability to match the source direction of GW150914 is $5.7 \times 10^{-3} \text{ MeV cm}^{-2} \text{ s}^{-1}$. The best upper limit inside the contour is $4.9 \times 10^{-3} \text{ MeV cm}^{-2} \text{ s}^{-1}$. On the left side of the contour (towards lower angles in right ascension) the upper limits rapidly grow ($k_{\gamma}^{\text{UL}} \rightarrow \infty$) at the point where the directions are observed for only a fraction of the time window and, thus, the exposure drops towards zero (cf. Fig. 8.5). To display these results for the most likely direction and the best and worst upper limits within the 90% contour, the

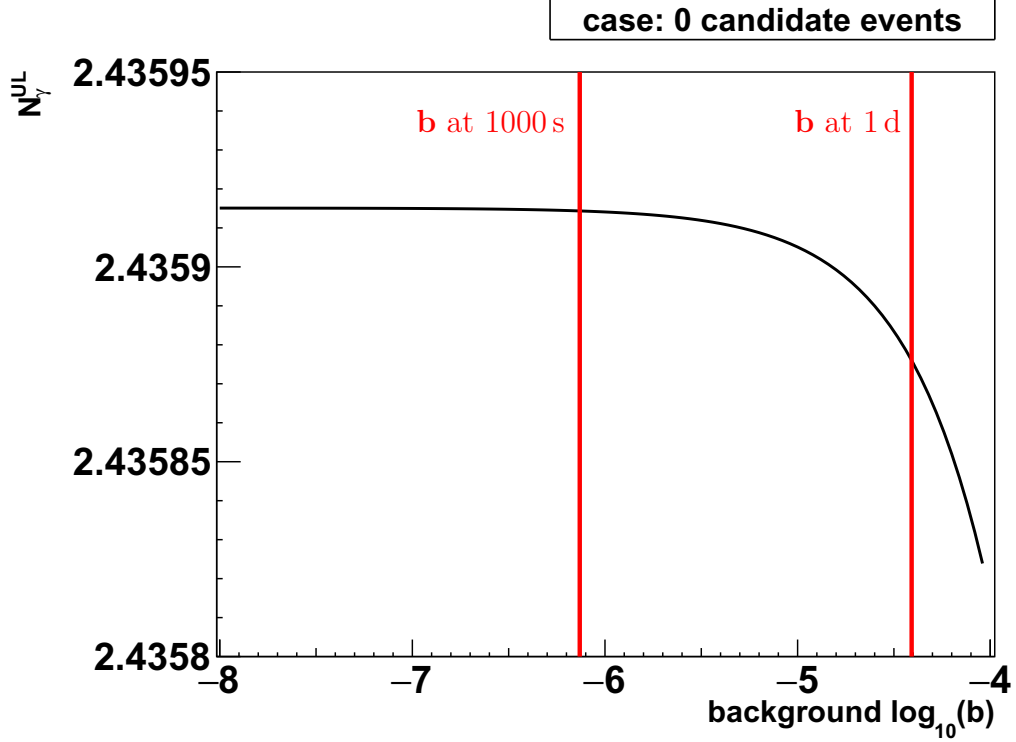


Figure 8.6: The Feldman-Cousins upper limits at 90% CL as a function of the expected background in the case of 0 measured photon candidate events. For background expectations close to zero, the variation of the upper limits is small. The background expected during the 1000 s and the 1 d time windows of GW150914 is indicated by the vertical lines. Comparing the expected background from within the 90% contour of GW150914 in the 1000 s and the 1 d time windows to the case with no background, the variation of the upper limits on the number of photon-induced air shower events is of the order of 10^{-5} .

following notation is used:

$$k_{\gamma}^{\text{UL}}(1000 \text{ s}) = 5.7 \in [4.9, \infty) \times 10^{-3} \text{ MeV cm}^{-2} \text{ s}^{-1}. \quad (8.15)$$

For the 1 d time window, the upper limit for the most likely direction of GW150914 is $12.6 \times 10^{-5} \text{ MeV cm}^{-2} \text{ s}^{-1}$ while inside the contour the upper limits k_{γ}^{UL} reach from $11.4 \times 10^{-5} \text{ MeV cm}^{-2} \text{ s}^{-1}$ to $28.8 \times 10^{-5} \text{ MeV cm}^{-2} \text{ s}^{-1}$, i.e.

$$k_{\gamma}^{\text{UL}}(1 \text{ d}) = 12.6 \in [11.4, 28.8] \times 10^{-5} \text{ MeV cm}^{-2} \text{ s}^{-1}. \quad (8.16)$$

8.2.6. Upper limits on \mathcal{F} and F

The corresponding upper limits on the spectral fluence between $10^{19.0} \text{ eV}$ and $10^{20.5} \text{ eV}$ are derived following Eqs. 8.7 and 8.8. A constant flux during each of

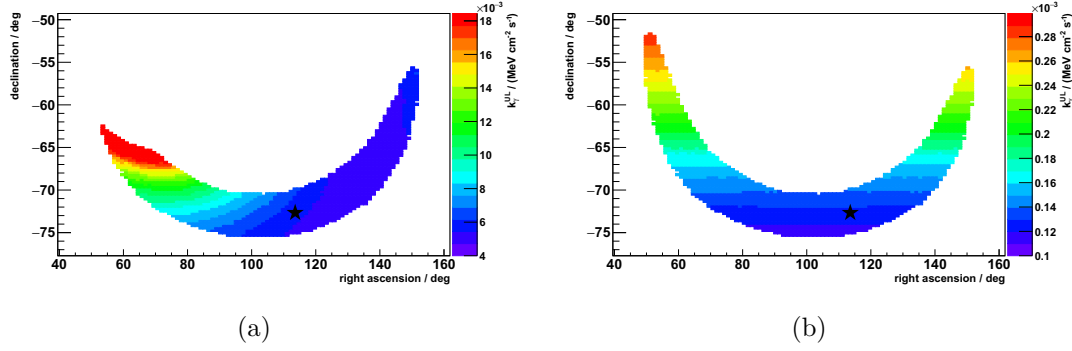


Figure 8.7: Upper limits at 90% CL on the flux normalization factor k_γ^{UL} as a function of right ascension and declination for all possible directions of GW150914 within the 90% CL region. In (a) $k_\gamma^{\text{UL}}(\alpha, \delta)$ is shown for the 1000 s time window. The value of k_γ^{UL} for the direction which has the highest probability to match the source direction of GW150914 (indicated by a star) is $5.7 \times 10^{-3} \text{ MeV cm}^{-2} \text{ s}^{-1}$. The best upper limit inside the contour is $4.9 \times 10^{-3} \text{ MeV cm}^{-2} \text{ s}^{-1}$. On the left side of the contour (towards lower angles in right ascension) the upper limits rapidly grow worse ($k_\gamma^{\text{UL}} \rightarrow \infty$) at the point where the directions are observed for only a fraction of the time window. In (b) $k_\gamma^{\text{UL}}(\alpha, \delta)$ is shown for the 1 d time window. The upper limit for the most likely direction of GW150914 is $12.6 \times 10^{-5} \text{ MeV cm}^{-2} \text{ s}^{-1}$ while inside the contour the values of k_γ^{UL} lie between $11.4 \times 10^{-5} \text{ MeV cm}^{-2} \text{ s}^{-1}$ and $28.8 \times 10^{-5} \text{ MeV cm}^{-2} \text{ s}^{-1}$.

the two time windows following an E^{-2} -power spectrum is assumed. With that, the relation between the upper limits on the flux normalization and the spectral fluence simplify to

$$\mathcal{F}^{\text{UL}} = \ln\left(\frac{10^{20.5} \text{ eV}}{10^{19.0} \text{ eV}}\right) (t_1 - t_0) k_\gamma^{\text{UL}} \begin{cases} = 3454 \text{ s } k_\gamma^{\text{UL}}, & (1000 \text{ s}) \\ = 297600 \text{ s } k_\gamma^{\text{UL}}, & (1 \text{ d}). \end{cases} \quad (8.17)$$

Using Eq. 8.10, the upper limits on the total fluence simplify to

$$F^{\text{UL}} = \frac{10^{20.5} \text{ eV} - 10^{19.0} \text{ eV}}{10^{39.5} \text{ eV}^2} (t_1 - t_0) k_\gamma^{\text{UL}} \begin{cases} = 9.684 \times 10^{-17} \frac{\text{s}}{\text{eV}} k_\gamma^{\text{UL}}, & (1000 \text{ s}) \\ = 8.344 \times 10^{-15} \frac{\text{s}}{\text{eV}} k_\gamma^{\text{UL}}, & (1 \text{ d}). \end{cases} \quad (8.18)$$

\mathcal{F}^{UL} and F^{UL} are related by a factor that is independent of the time window:

$$\mathcal{F}^{\text{UL}} = 3.567 \times 10^{19} \text{ eV } F^{\text{UL}}. \quad (8.19)$$

The upper limits \mathcal{F}^{UL} as a function of right ascension and declination are shown in Fig. 8.8. Using the notation introduced in the previous section, the upper limits on the spectral fluence in each time window can be summarized as

$$\mathcal{F}^{\text{UL}}(1000 \text{ s}) = 19.7 \in [17.0, \infty) \text{ MeV cm}^{-2} \quad (8.20)$$

and

$$\mathcal{F}^{\text{UL}}(1 \text{ d}) = 37.4 \in [33.8, 85.6] \text{ MeV cm}^{-2}. \quad (8.21)$$

Using Eq. 8.10, this translates into a total fluence of

$$F^{\text{UL}}(1000 \text{ s}) = 5.5 \in [4.8, \infty) \times 10^{-13} \text{ cm}^{-2} \quad (8.22)$$

and

$$F^{\text{UL}}(1 \text{ d}) = 10.5 \in [9.5, 24.0] \times 10^{-13} \text{ cm}^{-2}. \quad (8.23)$$

These are the upper limits on the energy (\mathcal{F}^{UL}) and the number of particles (F^{UL}) per square centimeter that reached the earth from the direction of the source of GW150914 in the form of photons between $10^{19.0} \text{ eV}$ and $10^{20.5} \text{ eV}$ during each of the two time windows.

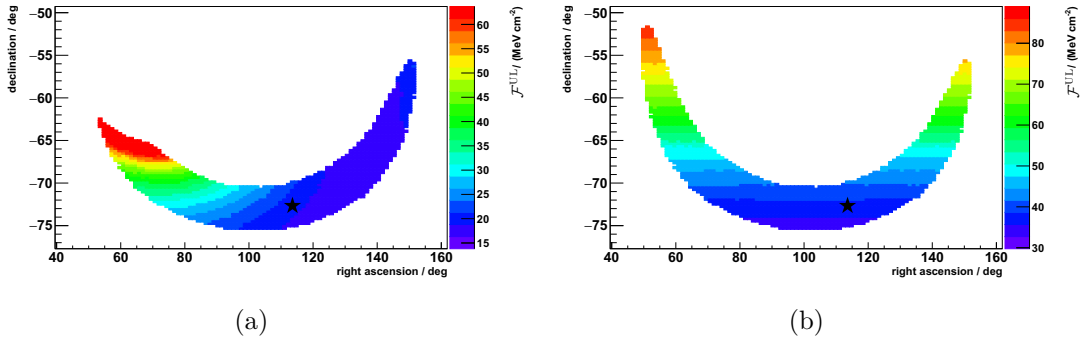


Figure 8.8: The upper limits at 90% CL on the spectral fluence as a function of right ascension and declination for all possible directions of GW150914 within the 90% CL region. In (a) $\mathcal{F}^{\text{UL}}(\alpha, \delta)$ is shown for the 1000 s time window. The value of \mathcal{F}^{UL} for the direction with highest probability to match the source direction of GW150914 (indicated by a star) is 19.7 MeV cm^{-2} . The best upper limit inside the contour is 17.0 MeV cm^{-2} . In (b) $\mathcal{F}^{\text{UL}}(\alpha, \delta)$ is shown for the 1 d time window. The upper limit for the most likely direction of GW150914 is 37.4 MeV cm^{-2} while inside the contour the values of \mathcal{F}^{UL} lie between 33.8 MeV cm^{-2} and 85.6 MeV cm^{-2} . The corresponding values of F^{UL} can be obtained by dividing \mathcal{F}^{UL} by the factor given in Eq. 8.19.

While for k_{γ}^{UL} the limits in the 1 d time window are about a factor of 45 better than in the 1000 s time window, for \mathcal{F}^{UL} and F^{UL} there is only a factor of about 2 in between the two time windows. This is because the exposure, which enters the calculation of k_{γ}^{UL} , increases only in proportion to the time for which a certain direction has been in the field of view. Hence, the longer a certain direction is in the field of view without a measured signal from that direction, the lower will be the upper limits k_{γ}^{UL} irrespective of the time that the direction has been outside the field of view (still under the assumption of constant emission during the whole observation period). For the 1000 s time window, most parts of the contour are

observed for the whole period while the regions with the largest exposure in the 1 d time window are in the field of view for only a fraction of about 60% of the time. Now, when deriving \mathcal{F}^{UL} and F^{UL} , the measurement results obtained during the periods when the direction was in the field of view, are being extrapolated to the whole observation time by just multiplying with the time period. For the 1000 s period, this roughly cancels out the time factor that has been introduced by the exposure (except for the small time dependencies of the aperture $A(t)$ and the zenith angle $\theta(t)$ which are both of the order ~ 1). For the 1 d period, the multiplication does not fully cancel out the time factor of the exposure. Thus, a factor remains that roughly resembles the fraction of the whole time window at which a given direction has been in the field of view. Since the directions inside the 90% contour were in the field of view for on average a little less than 50% of the sidereal day, the upper limits \mathcal{F}^{UL} and F^{UL} for the 1 d time window are about a factor of 2 larger than the limits for the 1000 s time window. This ratio in general only depends on the geometry of the GW localization and will therefore change from event to event.

8.2.7. Upper limits on E_{tot}

Knowing the luminosity distance of the source of GW150914 which has been measured by LIGO to be $D_L = 440_{-170}^{+150}$ Mpc, it is possible to place an upper limit on the total amount of energy that has been radiated by that source in the form of UHE photons. Given the simplifying condition that photons at those energies do not interact with the background radiation fields and therefore their flux does not undergo additional attenuation during their propagation through the universe (on top of the geometrical attenuation proportional to D_L^{-2}), a limit on the total amount of isotropically emitted energy can simply be obtained by extrapolating \mathcal{F}^{UL} to a 4π -sphere around the source (see Eq. 8.11). Taking into account the uncertainties in the direction and in the distance of GW150914, the limits on the total energy are

$$E_{\text{tot}}^{\text{UL}}(1000 \text{ s}) = 7.3_{-4.6}^{+6.0} \in [6.3_{-4.0}^{+5.1}, \infty) \times 10^{50} \text{ erg} \quad (8.24)$$

and

$$E_{\text{tot}}^{\text{UL}}(1 \text{ d}) = 14.4_{-9.3}^{+11.6} \in [13.0_{-8.2}^{+10.6}, 32.8_{-20.8}^{+27.0}) \times 10^{50} \text{ erg}, \quad (8.25)$$

where the given numbers again represent the limit for the most likely source direction as well as the best and worst limits inside the 90% contour. The errors of each number come from the uncertainty on the source distance. The total energy radiated by the source of GW150914 was $3.1 \pm 0.4 M_\odot$ (solar masses). Using the mean value of $3.1 M_\odot (\approx 5.55 \times 10^{54} \text{ erg})$, $E_{\text{tot}}^{\text{UL}}$ can be converted into an upper limit on the fraction of the total energy which has been radiated in terms of UHE photons

$$E_{\text{rel}}^{\text{UL}}(1000 \text{ s}) = 13.2_{-8.6}^{+10.7} \in [11.4_{-7.5}^{+9.2}, \infty) \times 10^{-5} \quad (8.26)$$

and

$$E_{\text{rel}}^{\text{UL}}(1 \text{ d}) = 25.9_{-16.4}^{+20.3} \in [22.6_{-14.8}^{+18.3}, 57.4_{-37.5}^{+46.5}] \times 10^{-5}. \quad (8.27)$$

Though these values seem like strong constraints, taking into account the attenuation of photons caused by interactions with the CMB and the URB generally leads to a significant suppression of the photon flux in the considered energy range.¹⁵ Estimating the magnitude of the effect by assuming the photons to be simply lost after their first interaction, the upper limits on the relative energy fraction $E_{\text{rel}}^{\text{UL}}$ were already in the order of 1 if the source of GW150914 were at a distance of ~ 9 interaction lengths since $e^{-9} \approx E_{\text{rel}}^{\text{UL}}$ (typically between 8 and 10 interaction lengths for other GW events depending on the fluence upper limit and the total radiated energy). This corresponds to a distance of about 20 Mpc to 70 Mpc depending on the photon energy (cf. Fig. 8.9). Dealing with sources of much larger distances – like the source of GW150914 – it is not possible to obtain a physically meaningful constraint (i.e. $E_{\text{rel}}^{\text{UL}} < 1$) on UHE photons at the source within the framework of standard model photon interactions. Also the assumption of isotropically emitted energy does not necessarily describe the physics of real CBM events since different combinations of spins and angular momenta might lead to high energy ejecta that are strongly beamed as suggested in [MK18] for the case of the neutron star merger GW170817.

8.2.8. Expected number of photons

To get an impression of how many UHE photons would be expected to traverse a perpendicular surface with the area of the SD array (SD aperture $A \approx 2400 \text{ km}^2$, cf. Tab. 13.3) after including a simplified attenuation model, the expected number of photons

$$\langle N_\gamma \rangle = \frac{A}{4\pi D_L^2} N_{\text{init}} \exp\left(-\frac{D_L}{\lambda}\right) \quad (8.28)$$

$$= \frac{A}{4\pi D_L^2} \frac{NM_\odot}{\int_{E_0}^{E_1} dE_\gamma k E_\gamma^\alpha} \exp\left(-\frac{D_L}{\lambda}\right) \quad (8.29)$$

has been studied as a function of luminosity distance D_L of the source and the amount of total radiated photon energy NM_\odot in units of solar masses (which is here assumed to be radiated isotropically). The normalization factor k is given by Eq. 7.16 and the results for a spectral index $\alpha = -2$ are summarized in Fig. 8.10. From this benchmark plot one can infer, for instance, that constraints ($E_{\text{rel}}^{\text{UL}} \lesssim 1$) are possible for BBH mergers (typical $E_{\text{rad}} \simeq 2 - 3M_\odot$) closer than ~ 100 Mpc and for BNS mergers like GW170817 (with $E_{\text{rad}} \geq 0.04M_\odot$) closer than ~ 70 Mpc. A non-observation of UHE photons from a merger event e.g. in the Virgo cluster ($D_L \approx 16.5 \text{ Mpc}$ [MS07]) could even lead to constraints below the permille level for a BNS merger (even stronger constraints for a BBH merger).

¹⁵Given the very hypothetical case that the GW source creates an outburst of UHE photons above $10^{20.5} \text{ eV}$, which is above the energy range considered in this analysis, a cascading down to lower energies could in principal lead to a flux enhancement when compared to a case without photon attenuation.

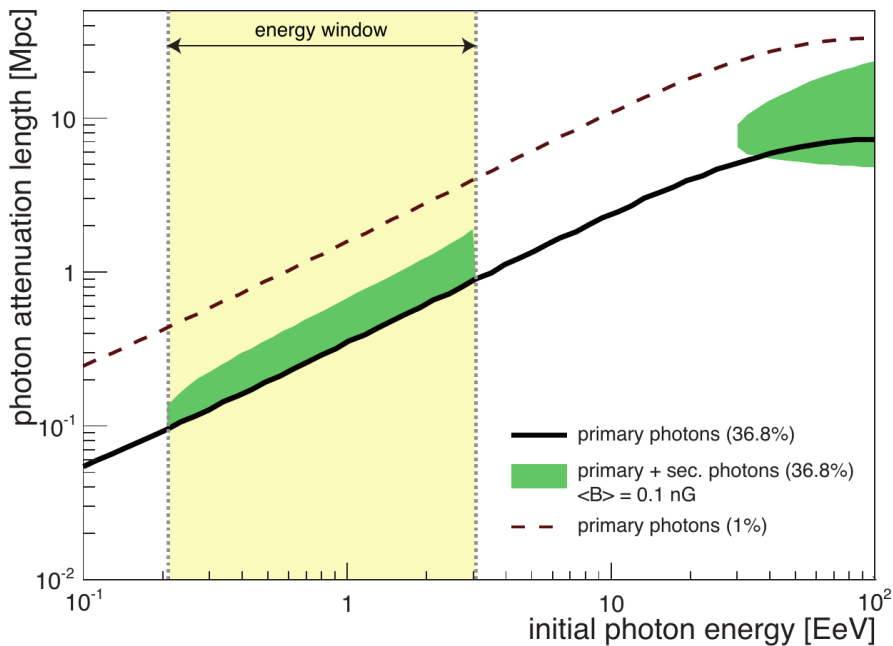


Figure 8.9: The photon attenuation length as a function of the primary photon energy at the source [AA16a]. The lines mark the propagation distances after which the survival probability for a single photon is reduced to 36.8% (solid) and 1% (dashed). The green areas mark the increased propagation distance (at 36.8% survival probability) if also secondary electrons are taken into account.

Considering, that photons are not simply absorbed after an interaction with the CMB, but initiate an electromagnetic cascade, multiple secondary photons at lower energy can be produced. Taking also those into account might lead to an increase of the maximum source distance for which the flux at the source can be reasonably constrained compared to Fig. 8.10. The influence of the cosmological redshift z however reduces the expected number of photons in this plot about a factor of $(1+z)^{-1}$ which leads to a reduction of $\langle N_\gamma \rangle$ about 3.5% at the high end of the distance range in Fig. 8.10 due to the fixed energy range of photons measured on earth. The impact of the cosmological redshift on the results of this analysis is further discussed in Sec. 8.5.5. Still, the source of GW150914 with a distance of 440 Mpc (270 Mpc at the best within the error margin) is clearly too far away to constrain the UHE photon flux at the source when taking also propagation effects into account unless new physics is involved. Nevertheless, the upper limit on the energy fraction $E_{\text{rel}}^{\text{UL}}$ as derived here may be treated as a benchmark value. For close sources like GW170817 (discussed in Sec. 8.3.3) on the other hand, this shows the potential of the analysis to place actual constraints on the UHE photon flux at the source.

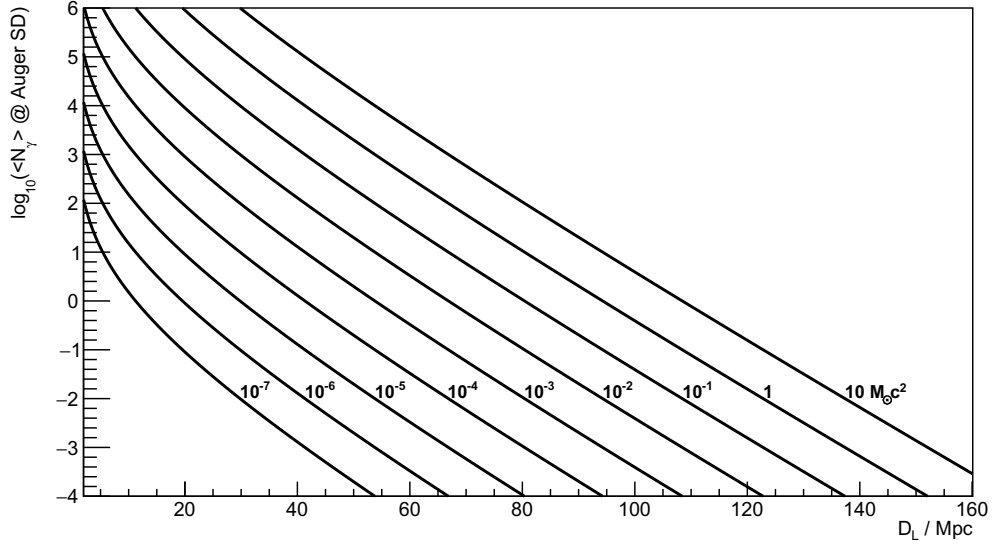


Figure 8.10: The number of UHE photons $\langle N_\gamma \rangle$ which would be expected to traverse a perpendicular surface with an area of 2400 km^2 (\approx aperture A of the Auger SD array, cf. Tab. 13.3) if an amount of $10, 1, 10^{-1}, \dots, 10^{-7}$ solar masses would be transferred into UHE photons between $10^{19.0} \text{ eV}$ and $10^{20.5} \text{ eV}$ isotropically at a distance D_L . The spectrum at the source is here assumed to follow an E^{-2} power spectrum and the photons are assumed to be attenuated with an interaction length of 7 Mpc independent of their energy. Possible secondary photons from electromagnetic cascading are not taken into account.

8.3. Results for all GW events from LIGO/Virgo runs O1 and O2

The observation runs O1 and O2 lasted from September 2015 until August 2017 and lead to the detection of eleven GW events. A compilation of the GW properties which are relevant for the analyses of this thesis is given in Tab. 13.2 [AB19b]. During the first run O1 from September 12th, 2015 until January 19th, 2016 three GW events have been detected and the sources have been identified as the coalescences and subsequent mergers of three binary systems of stellar mass black holes. Eight more GWs were detected during O2 from November 30th, 2016 to August 25th, 2017. Seven of those were identified as BBH mergers and one event, namely GW170817, turned out to have originated in a BNS merger. Independent of the type of the GW source, a search for UHE photons in coincidence with any of the eleven GWs has been carried out analogously to the procedure described in Sec. 8.2 on the example of GW150914. To give an overview, the 68%, 90% and 99%-contour lines of the original (unconvolved) source localization maps of all GW events and the respective fields of view of the Auger SD for the follow-up photon search and the different follow-up neutrino searches at the time of the merger are given in Fig. 13.12 in the appendix.

8.3.1. Exposure

The 90% CL regions of four out of the eleven events, namely GW150914, GW151226, GW170729 and GW170809, were partly covered by the instantaneous field of view and thus also during the 1000 s time window. However, GW150914 remains the only event with a considerably large overlap and the only event for which the most likely direction could be observed by the Auger SD at the GW event time. During the 1 d time window there were (at least partial) overlaps of the 90% CL regions and the field of view for all eleven GWs. Moreover, four events (GW150914, GW170809, GW170814 and GW170817) were fully contained at declination angles below $\delta = +24.6^\circ$ and could therefore be completely covered by the field of view during the 1 d time window.

As far as there was a non-zero overlap between the 90% CL region and the field of view at any moment of the respective time window, the exposure as a function of α and δ has been calculated. For the four events observable during the 1000 s time window, the exposure is shown in the appendix in Fig. 13.13. Here, GW170729 and GW170809 are special cases since the 90% contour is completely moving outside the field of view during that time. Hence, no direction is being covered for the whole period giving a comparably low exposure for a tiny fraction of the localization region while the exposure is zero for the rest of it. The exposure as a function of α and δ in the 1 d time window is shown for all eleven contours in Fig. 13.14. For reasons of comparability the z -axis of all plots in Figs. 13.13 and 13.14 respectively have the same range.

In the approximation of constant aperture A during a 1 d time window, the exposure $\tilde{\mathcal{E}}(\delta_{\text{GW}})$ solely depends on the source declination. The result for $\tilde{\mathcal{E}}(\delta_{\text{GW}})$ scanning the whole sky $-90^\circ \leq \delta_{\text{GW}} \leq 90^\circ$ is shown by the black curve in Fig. 8.11. In this plot $\tilde{\mathcal{E}}(\delta_{\text{GW}})$ is normalized by the average aperture for each event, which may be taken from Tab. 13.3. Since the aperture is approximately constant during the course of one day (variations in the order of $\lesssim 1\%$) the exposure for each event can be obtained by simply scaling the y -axis with the corresponding value of A . The colored bars in Fig. 8.11 indicate the spread in declination for each of the eleven GW events.

8.3.2. Upper limits

Analogous to the follow-up analysis procedure of GW150914, the Auger SD data have been searched for reconstructed air showers which were coincident with either of the two time windows and with reconstructed shower axes inside the 90% contours of any of the eleven GWs. Performing the photon candidate selection on all coincident air showers revealed no photon candidate event. Hence, upper limits were placed on the flux normalization factor k_γ^{UL} and the spectral fluence \mathcal{F}^{UL} for each GW event. The results for k_γ^{UL} as a function of α and δ are shown in the appendix in Fig. 13.15 for the 1000 s time window and in Fig. 13.16 for the 1 d time window. In Fig. 8.12, a compilation of $k_\gamma^{\text{UL}} \times A$ for all GW events during the 1 d time window is given under the approximation of constant aperture in each time window. The numerical values of the upper limits k_γ^{UL} for the directions which

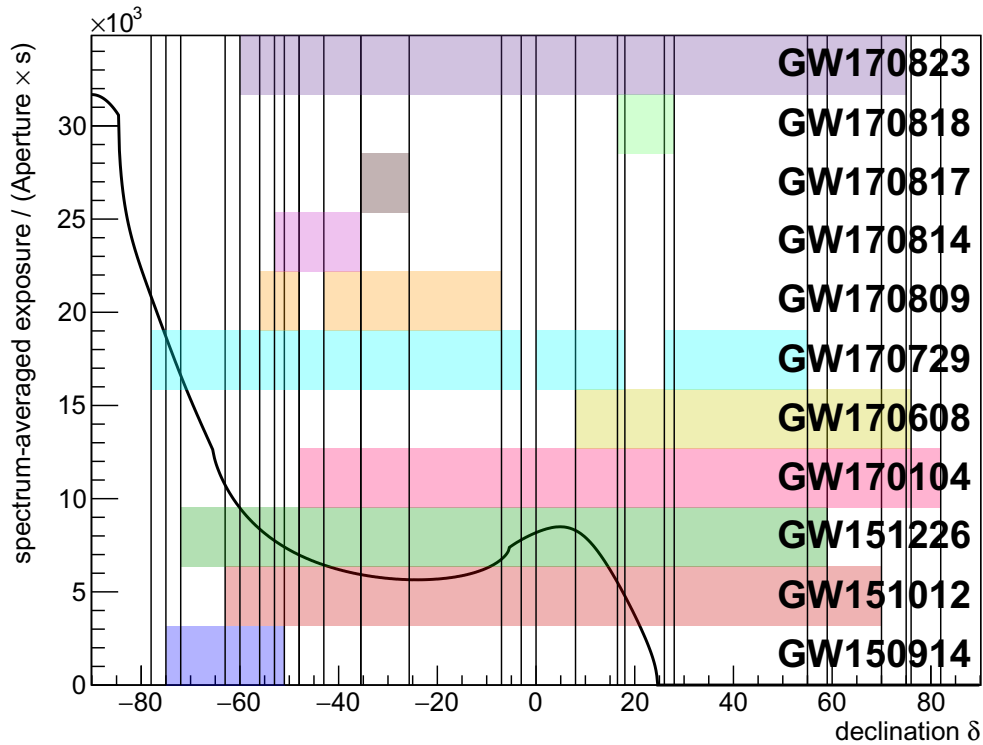


Figure 8.11: The spectrum-averaged exposure to UHE photons for an observation time of 1 sidereal day as a function of source declination δ divided by the aperture of the SD (black curve, cf. Tab. 13.3). In principle the aperture is not constant over time but its variations during one day have been found to be of the order $\lesssim 1\%$. Thus, it can be treated as approximately constant within the time window of a given event. The colored horizontal bars indicate the declination bands which are covered by the individual GW events. The black vertical lines mark the points where a declination band starts or ends and shall help to guide the eye to the corresponding spot on the exposure curve. As an example, the declination band of the 90% contour of GW150914 is marked by the blue shaded bar in the bottom row which reaches from $\delta = -75^\circ$ to $\delta = -51^\circ$. The range of the graph that displays the spectrum-averaged exposure in the 1 d time window of GW150914 is contained within this declination band.

have the highest probabilities to contain the GW sources as well as the maximum and minimum upper limits inside the contours are compiled in Tab. 13.4. The corresponding results for \mathcal{F}^{UL} can be found in Figs. 13.17, 13.18 and 8.13 and in Tab. 13.5. Numerical values for the upper limits on the energy fraction $E_{\text{rel}}^{\text{UL}}$ are compiled in Tab. 13.6.

When comparing these results to other multimessenger observations, one finds that these upper limits on the UHE photon fluence on top of the atmosphere are about two orders of magnitude lower than the limits on UHE neutrinos from GW sources between 0.1 EeV and 25 EeV measured by the Pierre Auger Observatory [AA16b] and between 100 GeV and 100 PeV measured by IceCube and

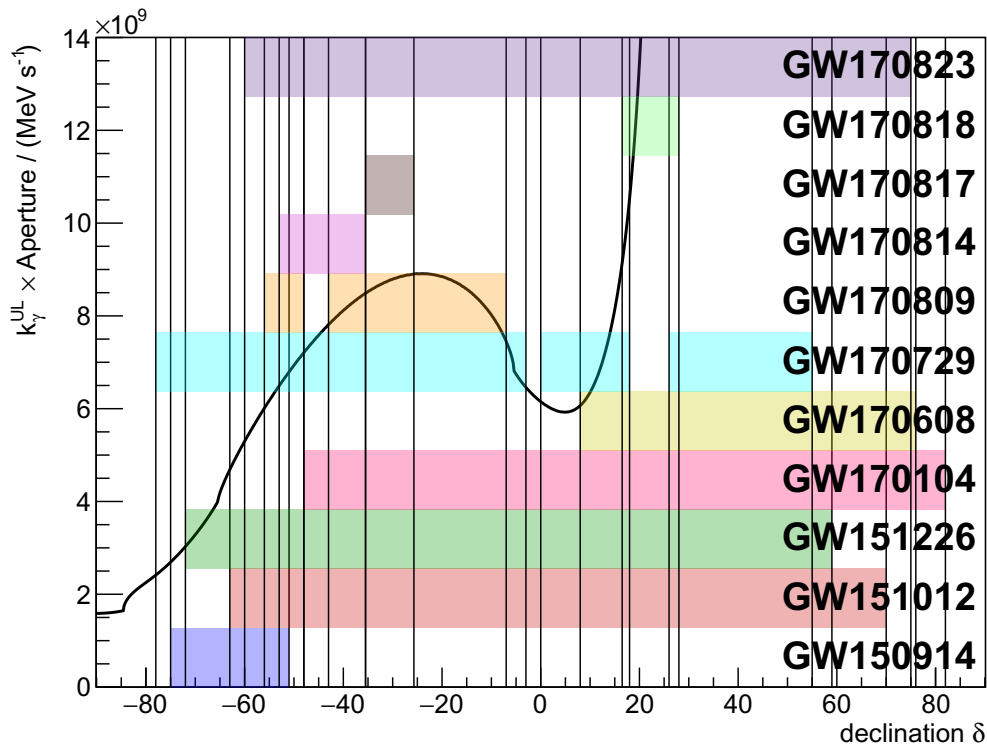


Figure 8.12: The upper limits on the flux normalization factor k_{γ}^{UL} for an observation time of 1 sidereal day as a function of source declination δ multiplied by the aperture of the SD (black curve, cf. Tab. 13.3). For a description of the notation see the caption of Fig. 8.11.

ANTARES [AS16b]. This difference is mainly caused by the higher detection efficiency of the Pierre Auger Observatory for primary photons than for neutrinos. The limits on the total energy transferred into neutrinos at the sources cannot directly be compared to the limits on the total energy transferred into UHE photon since these particles undergo different interactions during their propagation through the interstellar medium that lead to an additional exponential suppression of any UHE photon flux. However, since the detection efficiency for photons is high, the limits on the total energy in the form of UHE photons emitted by a close source (closer than about 30 Mpc) could possibly rival the limits on UHE neutrinos. When comparing the limits on the UHE photon fluence to the γ -ray measurements of the binary neutron star merger GW170817 by Fermi-GBM and INTEGRAL [AB17b], the isotropic peak luminosity of $1.6 \times 10^{47} \text{ erg s}^{-1}$ in the energy range between 1 keV and 10 MeV corresponds to a spectral fluence which is about two order of magnitude larger than the upper limits that have been placed here at energies above 1 EeV. However, when comparing these measurements one has to keep in mind that their respective energy ranges are separated by 13 orders of magnitude.

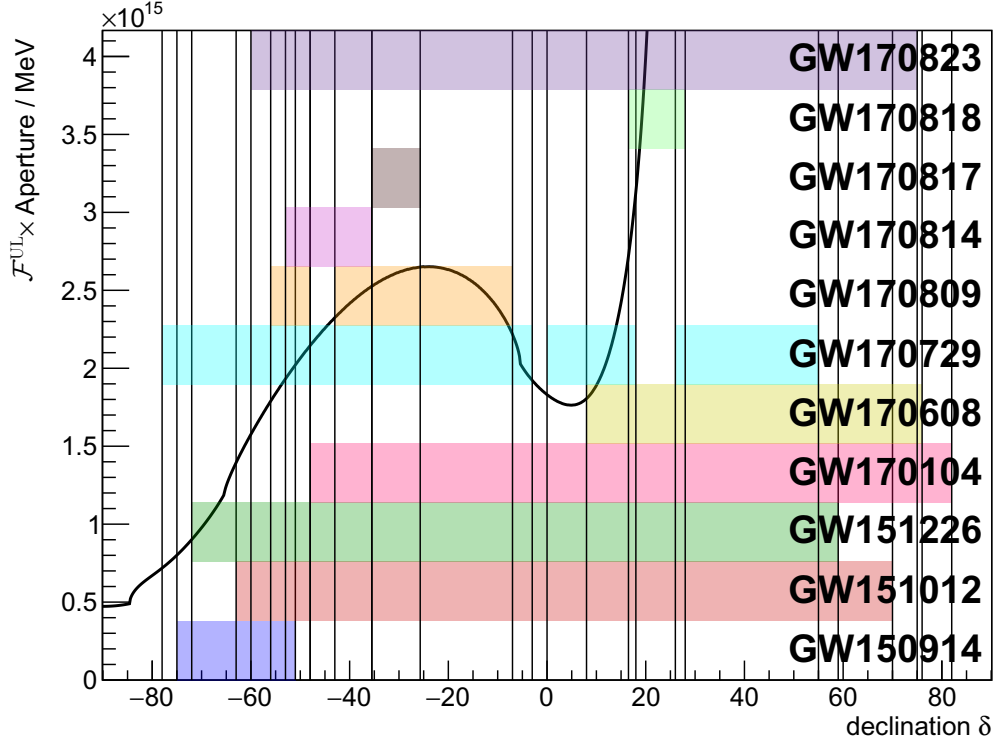


Figure 8.13: The upper limits on the spectral fluence \mathcal{F}^{UL} for an observation time of 1 sidereal day as a function of source declination δ multiplied by the aperture of the SD (black curve, cf. Tab. 13.3). For a description of the notation see the caption of Fig. 8.11.

8.3.3. Constraints on the BNS merger GW170817

After electromagnetic follow-up observations in various wavelengths [AB17a] the source of the neutron star merger event GW170817 has been identified to reside inside the galaxy NGC 4993 at $\delta = -23^\circ 23' 02''$, $\alpha = 13^h 09^m 47.7^s (\hat{=} -162^\circ 33' 4.5'')$ [NA19]. The luminosity distance of NGC 4993 has been independently measured to be $D_L(\text{NGC 4993}) = 41.0 \pm 3.1 \text{ Mpc}$ [HH17] ($40_{-15}^{+7} \text{ Mpc}$ from GW measurements alone [AB19b]). Using these additional information about the source localization, the limits for GW170817 can be set more precisely as $k_\gamma^{\text{UL}}(1 \text{ d}) = 38.9 \times 10^{-5} \text{ MeV cm}^{-2} \text{ s}^{-1}$ and $\mathcal{F}^{\text{UL}} = 115.7 \text{ MeV cm}^{-2}$ and (assuming no photon attenuation) $E_{\text{rel}}^{\text{UL}} = 52.1_{-7.6}^{+8.2} \times 10^{-5}$.

Taking into account attenuation effects during the propagation of potential UHE photons from the source of GW170817 to the earth by treating a photon that has undergone an interaction as “lost” for the analysis, the upper limit on the UHE photon fraction would be 1 if NGC 4993 were at a distance of 8.3 photon interaction lengths from the earth. Treating all photons in the energy range $10^{19.0} \text{ eV} < E_\gamma < 10^{20.5} \text{ eV}$ to have an attenuation length of $\sim 7 \text{ Mpc}$ (cf. Fig. 8.9) as an optimistic approximation, the luminosity distance of NGC 4993 corresponds to

about 6 interaction lengths. Calculating the limit on the total energy back to the source using these approximations, the limit on the total amount of energy is of the order $E_{\text{tot}}^{\text{UL}} \simeq 8.8 \times 10^{-3} M_{\odot} c^2$ which corresponds to an energy fraction of $E_{\text{rel}}^{\text{UL}} \simeq 22\%$ transferred into UHE photons (using the lower bound of the total energy radiated by the source of GW170817 as the reference value). This number is just a rough estimate but constitutes a first constraint on the production of photons in this energy regime by a BNS merger. For a more detailed study and a precise constraint of the physics at the source of GW170817, different models for the photon energy spectrum at the source together with the energy dependence of the photon attenuation length would have to be considered. Also a contribution of secondary particles in the electromagnetic cascade after the first photon interaction with the background radiation fields might have an impact at longer observation time windows due to their delayed arrival time with respect to the GW. GW170817 is the only GW event out of LIGO/Virgo run O1 and O2 for which a physical meaningful constraint on the energy fraction transferred into UHE photons may be placed under classical physics assumptions. The sources of the other GW events are clearly too far away to obtain limits on the energy fraction $E_{\text{rel}}^{\text{UL}} < 1$ considering classical photon attenuation even under the most optimistic approximations about the attenuation length, the source distance and the total radiated energy, or even with the assumption of a highly anisotropic emission in the form of a narrowly-collimated jet directly pointing towards earth (considering typical jets with opening angles of the order of a few degree [MK18]).

8.3.4. Coincident air shower events

Apart from a zero-detection of coincident photon candidate events, in total four non-candidate air showers with reconstructed photon energies between $10^{19.0}$ eV and $10^{20.5}$ eV have been found to be coincident with GW events during the 1 d time windows and to have reconstructed shower axes within the respective 90% CL regions. The first coincident event (SD event ID: sd_35040667) was recorded at UTC 2015-10-12T09:54:43, $16^h 21^m$ after GW151012 (see Fig. 8.14(a)) with a PC value of -0.015 . The second coincident event (sd_36127797) was recorded at UTC 2015-12-26T03:38:53, $5^h 37^m$ after GW151226 (Fig. 8.14(b)) with a PC value of -1.862 . The next event (sd_43861200) was recorded at UTC 2017-07-29T18:56:29, $10^h 36^m$ after GW170729 (Fig. 8.14(c)) and had a PC value of -2.411 and the last coincident event (sd_44195703) was recorded at UTC 2017-08-23T13:13:58 which is $15^h 14^m$ after GW170823 – the last GW measured during O2 – (Fig. 8.14(d)) with a PC value of -1.903 . The measured number of four air shower events is slightly larger than the expectation value of 1.55 events within an observation window of the same exposure as the combined exposure of all unblinded sky regions and time windows in this follow-up analysis. But the deviation is not significant. Assuming the rate of random air shower events within a fixed exposure to follow a Poisson distribution, the p -value for a measurement result of 4 events with an expectation value of 1.55 is $p = 0.072$, which is not small enough to reject the null-hypothesis that the air shower rate in the observed regions is the same as elsewhere. Also the

distribution of time delays of these four air shower events with respect to the GW event time is compatible with the hypothesis of random coincidences.

The PC values of the four coincident events are highlighted on top of the data distribution next to the photon candidate cut in Fig. 8.15. All four events have PC values below the photon candidate cut $PC_{\gamma\text{-cut}} \approx 0.875$ (see Sec. 7.4) and are well contained within the bulk of data. While the events `sd_36127797`, `sd_43861200` and `sd_44195703` are far away from the distribution of photon simulations, `sd_35040667` is consistent with both distributions, the bulk of data and photon simulations. Nevertheless, an interpretation of `sd_35040667` as a photon originating from the source of GW151012 is disfavored due to the large distance of the source $D_L(\text{GW151012}) = 1080^{+550}_{-490}$ Mpc compared to the attenuation length of a photon $\lambda_\gamma(E_\gamma = 12 \text{ EeV}) \approx 3 \text{ Mpc}$, with $E_\gamma = 12 \text{ EeV}$ being the reconstructed photon energy of `sd_35040667`. Even without photon attenuation, e.g. through the intermediate conversion into axions, the large distance of the source of GW151012 would necessarily lead to a strong geometrical attenuation of any particle flux.

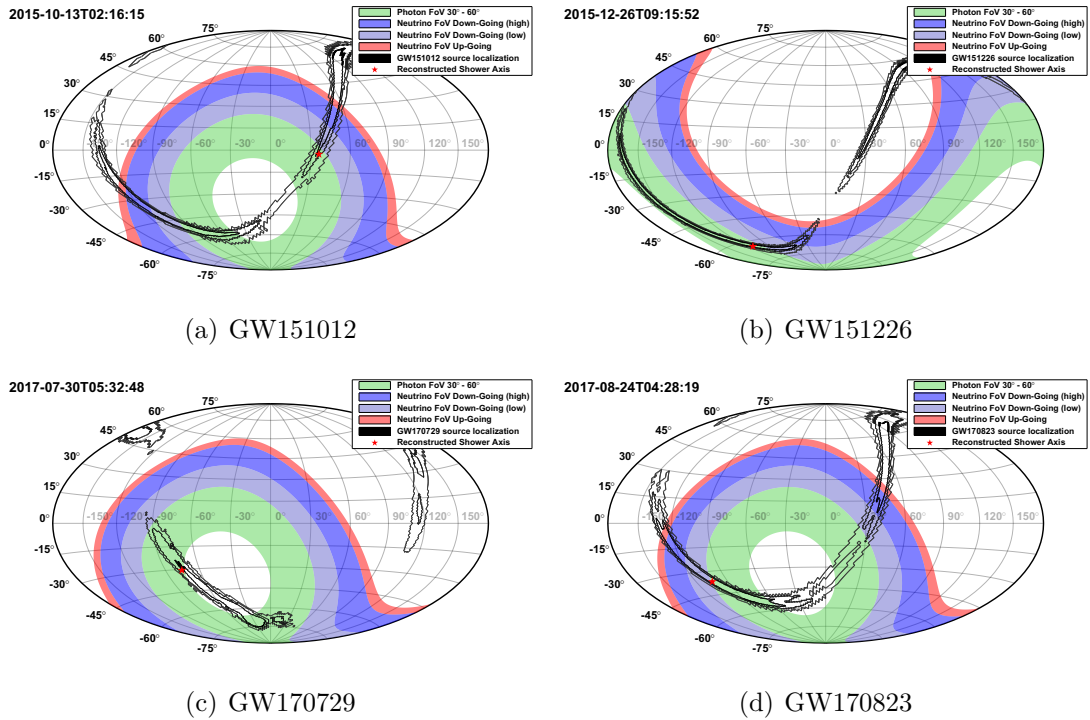


Figure 8.14: The field of view in equatorial coordinates (green shaded area) at the event times of the four air shower events which were coincident with a GW event in time and direction. The projection of the reconstructed shower axis on the (unconvolved) sky map is marked for each event by the red star. The event times of the coincident air shower events are given on the top left to each plot.

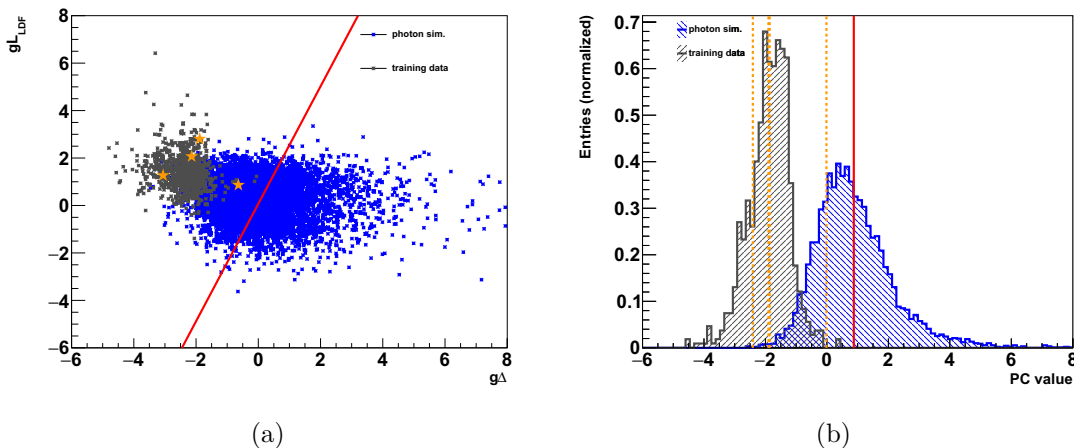


Figure 8.15: (a) The four coincident air shower events (yellow stars) highlighted in the scatter plot of the two normalized photon observables $g\Delta$ and gL_{LDF} . The photon candidate cut is represented by the red line. The gray markers show the distribution of the training data described in Sec. 6.2.2. The blue markers show the distribution of a set of simulated photon air showers (simulation set *A* described in Sec. 6.1.1). (b) The projection of the two distributions on the PC axis. The dotted lines highlight the PC values of the coincident events. All four values are well below the photon candidate cut which is indicated by the solid line.

8.4. Significance in case of a photon candidate detection

With the current SD photon analysis, the signal region, i.e. the region in the space of the PC where an event is considered a photon candidate, is not free of background. Hence, a possible photon candidate in coincidence with a GW could never unambiguously be identified as an actual photon. However, the smaller the expected background is, the lower is the chance to encounter a photon candidate with hadronic origin and, given a photon candidate detection, the higher would be the confidence at which the background hypothesis could be rejected. This raises the question about the significance at which a hypothetical photon candidate in coincidence with a future GW event could be claimed to be a correlating photon event.

For this consideration, one may assume there was a photon candidate event coincident with one of the GW events from O1 or O2. The chance to encounter a photon candidate from the isotropic background in coincidence with any of the GW events depends on the total exposure of the unblinded sky regions and is given by a Poissonian distribution. The expectation value of the Poissonian which is the expected number of background events b can be obtained by summing up the background contributions of all GW events as given by Eq. 7.29 using the spectrum-averaged photon exposure $\tilde{\mathcal{E}}(\alpha_{\text{GW}}, \delta_{\text{GW}})$ to a point-source on the celestial sphere (see Eq. 8.6). The expected accumulated background expectation values

for all GW events in the two distinct time windows are:

$$b(1000 \text{ s}) = 9.61 \times 10^{-7} \quad (8.30)$$

$$b(1 \text{ d}) = 4.67 \times 10^{-4}. \quad (8.31)$$

Since the significance shall be expressed in terms of a confidence level or a σ -value we need to know at which amount of background a given confidence interval is consistent with zero and when it is not (see Fig. 8.16). Or, the other way round, given an expected background (which is determined by the total exposure to the observed sky regions) and a measured signal of 1 photon candidate, we want to know, up to which confidence level the corresponding confidence interval does not include the zero anymore.

For the background values given above and a single photon candidate event ($N_\gamma^{\text{cand}} = 1$) in coincidence with any of the GW events, the lower limits of the Feldman-Cousins confidence intervals have been scanned through a range of confidence levels to find the critical confidence level CL_{crit} at which the transition $N_\gamma^{LL} > 0 \rightarrow N_\gamma^{LL} = 0$ occurs, i.e. CL_{crit} can be defined as

$$\text{CL}_{\text{crit}} := \max\{\text{CL} \in [0, 1] \mid N_\gamma^{LL}(\text{CL}, b) > 0\}. \quad (8.32)$$

CL_{crit} is the confidence level at which the measured signal is just not compatible with zero anymore and, thus, the degree of significance of the “photon detection.” For the two time windows again treated individually, the significance of a single measured photon candidate in the respective time window would thus be

$$\text{CL}_{\text{crit}}(1000 \text{ s}) = 0.999999028 \cong 4.90 \sigma \quad (8.33)$$

$$\text{CL}_{\text{crit}}(1 \text{ d}) = 0.999532 \cong 3.50 \sigma. \quad (8.34)$$

In other words, if a photon candidate had been observed, the background hypothesis could have been rejected at a 4.90σ (3.50σ) level for the 1000 s (1 d) time window. This number can be treated as a measure for the sensitivity of the analysis to a potential photon signal. To keep the sensitivity on a high level for future GW follow-up searches, a refined analysis procedure is elaborated in Chapter 9.

8.5. Discussion of systematical uncertainties

The results obtained up to this point contain a number of assumptions about physical parameters and simplifications that were introduced to obtain first benchmarks of the capability of the Pierre Auger Observatory to search for UHE photons from transient point sources. Allowing for variations of these parameters within a reasonable range allows the estimation of the systematic uncertainties that were introduced by these assumptions to the upper limits derived in Sec 8.2 and Sec. 8.3 and the sensitivity discussed in Sec. 8.4. The most significant sources of systematic uncertainties and their impact on the results of the analysis are discussed in the following.

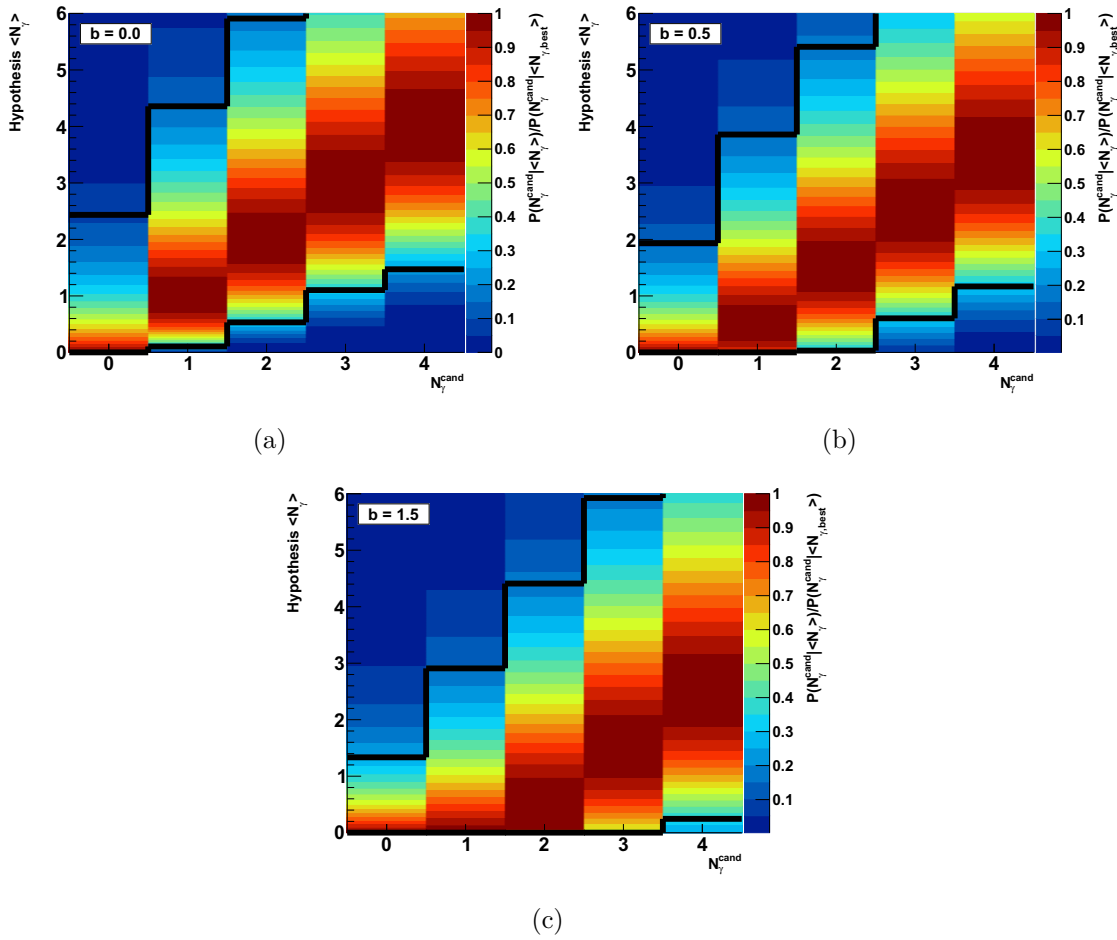


Figure 8.16: The construction of confidence belts at a confidence level of 90% with the Feldman-Cousins method [FG98]. For each hypothesis $\langle N_\gamma \rangle$ of the true expectation value of the number of photon events from the observed region, the Poisson distribution for the probability to get the measured result N_γ^{cand} divided by the probability to measure N_γ^{cand} given the “best hypothesis” $\langle N_{\gamma, \text{best}} \rangle$ is plotted along the abscissa taking also into account the expected amount of background b . The best hypothesis is the hypothesis under which a measurement has the highest probability to produce the measured value N_γ^{cand} . The black lines mark the upper and lower margins of the confidence intervals at 90% CL. The horizontal confidence intervals are constructed following the ordering principle described in [FG98]. For a given measurement result N_γ^{cand} , the vertical confidence interval over the accepted range of hypotheses spans from the lowest hypotheses for which the N_γ^{cand} lies within the horizontal confidence interval to the highest and can directly be read from the plot. With increasing background from (a) to (c), the confidence belt moves downwards. While at $b = 0$, a measured value of $N_\gamma^{\text{cand}} = 1$ is not consistent with the hypothesis of $N_\gamma = 0$, at a background of $b = 0.5$ however it is. At $b = 1.5$, up to three measured photon candidate events would be consistent with $N_\gamma = 0$ at 90% CL. Further details on the construction of the confidence intervals can be found in [FG98].

8.5.1. Variation of the spectral index α

Throughout this thesis the spectrum of photons between $10^{19.0}$ eV and $10^{20.5}$ eV on top of the atmosphere is assumed to follow a power law distribution with spectral index $\alpha = -2$. While being loosely motivated by the expected spectral shape of CR particles accelerated via first order Fermi acceleration, there are no actual measurements of a photon spectrum at these energies making the choice of α an obvious source of uncertainty. The numerical value of α enters the calculation of the physical quantities k_γ , \mathcal{F} and E_{tot} with the spectrum-weighted integral of the exposure in the denominator of Eq. 8.2. Due to the energy dependence of the photon detection efficiency $\epsilon_{\text{SD}}(E_\gamma)$, the spectrum-averaged exposure $\tilde{\mathcal{E}}$ between $10^{19.0}$ eV and $10^{20.5}$ eV does not strongly depend on the spectral index. For instance, the spectrum-averaged exposure $\tilde{\mathcal{E}}_{\text{diff}}$ to a diffuse flux of UHE photons between January 2004 and June 2018 (see Eq. 7.24) changes from $\tilde{\mathcal{E}}_{\text{diff}} \approx 4.9 \times 10^{21}$ cm² sr s for $\alpha = -3$ to $\tilde{\mathcal{E}}_{\text{diff}} \approx 7.6 \times 10^{21}$ cm² sr s for $\alpha = -1$ as shown in Fig. 8.17. This uncertainty of about $\pm 20\%$ translates into an uncertainty of the same order on \mathcal{F} and E_{tot} while the value of k_γ as a normalization factor has a different physical interpretation when calculated for another spectral distribution and, thus, can not directly be compared at different values of α . $\tilde{\mathcal{E}}_{\text{diff}}$ as a function of α is shown separately for three different zenith angle bins in Fig. 13.19 in the appendix. While at high zenith angles the impact of a variation of α on $\tilde{\mathcal{E}}_{\text{diff}}$ becomes stronger (i.e. $\sim +1.6\%$ between 30° and 40° , $\sim +10\%$ between 40° and 50° and $\sim +35\%$ between 50° and 60°), the benchmark value of $\alpha = -2$ coincides with a local maximum in the graph of $\tilde{\mathcal{E}}_{\text{diff}}(\alpha)$ leading to an asymmetric systematical uncertainty at lower zenith angles.

8.5.2. Bias due to the finite angular resolution of the SD

The upper limits derived for directions that are close to the edge of a search region are afflicted with an additional bias which has so far not been discussed. Since the directional resolution of the SD is finite, the probability to reconstruct the direction of an UHE photon from a source within the search region to be outside of that region increases with the proximity of the source to the edge of the search region. While the magnitude of this effect depends on the shape of the localization contour locally around the considered source direction, in the simplest case of a (locally) straight contour the photon detection efficiency for a source located exactly on the contour line is reduced by a factor of 0.5. Hence, the upper limits for that direction are about a factor of 2 higher. For sources which are close to the edge of the search region, the impact of this effect also depends on the energy dependence of the directional resolution which has been pointed out in Sec. 7.5. Due to the increase of the angular resolution with energy, the photon spectrum within the search region from a source close to the edge of the region would appear harder than the anticipated E^{-2} spectrum since relatively more photons of lower energy would be reconstructed to be outside of the search region than photons of higher energy. The expected change of the spectral shape with the proximity of a source to the edge of a search region is illustrated in Fig. 8.18. The maximum change of

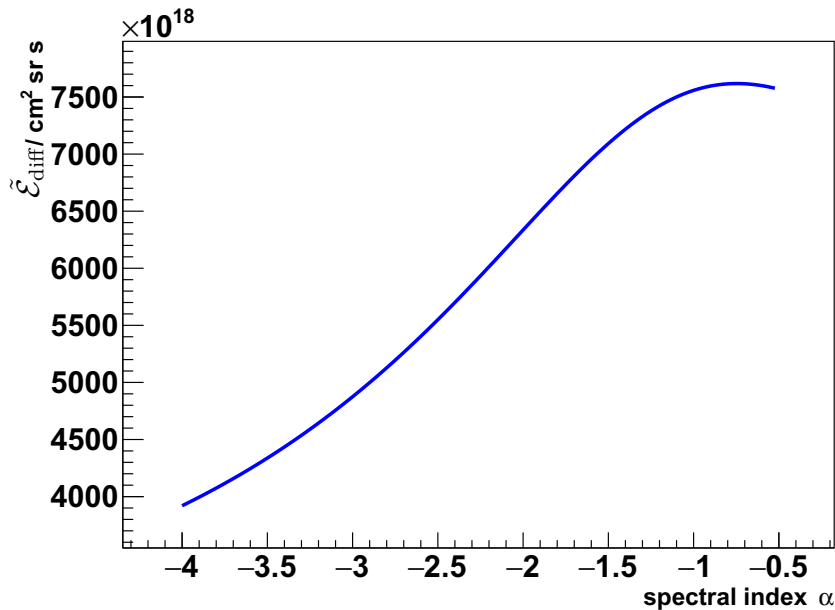


Figure 8.17: The dependence of the spectrum-averaged photon exposure $\tilde{\mathcal{E}}_{\text{diff}}$ in the search period from January 2004 to June 2018 on the spectral index α . The values of $\tilde{\mathcal{E}}_{\text{diff}}$ shown here are averaged over the zenith angle range between 30° and 60° . The corresponding curves for smaller bins in zenith angle are shown in Fig. 13.19 in the appendix.

the spectral index $\Delta\alpha \sim +0.05$ is expected for sources at an intermediate distance $d \sim 1^\circ$ to the edge. When estimating the impact of this change on the spectrum-averaged exposure (and hence, on the upper limits) by looking at Fig. 8.17, one can see that the impact of the energy dependence of the angular resolution is negligible (e.g. $\Delta\tilde{\mathcal{E}}_{\text{diff}} \lesssim +2\%$).

8.5.3. Uncertainty of the photon significance

While for the calculation of upper limits the expected amount of background was assumed to be zero (introducing only a negligible amount of conservatism), the sensitivity of the analysis to a photon signal which has been expressed through a photon significance in Sec. 8.4 depends on the diffuse background rate β_{diff} (Eq. 7.15). This background rate been estimated using the observed number of eleven photon candidate events found among the diffuse flux of cosmic rays in [RJ19] (see Eq. 7.25). To give an impression of the impact of the statistical uncertainty of β_{diff} on the photon significances given in Eqs. 8.33 and 8.34, the statistical uncertainty of β_{diff} has been translated into uncertainties on CL_{crit} in the two time windows as

$$\text{CL}_{\text{crit}}(1000 \text{ s}) \cong 4.90_{-0.07}^{+0.04} \sigma \quad (8.35)$$

$$\text{CL}_{\text{crit}}(1 \text{ d}) \cong 3.50_{-0.09}^{+0.09} \sigma. \quad (8.36)$$

Among the eleven photon candidate events found in [RJ19] may possibly be a contribution of an actual photon signal originating in compact binary mergers

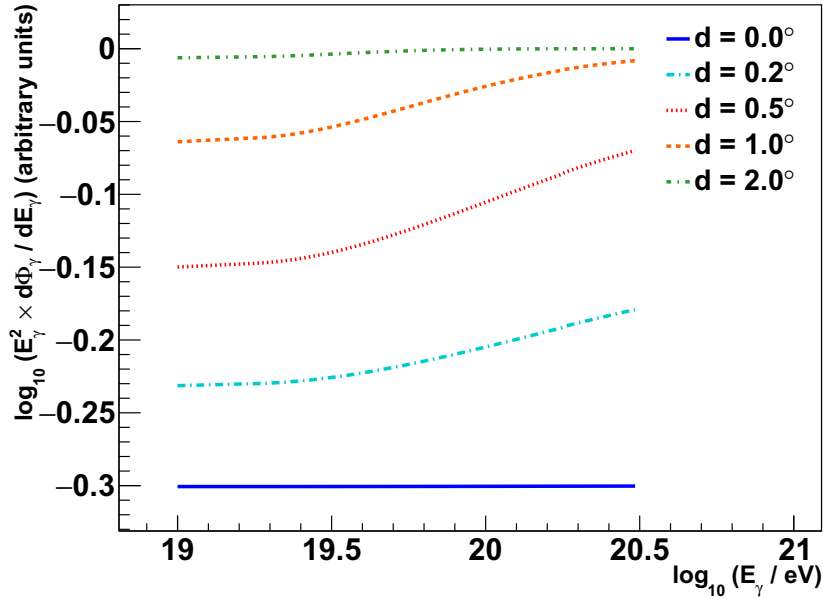


Figure 8.18: The spectrum of photons with reconstructed shower axes inside the search region from a point source with an angular distance d to the edge of that region. The source is assumed to produce a flux of photons between $10^{19.0}$ eV and $10^{20.5}$ eV following a spectral distribution $\frac{d\Phi_\gamma^{\text{GW}}}{dE_\gamma} \propto E_\gamma^{-2}$ at the earth. Due to the energy dependence of the angular resolution of the SD, the spectrum of photons with reconstructed directions inside the search region (shown here) becomes harder for sources of intermediate distance $d \lesssim 2^\circ$. The relative change of the spectral index is about $\Delta\alpha \sim +0.05$. The absolute reduction of the flux about 50% with decreasing distance d is also visible.

which could so far not be separated from the hadronic background and a possible background contribution from a diffuse UHE photon flux. Thus, β_{diff} may very well overestimate the true background rate. This bias however, cannot be estimated reliably without any significant UHE photon detection. In addition to its statistical uncertainty and a possible overestimation due to an unresolved photon signal, the background rate β_{diff} also inherits the systematical uncertainty of $\tilde{\mathcal{E}}_{\text{diff}}$ in a similar way as discussed in Sec. 8.5.1.

8.5.4. Anisotropic emission

Further sources of uncertainty are introduced when extrapolating the results of the photon flux measurements at earth to the GW sources. In addition to the simplifications made by assuming an effective attenuation length for all photons in the analyzed energy range – which might even not be relevant when considering the possibility of photon-axion conversions –, a possible anisotropic emission of UHE photons in the form of jets could lead to an under-estimation (if the jets point away from the observation axis) or even an over-estimation (if the jets are aligned with the observation axis) of the UHE photon luminosity of the source.

The magnitude of this uncertainty strongly depends on the degree of anisotropy of the emission and could easily reach factors of $10^{\pm 2 \dots 3}$ in the case of strongly collimated jets as they have been observed for the gamma ray emissions of the BNS merger GW170817 [MK18].

8.5.5. Cosmological redshift

Finally, an effect that has also not been quantified so far is the impact of the cosmological redshift z of distant sources which changes the wavelength of a photon according to

$$\lambda = (1 + z)\lambda' \quad (8.37)$$

where λ' is the initial wavelength of the photon at its source and λ is its redshifted wavelength at the earth. Hence, its redshifted energy is

$$E_\gamma = \frac{E'_\gamma}{1 + z} \quad (8.38)$$

with $E'_\gamma = \frac{2\pi\hbar c}{\lambda'}$ being the photon energy at the source (with the reduced Planck constant \hbar and the speed of light in vacuum c). While the cosmological redshift does not change the results for the quantities measured on earth, it has to be considered when extrapolating these results to the sources. The quantity which is not affected by the redshift is the total fluence F (Eq. 8.9) since it represents simply a number of particles that traverse a perpendicular surface. However, after extrapolating F to the total fluence at the source, the energy range for which the result is valid shifts from $[E_0, E_1]$ to $[(1 + z)E_0, (1 + z)E_1]$ due to the expansion of the universe. Hence, tracking this modification through Eqs. 8.7 to 8.11, the results for k_γ , \mathcal{F} and E_{tot} have to be corrected by factor of $(1 + z)$ when extrapolating them to the sources. For relatively close sources like the source of GW170817 with a luminosity distance of 40 Mpc this factor is negligibly small (less than 1%). The constraints on typical sources at intermediate distances (like e.g. the source of GW150914 at a distance of 440 Mpc) experience shifts in the order of $\sim 10\%$ towards higher values while the constraints on the most distant source measured until the end of O2, GW170729 at a distance of 2840 Mpc, are affected by a shift of almost 50%.¹⁶

¹⁶The conversion between luminosity distance and redshift has been done using the functionality of the CRPropa 3 framework [BR16] (Git branch master, commit 9636596).

Improving the GW event selection for future follow-up searches

THE end of the GW data taking period O2 only marks the prelude to an era of multimessenger astronomy with GWs. The third observation run O3 of the LIGO and Virgo detectors started on April 1st 2019 and concluded after an operation period of one year (with a one-month maintenance break during October 2019) on March 31st 2020 with a total number of 56 GW observations. The event rate of O3 has been significantly increased compared to the preceding observation runs due to refined measurement techniques. The KAGRA Collaboration joined in on the GW measurement campaign in February 2020 [AB19b, AB20a]. Hence, new sources are already being identified on a weekly base with further improvements to be expected in the future. An overview of the observation plans until 2026 is shown in Fig. 9.1.

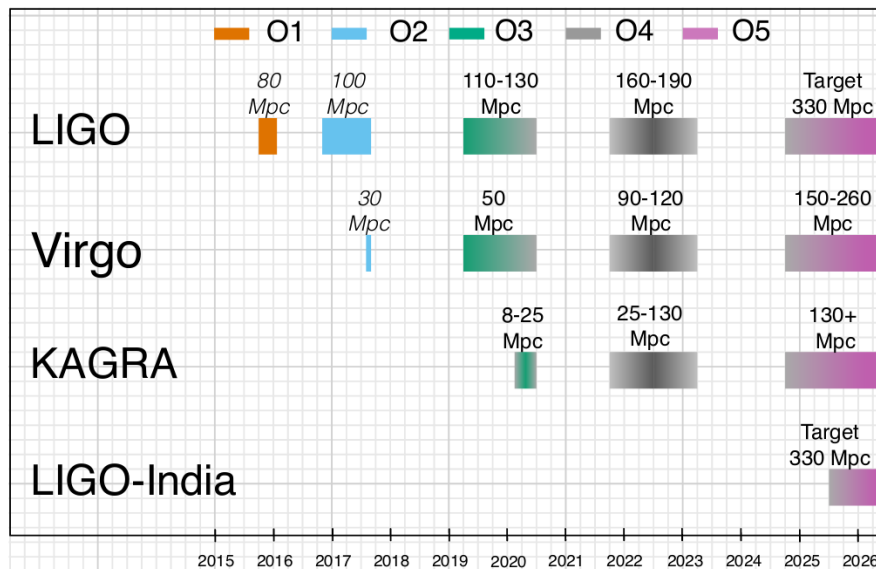


Figure 9.1: The schedule projection of GW observation runs as planned until 2026 [AB20a]. The distances given next to each shaded area are benchmark values for the achieved/expected sensitivities and represent the average distance up to which BNS mergers are expected to be detected.

Now, if more GW events, i.e. from O3 and beyond, are included in a future follow-up analysis with the same photon selection criteria, the background expect-

tation values given in Eqs. 8.30 and 8.31 have to be added on top of the new background gained by unblinding further data in the sky regions of interest. Thus, the significance of a future photon candidate detection will decrease over time as follow-up analyses are being performed after successively more GW events. Likewise, the significance of an already detected photon candidate would decrease over time due to the time dependent penalization that is necessary to account for the look-elsewhere effect (LEE) of an ongoing measurement.

The content of this chapter is the development of a revised analysis procedure that aims to minimize the statistical penalization of its results and yet keep a window open for possible discoveries. First, in Sec. 9.1, the impact of the time dependent penalization factor on the analysis results is discussed in order to motivate the necessity of an event selection strategy for GWs before applying the follow-up analysis. Different options on how to establish a GW event selection and how to minimize the additional penalization introduced by individual GW events are discussed in Sec. 9.3. The most reasonable options are then elaborated in Sec. 9.4 to satisfy the design goals of the follow-up photon search after GW events from the data taking period O3. In the final section, Sec. 9.5, of this chapter, an alternative approach that aims to improve the upper limits on the photon flux from a class of comparable sources as a whole is introduced. It turns out that this so called “stacking method” would however not provide significant improvements in the near future since a certain amount of rather close GW sources of the same source class would be needed which is not given at present time.

9.1. The problem of time dependent penalization

As discussed in Sec. 8.4, a hypothetical photon candidate detection coincident with one of the GW events from O1 or O2 could have been excluded to occur by chance at a confidence level corresponding to a significance of 4.90σ if it had been detected in one of the 1000 s time windows and 3.50σ in one of the 1 d time windows. Using the FC approach for the calculation of confidence intervals at a measured signal (i.e. the detected number of coincident photon candidate events) and an expected background (i.e. the expected amount of coincident photon candidate events that were not induced by primary photons), the significance of a single measured photon candidate event only depends on the expected background. The significance can be defined as the lowest confidence level, at which the lower FC limit is not compatible with zero any more (see also the discussion in Sec. 8.4).

As the probability of a background event to pass the photon candidate cut increases – which may just be due to a larger exposure –, the significance of a photon candidate detection drops. The significance expressed in units of the standard deviation σ as a function of the expected accumulated background is shown in Fig. 9.2. The plotted curve starts at a background of $b_0 = 4.67 \times 10^{-4}$ expected background events in the signal region. This number corresponds to the expected background from all unblinded sky regions of the eleven GW events of O1 and O2 in their respective 1 d time windows. At a background of $10b_0$, the

significance of a photon candidate detection would already be well below 3σ . Of course, the same would be true for a photon candidate that has a high significance at its time of detection but over time suffers under gradual penalization with each further follow-up analysis without a measured signal. The significance of such a photon candidate would also follow the curve shown in Fig. 9.2. This time-dependent penalization factor can be understood as a form of accounting for the LEE that comes with a constantly growing set of trials. Hence, while the sensitivity to a photon signal will inevitably drop over time, a reduction of the average background contribution of each GW event will help to decrease the rate at which the photon significance decreases and therefore to maintain a high sensitivity over a longer period of time.

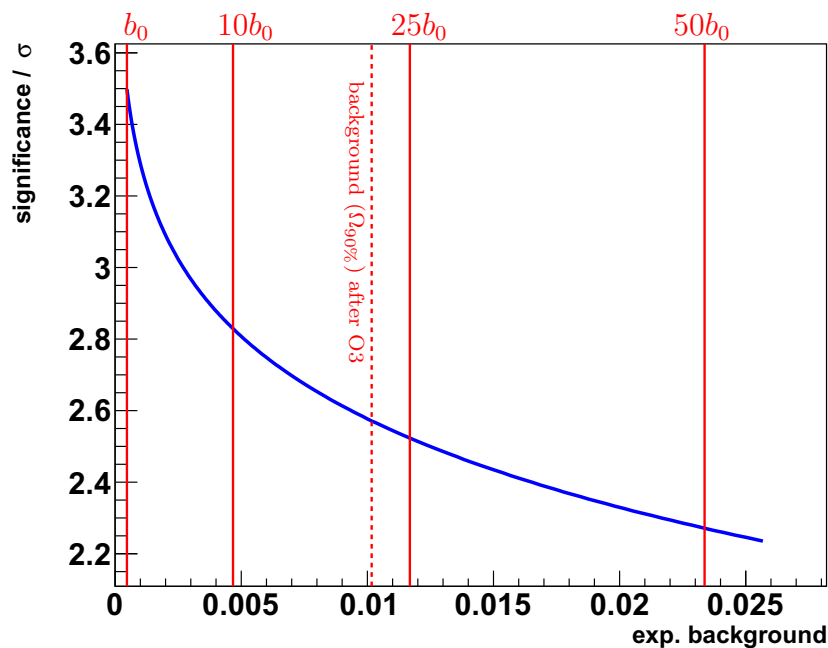


Figure 9.2: The significance of a single photon candidate event as a function of the expected amount of background. The curve has been calculated numerically using the Feldman-Cousins method [FG98] for the derivation of two-sided confidence belts at a given CL. At each value of the expected background, the highest CL, at which the lower limit is not compatible with zero anymore is called the significance of the photon candidate detection. The part of the curve shown here starts at $b_0 = 4.67 \times 10^{-4}$ background events expected from the 90% contour regions of all events from O1 and O2 during the 1 d time windows (vertical line on the very left). Additionally, the positions of (from left to right) $10b_0$, $25b_0$ and $50b_0$ are indicated by the other solid vertical lines. The dotted line illustrates the combined amount of background for O1, O2 and O3 if the follow-up procedure would be continued in the same way as for O1 and O2.

The directions of GW sources are communicated by LIGO and Virgo through probability density distributions over the full sky as described in Sec. 6.3. The 90% contour region, i.e. the solid angle inside the 90% contour of that distribution, was the sky region that has been searched for coincident photon candidate events

for each of the eleven GW events from O1 and O2 in Chapter 8. The size of this region differs heavily between individual events (between $\sim 10 \text{ deg}^2$ and $\sim 10.000 \text{ deg}^2$) and can be used as a measure for the localization quality of the GW source. By estimating the background contributions that would be expected from the respective regions in the sky for each individual GW event, those differences in localization quality are naturally taken into account in the calculation of the penalization of the photon significance. The background contributions b_i differ between different GW events with the quality of the source localization. The values of b_i that would be expected during the 1 d time windows from the 90% contour regions of all GW events until the end of O3 reach from $\sim 1.4 \times 10^{-8}$ to $\sim 1.9 \times 10^{-3}$. The distribution of background contributions is shown in Fig. 9.3 and the corresponding numerical values are additionally compiled in Tab 13.7 in the appendix. Fig. 9.4 gives an impression of the penalization of the photon significance which drops with each GW event that is analyzed for coincident UHE photons (as an example here also only shown for the 1 d time windows). If a candidate event would have been observed in coincidence with the first GW event, GW150914, after unblinding the 90% contour region for 1 sidereal day after the GW event time, the confidence at which a chance coincidence could be excluded would initially have been at a level of 4.1σ . If no other photon candidate events were observed from that moment on, that confidence level would have dropped to 3.50σ at the end of O2. If one would proceed with the follow-up procedure for O3 in the same way as it has been done for O1 and O2, the significance after O3 would already be well below the 3σ mark. In Fig. 9.4 the variation of the impact on the penalization factor between individual events becomes directly visible in the form of the significance drop between single GW events in the chronological order they were detected. Due to the large differences in the quality of localization, the largest part of the overall penalization factor is contributed by only a few of the worst localized events. With the prospects of an ongoing supply of new GW detection in the future rather than having only a limited set of GW events to analyze for coincident UHE photons, it deems reasonable to introduce selection criteria for the GW events before applying further follow-up photon searches. Those selection criteria, should aim to keep the penalization factor as small as possible by, for instance, rejecting badly localized events, while accepting at the same time those events which have the most promising source properties like e.g. sources that are especially close to earth.

9.2. Reevaluation of the photon significance with additional knowledge about the GW sources

The capability of each source class (like BBH or BNS mergers) to produce UHE photons most likely differs between different classes. Thus, one could now ask if different GW source classes may be treated separately when it comes to penalizing the significance of a photon candidate event. However, even if the GWs are produced in a variety of different source classes, the different classes could currently

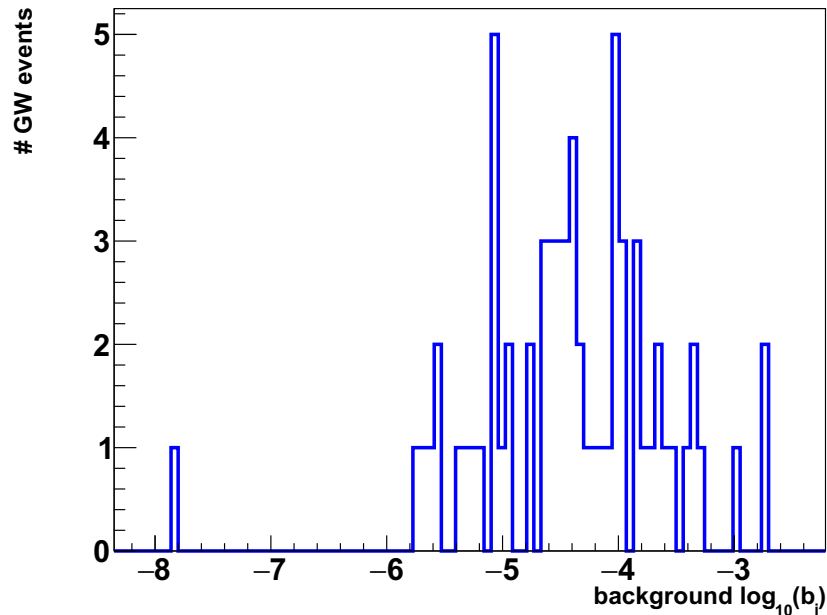


Figure 9.3: The individual background contributions during the 1d time windows from the (convolved) 90% localization regions of all GW events detected during O1, O2 and O3 except for the GW which was detected on February 25th 2020, GraceDB ID S200225q, since its 90% localization region has no overlap with the field of view. The numerical values shown in this plot are compiled in Tab. 13.7

not be treated independently when it comes to compensation for the LEE since the follow-up analysis itself is applied to all GW events equally not distinguishing between possibly different source types. Thus, the interpretation of a photon candidate event from a BNS merger could not be different from one that came in coincidence with a BBH merger or a black hole-neutron star (BHNS) merger. In order to treat the penalization factor differently for different source types, additional knowledge about the capability of a source to produce UHE photons would be necessary. In that case the analysis procedure could be fine-tuned accordingly to take into account the source characteristics that are already known (like possibly the energy spectrum or the time dependence of the luminosity). Depending on the amount and quality of the additional information, it might then be possible to decouple the results for each source class. It can be argued in a similar way, that in the case that a possible future GW event will be found to have a source that is somehow unique or differs from other GW sources such that measurements of their UHE photon emissions cannot directly be compared, the significance of a photon candidate detection would not have to be penalized. The prerequisite for such an interpretation, however, would be an independent measurement of a different source property that would lead to the conclusion of the source being unique among the other GW sources like, for instance, the measurement of an electromagnetic counterpart as in the case of GW170817. However, for most GW sources such additional knowledge is currently not available.

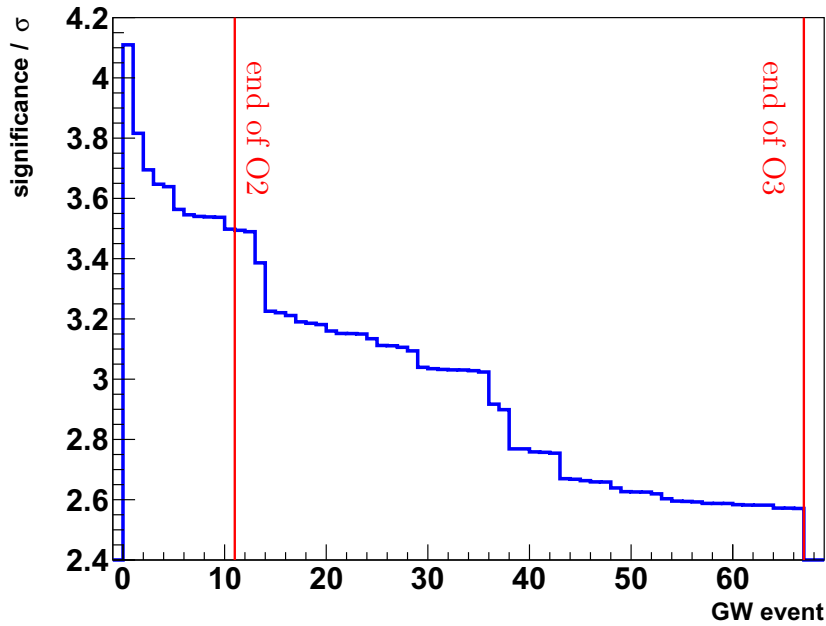


Figure 9.4: The significance of a single photon candidate detection during the 1 d time window as it drops with each GW event for the data of the Pierre Auger Observatory is unblinded in the process of the follow-up analysis. The GW events on the abscissa are ordered chronologically. One may keep in mind that due to the non-linear behavior of the significance with the background (Fig. 9.2), a comparable background contribution causes a more severe drop in significance at an early GW event than at a late event. The vertical lines indicate the end of O2 and O3.

9.3. Options for a GW event selection

A brief summary of possibilities to tune the analysis is given in table Tab. 9.1. The feasibility and the potential gain of tuning any of these options are discussed shortly in the following before the final version of the proposed event selection strategy shall be quantified in the next section.

	analysis tuning options	
1.	photon-hadron separation	
2.	choice of directional search region	✓
	• fixed confidence level	✓
	• fixed probability level	
3.	cut on source localization	✓
4.	cut on background expectation	
5.	cut on source distance	✓
6.	selection by source class	

Table 9.1: List of parameters that can be tuned/selected to reduce the expected background. The options that are tagged with a checkmark are proposed to be adopted in a future application of the analysis for reasons which are outlined in the text.

An obvious strategy to reduce the background expectation while keeping a high photon detection efficiency is improving the photon-hadron separation power of the SD photon analysis itself (item 1). Improvements to the photon-hadron separation however were discussed extensively in [KN17, PP15, PP18b, URL1] and shall not be content of this thesis. Thus, the photon analysis procedure for primary photon energies $E_\gamma > 10 \text{ EeV}$ and zenith angles $30^\circ \leq \theta \leq 60^\circ$ adopted from [RJ19] will be kept for the time being.

Another parameter that can be tuned to reduce the background is the size of the contour that is used as the directional search region (item 2). So far, for each GW, the follow-up search has been applied to the 90% contour of the source localization. As it will be discussed in Sec. 9.4.1, a reduction of the contour size to the 50%-contour instead of 90% seems to be worth the loss in confidence that the actual source is inside the unblinded sky region.

Instead of staying at a fixed CL, one could also think about drawing a contour at a fixed level of probability density. This way, well localized sources might be observed at a higher CL than sources with worse localization. However, defining a selection like this may give rise to pathological cases in which the CL of the source localization is reduced to a very small number. The conclusions from finally observing a photon candidate from a region which, for instance, has only a chance of 1% to contain the true source direction would be very vague. Such a case should be avoided. Another undesirable case when unblinding a contour along a fixed level of probability density comes with very well localized events for which a contour at a very high CL would be unblinded. In such a case, it might occur that the amount of expected background is increased by a large factor compared to the 90% contour, but the gain in confidence that the source is inside the unblinded sky region is, of course, still less than 10%.

In order to keep the significance in the case of a coincident photon candidate detection as high as possible, a cut on the absolute size of the contour (item 3) from which the data of the Pierre Auger Observatory shall be unblinded seems to be necessary since the quality of localization fluctuates heavily between different GW events. Thus, based on the size of the 50%-contour, a reasonable cut on the absolute contour size will be discussed in 9.4.2.

However, the quantity that actually enters the calculation of the expected background is only the overlap region between the contour and the field of view of the SD between 30° and 60° in zenith angle. A poorly localized event which has most parts of its localization contour on the northern hemisphere and only a minor fraction at declination angles below 24° might contribute less background than a GW with better directional resolution but for which the contour region is fully covered by the field of view for most of the observation time. Selecting GW events by the amount of expected background (item 4) might give direct control over the associated penalization factor, but prioritizing events which can barely be seen with Auger over those which are almost certainly within in the field of view would be a rather paradox choice for an event selection criterion. The same argument holds for the difference in exposure between high and low zenith angles since the

exposure is affected both signal events and background events in the signal region in a similar way. Thus, there is no convincing reason why a localization cut should depend on the geometrical orientation of the SD with respect to the GW.

Another source property which is more suited as a selection criterion is the distance of the source to the earth (item 5). Considering extragalactic photon fields, the mean free path of a UHE photons is reduced to a few Mpc. In Sec. 9.4.3, a maximum source distance will be estimated for which the UHE photon production at the GW source still could be constrained when taking into account photon attenuation.

Since BNS mergers are currently thought to be more suitable sites for UHE cosmic ray acceleration [PA16, KS19a, DV19a] than BBH mergers due to the incapability of matter (or electromagnetic radiation) to escape the event horizon, one could think about giving GWs from BNSs priority over GWs from BBHs (item 6). According to the data currently provided by LIGO/Virgo via the GraceDB however, the source class can not always be identified unambiguously which makes a cut on the source type difficult in those cases and even when comparing sources of the same class, there might still be differences depending on the amount of debris in the orbit of the binary system, the orientation of the angular momenta and spins with respect to earth and other parameters. Also, by treating the different source classes equally and unbiased by theory predictions, the follow-up analysis is more open to unknown or unexpected physical processes at the sources which is especially desirable for objects like CBMs about which still little is known at this point. So for now, we refrain from using information about the GW source type to apply an additional event selection, but leave this possibility for a refined search strategy in the future.

9.4. Tuning of the analysis parameters

9.4.1. Choice of directional search area Ω_{CL}

By aiming to cover the true source direction with the search region of the follow-up search at a higher CL one increases the amount of expected background since a higher confidence can only be achieved by increasing the size of the search region. To obtain an impression of how much the contour size of a localization map changes with the CL, on the exemplary case of GW150914 different (un-convolved) contours at the 68%, 90%, 99% and 99.9% levels have been shown in Fig. 8.3. The innermost contour containing the smallest area belongs to the 68% level and the outermost one to the 99.9% level. With the CL also the contour size increases and finally contains the full sky as the confidence reaches 100%.¹⁷ The size of the contour of GW150914 as a function of the CL is shown by the blue curve in Fig. 9.5. This

¹⁷Since the directional probability distributions prior to and after the convolution with directional resolution of the Auger SD share their qualitative features, the analyses within Sec. 9.4.1 have been done using the un-convolved distributions in order to save computation time. The conclusions that are drawn from the results should be valid for both convolved and un-convolved distributions.

curve represents the average profile of the probability density distribution of the GW source localization. From such a localization profile one can directly get an impression of the quality of localization: for increasingly well localized events, the curve approaches the limit of a step function

$$\Omega_{\text{CL, point source}}(\text{CL}) = \begin{cases} 0 & \text{for CL} \in [0, 1) \\ 4\pi (\approx 41253 \text{ deg}^2) & \text{for CL} = 1. \end{cases} \quad (9.1)$$

On the contrary a uniform distribution, i.e. a GW event with no directional information at all, would have a linear localization profile given by

$$\Omega_{\text{CL, uniform dist.}}(\text{CL}) = 4\pi \times \text{CL}. \quad (9.2)$$

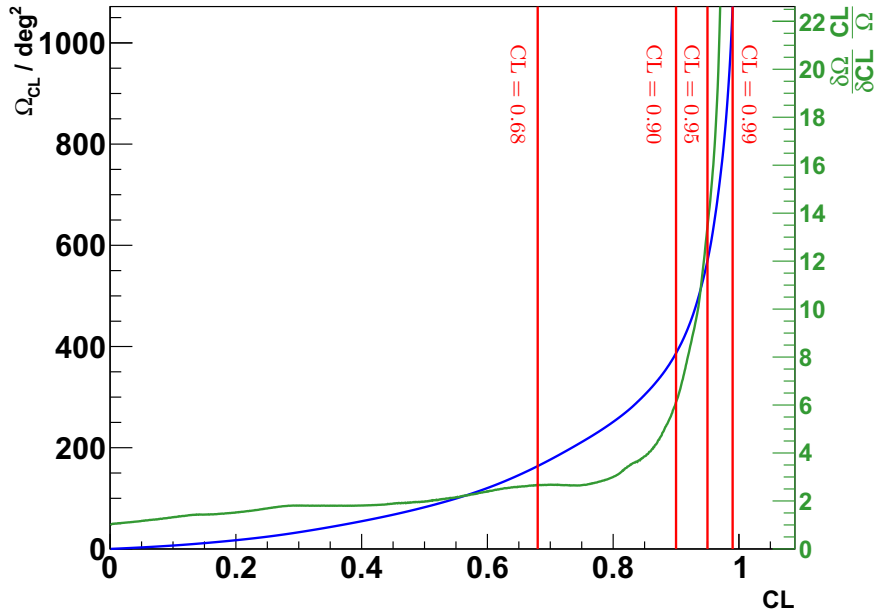


Figure 9.5: The localization profile (blue line, left ordinate) of GW150914 shows the solid angle Ω_{CL} inside the contour as a function of the CL. The green line represents the relative variation of the contour size $\mathcal{D} = \frac{\delta\Omega}{\delta\text{CL}} \frac{\text{CL}}{\Omega}$ (see Eq. 9.3). The vertical lines are placed at CL = 0.68, 0.9, 0.95 and 0.99 in order to highlight the respective points on the graphs.

The localization profile can be used to extract a measure for the relative change of the contour size with a variation of the CL at given value of CL. When comparing the contour size of GW150914 at CL = 68% to the size at CL = 90%, one finds that by increasing the confidence of covering the source direction by $\frac{0.90}{0.68} \approx 1.32$, the size of the contour is increased by more than a factor of 2. With that, also the amount of expected background is increased by approximately the same factor. When comparing the 90% level to the 95% or higher levels, this tradeoff becomes even worse. As a measure for the relative increase in contour size $\frac{\Delta\Omega}{\Omega}$ in proportion

to the relative gain in confidence $\frac{\Delta\text{CL}}{\text{CL}}$ one can define the infinitesimal limit for $\Delta\text{CL} \rightarrow 0$ as

$$\mathcal{D}(\text{CL}) := \lim_{\Delta\text{CL} \rightarrow 0} \left(\frac{\Delta\Omega(\text{CL}, \Delta\text{CL})}{\Omega(\text{CL})} \right) / \left(\frac{\Delta\text{CL}}{\text{CL}} \right) = \frac{\delta\Omega(\text{CL}, \delta\text{CL})}{\delta\text{CL}} \frac{\text{CL}}{\Omega(\text{CL})}. \quad (9.3)$$

\mathcal{D} is the ratio of the relative variation of the contour size $\frac{\delta\Omega}{\Omega}$ as caused by a variation of the confidence level δCL and the relative variation of the confidence level $\frac{\delta\text{CL}}{\text{CL}}$ itself. Using the example of the localization profile $\Omega(\text{CL})$ of GW150914, the graph of $\mathcal{D}(\text{CL})$ is shown by the green curve in Fig. 9.5. The limit $\text{CL} \rightarrow 0 \Rightarrow \mathcal{D}(\text{CL}) \rightarrow 1$ holds for all GW events. This behavior is not a unique feature of the GW events, but inherent to the construction of the contour and the definition of \mathcal{D} . Every value of $\text{CL} > 0$ leads to $\mathcal{D}(\text{CL}) > 1$, which means that the size of the contour is increasing faster than the level of confidence at which the source is inside the contour. But restricting the follow-up search to a region of small Ω_{CL} and hence \mathcal{D} being close to the minimum value of 1 would result in follow-up analyses applied to regions in the sky which in most cases do not contain the GW source. As a compromise between CL and \mathcal{D} , choosing the CL such that $\mathcal{D} \lesssim 2$ is fulfilled seems reasonable. This way, a variation of the CL leads to a relative variation of the contour size that is less than two times the relative variation of the CL.

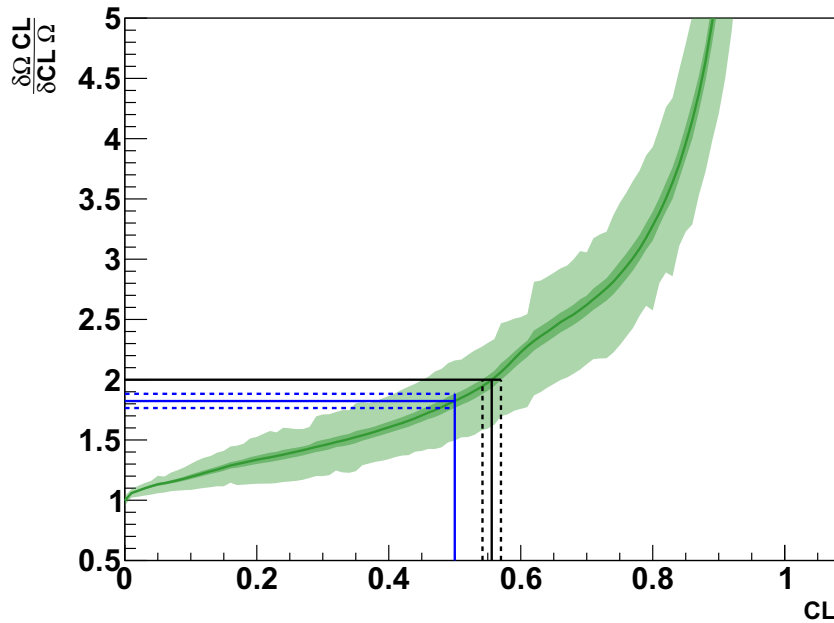


Figure 9.6: The average $\mathcal{D} (= \frac{\delta\Omega}{\delta\text{CL}} \frac{\text{CL}}{\Omega})$ for all GW events from O1, O2 and O3 with the 1σ spread shown by the light green band and the 1σ uncertainty on the mean shown by the darker green band. The vertical black lines indicate the mean value of the CL together with the corresponding error margins that would lead to the desired maximum value of $\mathcal{D}(\text{CL}) = 2$ (horizontal black line). The mean value of \mathcal{D} for the ultimately proposed cut value of $\text{CL} = 0.5$ (vertical blue line) is indicated with its error margin by the horizontal blue lines.

Since the localization profile and hence $\mathcal{D}(\text{CL})$ differs between different GW events, the average $\langle \mathcal{D}(\text{CL}) \rangle$ has been calculated for all GW events from O1, O2 and O3. $\langle \mathcal{D}(\text{CL}) \rangle$ together with the 1σ -standard deviations of the distribution of $\mathcal{D}(\text{CL})$ and of the mean value $\langle \mathcal{D}(\text{CL}) \rangle$ itself are shown in Fig. 9.6. $\langle \mathcal{D} \rangle = 2$ is fulfilled for $\text{CL} = 0.556 \pm 0.014$. By choosing $\text{CL} = 0.5$ for the contour that shall be used for the follow-up analysis, one can achieve that a vast majority of events does not exceed $\mathcal{D} = 2$. At $\text{CL} = 0.5$, the mean value of \mathcal{D} of all GW events is $\langle \mathcal{D}(\text{CL}=0.5) \rangle = 1.823^{+0.060}_{-0.058}$. Restricting the contour from 90% to 50% typically reduces the size of the contour by a factor of 4-5. Averaged over a number of events, this directly translates into a background reduction by the same factor. The tradeoff for this background reduction is that the CL is reduced by 40%. Thus, in one out of two follow-up analyses, the source will not be covered by the search region. However, when analyzing data only from the 50% contour instead of 90%, 4-5 times as many GW events can be analyzed until the same background is reached. This outweighs the loss in CL.

An exception to this strategy is proposed for cases where the GW source localization outperforms the angular resolution of the Auger SD, be it through the detection of an electromagnetic or neutrino counterpart or a precise triangulation of the GW wave front. Such sources which can be considered to be point sources to the SD may be covered at a higher confidence level. A detection of a coincident photon candidate event from such a source would have considerable physics implications due to its high photon significance. Hence, using again the 90% contour instead of the 50% contour in these cases is a reasonable choice that has only negligible contribution to the total accumulated background. This strategy is already applied in Chapter 10 to the analysis of the point source TXS 0506+056.

9.4.2. Cut on source localization $\Omega_{50\%}$

Also with the search area for the follow-up search restricted to the 50%-contour, there are huge differences in the contour sizes of different GW source localization maps. The sizes of the 50%-contours reach from a few deg^2 up to several 1000 deg^2 . To avoid a large background contribution from poorly localized events, a hard cut on the absolute size of the contour should be applied as discussed in Sec. 9.3. The choice of the maximum allowed contour has to be based on the anticipated physics results of the analysis. The physical interpretation of a coincident photon candidate event depends on its photon significance. Hence, a minimum photon significance of a possible coincident photon candidate has to be defined considering only the expected background from that single GW event. Of course, if there are no other criteria by which that respective GW event sticks out of the bulk of GW observations, the LEE-penalized significance will be much lower and will drop further with each follow-up analysis. But since this effect does not depend on an individual GW event, it cannot be accounted for with a proper selection criterion.

The design goal of this analysis shall be that a single photon candidate detected within the convolved 50% contour of the localization map during the 1000s time window should not have a significance less than 5σ . With this benchmark set,

a maximum allowed contour size can be estimated. Using the Feldman-Cousins confidence intervals at 5σ CL, the maximum amount of background that leads to a lower limit larger than zero at a measured signal of one photon candidate is $b_{\text{crit}} = 5.73 \times 10^{-7}$. The size of the solid angle from which that amount of background would be expected within 1000 s depends on the zenith angle θ since

$$b \propto \iint_{\Omega_{50\%}} d\Omega \tilde{\mathcal{E}}(\theta) \quad (9.4)$$

(c.f. Eq. 7.29). Moreover, the effective aperture of the SD array is not exactly constant but typically varies in the order of $\pm 1\%..10\%$. In fact, it infrequently occurs, that the aperture suffers a significant drop as it has been the case during the follow-up time window of GW170823 (see Tab. 13.3) where the aperture was reduced by $\sim 50\%$. These effects cannot be anticipated a priori. To define a fixed maximum contour size for all GW events, an upper bound on the background rate which depends on zenith angle and aperture has to be found. From Fig. 7.7 one can see that the spectrum averaged exposure $\tilde{\mathcal{E}}(\theta)$ has a maximum at $\theta \approx 48^\circ$. Thus, treating all directions inside the contour such as if $\theta = 48^\circ$ (even if the direction is not inside the field of view) gives an upper bound on the amount of expected background. The aperture of the SD array can be estimated conservatively by choosing a large value $A \lesssim 2.4 \times 10^{13} \text{ cm}^2$.

With fixed values for zenith angle and aperture, the critical contour size Ω_{crit} from which a maximum amount of background of b_{crit} can be expected can be estimated by $\Omega_{\text{crit}} \approx 100 \text{ deg}^2$. A search region which is not larger than 100 deg^2 should in any case allow for a photon significance larger than 5σ .

9.4.3. Cut on source distance D_L

Assuming standard model physics, the universe is opaque for UHE photons. The mean free path of photons with energies $E_\gamma > 10^{19} \text{ eV}$ is limited to just a few Mpc [AA16a, HC18a]. As a consequence, from very distant sources one would not expect any photon signal. An additional penalization of the analysis results by unblinding data from those distant sources can easily be avoided by applying an event selection based on the source distance. The decision about the cut distance again depends on the choice of the design goals of the analysis. If the analysis would aim to only follow up on GW events from sources from which a significant fraction of UHE photons could be expected under realistic assumptions and thus strong constraints could be placed on the photon production at the source, one would decide for a fairly strict cut on the distance. However, it is unclear how efficiently UHE photons might be produced by the different sources. This together with the circumstance, that there is currently no other detector that has an exposure to UHE photons comparable to the Auger SD makes it worth looking into the data for every GW source for which some constraint on the energy transferred into UHE photons could possibly be obtained.

To be able to place meaningful upper limits on the fraction of energy that has been transferred into UHE photons, the upper limit on the total amount of energy

in the form of UHE photons has to be less than the total amount of energy radiated by the GW source. Thus, the upper limit on the photon fluence in the case of no photon candidate detection has to be extrapolated to the total photon energy at the source. Assuming UHE photons to be radiated isotropically and to be simply “lost” for the analysis after their first interaction, the upper limit on the total energy in the form of UHE photons $E_{\gamma,\text{source}}^{\text{UL}}$ can be derived from the upper limits on the spectral fluence \mathcal{F}^{UL} as

$$E_{\gamma,\text{source}}^{\text{UL}} = \mathcal{F}^{\text{UL}} 4\pi D_L^2 e^{\frac{D_L}{\lambda_\gamma}} \quad (9.5)$$

with λ_γ being the photon attenuation length and D_L the luminosity distance of the GW source. This formula includes the simplification of an energy independent photon attenuation length and can thus only lead to rough estimates of the magnitude of $E_{\gamma,\text{source}}^{\text{UL}}$. But it is sufficient to obtain optimistically low upper limits by inserting a large value $\lambda_{\gamma,\text{max}} \approx 8 \text{ Mpc}$ for the attenuation length. A different approach to obtain more realistic upper limits on the total energy in the form of UHE photons at the source is discussed in Sec. 9.5.

The total amount of energy radiated by the source types measured by LIGO and Virgo is typically of the order of a few solar masses: for the GW events observed during O1 and O2, the total amount of energy radiated by a single CBM lies between $0.04 M_\odot$ and $6.5 M_\odot$ within the error margins published in [AB19b]. For those events, the maximum source distance at which the energy fraction of UHE photons could be constrained to be less than the total amount of radiated energy is about $d_h \lesssim 10 \lambda_\gamma$. Using the optimistic estimation for the photon attenuation length $\lambda_\gamma = 8 \text{ Mpc}$, one can obtain an estimate for the “photon horizon” $d_h \lesssim 80 \text{ Mpc}$ for a typical GW source. To further account for any possible sources of uncertainty like e.g. uncertainties on the photon attenuation length, the source distance or sources with strongly beamed jets of UHE ejecta,¹⁸ a cut on the GW source distance should be placed at a larger distance. At this point, a cut value of $d_{\text{cut}} = 2d_h$ is proposed which should cover possible further uncertainties or possible upward fluctuations of the signal and make sure that only GW events are excluded from the follow-up analysis which are clearly too far away to obtain any photon signal from them.

9.4.4. Cross-dependent event selection based on source distance and localization

The cuts on the source localization and distance as discussed in the previous sections define a set of GW events that are both close enough to be interesting from a physical point of view and localized well enough so that the follow-up search region is poor of background. Aside from this subset there are other subsets of GW events that might not pass one of the aforementioned criteria but would still be

¹⁸If a source emits UHE photons anisotropically in the form of a beam, the expected photon horizon for that source can be much larger compared to an isotropic emission of the same total amount of energy if the beam points directly towards earth.

interesting enough to analyze them for coincident photon events. One class of potentially interesting events are such with a very close source. If UHE photons were produced by such sources, there would be a high chance to observe them at earth. If no photons are observed, in any case, stringent upper limits on the UHE photon production could be placed. As a compromise between the desired proximity and a reasonable number of GW events that can be expected to pass the additional distance cut, we label the class of “very close events” as the set of events with sources that are closer or as close as the closest GW source measured so far – the source of the BNS merger GW170817, which has a distance of ~ 40 Mpc ($= \frac{d_h}{2}$). For those events with source distances $D_L \leq \frac{d_h}{2}$ the localization cut should be relaxed even if a photon candidate event from such a source had an un-penalized significance of less than 5σ . To nevertheless avoid unblinding arbitrarily large fractions of the sky, an additional relaxed version of the localization cut should be placed such, that the bulk of reasonably well localized GW events still is accepted. Looking at the distribution of solid angles $\Omega_{50\%}$ of the 50% contour regions in Fig. 9.7, such a bulk can indeed be identified below $\Omega_{50\%} = 720 \text{ deg}^2$. the significance of a possible photon candidate from a contour of less than 720 deg^2 had an un-penalized significance that would necessarily still be larger than 4.6σ . The seven GW events with $\Omega_{50\%} > 720 \text{ deg}^2$ have significantly worse localizations and analyzing those events would almost be like performing a blind search. Doing so would have a large impact on the penalization factor and even if a photon candidate would be found in the process it could not be interpreted as a primary photon due to the large background contamination.

Another subset of potentially interesting GW events would be such events which are very well localized. Including such events into the analysis has negligible effect on the penalization factor as the additional amount of expected background would very low and a photon candidate would have a high un-penalized significance ($> 5\sigma$). The definition of a “very well localized” event of course depends on the average quality of localization which might improve over time as the GW detectors evolve and more GW detectors join the search in the future. A compromise between the maximum allowed localization region and a reasonable abundance of accepted GW events can be found when looking at the distribution in Fig. 9.7. Apart from the bulk of poorly localized events on the high-end of the localization scale, another bulk of events with exceptionally good localization can be found at the lower end. Though the final value of the maximum allowed contour size for GWs from distant sources is to some extent an arbitrary choice, at this point a cut at $\Omega_{50\%} < 20 \text{ deg}^2$ is being proposed. Selecting GW events with localization regions smaller than 20 deg^2 has a only a small impact on the penalization factor but measuring a photon candidate event from such a distant but well localized source at a high significance could give a hint towards new physics that might enable photons to propagate through a universe that should be opaque to them according to the physical standard models.

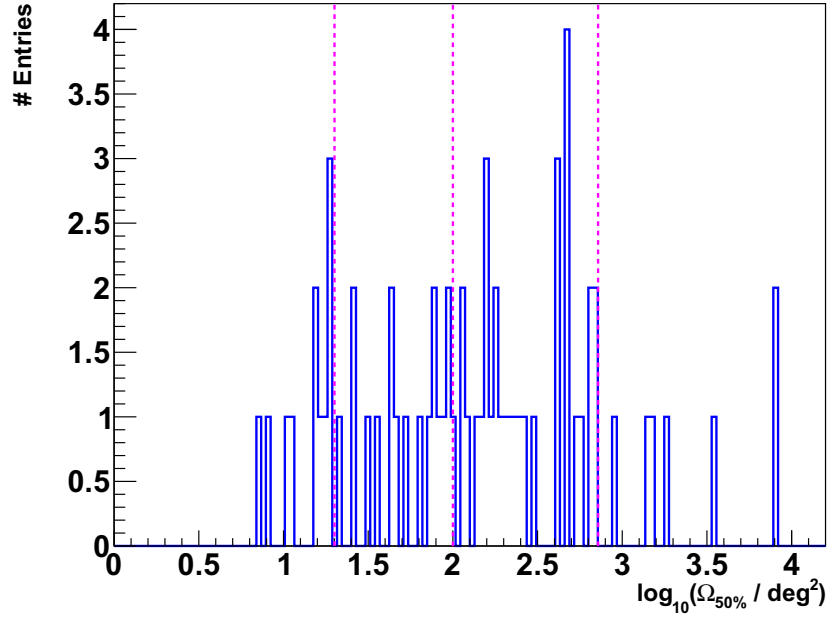


Figure 9.7: The distribution of solid angles $\Omega_{50\%}$ of the 50% contours for all GW events observed during O3 (in log-scale). The vertical lines indicate the proposed cut values at 20 deg^2 , 100 deg^2 and 720 deg^2 which serve as upper bounds on the localization quality for the three different sets of GW events characterized by their respective source distance as discussed in the text.

9.4.5. Summary of proposed selection criteria

A strategy on how to proceed with the follow-up UHE photon search after GW events observed until the end of O3 has been elaborated. Compared to the follow-up search analysis of O1 and O2 presented in Sec. 8, the solid angle of the search region should be restricted to the 50% CL region instead of 90%. This leads to a more favorable relation between confidence in source coverage and background expectation as discussed in Sec. 9.4.1. In Sec. 9.4.2 to 9.4.4, possible event selection criteria for GW events were discussed. Such an event selection is necessary to reduce the expected amount of hadronic background in the photon signal region which is mainly contributed by the large search regions of poorly localized GW events. For a follow-up analysis of O3, three classes of accepted GW events are proposed: events with a mean source luminosity distance $D_L < 160 \text{ Mpc}$ and at the same time a localization of $\Omega_{50\%} < 100 \text{ deg}^2$ (class 1), events with a very close source of $D_L < 40 \text{ Mpc}$ and a localization of $\Omega_{50\%} < 720 \text{ deg}^2$ (class 2) and all events with a good localization of $\Omega_{50\%} < 20 \text{ deg}^2$ (class 3). The accepted regions in the space of D_L and $\Omega_{50\%}$ are illustrated in Fig. 9.8 by the shaded area and logically summarized in Tab. 9.2. Out of all GW events of run O3, nine events pass the selection criterion for class 3. From run O1 and O2, two additional events pass the class 3 criterion from which one event, the BNS merger GW170817, by definition also passes the criterion of class 2 and, hence, also of class 1. So far, no GW event exclusively belongs to class 1 or class 2.

$(D_L < 160 \text{ Mpc} \quad \text{and} \quad \Omega_{50\%} < 100 \text{ deg}^2)$ “class 1” or $(D_L < 40 \text{ Mpc} \quad \text{and} \quad \Omega_{50\%} < 720 \text{ deg}^2)$ “class 2” or $(D_L < \infty \quad \text{and} \quad \Omega_{50\%} < 20 \text{ deg}^2)$ “class 3”

Table 9.2: The logical concatenation of the GW event selection criteria as they are proposed for a follow-up UHE photon search analysis of GW data from O3. A visualization of the accepted regions in the space of source luminosity distance D_L and solid angle of the search region $\Omega_{50\%}$ is shown in Fig. 9.8.

The proposed event selection has been optimized for the GW events measured until the end of O3. Depending on how dramatically the quality of the GW data changes with future observation runs, the event selection strategy might have to be adjusted to select only the best localized events in order to maintain a high significance in the case of a coincident UHE photon detection. Depending on future rates of GW detections and maybe also on the results of future multimessenger follow-up searches, one could still consider to place different cuts on different GW source types at a later step. This, however, would require knowledge about the source types of all GW events and, thus, a strategy on how to deal with events with ambiguous or unclear source classification.

9.5. Constraining GW sources with the stacking method

When follow-up analyses are performed after multiple GW events of the same source class (like all BBH mergers or all BNS mergers), a non-observation of coincident photon candidate events from any of the analyzed sources may be used to improve the constraints to that respective source class as a whole as it has been done for the follow-up neutrino search with Auger [SM19].

Any non-observation of photon candidate events from a single GW source within a time window always leads to an upper limit of $N_\gamma^{\text{UL}} \simeq 2.44$ on the number of expected photon candidate events in that respective time window. This limit can be converted into an upper limit on the total energy in UHE photons from that GW source (c.f. Eq. 9.5). If such a limit can be placed for more than one GW event, the limits can be statistically combined to obtain an upper limit that is even lower than each of the individual limits. To do so, the distance of each GW source and the exposure to UHE photons from that source have to be taken into account as weighting factors for the individual upper limits. Such a combined limit would thus hold for the average GW source out of the respective source class.

Assuming that UHE photons are produced by the GW source (distance D_L , right ascension α , declination δ , observed at a zenith angle $\theta_{\text{GW}}(\alpha, \delta, t)$ from the

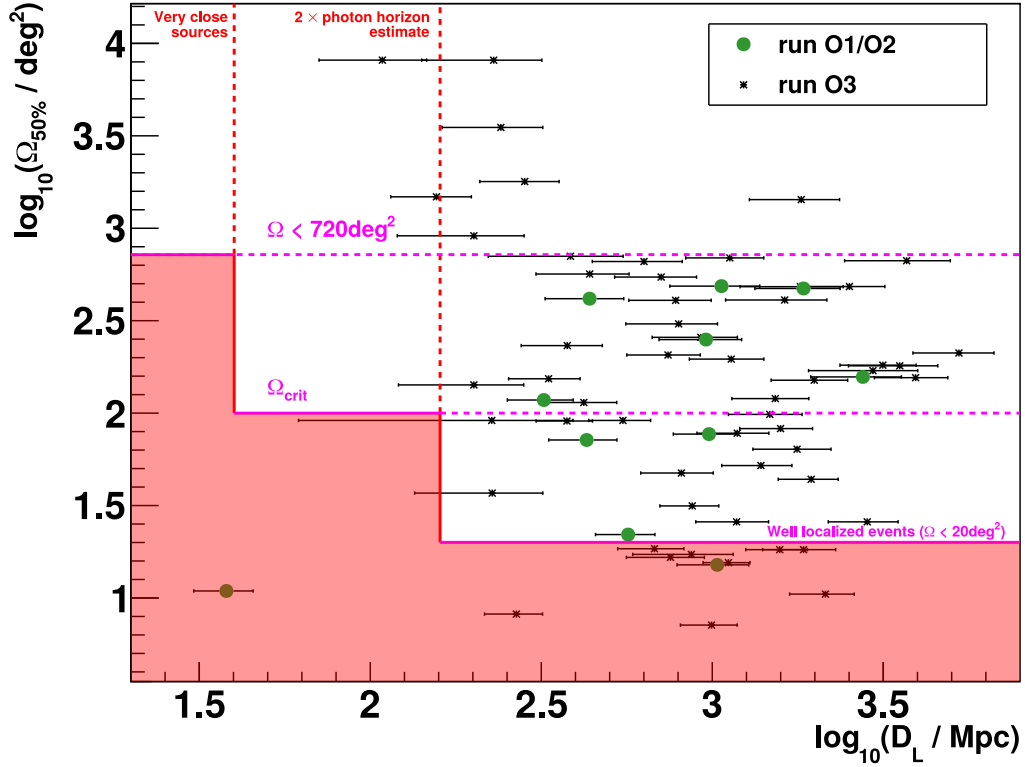


Figure 9.8: The distribution of all GW events from O1 and O2 (green markers) and O3 (black markers) in the space of source distance D_L and (convolved) localization $\Omega_{50\%}$ (both in log-scale). The shaded area indicates the GW event acceptance region as proposed in this thesis. This figure only shows 66 out of a total number of 67 GW events. The event that is not shown in the plot (GraceDB Event ID: S200114f, detected on 2020-01-14T02:08:18 UTC) has a localization of $\Omega_{50\%} \approx 42 \text{ deg}^2$ but no information on the source distance has yet been made publicly available.

perspective of the Pierre Auger Observatory) with an energy spectrum following a power law $\propto E_\gamma^{\beta_s}$, the number of expected photon candidate events in the energy range $E_0 \leq E < E_1$ from that source can be expressed by

$$N_\gamma = \int_{E_0}^{E_1} dE_\gamma L_\gamma E_\gamma^{\beta_s} \frac{p_{\gamma\text{-cut}} \mathcal{E}(E_\gamma, \theta_{\text{GW}}(\alpha, \delta, \Delta t), \Delta t)}{4\pi D_L^2 \exp(D_L/\lambda_\gamma(E_\gamma))}. \quad (9.6)$$

This formula is derived by solving Eq. 8.2 for N_γ and replacing the flux normalization factor k_γ of the UHE photon flux at earth with the time-averaged *UHE photon luminosity* L_γ of the source. The additional factors in the denominator account for the geometrical attenuation of the photon flux due to the source distance and the attenuation of photons due to interactions with the background photon fields on their way from the source to the earth. The attenuation length λ_γ of UHE photons in general depends on the photon energy and can therefore not be separated from the energy dependent exposure \mathcal{E} in the energy integral like in [SM19]. L_γ

is defined such that the expected total number of UHE photons initiated by the source is given by

$$N_\gamma^{init} = \int_{E_0}^{E_1} \int_{t_0}^{t_1} dE_\gamma dt L_\gamma E_\gamma^{\beta_s}. \quad (9.7)$$

To obtain a result that does not depend on the source direction, the uncertainty in the source localization can be taken into account by averaging N_γ over all directions inside the 50%-contour with the underlying probability density distribution $P(\alpha, \delta)$ of the source localization as a weighting function:

$$N_\gamma = \iint_{\Omega_{50\%}} \int_{E_0}^{E_1} d\Omega dE_\gamma L_\gamma E_\gamma^{\beta_s} P(\alpha, \delta) \frac{p_{\gamma\text{-cut}} \mathcal{E}(E_\gamma, \theta_{\text{GW}}(\alpha, \delta, \Delta t), \Delta t)}{4\pi D_L^2 \exp(D_L/\lambda_\gamma(E_\gamma))}. \quad (9.8)$$

The fact that the normalization $\iint_{\Omega_{50\%}} d\Omega P(\alpha, \delta) = 0.5$ reduces the number of expected photon candidate events to 50% compared to Eq. 9.6 accounts for the lack of knowledge about the true source direction being inside the analyzed sky region or not. Hence, this is a Bayesian probability multiplied with a frequentist expectation value N_γ and as such has no clear interpretation for a single GW source. Only if multiple GW sources are analyzed, each source contributes an expected number of photon candidate events given by Eq. 9.8 which can be stacked resulting in a total amount of expected photon candidate events from all GW sources combined:

$$N_{\gamma,tot} = \sum_s \iint_{\Omega_{50\%}} \int_{E_0}^{E_1} d\Omega dE_\gamma L_\gamma E_\gamma^{\beta_s} P_s(\alpha_s, \delta_s) \frac{p_{\gamma\text{-cut}} \mathcal{E}(E_\gamma, \theta_{\text{GW}}(\alpha_s, \delta_s, \Delta t), \Delta t)}{4\pi D_{L,s}^2 \exp(D_{L,s}/\lambda_\gamma(E_\gamma))}. \quad (9.9)$$

Note that an additional index s has been introduced for each quantity that is explicitly a characteristic of an individual source. If no photon candidate events are measured with any of the GW events added to the sum in Eq. 9.9, an upper limit of $N_{\gamma,tot}^{\text{UL}} = 2.44$ at 90% CL can be used to replace the left side of the equation. Since the average luminosity L_γ is constant by assumption, an upper limit L_γ^{UL} can be found by solving Eq. 9.9 for the luminosity

$$L_\gamma^{\text{UL}} = N_{\gamma,tot}^{\text{UL}} \left(\sum_s \int_{E_0}^{E_1} dE_\gamma E_\gamma^{\beta_s} \frac{p_{\gamma\text{-cut}} \iint_{\Omega_{50\%}} d\Omega P_s(\alpha_s, \delta_s) \mathcal{E}(E_\gamma, \theta_{\text{GW}}(\alpha_s, \delta_s, \Delta t), \Delta t)}{4\pi D_{L,s}^2 \exp(D_{L,s}/\lambda_\gamma(E_\gamma))} \right)^{-1}. \quad (9.10)$$

Eq. 9.10 may be compared to the corresponding formula¹⁹ for the UHE neutrino luminosity given in [SM19].

¹⁹The formulas slightly differ by the fact that in [SM19] the neutrino luminosity is derived as a function of time passed since the merger event, while here a time-averaged luminosity is derived.

This formula can further be improved by introducing an additional integral over the source distance D_L to account for the large uncertainties associated to the source distances of many GW events (c.f. Fig. 9.8):

$$L_\gamma^{\text{UL}} = N_{\gamma, \text{tot}}^{\text{UL}} \left(\sum_s \iint_{\Omega_{50\%}} \int_0^\infty \int_{E_0}^{E_1} d\Omega dD_L dE_\gamma E_\gamma^{\beta_s} \hat{P}(\alpha_s, \delta_s, D_L) \frac{p_{\gamma\text{-cut}} \mathcal{E}(E_\gamma, \theta_{\text{GW}}, \Delta t)}{4\pi D_L^2 \exp(D_L/\lambda_\gamma(E_\gamma))} \right)^{-1} \quad (9.11)$$

where $\hat{P}(\alpha_s, \delta_s, D_L)$ is the volumetric probability distribution of possible source localizations. Information on $\hat{P}(\alpha_s, \delta_s, D_L)$ for all source directions (α_s, δ_s) is communicated by the LIGO/Virgo Collaborations via the publicly available FITS files through a median distance $\mu(D_L)$ and a standard deviation $\sigma(D_L)$ for each direction. The ansatz distribution is claimed to follow a distance-weighted normal distribution with $P_s(\alpha_s, \delta_s)$ as a normalization factor [SL16a, SL16b]:

$$\hat{P}(\alpha_s, \delta_s, D_L) = \frac{D_L^2}{\sigma(D_L)\sqrt{2\pi}} P_s(\alpha_s, \delta_s) \exp\left(-\frac{D_L - \mu(D_L)}{2\sigma(D_L)}\right)^2. \quad (9.12)$$

Since sources at large distances are strongly suppressed by geometry and photon attenuation, taking into account the uncertainties on the source distance for each GW event might provide limits to the luminosity that are both more accurate as well as significantly lower compared to the limits obtained with Eq. 9.10.

To finally obtain a limit on the total energy E_γ^{UL} in the form of UHE photons at the source emitted during the observation time window Δt , the spectrum at the source has to be integrated over the respective energy range and time window

$$E_\gamma^{\text{UL}} = \int_{E_0}^{E_1} \int_{t_0}^{t_1} dE_\gamma dt \left(L_\gamma^{\text{UL}} E_\gamma^{\beta_s} \right) E_\gamma \quad (9.13)$$

$$\stackrel{\beta_s = -2}{=} \Delta t \ln\left(\frac{E_1}{E_0}\right) L_\gamma^{\text{UL}}. \quad (9.14)$$

From a technical point of view, this stacking method could in principle already be applied to the set of BBH mergers from O1, O2 and O3 with a localization of $< 20 \text{ deg}^2$ (see Fig. 9.8). However, only the neutron star merger of GW170817 was close enough to actually constrain the source luminosity. The other GW events inside the acceptance region are – even within their error margins – so far away that they would effectively only contribute zeros to the sums in Eqs. 9.10 to 9.11. Thus, unless more GW sources within the estimated photon horizon are observed in future observation runs, an application of the stacking method to data will not provide any significant improvements to the results.

A search for UHE photons from the blazar TXS 0506+056

*W*HILE the focus of this thesis are the sources of GWs, the methods developed within can be applied in a straightforward way to search for UHE photons from other transient astrophysical objects. Here, the application to the blazar TXS 0506+056 is described.

In 1986, the astronomical object TXS 0506+056 has been discovered as a radio source by the Arecibo radio telescope [LC83, AD02] and included in the Texas survey of radio sources (TXS) [DJ96] hence its most commonly used name. The source of the radio signal was later confirmed to be a high energy gamma ray blazar of BL LAC type at a redshift of $z = 0.3365 \pm 0.0010$ [PP18a, PS18]. In 2018, the blazar TXS 0506+056 has been suggested to be the source of the high-energy neutrino event IceCube-170922A, which has been measured with the IceCube detector on UTC 2017-09-22T20:54:30.43 with a reconstructed energy of ~ 290 TeV (between 183 TeV and 4.3 PeV at 90% confidence level) [AM18a]. The hypothesis of that event being by chance coincident with the direction of the blazar could be rejected a 3σ level. Moreover, this neutrino event was coincident with a period of enhanced gamma ray activity as reported by the Fermi-LAT [TY17] and MAGIC [MR17] Collaborations. A posterior analysis of IceCube data revealed a 3.5σ -evidence for further neutrino emissions from the direction of TXS 0506+056 between September 2014 and March 2015 [AM18b]. With those observations, the blazar might be the first extragalactic source of high energy neutrinos to be identified [PP18a].

Implications from multi-wavelength observations together with the newly obtained multimessenger measurements gave rise to a re-discussion of the physics at the source of TXS 0506+056. Difficulties to describe the two phases of enhanced high energy neutrino production with conventional models [WW19] might imply that TXS 0506+056 is actually an atypical blazar involving a highly curved jet or a binary black hole system with two colliding jets [BS19a, BS19b]. If one of these rare scenarios is true for TXS 0506+056, it might be a type of source that is unique within our presently accessible universe from an observational point of view.

Following up on the IceCube observations, the Pierre Auger Observatory has searched the sky region of TXS 0506+056 for coincident UHE neutrino and photon candidates [SM19, AA20a]. The results of the follow-up neutrino search are briefly summarized in the following in Sec. 10.1. The follow-up photon search is presented

as a part of this thesis in Sec. 10.2 to 10.3.

10.1. UHE neutrinos from the blazar TXS 0506+056

A search for neutrinos from the direction of TXS 0506+056 with the Pierre Auger Observatory during the two time windows of enhanced neutrino activity (i.e. 2014-10-19 to 2015-02-06 and 2017-03-22 to 2017-09-22) revealed no neutrino candidate event in the neutrino energy range covered by Auger. Extrapolations of the neutrino flux measured by IceCube to the Auger energy range showed that very hard neutrino spectra with spectral index larger than -1.5 are disfavored by the Auger measurements [SM19, AA20a].

A comparison of the neutrino flux that would produce an expectation value of one neutrino candidate event at the Auger SD between October 19th 2014 and February 6th 2015 to the neutrino and photon fluxes measured by IceCube and Fermi-LAT at lower energies is shown in Fig. 10.1.

10.2. Photon search analysis

It should be kept in mind that due to large red shift of $z \approx 0.34$ (corresponding to a luminosity distance of $D_L \approx 1.8$ Gpc) of the blazar and the limited mean free path $\lambda_\gamma \lesssim 7$ Mpc [AA16a] of UHE photons in the extragalactic medium, the detection of an UHE photon produced close to the blazar is not expected in classical photon propagation scenarios. However, due to the well known localization of TXS 0506+056, a correlating UHE photon signal would have a high significance and could help probing exotic models like e.g. the UHE axion hypothesis as proposed in [FM11].

To discriminate photon-induced air shower events from the bulk of hadronic background events, the analysis procedure described in Sec. 7 has been used. The field of view for this analysis is limited to zenith angles $30^\circ \leq \theta \leq 60^\circ$ and the energy range is $10^{19.0} \text{ eV} \leq E_\gamma < 10^{20.5} \text{ eV}$. The technical application of the analysis to search for photons from a transient astrophysical source is done analogously to the GW follow-up searches discussed in Sec. 8.

As the search region around the location of TXS 0506+056, which is at right ascension $05^{\text{h}} 09^{\text{m}} 25.96^{\text{s}}$ and declination $+5.69314^\circ$, a circle with angular radius of $\Delta\psi = 1.8^\circ$ has been chosen, which leads to a search region of the size $\Omega = 2\pi(1 - \cos(\Delta\psi)) \approx 10.2 \text{ deg}^2$. The radius has been chosen such that 90% of all primary photons from the direction of TXS 0506+056 would be expected to have reconstructed shower axes within the analyzed sky region (c.f. Fig. 7.5). Note that in contrast to the GW follow-up searches discussed previously, the confidence level $\text{CL} = 90\%$ in this case does not reflect the confidence of the source being inside the analyzed sky region but the confidence of correctly assigning the arrival direction of a primary photon to a point source.

The two time windows for the photon search are – in coherence with the time windows used in the neutrino search – from UTC 2014-10-19T19:12:29.99 un-

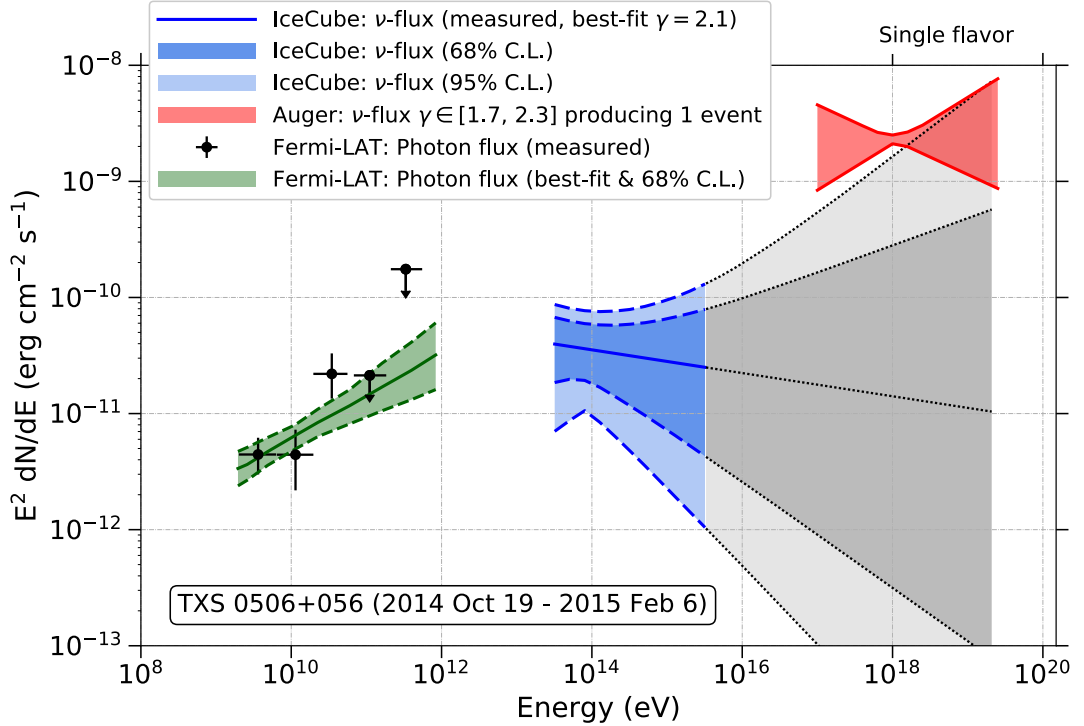


Figure 10.1: The neutrino flux from TXS 0506+056 above 0.1 EeV (red band) that would lead to an expected number of one neutrino candidate event at the Pierre Auger Observatory assuming a constant emission during the 110 d observation period between October 19th 2014 and February 6th 2015 [AA20a]. The flux is compared to the gamma ray and neutrino fluxes measured by Fermi-LAT (green band) and IceCube (blue band). The red shaded region indicates the range of uncertainty from varying the spectral index between $\gamma(= -\alpha) = 1.7$ and $\gamma = 2.3$. The range of uncertainty for the IceCube measurement includes variations of the spectral index between $\gamma \approx 1.75$ and $\gamma \approx 2.45$ for the 68% CL band and between $\gamma \approx 1.5$ and $\gamma \approx 2.7$ for the 95% CL band.

til UTC 2015-02-06T12:00:00.00 and from UTC 2017-03-22T09:01:53.60 to UTC 2017-09-22T20:54:30.43. The time windows are chosen such that they correspond to multiples of a full sidereal day, which are 110 sidereal days for the earlier and 185 sidereal days for the later time window.

10.3. Results

No coincident photon candidate events were found in any of the two time windows. Thus, upper limits on the expected number of photons $N_\gamma \leq 2.44$ were placed at 90% CL in both time windows using the Feldman-Cousins method [FG98].

For the earlier time window (starting in 2014) the spectrum-averaged exposure to UHE photons from the source direction of TXS 0506+056 has been derived to be $\tilde{\mathcal{E}} = 1.87 \times 10^{19} \text{ cm}^2 \text{ s}$. Estimating the background rate from the eleven photon candidate events found in the all-sky search for a diffuse photon flux (c.f.

Eqs. 7.15 and 7.25), the expected amount of background events passing the photon candidate cut is 9.98×10^{-5} . With the assumption of a photon energy spectrum $\frac{d\Phi_\gamma}{dE_\gamma} \propto E_\gamma^{-2}$ at earth, and the upper limit on the number of photon candidate events, the flux normalization factor (cf. Eq. 8.2) can be constrained to be $k_\gamma \leq 2.70 \times 10^{-6} \text{ MeV cm}^{-2} \text{ s}^{-1}$ ($= 4.3 \times 10^{-12} \text{ erg cm}^{-2} \text{ s}^{-1}$) at 90% CL. For better comparison to the fluxes shown in Fig. 10.1, this limit translates into an UHE photon flux that would lead to an expectation value of one photon candidate event at the Auger SD of $1.8 \times 10^{-12} \text{ erg cm}^{-2} \text{ s}^{-1}$. Extrapolating that flux to the whole period of 110 sidereal days, upper limits on the spectral fluence (c.f. Eq. 8.8) of UHE photons from TXS 0506+056 can be placed as $\mathcal{F} \leq 88.3 \text{ MeV cm}^{-2}$.

The event with the reconstructed arrival direction closest to TXS 0506+056 had an angular distance of 2.1° to the blazar. The p -value for a primary photon in the analyzed energy and zenith region to have a reconstructed shower axis that deviates more than 2.1° from its true value is 0.059. If the event would have been initiated by a primary photon, an association of that event to TXS 0506+056 would be unlikely but could not be completely ruled out by its directional reconstruction alone. Taking a closer look at that event, reveals a value of the photon-discriminating principal component of $\text{PC} = -2.02$. Since 61.3% of all air shower events in the analyzed zenith and energy region have a larger (i.e. more photon-like) PC value while less than 0.1% of a set of simulated photon showers have a PC value that is lower, an interpretation of that event as a primary photon is strongly disfavored.

For the later time window of 2017, the spectrum-averaged exposure to UHE photons from TXS 0506+056 was $\tilde{\mathcal{E}} = 3.26 \times 10^{19} \text{ cm}^2 \text{ s}$ with an expected background of 17.9×10^{-5} . The flux normalization factor could be constrained to $k_\gamma \leq 1.54 \times 10^{-6} \text{ MeV cm}^{-2} \text{ s}^{-1}$ ($= 2.5 \times 10^{-12} \text{ erg cm}^{-2} \text{ s}^{-1}$) at 90% CL. The corresponding flux that would lead to one photon candidate event at the Auger SD is $1.0 \times 10^{-12} \text{ erg cm}^{-2} \text{ s}^{-1}$. The difference of that limit compared to the earlier time window is mainly caused by the longer search period. This effect largely cancels out when placing upper limits on the spectral fluence for the whole period $\mathcal{F} \leq 84.9 \text{ MeV cm}^{-2}$.

The event which was closest to the direction of TXS 0506+056 during the 2017 search period had an angular distance of 3.0° to the latter. With that distance an association of this event to TXS 0506+056 is unlikely with a p -value of 0.014. Also its interpretation as a primary photon is disfavored due to the low PC value of -1.81 . Out of all air shower events in the analyzed data 48% of the events have a PC value that is larger and only $\sim 0.1\%$ of the set of simulated photon showers have a lower PC value.

Lowering the energy threshold of the SD photon search

BETWEEN the highest energy gamma rays observed during the follow-up observations of the BNS merger GW170817 and the photon energy threshold of the Auger SD exists an energy gap that spans over several orders of magnitude. Moreover, theoretical predictions on the maximum energy up to which BNS mergers could be able to accelerate cosmic rays give an upper bound to subsequent GZK photon energies in the order of a few EeV. To test these predictions, an extension of the energy range of the follow-up photon search analysis towards lower energies is needed. Since the analysis used so far is restricted to energies above 10 EeV and cannot easily be extended to lower energies due to the drop in photon detection efficiency below 10 EeV, an alternative analysis method shall be investigated here. The idea of that analysis is to make use of the detailed information about the shower front that is provided by the PMT time traces of the SD stations rather than considering just an integrated value like the total signal or quantiles of the time traces like in the risetime parameter Δ . For that purpose, a new air shower observable named R_{MoPS} has been developed and is studied here using air shower simulations. A technical description of R_{MoPS} as well as some first analyses on its photon-hadron separation power, its photon detection efficiency and its systematical properties are presented in the following. This chapter shall pose an addition to the analysis and the results presented in this work so far and is meant to be a first stepping stone for future efforts to extend the search for UHE photons from transient sources.

11.1. Definition of R_{MoPS}

In mid 2013, two additional trigger types were implemented in the station firmware of the Pierre Auger surface detector (SD), namely the Multiplicity of Positive Steps (MoPS) and the Time over Threshold deconvolved (ToTd). The new trigger types were designed to lower the trigger threshold and increase the sensitivity to the electromagnetic component of air showers [BP09, BP11]. The muonic component of hadron-induced air showers is typically larger than that of photon-induced air showers, which are almost purely electromagnetic. Therefore, the algorithms behind the new triggers were examined for their ability to actually discriminate between electromagnetic and muonic particles aiming to find a photon discrimi-

nating observable based on the shapes of the signal time traces of the PMTs within the SD stations. As a result of this study, the ratio

$$R_{\text{MoPS}} := \frac{M_v}{T} \quad (11.1)$$

has been found to have a significantly lower mean value for sets of simulated photon showers than for simulated proton showers²⁰ of the same energy (see Fig. 11.2). Here, M_v is the number of *MoPS-veto counts* (Sec. 11.1.1) and T is the number of *ToTd counts* (Sec. 11.1.2). In [BP11], the MoPS veto has been introduced to reject fluctuations in the exponential tails of large signals that can be caused by through-going muons. M_v is thus expected to be larger for events which are rich of muons. T is designed to serve as an estimator of the raw number of particles inside an SD station independent of the particle type [BP09]. This is achieved by a transformation of the signal time trace which maps the smeared signal corresponding to a single particle onto a single sharp peak by applying a deconvolution to the trace. Hence, R_{MoPS} is designed to be an indicator for the ratio of muonic and electromagnetic shower components on the ground level and is expected to be larger for air showers that have hadronic primary particles.

11.1.1. MoPS-veto counts

The MoPS-veto counts M_v are derived from the raw FADC traces which are obtained from the HG channel of the PMTs. Each FADC time bin ($\hat{=} 25$ ns) which is rejected by the MoPS veto increases M_v by 1. The considered time window begins 246 time bins before and ends 521 time bins after the latch trigger bin. Thus, in total 768 time bins are taken into account to derive the MoPS-veto counts.

The MoPS veto is activated after a series of consecutive positive steps in the trace when the height of the cumulated step is larger than or equal to 16 FADC counts (c.f. Fig. 11.1(a)). In this case, a certain number of bins is excluded from contributing to the MoPS trigger. The number N_r of rejected bins depends on the height of the cumulated step h :

$$\begin{aligned} 16 \leq h < 31 &\rightarrow N_r = 2 \\ 32 \leq h < 63 &\rightarrow N_r = 3 \\ 64 \leq h < 127 &\rightarrow N_r = 4 \\ 128 \leq h < 255 &\rightarrow N_r = 5 \\ 256 \leq h < 511 &\rightarrow N_r = 6 \\ 512 \leq h \leq 1000 &\rightarrow N_r = 7 \end{aligned} \quad (11.2)$$

²⁰Since protons are the lightest hadronic candidates for UHE cosmic ray primaries, they are expected to produce the lowest fraction of muons compared to electromagnetic particles in air shower events, thus being the most “photon-like” cosmic ray particles. Since recent results indicate a heavier composition at the highest energies [AA17d] a comparison to a simulated set of pure protons provides the most conservative benchmark for the capability of an analysis to identify photon showers.

while 1000 is the maximum value of the FADC. From all three PMTs in an SD station, the second highest number of bins that are rejected by the MoPS veto is the contribution of that station to M_v . M_v is the sum of these values from all triggered SD stations.

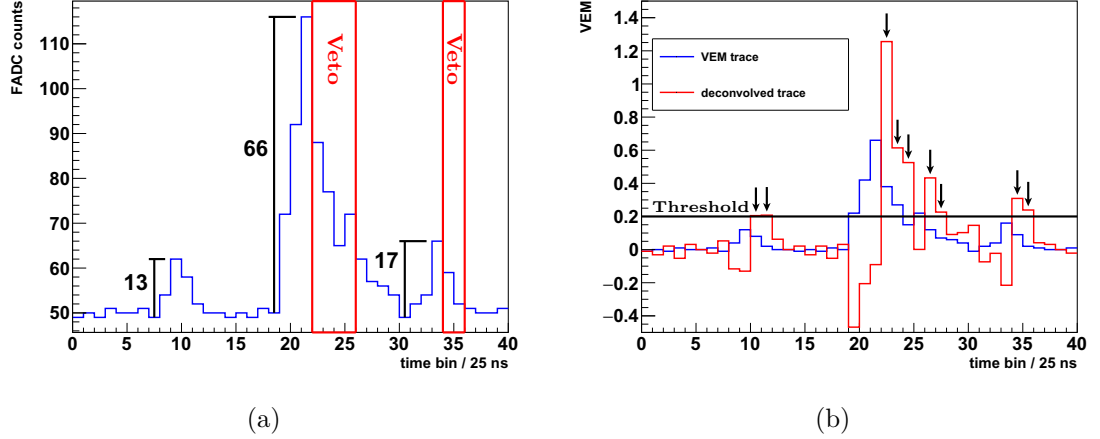


Figure 11.1: (a) A schematic example of an FADC trace to illustrate the algorithm used to derive the contribution to M_v of a single SD station. The contribution in this part of the trace are $N_r = 4$ rejected bins after a series of three consecutive positive steps with a cumulated height of 66 FADC counts plus another $N_r = 2$ rejected bins after a step height of 17 (see Eq. 11.2). (b) An exemplary VEM trace (blue line) and its deconvolution (red line) according to the ToTd algorithm. Every bin in the devonvolved trace above the black threshold line at 0.2 VEM (indicated by the black arrows) adds to the ToTd counts. This part of the trace would add 9 ToTd counts to the total value of T .

11.1.2. ToTd counts

The ToTd counts T are derived from the calibrated VEM traces. In the first step, a deconvolution [BP09] of the VEM trace is applied:

$$d_i = \frac{a_i - f a_{i+1}}{1 - f}, \quad \text{with } f = \exp\left(-\frac{25 \text{ ns}}{\tau_{\text{PMT}}}\right), \quad (11.3)$$

where a_i is the i -th bin of the original VEM trace, d_i is the i -th bin of the deconvolved trace (see Fig. 11.1(b)) and τ_{PMT} is the signal decay time constant of the respective PMT.²¹ Then, a threshold value $th = 0.2$ VEM is applied. Every bin in the deconvolved trace above th adds to T . As for M_v , the second highest values from all three PMTs in each station are summed up over all stations in the event.

Both M_v and T are strongly correlated with the total signal deposited in the SD stations and hence, correlated with the energy and the mass of the primary particle.

²¹For simulated PMTs, which are identically implemented in the `Offline` software framework and do not undergo any aging effects that could change the signal decay time, τ_{PMT} is set to a fixed value of 65 ns. Hence, $f \approx 0.68$ for simulated events. This value also corresponds to the decay time that is implemented in the SD station firmware for the ToTd trigger algorithm.

However, when taking the ratio of the two quantities, it turns out that most of their energy dependence cancels out while conversely, the primary particle type affects M_v and T differently. As a consequence, the resulting observable R_{MoPS} shows only a small energy dependence, but a significant amount of separation power between primary photons and protons. Therefore, dedicated sets of air shower simulations have been produced with photons (set B_γ) and protons (set B_p) as primary particles (for detailed information about the simulation sets see Sec. 6.1.2 and Sec. 6.2). The distributions of R_{MoPS} for both primary particle types at $10^{18.4}$ eV are shown in Fig. 11.2. The corresponding distributions for higher energies up to $10^{19.0}$ eV can be found in the appendix in Figs. 13.20 and 13.21.

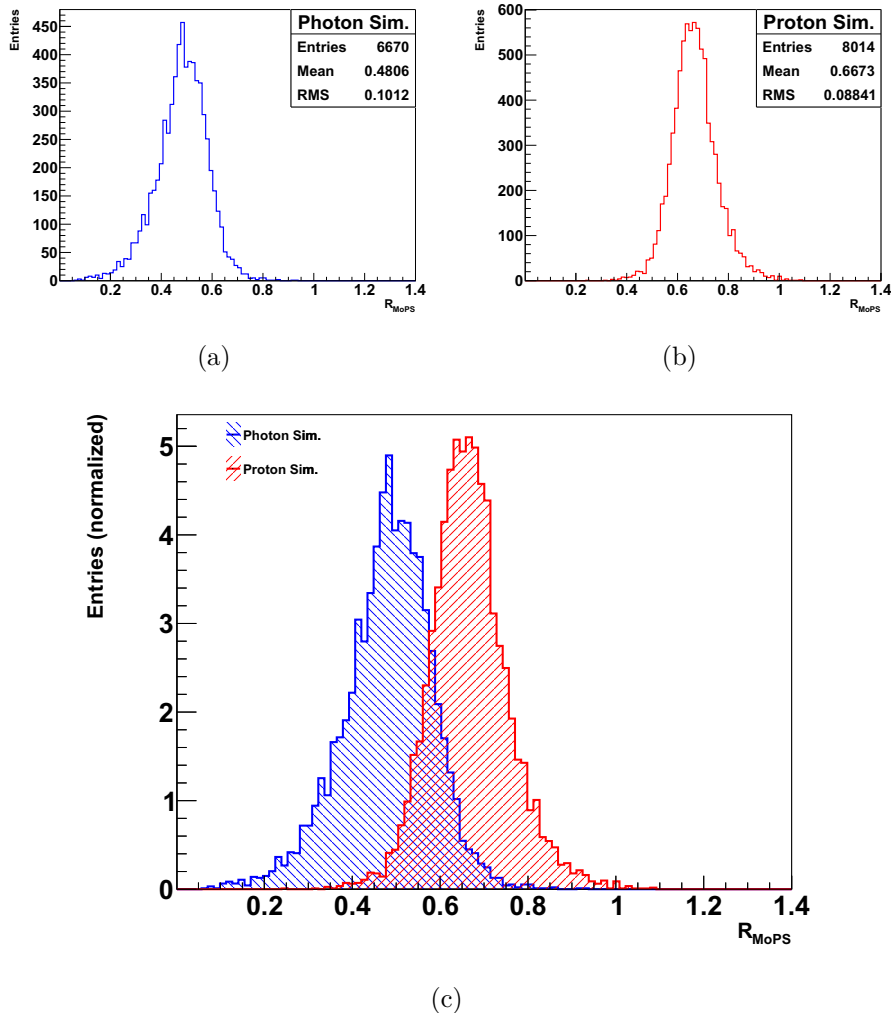


Figure 11.2: The distributions of R_{MoPS} from (a) a set of simulated photon events (simulation set B_γ) and (b) a set of simulated proton events (simulation set B_p) at $10^{18.4}$ eV. In (c) the normalized overlay of both distributions is shown. The distributions of R_{MoPS} for higher energies up to $10^{19.0}$ eV are shown in Figs. 13.20 and 13.21 in the appendix.

11.2. R_{MoPS} event selection

Technically, the only requirement for the calculation of R_{MoPS} is at least a single triggered SD station. For an application to the task of studying transient sources with the SD, further event selection cuts are necessary. Since R_{MoPS} is not completely independent of the primary particle energy, a photon search analysis can only be applied to events that have successfully reconstructed photon energy estimators. Though the photon energy estimator E_γ described in Sec 7.1 has been derived for photon showers between $10^{19.0}$ eV and $10^{20.5}$ eV and only for those events which have a reconstructed LDF, it has been found that an extrapolation down to $10^{18.4}$ eV and to events that do not necessarily have a reconstructed LDF does only introduce an average bias of $\sim -17\%$ towards lower energies in all energy bins. This bias is still smaller than the typical shower-to-shower fluctuations of the photon energy. Hence, for the purpose of studying the energy-dependent properties of the observable R_{MoPS} , E_γ is nevertheless a sufficient energy estimator. As for the analysis of Chapter 7, the reconstruction of E_γ imposes an event selection criterion on the data set that has previously been discussed in Sec. 7.2 and labeled as “ E_γ -flag.” Furthermore, as the analysis is designed for the purpose of directional studies, a minimum number of three triggered SD stations is required for the reconstruction of the shower axis. Also, a 6T5 quality trigger is required to ensure a consistent detector geometry for all events and to avoid a bias on E_γ at events with shower cores outside the SD array. For consistency with previous analyses the zenith angle range has been restricted to $\theta < 60^\circ$. An additional quality cut on zenith angles below 30° as applied to the analysis of Chapter 7 has been omitted in a first approach for the purpose of studying R_{MoPS} in all of the available phase space.

The only necessary requirement for the reconstruction of R_{MoPS} itself is that the denominator T has to be larger than zero. Also, when M_ν is zero, R_{MoPS} becomes zero independently of the value of T which effectively leads to a loss of information. Events with $T = 0$ or $M_\nu = 0$ are therefore excluded from the analysis. The selection criterion imposed by those conditions on R_{MoPS} shall from here on be labeled “ R_{MoPS} -flag” and events which pass that criterion are labeled with R_{MoPS} -flag = 1. However, a dedicated analysis [SD20] has shown that the number of events which have an R_{MoPS} -flag = 0 is negligibly small (less than 0.1%) at photon energies above $10^{18.5}$ eV. The impact on the photon detection efficiency of these event selection cuts in the four energy bins is shown in Fig. 11.3. Another restriction which had to be taken due to technical reasons is that only the traces from the high-gain channel (HG) (connected to the dynode of the PMT) could be used for a consistent reconstruction of R_{MoPS} . Since the baseline fluctuations of the low-gain channel (LG) (connected to the PMT anode) are larger than in the HG channel, they lead to artificially high values of T (see Fig. 11.4). Also the value of M_ν reconstructed from the LG can not directly be compared to the one reconstructed from the HG since there is an amplification factor in between. The latter issue could be handled by reconstructing M_ν from the VEM traces. The baseline fluctuations of the VEM traces derived from the LG are only an issue

for T , not for M_V since they are not large enough to activate the MoPS veto. To handle the reconstruction of T from the LG traces one would need an algorithm which efficiently identifies the beginning and the end point of the signal trace in order to avoid as much interference with the fluctuating baseline as possible. For a first study of R_{MoPS} in this thesis, the reconstruction of the observable has been restricted to stations with unsaturated HG channels.

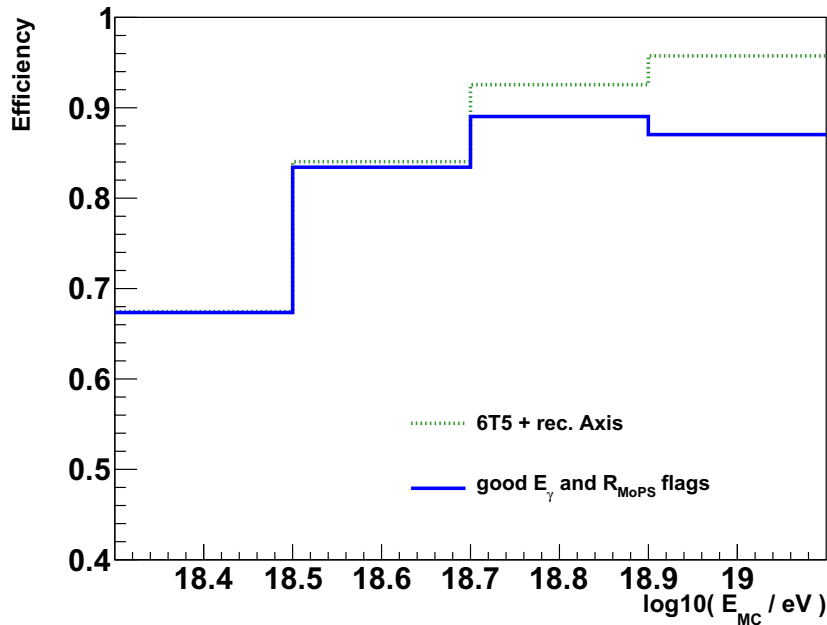


Figure 11.3: The photon selection efficiency evaluated at fixed energies $E_{\text{MC}} = 10^{18.4} \text{ eV}$, $10^{18.6} \text{ eV}$, $10^{18.8} \text{ eV}$ and $10^{19.0} \text{ eV}$ and zenith angles $\theta < 60^\circ$ (simulation set B_γ). The green dotted line shows the efficiency after application of the 6T5 criterion and the requirement of a successfully reconstructed shower axis. The final efficiency is depicted by the blue line after additionally applying the cuts on the E_γ - and R_{MoPS} -flags. The latter is not shown separately since the fraction of events that are labeled with a bad R_{MoPS} -flag are of the order of $\lesssim 0.1\%$.

11.3. Performance of R_{MoPS}

In order to quantify the separation power of R_{MoPS} an appropriate measure is needed. The final step of a fully developed photon search analysis would be the application to data with a discriminating photon candidate cut in the space of the finalized air shower observable to separate the signal region from the background. In the case of the analysis described in Chapter 7, this photon candidate cut has been placed at the median of the photon distribution. The fraction of background ρ_{50} that is rejected by a cut at the median of the photon R_{MoPS} distribution, i.e. at a signal efficiency of 50%, is thus a convenient measure for the separation power of the observable. The full graph of the ROC for the separation between photon and proton simulations at $10^{18.4} \text{ eV}$ is shown in Fig. 11.5. Highlighted is the cut

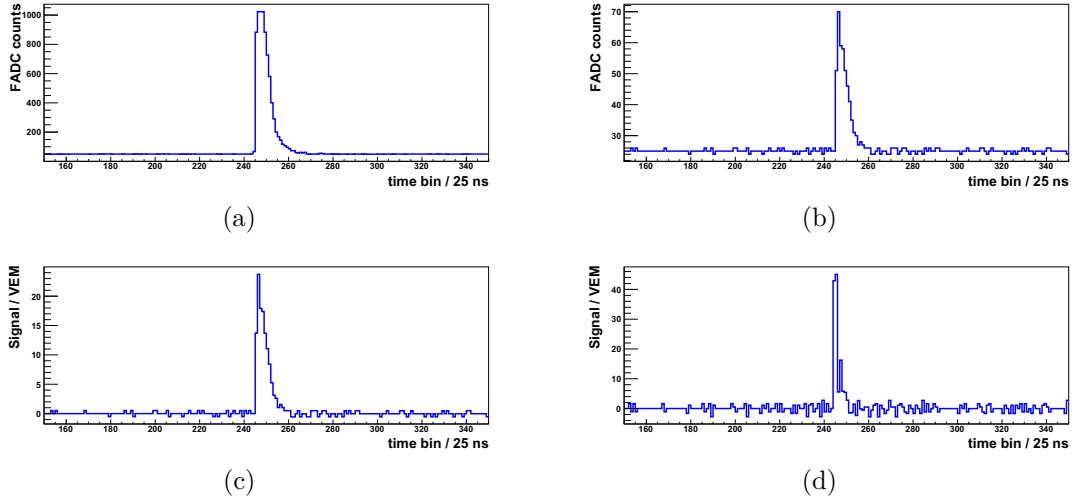


Figure 11.4: (a) An example of a saturated HG trace in which the signal in the highest bins exceeds the maximum value of 1000 FADC counts. (b) The corresponding LG trace of the same PMT. The amplitude of baseline fluctuations is comparable to the one in the HG trace but the fluctuations relative to the peak value of the signal are larger. (c) The calibrated VEM trace in this example is reconstructed from the LG channel since the HG channel is saturated. (d) The deconvolved VEM trace. The baseline fluctuations are further amplified by the deconvolution algorithm (Eq. 11.3) so that many fluctuating bins exceed the threshold of 0.2 VEM and hence contribute artificial counts to T .

value at the signal median which leads to a background rejection of

$$\rho_{50}(R_{\text{MoPS}})|_{E_{\text{MC}}=10^{18.4} \text{ eV}} = 98.4\%. \quad (11.4)$$

Another measure for the separation power is the merit factor η (see Eq. 7.6). For the two distributions from Fig. 11.2, the merit factor evaluates to $\eta = 1.39$.

However, since R_{MoPS} has a small remnant dependency on the primary particle energy, a comparison between primary photons and protons at the same MC energy leads to a separation power that could not be achieved in a data application without knowledge of the true energy. Therefore, the set of photon showers at $E_{\text{MC}} = 10^{18.4} \text{ eV}$ has also been compared to a set of protons showers at $E_{\text{MC}} = 10^{18.0} \text{ eV}$ since both sets have mean reconstructed photon energies of $\langle E_\gamma \rangle \approx 10^{18.3} \text{ eV}$.²² The resulting background rejection is

$$\rho_{50}(R_{\text{MoPS}})|_{\langle E_\gamma \rangle \approx 10^{18.3} \text{ eV}} = 92.8\% \quad (\eta(R_{\text{MoPS}}) = 1.05) \quad (11.5)$$

and the ROC curve is shown in Fig. 11.6. At higher simulated energies the separation between the photon and proton distributions increases. At a simulated

²²It turns out that the mean values of reconstructed photon energies E_γ of proton-induced air showers simulated between $10^{18.0} \text{ eV}$ and $10^{18.6} \text{ eV}$ are comparable to the mean values of E_γ of photon-induced air showers simulated at energies that are about a factor of $10^{0.4}$ higher. The width of the E_γ distributions at fixed MC energies are typically about 10% larger for primary protons than for photons of comparable E_γ .

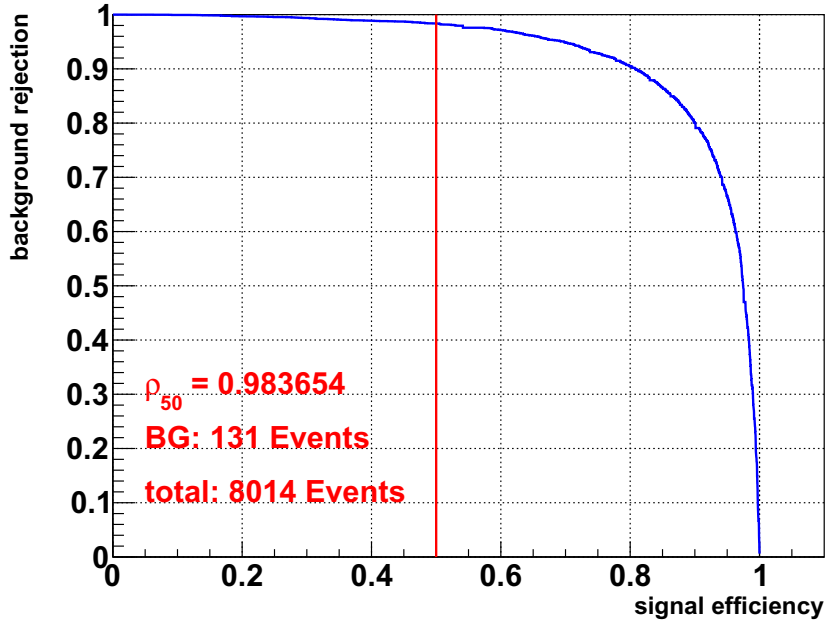


Figure 11.5: The background rejection as a function of the signal efficiency for the distributions of R_{MoPS} shown in Fig. 11.2. Both, the signal (photons) and the background (protons) are simulated at $10^{18.4}$ eV.

photon energy of $10^{19.0}$ eV, the rejection of a background of protons at $10^{18.6}$ eV (corresponding to a comparable reconstructed photon energy $\langle E_\gamma \rangle \approx 10^{18.9}$ eV) is

$$\rho_{50}(R_{\text{MoPS}})|_{\langle E_\gamma \rangle \approx 10^{18.9} \text{ eV}} = 97.2\% \quad (\eta(R_{\text{MoPS}}) = 1.31). \quad (11.6)$$

The ROC curves for all four energy bins together with the corresponding R_{MoPS} distributions can be found in the appendix in Figs. 13.22 and 13.23. The results are compiled in Tab. 11.1.

$\log(E_{\text{MC}}/\text{eV})$	N_γ	N_p	μ_γ	μ_p	σ_γ	σ_p	ρ_{50}	η
18.4	6670	4551	0.481	0.635	0.1012	0.1072	0.928	1.05
18.6	8173	7450	0.500	0.649	0.0897	0.0976	0.934	1.12
18.8	8593	8014	0.521	0.667	0.0799	0.0884	0.960	1.23
19.0	8136	7650	0.540	0.679	0.0738	0.0765	0.972	1.31

Table 11.1: The statistics for the distributions shown in Figs. 13.22 and 13.23 in the appendix: the simulated energy E_{MC} of the photon set, the sample size N , the mean value μ , the RMS deviation σ , the background rejection at 50% signal efficiency ρ_{50} and the merit factor η . The proton sets to which the photon distributions are compared to have simulated energies that are by a factor of $10^{-0.4}$ lower which leads to comparable photon energies E_γ .

While the separation power of R_{MoPS} cannot directly be compared to the separation power of the air shower observables $g\Delta$ and gL_{LDF} analyzed in Sec. 7.3 due

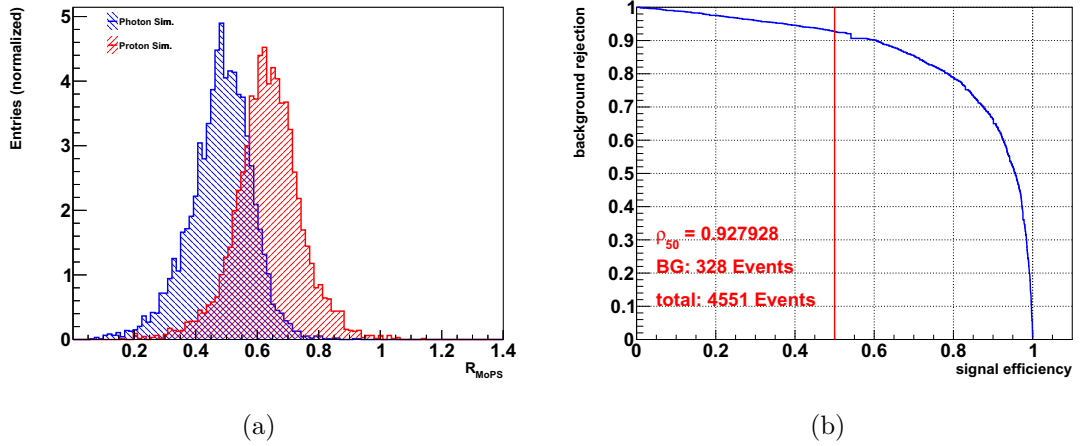


Figure 11.6: (a) The R_{MoPS} distributions and (b) the corresponding ROC curve for the signal (photons) simulated at $10^{18.4}$ eV and the background (protons) simulated at $10^{18.0}$ eV. The energies are chosen such that the two sets have comparable median photon energies which are $E_\gamma = 10^{18.319 \pm 0.002}$ eV for the set of photons and $E_\gamma = 10^{18.290 \pm 0.002}$ eV for the proton set.

to the different energy range and the comparison to data instead of proton simulations, a comparison to the observables X_{max} and S_b used in [AA17a] to search for a diffuse flux of UHE photons with the Auger hybrid detector is done here instead. In [NM15], the separation power of X_{max} between simulated photons and protons has been found to be between

$$\rho_{50}(X_{\text{max}})|_{E_{\text{MC}}=10^{18.4\dots 18.5} \text{ eV}} = 94.42\% \quad (\eta(X_{\text{max}}) = 1.45) \quad (11.7)$$

and

$$\rho_{50}(X_{\text{max}})|_{E_{\text{MC}}=10^{18.9\dots 19.0} \text{ eV}} = 97.87\% \quad (\eta(X_{\text{max}}) = 1.89). \quad (11.8)$$

The separation power of S_b has also been analyzed in [NM15] and (including the revised event selection used in [AA17a]) in [RP16]. The separation power in the corresponding energy bins has been found to reach from

$$\rho_{50}(S_b)|_{E_{\text{MC}}=10^{18.4\dots 18.5} \text{ eV}} = 97.77\% \quad (\eta(S_b) = 1.13) \quad (11.9)$$

to

$$\rho_{50}(S_b)|_{E_{\text{MC}}=10^{18.9\dots 19.0} \text{ eV}} = 99.66\% \quad (\eta(S_b) = 1.78). \quad (11.10)$$

Though, an observable like R_{MoPS} which is derived from SD data alone is not expected to rival the separation power of hybrid observables like X_{max} or S_b , one has to keep in mind that these benchmark values do not account for the energy dependence of the observables. In [AA17a], this dependence is considered in a later step during the combination of the observables in a multivariate analysis (MVA) which is possible in an analysis that uses the hybrid detector since the energy of

the primary particle is directly accessible through the calorimetric measurement of the FD.

Though, in principle R_{MoPS} can be derived for most air showers with $\theta < 60^\circ$ and $E_{\text{MC}} > 10^{18.4}$ eV, a restriction of the zenith angle or energy range might nevertheless be needed to reach the desired sensitivity to a possible photon signal in data. To test the zenith angle dependence of the photon-proton separation power of R_{MoPS} , the simulation sets have been separated into three zenith angle bins $0^\circ \leq \theta < 30^\circ$, $30^\circ \leq \theta < 45^\circ$ and $45^\circ \leq \theta < 60^\circ$. For each zenith angle bin, the background rejection ρ_{50} is plotted as a function of the energy at which the photon set has been simulated (see Fig. 11.7). The background events in each bin are composed of protons at energies of $10^{-0.4}$ times the energy of the photons in order to have comparable reconstructed photon energies E_γ . The best separation power is achieved in the bin with the highest zenith angles. For zenith angles below 45° there seems to be trend towards better separation power with increasing energy and zenith angle. Above 45° , there is no obvious trend and the separation power seems to remain at a more constant level with increasing energy.

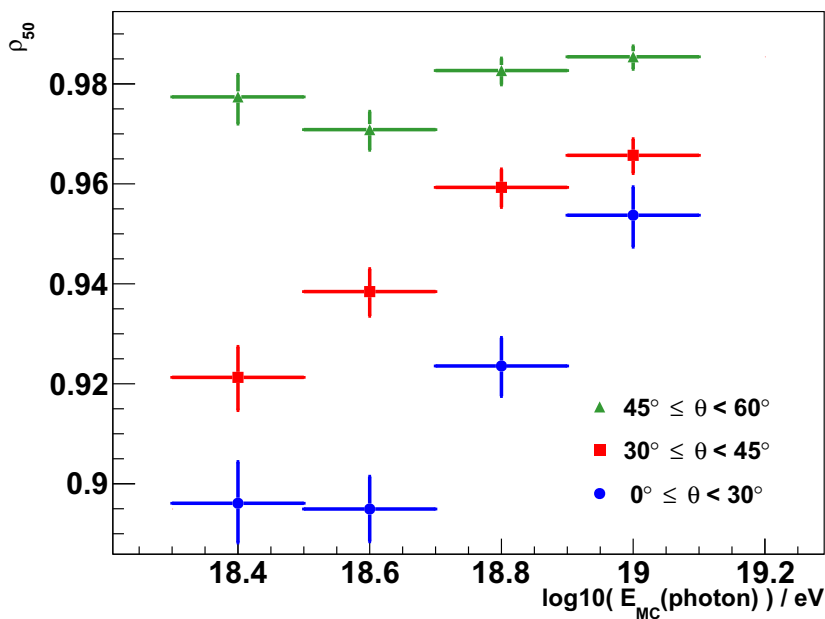


Figure 11.7: The background rejection ρ_{50} in the four energy bins, each energy bin separated into three bins in zenith angle. The vertical error bars are derived with the Clopper-Pearson method [CC34].

11.4. Conclusion and further steps

In this chapter, a first step towards an extension of the GW follow-up search for UHE photons towards energies below the current threshold of 10 EeV has been made by constructing a novel air shower observable R_{MoPS} that is capable to separate between primary photons and hadrons. Though, the separation power of this

new observable alone can not reach the background rejection of the established SD photon search analysis above 10 EeV from [RJ19] or of the hybrid detector in the same energy regime [AA17a], it has some intriguing properties which makes it especially interesting for an application to follow-up searches after transient point sources. The application of R_{MoPS} comes with little to almost no impact at all on the total photon detection efficiency which allows for a high efficiency down to energies even below $10^{18.4}$ eV. Since the reconstruction of R_{MoPS} only requires data from the SD, an analysis using R_{MoPS} can benefit from the high duty cycle of that detector. This high duty cycle is important for the analysis of short-lived transients like CBMs since the hybrid detector would on average miss five out of six CBMs in its field of view due to its operation time limitations.

Still, R_{MoPS} is only a first step towards a photon search below 10 EeV with the SD 1500 m array. As a standalone photon discriminating observable its separation power is not high enough to make a photon interpretation of a potential photon candidate possible. Future work should seek to combine R_{MoPS} with other discriminating observables in a multivariate analysis to maximize its separation power and at the same time keep the photon detection efficiency as high as possible. Also further studies on the systematical properties of R_{MoPS} are needed before it should be applied to data. Compared to other observables like Δ or L_{LDF} (see Chapter 7), R_{MoPS} utilizes the differential signal traces of the SD PMTs in much more detail. For that reason the impact of the air shower thinning algorithms implemented in CORSIKA on R_{MoPS} has to be studied specifically. Apart from simulations also data-specific effects in the signal traces that come with electronic noise and aging of the PMTs could have stronger impact on R_{MoPS} than on other higher-level observables due to its sensitivity on the detailed shape of the traces. In order to understand the effects of individual features in the signal traces on R_{MoPS} , the behavior of R_{MoPS} in an application to data should be studied thoroughly on a training data set before the actual data application of the finalized analysis. Also, the impact of the new SD station triggers MoPS and ToTd on the reconstruction of the observable has not been studied yet. Despite utilizing the algorithms behind those triggers, R_{MoPS} can still be reconstructed when stations are rejected which are solely triggered by one of the new trigger types.

Summary and outlook

I^N this thesis, constraints on UHE photons from GW sources and the anomalous blazar TXS 0506+056 have been placed for the first time using data collected by the Pierre Auger Observatory. To separate a possible photon signal from the predominant background of hadronic cosmic rays with the Auger SD, the photon discriminating analysis from [RJ19] has been adopted. In preparation for the GW follow-up photon search, an analytical expression for the photon selection efficiency curve as a function of energy and zenith angle has been fitted using photon simulations (see Eqs. 7.22 and 7.23). The uncertainty on the reconstructed direction of primary photons between $10^{19.0}$ eV and $10^{20.5}$ eV following a spectral distribution $\propto E^{-2}$ has been approximated with a symmetric Kent distribution with a width of $1.128^{+0.011}_{-0.013}$ deg (68%-quantile) in order to account for the finite directional resolution of the SD when analyzing point sources of UHE photons.

Using the results from this preparatory work, the data taken by the Auger SD have been analyzed for air shower events that were directionally coincident with the 90% contour of the GW sky localization after a convolution with the directional resolution of the SD to primary photons. All eleven GW events from LIGO/Virgo run O1 and O2 were analyzed within two mutually exclusive time windows of 1000 s centered on the GW event time and of one sidereal day starting 500 s after the GW event time. In total, four coincident air shower events were found during the 1 d time windows of four different GWs. None of those events passed the final photon candidate cut, hence the photon hypothesis was rejected for all four coincident air showers. Since no photon candidate events were found, upper limits on the photon flux and the spectral photon fluence were derived for each time window and GW event separately. The photon flux limits have also been extrapolated to the GW sources to obtain limits on the total energy transferred into UHE photons albeit neglecting the attenuation of photons during their propagation through the universe. Taking into account a simple attenuation model, only the source of GW170817 – a BNS merger – could be constrained to have transferred less than 22% of its total radiated energy into UHE photons (at 90% CL). Further studies on the sensitivity of the analysis to a hypothetical photon signal revealed that if a single photon candidate would have been found within one of the 1000 s (1 d) time windows, the background hypothesis could have been rejected at a confidence level of 4.90σ (3.50σ).

In a similar approach, the analysis has also been applied to the blazar TXS

0506+056 during two periods of possible high-energy neutrino emission. No coincident air shower events have been found in either of the periods. The air showers which had their reconstructed axis pointing closest to the direction of the blazar have been found unlikely to be induced by primary photons.

Aiming to prepare and fine tune the analysis for the application to LIGO/Virgo run O3 and future observation runs, public but yet preliminary GW data from O3 have been used to develop an analysis strategy that optimizes the physics results of the analysis within capabilities of the Auger SD. Using the 50% counter instead of the 90% contour of the convolved localization sky maps turned out to be a more advantageous choice and a good compromise between background contamination and confidence of source coverage. In addition, a GW event selection is proposed which prioritizes GWs from well localized or comparably close sources. The choices of the proposed cut values which are summarized in Tab. 9.2 have explicitly been tuned for the application to data until the end of O3. Follow-up analyses of future GW observation runs might require further fine-tuning of the cuts values depending on the general localization quality, the source distances, GW detection frequency and possibly other information about the GWs that might be available in the future. To constrain source classes of CBMs as a whole, the stacking method that has been applied to the search for UHE neutrinos in [SM19] has been modified and adjusted for the application to the follow-up photon search. An application of the stacking method to GW data until the end of O3 would not yet significantly improve the results due to the large distances of most GW sources and the still rather low statistics of only 12 events that pass the GW selection cuts. However, the method will eventually become relevant if more close CBMs like the source of GW170817 will be detected in the future.

So far, the lower energy threshold of the photon search analysis with the SD is at $10^{19.0}$ eV. However, most conservative models of cosmic ray acceleration at CBMs predict cosmic rays to be accelerated only up to the EeV scale. Therefore, a first step to lower the photon energy threshold of the Auger SD has been taken here. For this purpose the novel air shower observable R_{MoPS} has been developed and its basic properties as well as its photon-hadron separation power have been analyzed in a simulation study. First results have shown that in addition to a good separation power, R_{MoPS} comes with little to no impact on the photon detection efficiency at photon energies above $10^{18.4}$ eV. If in a future work other discriminating observables could be found that are applicable to photon events below $10^{19.0}$ eV and complementary to R_{MoPS} , R_{MoPS} could be combined with those observables in an MVA with negligible impact on the photon detection efficiency. Such a combination could potentially improve the separation power to a level that would allow for a sufficient sensitivity to a photon signal from GW sources below the current energy threshold.

This thesis represents the first step to thoroughly probe the sources of GWs in the light of UHE photons. Still, the potential of the Pierre Auger Observatory as a whole is far from being exhausted. Though being unrivaled in exposure, the SD 1500m array is only one component of Auger. A reduction of the photon

energy threshold down to 1 EeV can also be achieved with the hybrid detector or even down to 0.2 EeV using the low-energy extensions of the SD 750 m array and HECO as summarized in [RJ19]. The duty cycle of the hybrid detector still poses an obstacle for follow-up searches after short-timescale transient events like CBMs, but the expected abundance of GW observations in the near future will eventually compensate this issue offering a great opportunity to study UHE photons from GW sources in a whole new energy regime.

Also the Auger Prime upgrade provides promising opportunities to search for UHE photons with the SSDs and the RDs on top of each SD station and the underground muon detector array of the finalized AMIGA extension. The different detection techniques that are implemented with Auger Prime are expected to increase the sensitivity to UHE photons as well as the photon-hadron separation power in a wide energy range. First GW follow-up photon searches with the upgraded Auger Observatory could possibly already be applied to the data that will be taken during the upcoming GW observation run O4 which is scheduled to start in the fourth quarter of 2021.

In a continuative study, the results of this work could be used to probe theories of photon-axion conversion in the strong magnetic fields of astrophysical sources like CBMs as suggested in [GD01] and [FM11]. The non-observation of UHE photons from sources which are well beyond the photon horizon could potentially help to constrain the allowed phase space of axion mass and coupling strength. Though still depending on theoretical models that describe the production of UHE photons at these sources, this approach might aid the search for axions in regions of that phase space which are not easily accessible in laboratory experiments.

Appendix

13.1. Appendix of Chapter 6

```
RUNNR      1
EVTNR      1
NSHOW      1

SEED       163936893  0  0
SEED       209546724  0  0
SEED       109293136  0  0
SEED       191372284  0  0
SEED       403705832  0  0

PRMPAR     1
ESLOPE     -1
ERANGE     3.16228e+09  3.16228e+11
THETAP     0.0  65.0
PHIP       -180  180

OBSLEV     145200
MAGNET     20.1  -14.2
ATMOD      1
ARRANG     0.

HADFLG     0  0  0  0  0  2
ELMFLG     T  T
STEPFC     1.0
RADNKG     200.E2
LONGI      T  5.  T  T
MUMULT     T

THIN       1e-6  3162.28  3.0e4
THINH      1.00  1.0e2
ECUTS      0.1  0.05  2.5e-4  2.5e-4

MUADDI     T
FLUDBG     T
MAXPRT     1
ECTMAP     10000
PAROUT     T  T
DATBAS     F
DEBUG      F  6  F  1000000

DATDIR     /products/auger/CORSIKA/corsika-75600/run

EPOPAR     input  /products/auger/CORSIKA/corsika-75600/epos/epos.param
EPOPAR     fname  inics  /products/auger/CORSIKA/corsika-75600/epos/epos.inics
EPOPAR     fname  iniev  /products/auger/CORSIKA/corsika-75600/epos/epos.iniev
EPOPAR     fname  initl  /products/auger/CORSIKA/corsika-75600/epos/epos.initl
EPOPAR     fname  inirj  /products/auger/CORSIKA/corsika-75600/epos/epos.inirj
EPOPAR     fname  inihy  /products/auger/CORSIKA/corsika-75600/epos/epos.inihy
EPOPAR     fname  check  none
EPOPAR     fname  histo  none
EPOPAR     fname  data   none
EPOPAR     fname  copy   none

DIRECT     /nfs/cs02/scratch/ruehl/2672203/1/

EXIT
```

Figure 13.1: An example of a CORSIKA steering card used to simulate a photon-induced air shower of the simulation set used in the analysis of Sec. 7. The 9 digit numbers given as seeds for sequences of random numbers have been generated with the random number generator routine *rand()* of the C++ standard library (*cstdlib*).

```

<!-- A sequence for an SD only reconstruction -->
<!DOCTYPE sequenceFile [
<!ENTITY % sd SYSTEM "/data/auger4/Offline_ruehl/r31920_for_SDPhoton/Install_SQLite/share/auger
-offline/config/standardSdSequences.dtd">
%sd;
] >
<sequenceFile
  xmlns:xsi="http://www.w3.org/2001/XMLSchema-instance"
  xsi:noNamespaceSchemaLocation="/data/auger4/Offline_ruehl/r31920_for_SDPhoton/
  Install_SQLite/share/auger-offline/config/ModuleSequence.xsd">
  <enableTiming/>
  <moduleControl>
    <loop numTimes="1" pushEventToStack="yes">
      <module> EventFileReaderOG </module>
      <loop numTimes="5" pushEventToStack="yes">
        <module> EventGeneratorOG </module>
        <module> SdAccidentalInjectorKG </module>
        <module> G4StationSimulatorOG </module>
        <loop numTimes="unbounded" pushEventToStack="no">
          <module> CachedShowerRegeneratorOG </module>
          <module> G4StationSimulatorOG </module>
        </loop>
        <try>
          <module> ClearParticleLists </module>
          <module> SdSimulationCalibrationFillerOG </module>
          <module> SdPMTSimulatorOG </module>
          <module> SdFilterFADCSimulatorMTU </module>
          <module> SdBaselineSimulatorOG </module>
          <module> TankTriggerSimulatorOG </module>
          <module> TankGPSSimulatorOG </module>
          <module> CentralTriggerSimulatorXb </module>
          <module> CentralTriggerEventBuilderOG </module>
          <module> EventBuilderOG </module>
          <module> EventCheckerOG </module>
          <module> SdPMTQualityCheckerKG </module>
        <try>
          <module> SdCalibratorOG </module>
          <module> SdSignalRecoveryKLT </module>
          <module> SdMonteCarloEventSelectorOG </module>
          <module> SdEventSelectorOG </module>
          <module> SdPlaneFitOG </module>
          <module> LDFFinderKG </module>
          <module> DLECorrectionWG </module>
          <module> SdCompositionParameters </module>
          <module> SdEventPosteriorSelectorOG </module>
          <module> Risetime1000LLL </module>
        </try>
      </try>
      <module> EventFileExporterOG </module>
      <module> RecDataWriterNG </module>
    </loop>
  </moduleControl>
</sequenceFile>

```

Figure 13.2: An example of an Offline module sequence used to simulate and reconstruct the detector response of an air shower that has been produced with CORSIKA. The module sequence is written in XML and parsed within Offline with the Xerces-C++ libraries.

```

<!-- A sequence for an SD only reconstruction -->
<!DOCTYPE sequenceFile [
<!ENTITY % sd SYSTEM "/data/auger4/Offline_ruehl/r31920_for_SDPhoton/Install_SQLite/share/auger
-offline/config/standardSdSequences.dtd">
%sd;
] >
<sequenceFile
  xmlns:xsi="http://www.w3.org/2001/XMLSchema-instance"
  xsi:noNamespaceSchemaLocation="/data/auger4/Offline_ruehl/r31920_for_SDPhoton/
  Install_SQLite/share/auger-offline/config/ModuleSequence.xsd">
  <enableTiming/>
  <moduleControl>
    <loop numTimes="unbounded" pushEventToStack="yes">
      <module> EventFileReaderOG </module>
      <module> EventCheckerOG </module>
      <module> SdPMTQualityCheckerKG </module>
      <module> TriggerTimeCorrection </module>
      <module> SdCalibratorOG </module>
      <module> SdPMTSignalShapeQualityChecker </module>
      <module> SdStationPositionCorrection </module>
      <module> SdBadStationRejectorKG </module>
      <module> SdSignalRecoveryKLT </module>
      <module> SdEventSelectorOG </module>
      <module> SdPlaneFitOG </module>
      <module> LDFFinderKG </module>
      <module> DLECorrectionWG </module>
      <module> SdCompositionParameters </module>
      <module> SdEventPosteriorSelectorOG </module>
      <module> RecDataWriterNG </module>
    </loop>
  </moduleControl>
</sequenceFile>

```

Figure 13.3: An example of an Offline module sequence used to reconstruct the raw data of the Auger SD. The module sequence is written in XML and parsed within Offline with the Xerces-C++ libraries.

13.2. Appendix of Chapter 7

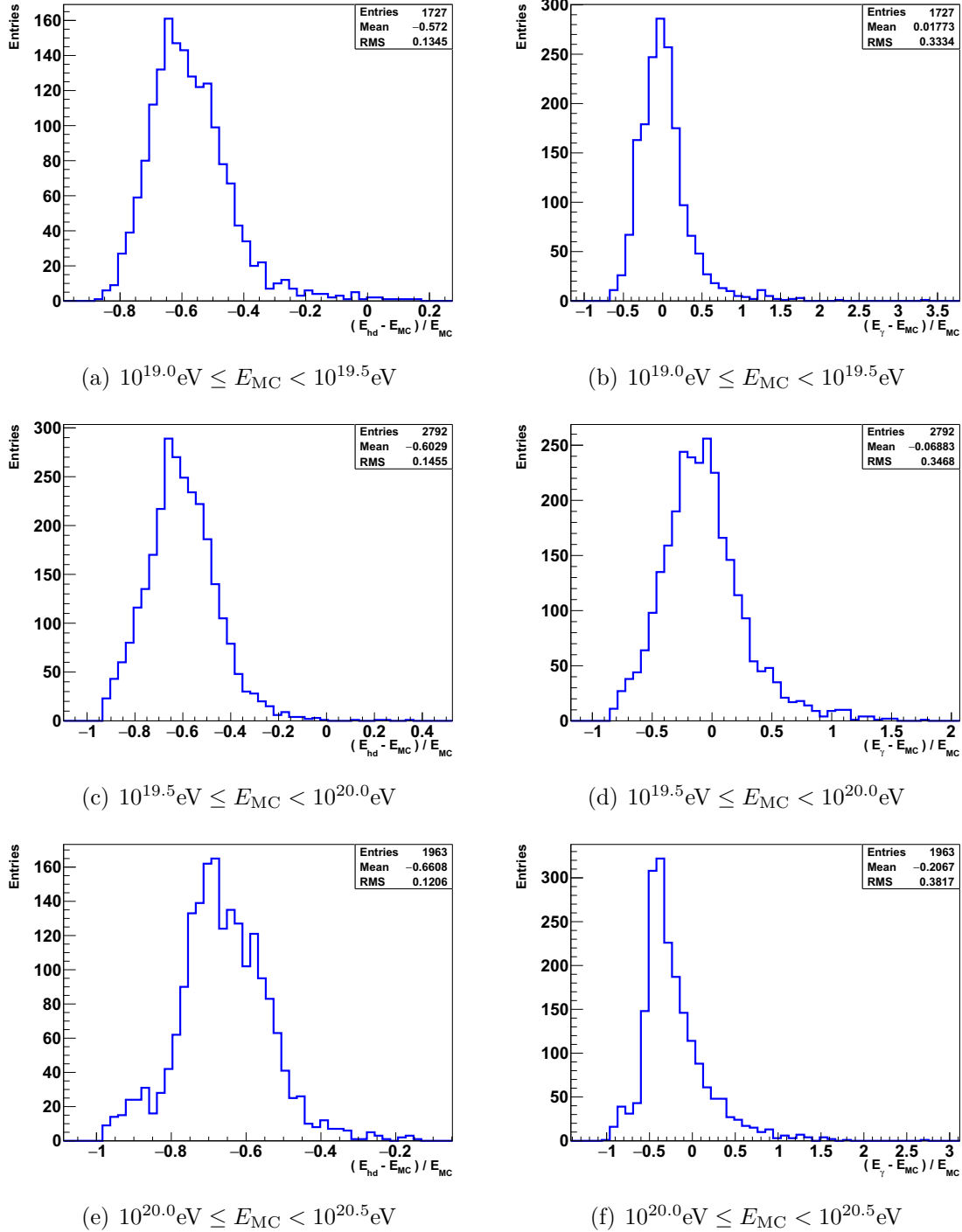


Figure 13.4: The residual between the Monte Carlo energy E_{MC} and the reconstructed hadron energy E_{hd} (left column) and photon energy E_{γ} (right column). Shown are the distributions for simulated photon showers with zenith angles between 30° and 60° divided into three energy bins between $10^{19.0}\text{eV}$ and $10^{20.5}\text{eV}$ (simulation set A described in Sec 6.1.1).

		E_γ -bin 1	E_γ -bin 2	E_γ -bin 3	E_γ -bin 4	E_γ -bin 5
$\langle\Delta\rangle$	θ -bin 1	5.23711	7.41444	9.39136	12.1663	17.71357
	θ -bin 2	4.213	5.79398	7.1109	8.6722	10.6336
	θ -bin 3	3.18535	4.49599	5.15013	6.62771	7.92643
	θ -bin 4	2.65194	3.56604	4.70817	5.48378	6.54047
	θ -bin 5	2.34778	3.07013	3.77732	3.86504	5.42009
	θ -bin 6	1.90826	2.29986	2.96273	3.46059	3.77486
$\sigma(\Delta)$	θ -bin 1	2.77095	3.25911	3.9813	5.25757	6.28267
	θ -bin 2	1.93495	1.89181	2.13178	2.80999	3.37095
	θ -bin 3	1.42478	1.48255	1.22139	1.72453	1.7884
	θ -bin 4	1.05556	1.05064	1.84619	1.69618	1.92758
	θ -bin 5	1.0177	1.24319	1.2607	1.63798	3.86937
	θ -bin 6	1.0952	1.22046	1.6759	2.05261	1.84002
$\langle L_{\text{LDF}}\rangle$	θ -bin 1	-0.0624489	-0.108729	-0.161782	-0.181346	-0.235338
	θ -bin 2	-0.121589	-0.161479	-0.17861	-0.191349	-0.229831
	θ -bin 3	-0.110666	-0.134816	-0.1734	-0.166803	-0.175929
	θ -bin 4	-0.0883975	-0.112252	-0.110545	-0.11483	-0.13109
	θ -bin 5	-0.0556469	-0.0626352	-0.0721802	-0.0817056	-0.089013
	θ -bin 6	-0.0114958	-0.0340138	-0.0300594	-0.0473377	-0.0501441
$\sigma(L_{\text{LDF}})$	θ -bin 1	0.160158	0.132691	0.115331	0.115651	0.115157
	θ -bin 2	0.115924	0.113517	0.113498	0.113794	0.10973
	θ -bin 3	0.116293	0.102508	0.100176	0.115561	0.117913
	θ -bin 4	0.121362	0.0936684	0.0958178	0.117338	0.106711
	θ -bin 5	0.095002	0.0973324	0.0966184	0.0955022	0.109294
	θ -bin 6	0.0945239	0.0789862	0.0835552	0.0883046	0.0905818

Table 13.1: The mean values $\langle\Delta\rangle$ and $\langle L_{\text{LDF}}\rangle$ of the unnormalized air shower observables and the RMS deviations of their distributions $\sigma(\Delta)$ and $\sigma(L_{\text{LDF}})$ separately in 6×5 bins in $\theta \times E_\gamma$. The bin margins for the reconstructed zenith angle θ are given by $\sec(\theta) = 1.00000, 1.17269, 1.28975, 1.41138, 1.53616, 1.70603, 2.00000$. The bin margins for the photon energy E_γ are given by $\log(E/\text{eV}) = 19, 19.3769, 19.5682, 19.7482, 19.9323, 20.5$. The values have been derived in [KN17] and were obtained in private communication with P. Papenbreer (University of Wuppertal) for the purpose of precisely reproducing the analysis therein.

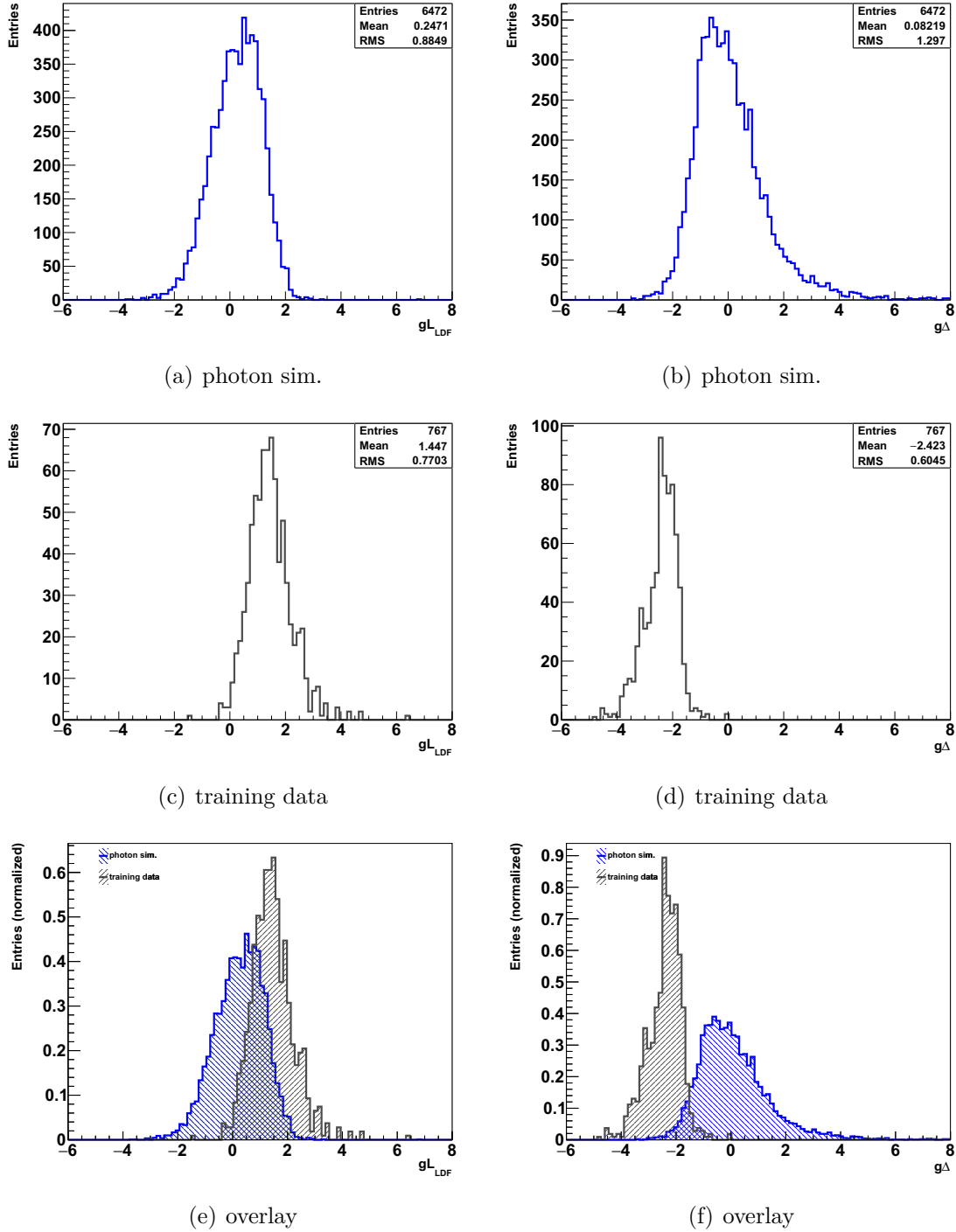
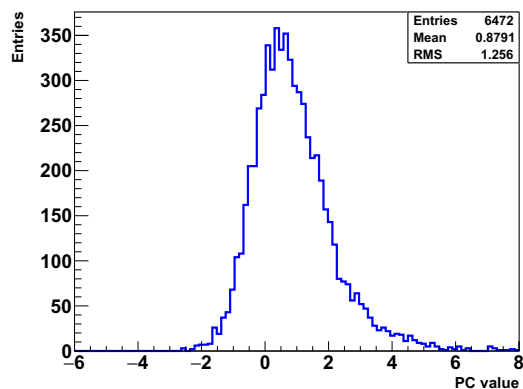
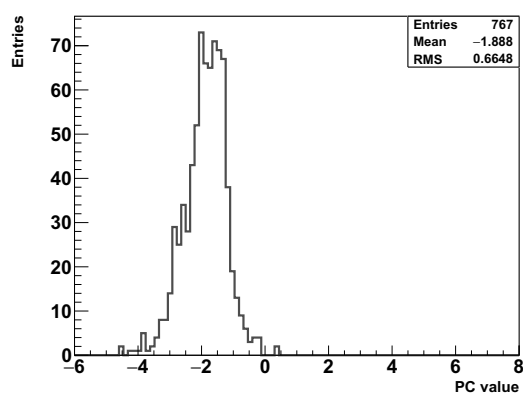


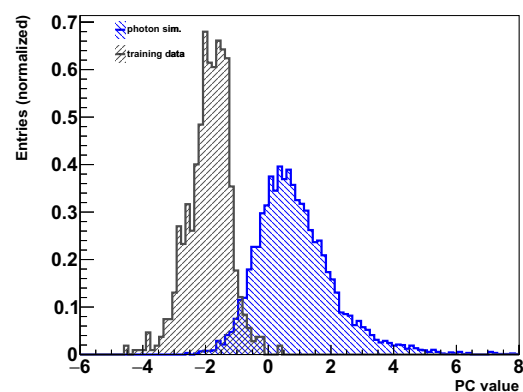
Figure 13.5: The distributions of the normalized observables gL_{LDF} (left column) and $g\Delta$ (right column) for simulated photon showers (top row), a training set of 767 data events (middle row) and the overlay of both distributions (bottom row). Both sets only contain events with reconstructed photon energy between $10^{19.0}$ eV and $10^{20.5}$ eV and reconstructed zenith angles between 30° and 60° (simulation set *A* described in Sec 6.1.1).



(a) photon sim.

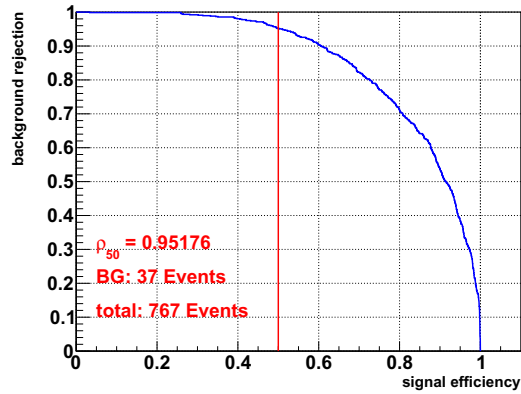
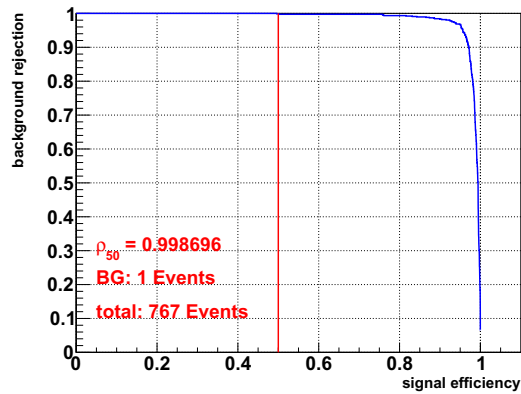
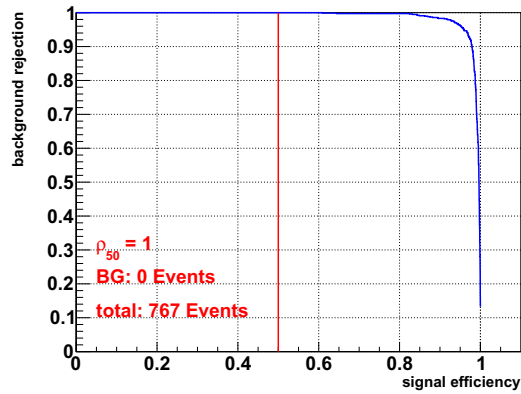


(b) training data.



(c) overlay

Figure 13.6: The distributions of the principal component PC for (a) simulated photon showers, (b) a training set of 767 data events and (c) the overlay of both distributions. Both sets only contain events with reconstructed photon energy between $10^{19.0}$ eV and $10^{20.5}$ eV and reconstructed zenith angles between 30° and 60° (simulation set *A* described in Sec 6.1.1).

(a) gL_{LDF} (b) $g\Delta$ 

(c) PC

Figure 13.7: The ROC curves of the distributions of (b) gL_{LDF} and (a) $g\Delta$ shown in Fig. 13.5 and (c) the PC of those observables shown in Fig. 13.6. In each plot the value of ρ_{50} is indicated by the red line, though the low number of 767 events in the training data sample induce large statistic uncertainties on ρ_{50} . The total number of background events (“total”) and the number of background events which pass the cut at the median of the photon distribution (“BG”) are also given for each curve.

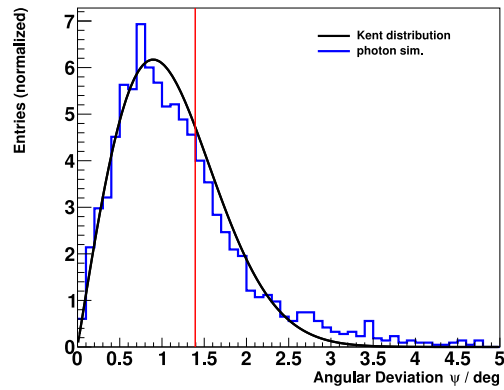
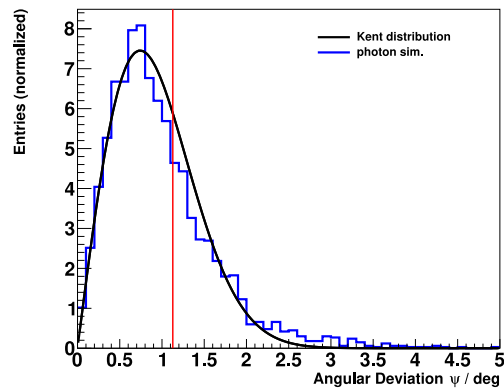
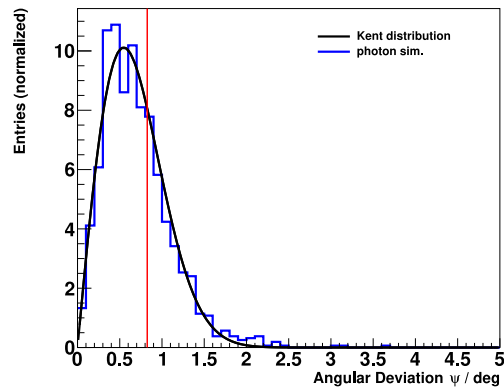
(a) $10^{19.0}\text{eV} \leq E_{\text{MC}} < 10^{19.5}\text{eV}$ (b) $10^{19.5}\text{eV} \leq E_{\text{MC}} < 10^{20.0}\text{eV}$ (c) $10^{20.0}\text{eV} \leq E_{\text{MC}} < 10^{20.5}\text{eV}$

Figure 13.8: The distributions of angular deviations ψ between simulated (true) and reconstructed directions of primary photons (simulation set *A*) in three different energy bins. The vertical line in each plot marks the 68% quantile. The distributions are fitted with Kent distributions (using the χ^2 method) and the resulting κ parameters are (a) $\kappa = 4100 \pm 500$ (b) $\kappa = 6000 \pm 800$ and (c) $\kappa = 11000 \pm 1300$.

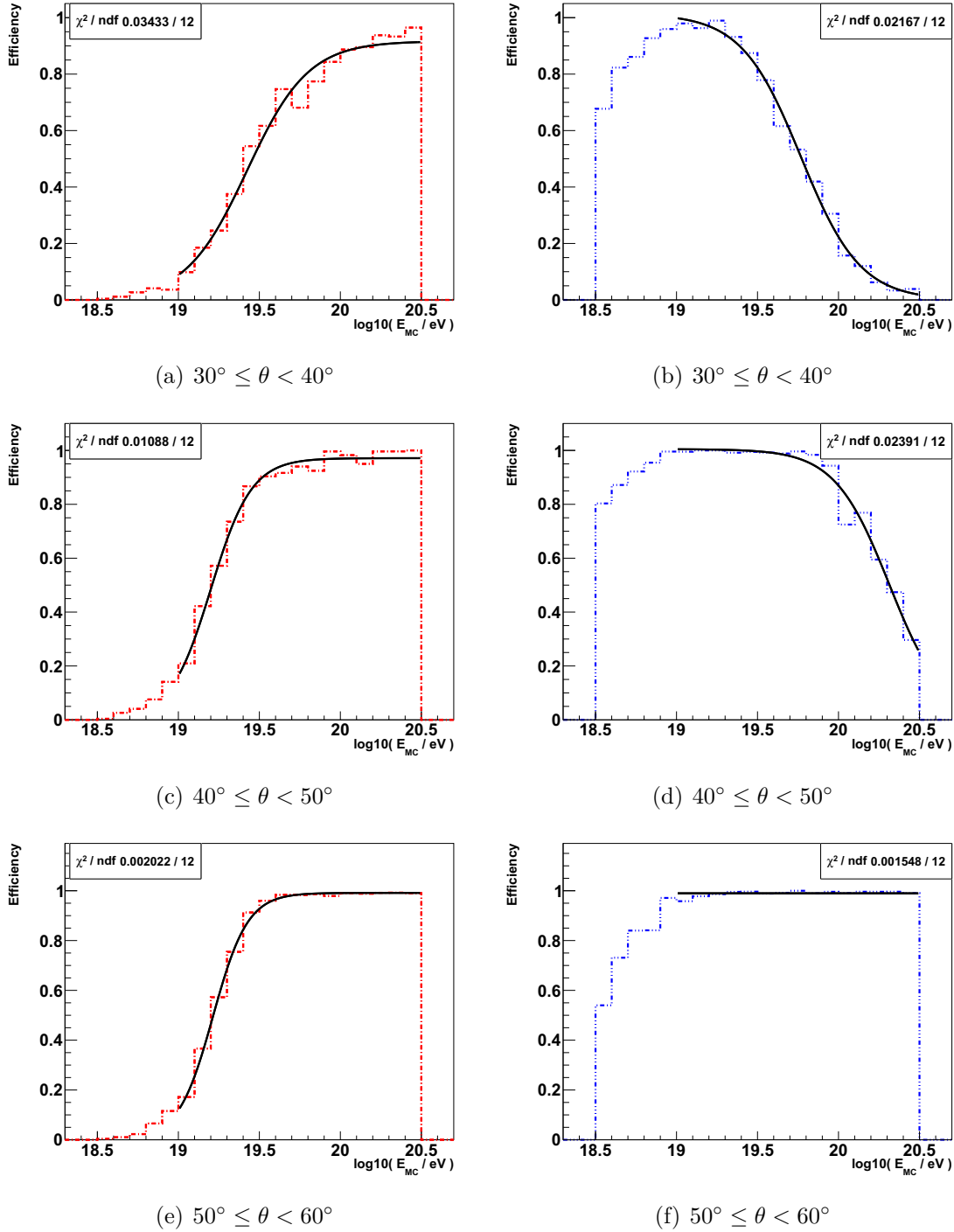


Figure 13.9: The photon detection efficiencies in each of the three zenith angle bins after application of the selection criteria imposed by the observables Δ and L_{LDF} (left column) and after application of the selection criterion imposed by the reconstruction of the photon energy (right column). The fitted curves are given by Eqs. 7.20 and 7.21 respectively and the corresponding fit parameters are summarized in Tab. 7.1.

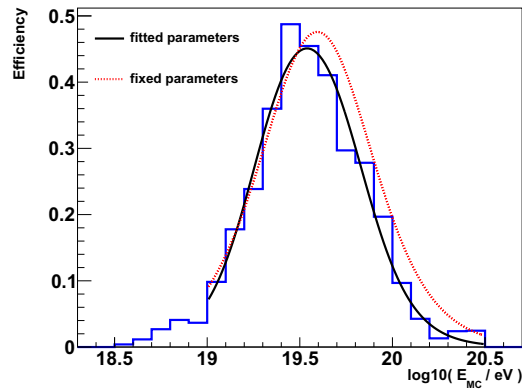
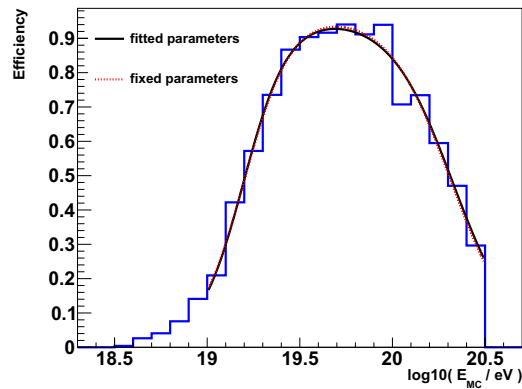
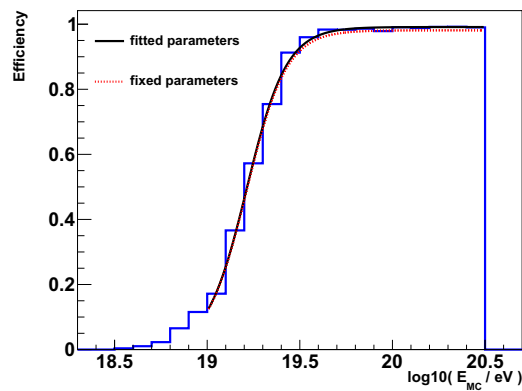
(a) $30^\circ \leq \theta < 40^\circ$ (b) $40^\circ \leq \theta < 50^\circ$ (c) $50^\circ \leq \theta < 60^\circ$

Figure 13.10: The total photon detection efficiency in each of the three zenith angle bins after application of all selection criteria. The fitted curves (black solid lines) are given by Eq. 7.22 and the corresponding fit parameters are summarized in Tab. 7.1. The red dotted curves are the result of the multiplications of the individual efficiency curves shown in Fig. 13.9 within each bin. Discrepancies between the two curves (e.g. as visible in (a)) are caused by correlations of the selection cuts.

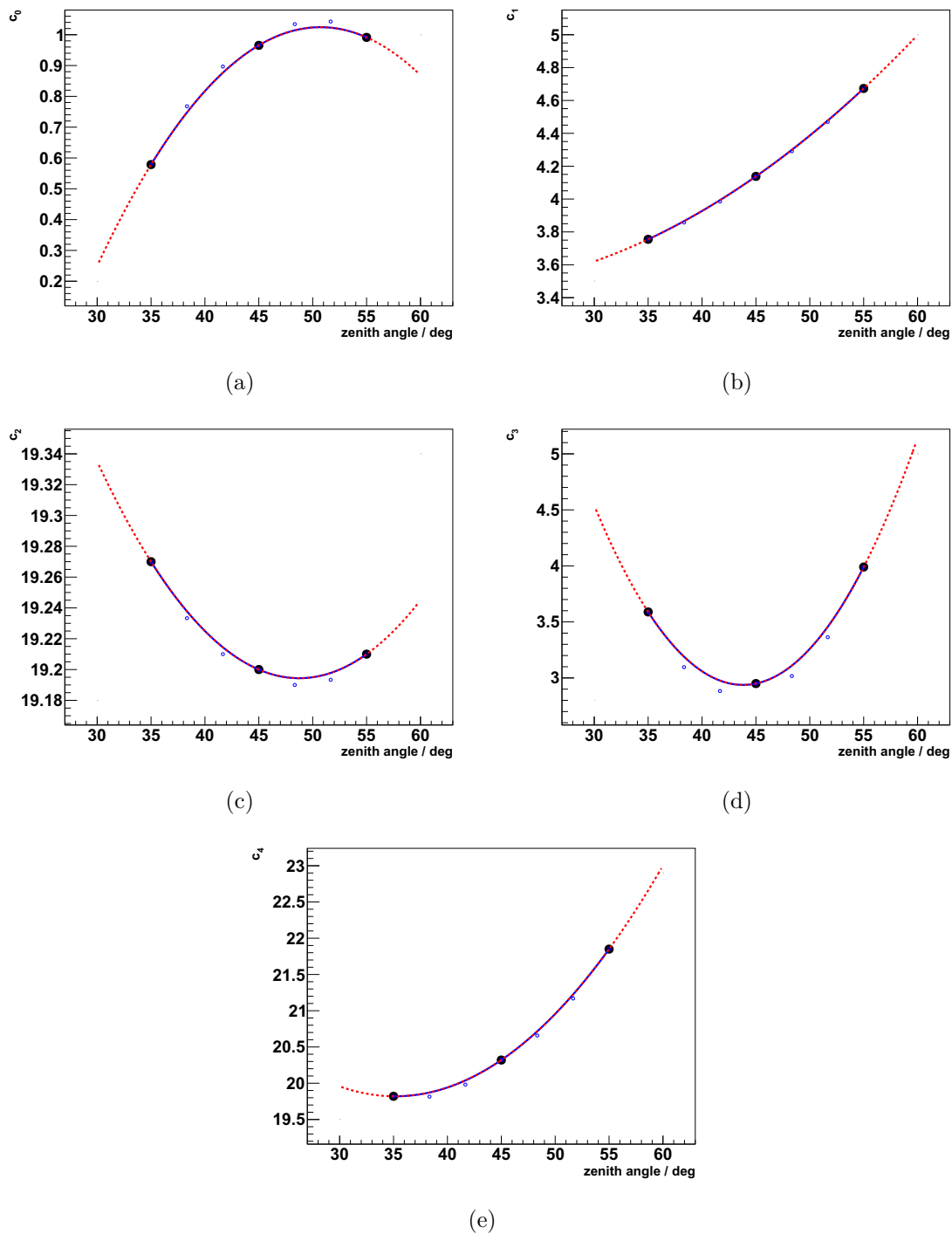


Figure 13.11: The five fit parameters c_i , $i \in \{0, \dots, 4\}$, as obtained from fitting Eq. 7.22 to the efficiency histograms shown in Fig. 13.10 in three different zenith angle bins plotted against the central values of each bin. The three values for each $c_i(\theta)$ (black dots) have been interpolated for the zenith angle range $35^\circ \leq \theta < 55^\circ$ using quadratic Catmull-Rom splines (blue solid curves). The red dotted curves represent the parabolic extrapolations of the splines to the full zenith range $30^\circ \leq \theta < 60^\circ$ and are parameterized as given in Eq. 7.23. The blue circles depict the virtual control points that are needed for the Catmull-Rom construction.

13.3. Appendix of Chapter 8

GW event	UTC time	$E_{\text{rad}}/(M_{\odot}c^2)$	D_L/Mpc
GW150914	09:50:45.4	$3.1^{+0.4}_{-0.4}$	440^{+150}_{-170}
GW151012	09:54:43.4	$1.6^{+0.6}_{-0.5}$	1080^{+550}_{-490}
GW151226	03:38:53.6	$1.0^{+0.1}_{-0.2}$	450^{+180}_{-190}
GW170104	10:11:58.6	$2.2^{+0.5}_{-0.5}$	990^{+440}_{-430}
GW170608	02:01:16.5	$0.9^{+0.0}_{-0.1}$	320^{+120}_{-110}
GW170729	18:56:29.3	$4.8^{+1.7}_{-1.7}$	2840^{+1400}_{-1360}
GW170809	08:28:21.8	$2.7^{+0.6}_{-0.6}$	1030^{+320}_{-390}
GW170814	10:30:43.5	$2.7^{+0.4}_{-0.3}$	600^{+150}_{-220}
GW170817	12:41:04.4	≥ 0.04	40^{+7}_{-15} (41.0 \pm 3.1)
GW170818	02:25:09.1	$2.7^{+0.5}_{-0.5}$	1060^{+420}_{-380}
GW170823	13:13:58.5	$3.3^{+1.0}_{-0.9}$	1940^{+970}_{-900}

Table 13.2: The UTC time, the total radiated energy E_{rad} and the source luminosity distance D_L of all eleven GW events from LIGO/Virgo runs O1 and O2 [AB19b]. The value of D_L for the NS merger event GW170817 given in parenthesis is the distance of the host Galaxy NGC 4993 obtained in an independent measurement [HH17].

GW event	average SD aperture $A/10^{13} \text{ cm}^2$ during 1 d
GW150914	2.336 ± 0.017
GW151012	2.15 ± 0.19
GW151226	2.312 ± 0.064
GW170104	2.231 ± 0.021
GW170608	2.277 ± 0.020
GW170729	2.2505 ± 0.0090
GW170809	2.260 ± 0.017
GW170814	2.210 ± 0.022
GW170817	2.290 ± 0.025
GW170818	2.227 ± 0.065
GW170823	1.387 ± 0.015

Table 13.3: The mean value and the RMS deviation of the aperture during the 1 d time window for each of the eleven GW events from LIGO/Virgo run O1 and O2. In most cases the aperture is rather stable with relative deviations of $\sim 1\%$. However, there was a temporary drop in aperture in the time window of GW151012 leading to a larger deviation and another more constant drop during the time window of GW170823.

GW event	k_γ^{UL} hottest direc.		k_γ^{UL} min.		k_γ^{UL} max.	
	1000 s	/ 1 d	1000 s	/ 1 d	1000 s	/ 1 d
GW150914	5.7	/ 12.6	4.9	/ 11.4	∞	/ 28.8
GW151012	-	/ 38.5	-	/ 21.2	-	/ ∞
GW151226	-	/ 34.2	6.8	/ 13.5	∞	/ ∞
GW170104	-	/ -	-	/ 26.4	-	/ ∞
GW170608	-	/ 81.6	-	/ 26.0	-	/ ∞
GW170729	-	/ 14.7	6.9	/ 11.2	∞	/ ∞
GW170809	-	/ 39.2	47.7	/ 26.6	∞	/ 39.8
GW170814	-	/ 34.7	-	/ 29.7	-	/ 38.8
GW170817	-	/ 38.9	-	/ 37.5	-	/ 39.1
GW170818	-	/ -	-	/ 35.6	-	/ ∞
GW170823	-	/ -	-	/ 38.6	-	/ ∞

Table 13.4: The upper limits on the flux normalization factor (in units of 10^{-3} MeV cm $^{-2}$ s $^{-1}$ for the 1000 s time window and 10^{-5} MeV cm $^{-2}$ s $^{-1}$ for the 1 d time window) for the direction with the highest probability to contain the GW source “hottest direction” (first column), the lowest upper limit inside the 90% contour (second column) and the highest upper limit inside the 90% contour (right column). Each column itself is divided into two columns with the corresponding results for the 1000 s and the 1 d time window. A dash in the column for the hottest direction, like e.g. in the row of GW151226 for the 1000 s window, indicates that the hottest direction was not inside the field of view during that time window. If there was no overlap at all of the 90% contour and the field of view, this is indicated by dashes in the columns for the minimum and maximum upper limit, like e.g. in the case of GW151012 for the 1000 s window. If a contour is only partly covered by the field of view during the observation time, the exposure to directions on the edge of the field of is close to zero, hence numbers for the upper limit can be arbitrarily large depending on the distance to the edge. Thus, the maximum upper limits inside the 90% contour for those cases is indicated by a “ ∞ ”-sign, like e.g. in the case of GW170729 for both time windows.

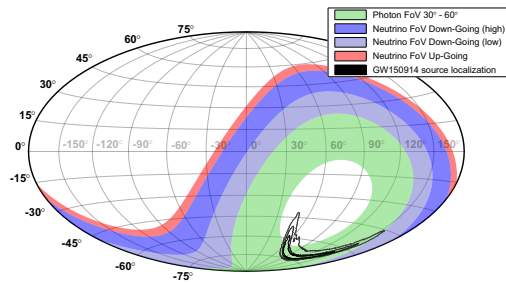
GW event	\mathcal{F}^{UL} hottest direc.		\mathcal{F}^{UL} min.		\mathcal{F}^{UL} max.	
	1000 s	/ 1 d	1000 s	/ 1 d	1000 s	/ 1 d
GW150914	19.7	/ 37.4	17.0	/ 33.8	∞	/ 85.6
GW151012	-	/ 114.5	-	/ 63.2	-	/ ∞
GW151226	-	/ 101.6	23.5	/ 40.2	∞	/ ∞
GW170104	-	/ -	-	/ 78.4	-	/ ∞
GW170608	-	/ -	-	/ 77.5	-	/ ∞
GW170729	-	/ 43.7	23.9	/ 33.4	∞	/ ∞
GW170809	-	/ 116.8	164.7	/ 79.3	∞	/ 118.4
GW170814	-	/ 103.4	-	/ 88.4	-	/ 115.6
GW170817	-	/ 115.6	-	/ 111.7	-	/ 116.5
GW170818	-	/ -	-	/ 106.0	-	/ ∞
GW170823	-	/ -	-	/ 114.9	-	/ ∞

Table 13.5: The upper limits on the spectral fluence (in units of MeV cm $^{-2}$). For a description of the notations in this table see Tab. 13.4.

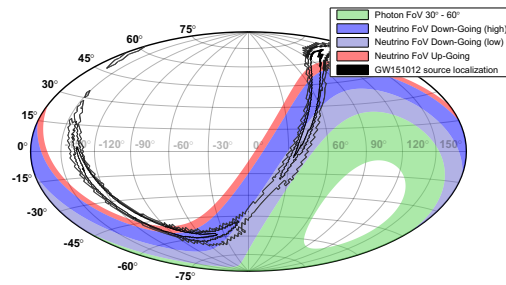
GW event	$E_{\text{rel}}^{\text{UL}}$ hottest direc.		$E_{\text{rel}}^{\text{UL}}$ min.		$E_{\text{rel}}^{\text{UL}}$ max.	
	1000 s	1 d	1000 s	1 d	1000 s	1 d
GW150914	$13.2^{+10.7}_{-8.6}$	$25.9^{+20.3}_{-16.4}$	$11.4^{+9.2}_{-7.5}$	$22.6^{+18.3}_{-14.8}$	∞	$57.4^{+46.5}_{-37.5}$
GW151012	-	895^{+1144}_{-625}	-	494^{+632}_{-345}	-	∞
GW151226	-	221^{+215}_{-155}	$51.0^{+49.7}_{-35.7}$	$87.3^{+85.0}_{-61.2}$	∞	∞
GW170104	-	-	-	552^{+641}_{-384}	-	∞
GW170608	-	-	-	$94.6^{+84.2}_{-53.8}$	-	∞
GW170729	-	787^{+965}_{-577}	430^{+528}_{-315}	601^{+738}_{-441}	∞	∞
GW170809	-	493^{+363}_{-311}	694^{+511}_{-438}	335^{+246}_{-211}	∞	499^{+368}_{-315}
GW170814	-	148^{+89}_{-86}	-	126^{+76}_{-73}	-	165^{+100}_{-97}
GW170817 [†]	-	$52.1^{+8.2}_{-7.6}$	-	$50.3^{+7.9}_{-7.3}$	-	$52.5^{+8.2}_{-7.6}$
GW170818	-	-	-	473^{+466}_{-270}	-	∞
GW170823	-	-	-	1400^{+1670}_{-950}	-	∞

Table 13.6: The upper limits $E_{\text{rel}}^{\text{UL}}$ on the fraction of energy which has been transferred into UHE photons relative to the total amount of energy radiated by the gravitational wave source (cf. Tab. 13.2) in units of 10^{-5} . The limits are calculated under the assumptions that potential UHE photons are do not undergo any interactions during their propagation through the interstellar medium and that they are radiated isotropically. For a description of the notations in this table see Tab. 13.4. The upper and lower uncertainty bounds of each number are inherited from the uncertainty of the source luminosity distance. The uncertainties on the total radiated energy are not included. Instead only the mean values were used to derive the results given in this table. The luminosity distances of the sources together with their uncertainties and the mean values of the total radiated energies were taken from [AB19b] and are compiled in Tab 13.2.

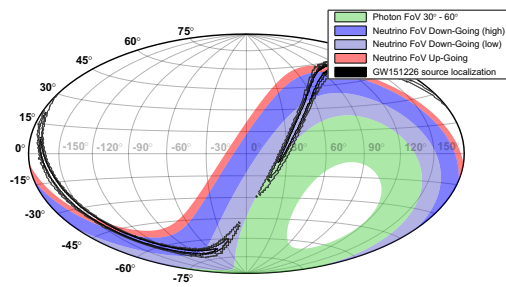
[†] In [AB19b], the radiated energy of GW170817 is only given by a lower bound ($E_{\text{tot}}^{\text{rad}} \geq 0.04M_{\odot}$) thus the values of $E_{\text{rel}}^{\text{UL}}$ given in this table are derived using this lower bound. For the mean value and the uncertainty of the distance of GW170817, the distance of its host galaxy NGC 4993 were taken.



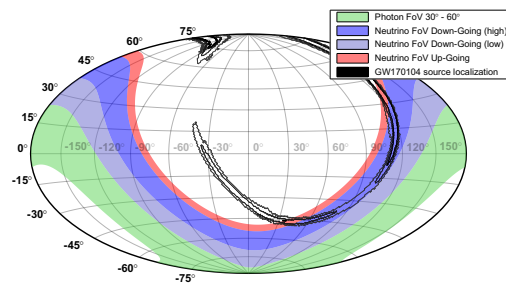
(a) GW150914



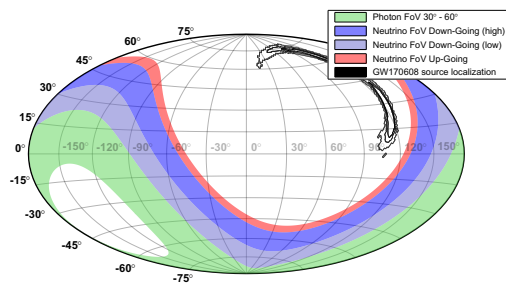
(b) GW151012



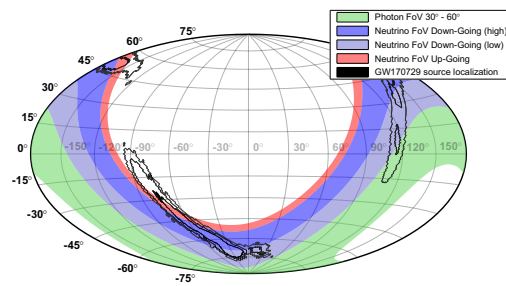
(c) GW151226



(d) GW170104



(e) GW170608



(f) GW170729

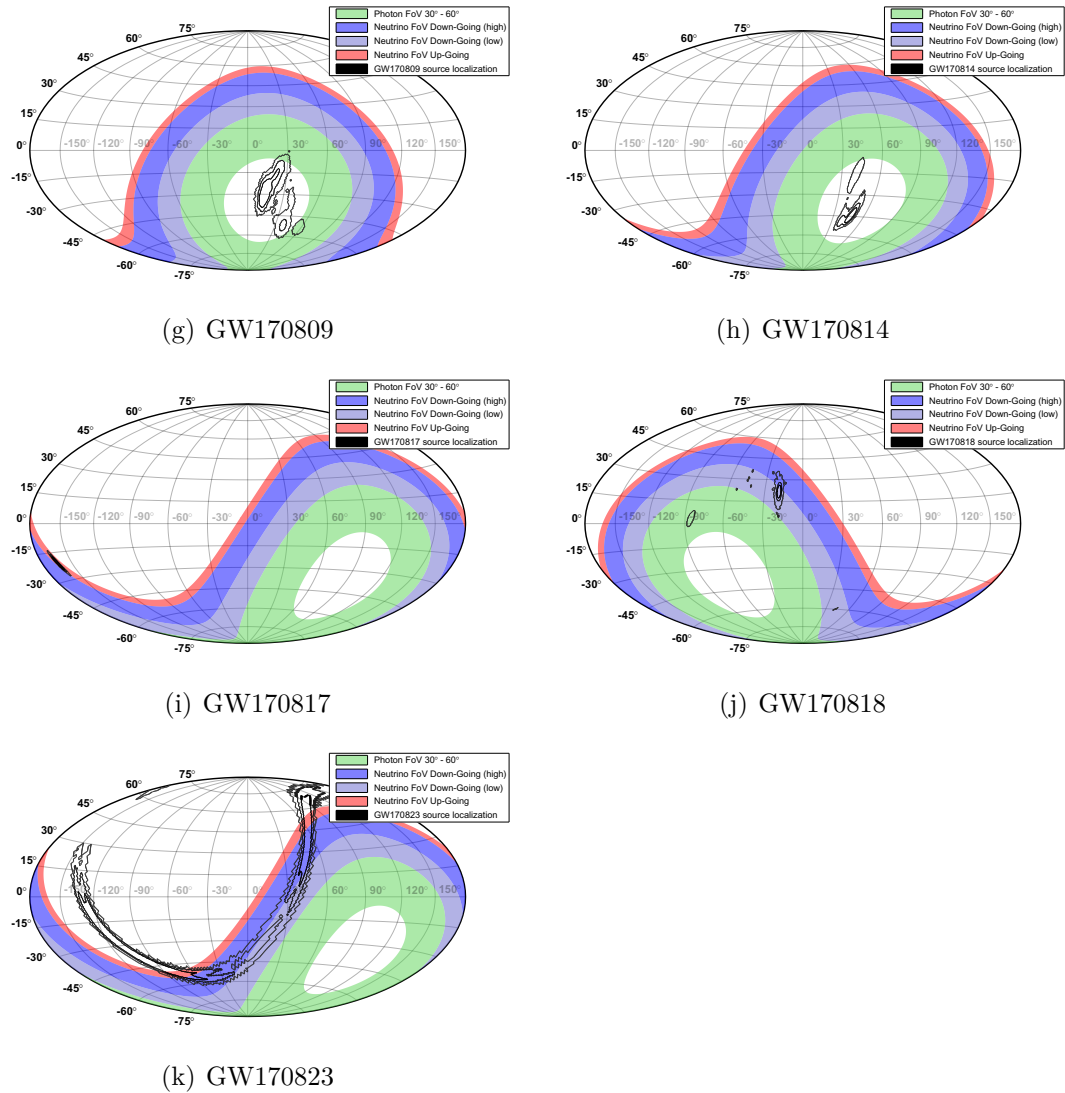


Figure 13.12: The 68%, 90% and 99%-contour lines for the original (unconvolved) probability distributions of the localizations of all eleven GW events and the respective fields of view of Auger for the different follow-up neutrino searches and the follow-up photon search.

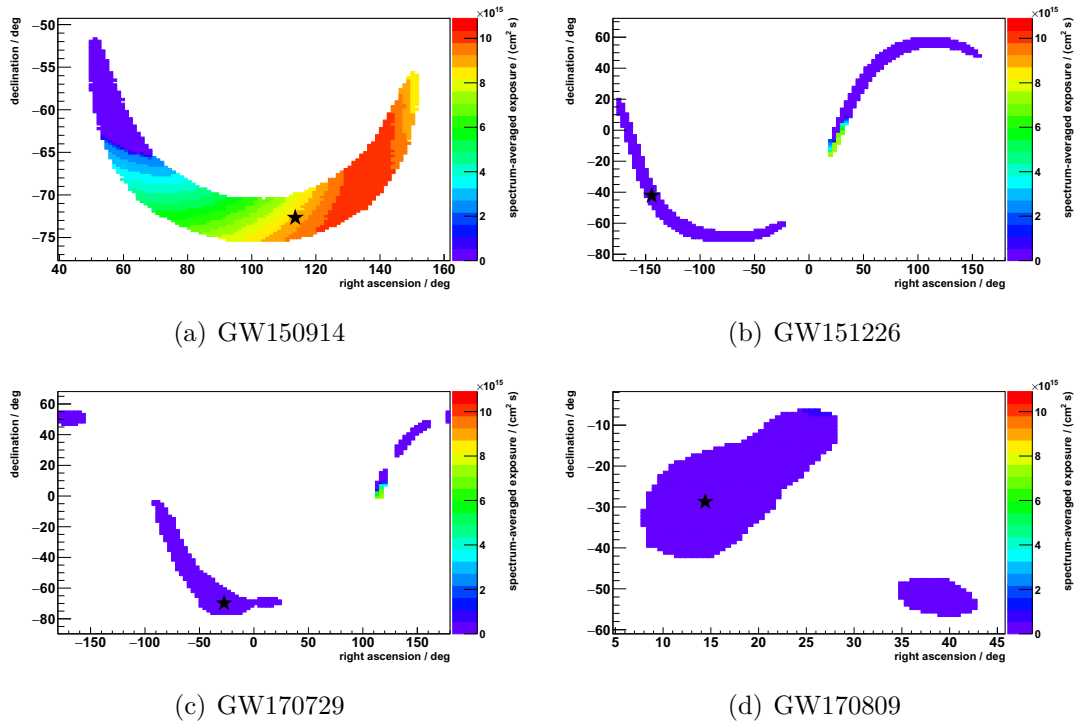
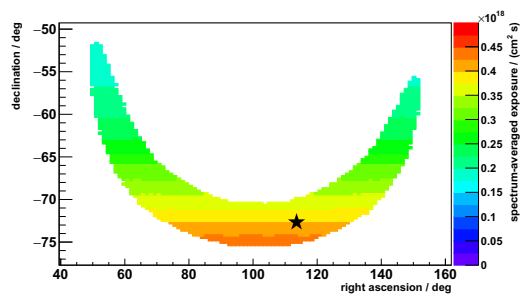
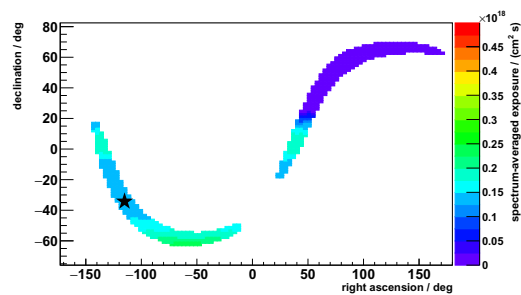


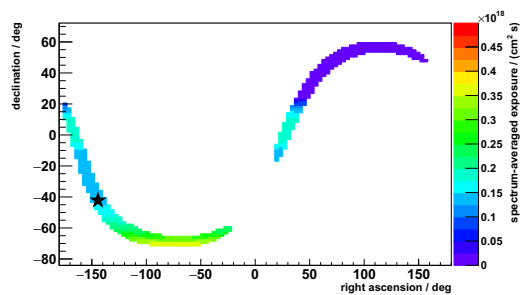
Figure 13.13: The spectrum-averaged exposure to UHE photons for source directions inside the 90% contours for all GW events with a non-zero overlap between their 90% contour region and the field of view of the photon search during the 1000 s time window. The black stars mark the directions with the highest probabilities to contain the source. While 80% of the region enclosed by the 90% contour of GW150914 have been observed during the 1000 s time window, most parts of the 90% regions of GW151226 (6.4% inside the field of view), GW170729 (2.3% inside the field of view) and GW170809 (0.42 % inside field of view – at declination angles $\gtrsim -8^\circ$) could not be observed during that period.



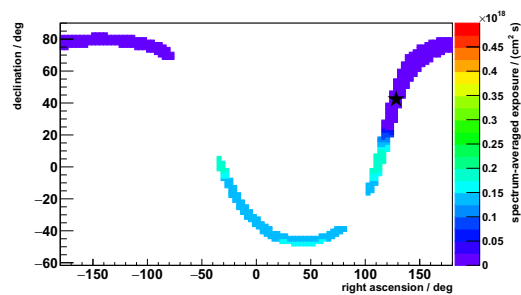
(a) GW150914



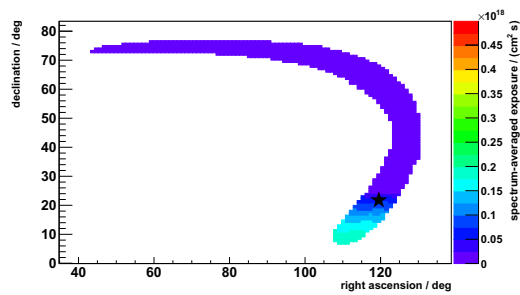
(b) GW151012



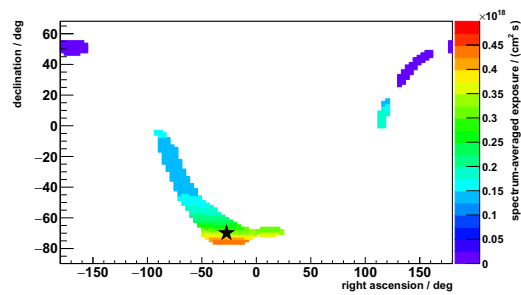
(c) GW151226



(d) GW170104



(e) GW170608



(f) GW170729

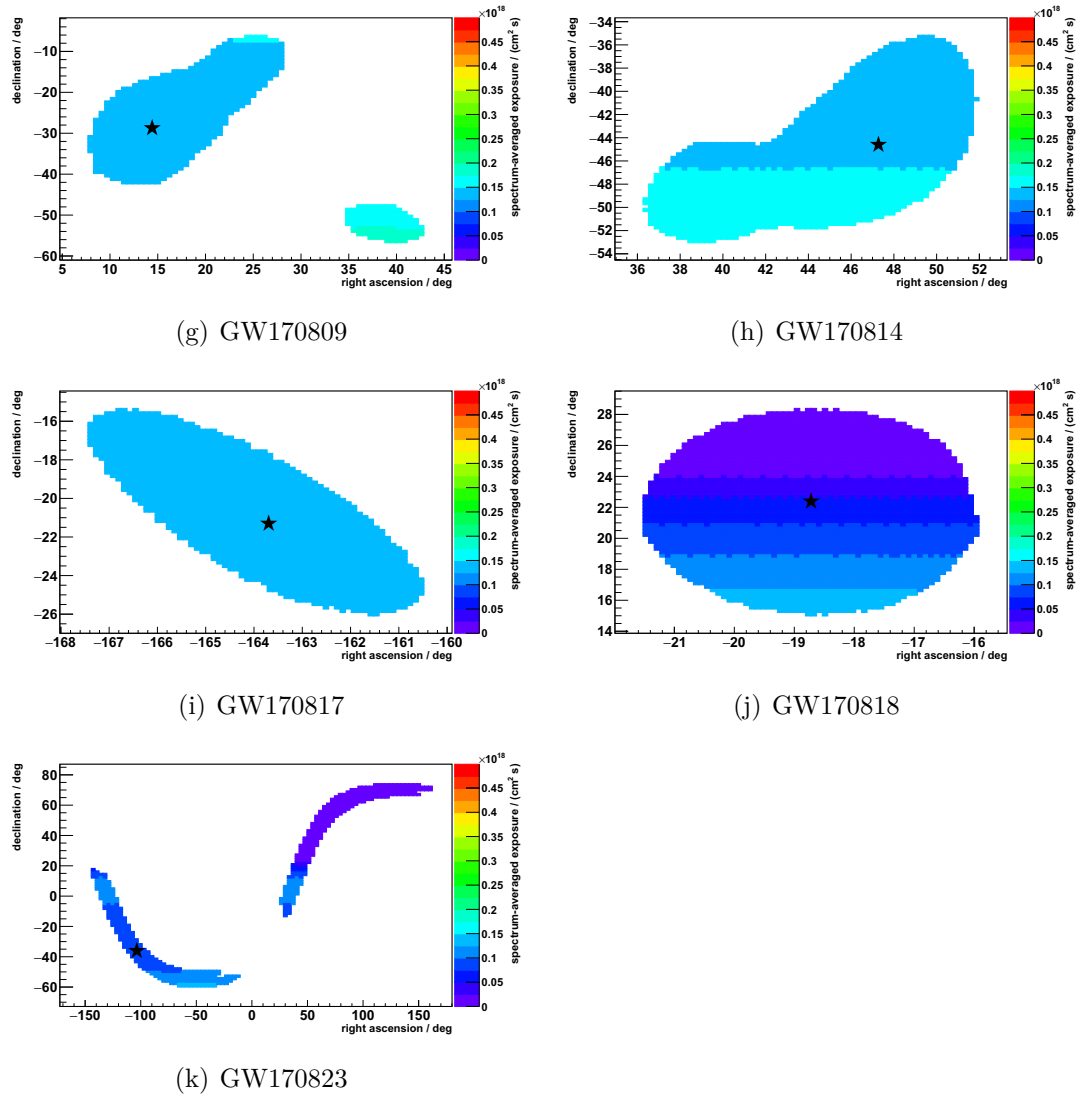


Figure 13.14: The spectrum-averaged exposure to UHE photons for source directions inside the 90% contours for all eleven GW events during the 1 d time window. The black stars mark the directions with the highest probabilities to contain the source. For comparability, the z-axis of all plots cover the same range.

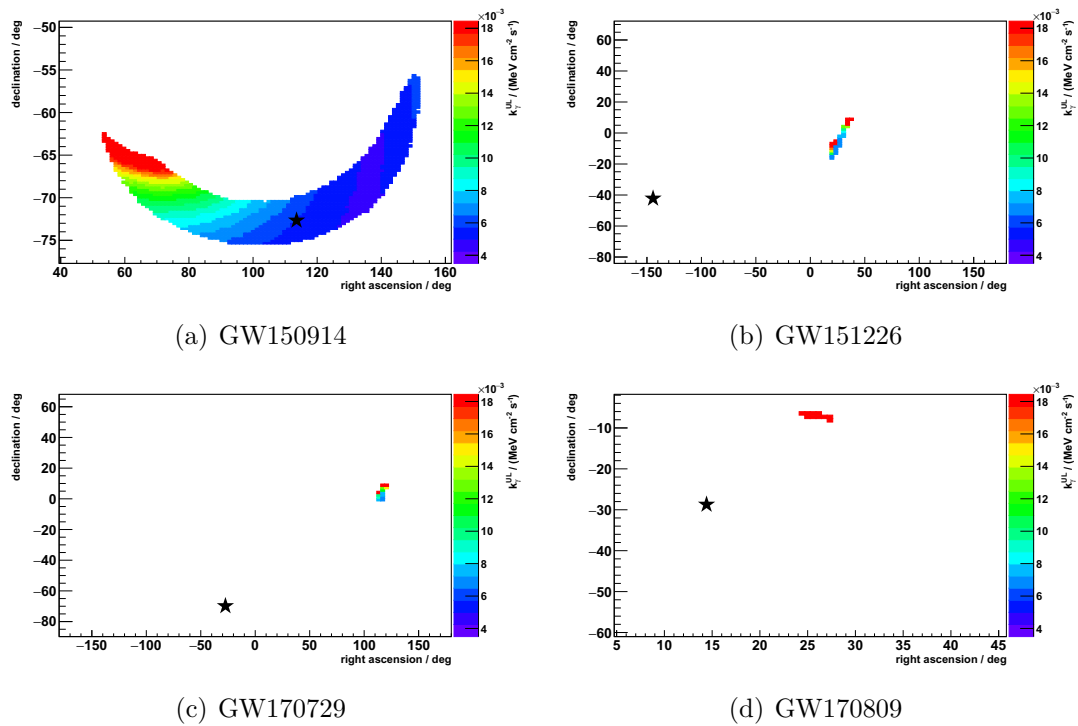
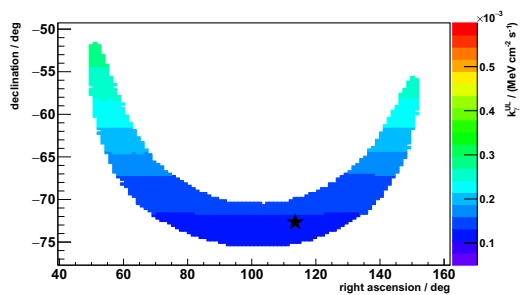
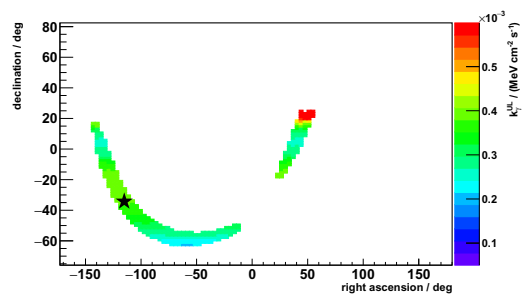


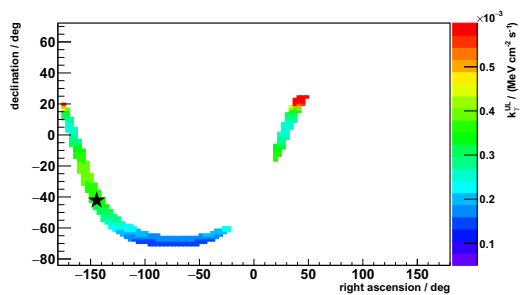
Figure 13.15: The upper limits on the flux normalization factor k_γ for source directions inside the 90% contours for all GW events with a non-zero overlap between their 90% contour region and the field of view of the photon search during the 1000 s time window. The black stars mark the directions with the highest probabilities to contain the source.



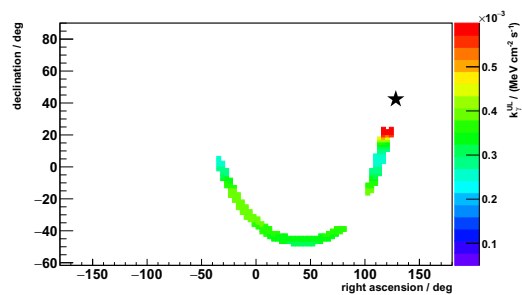
(a) GW150914



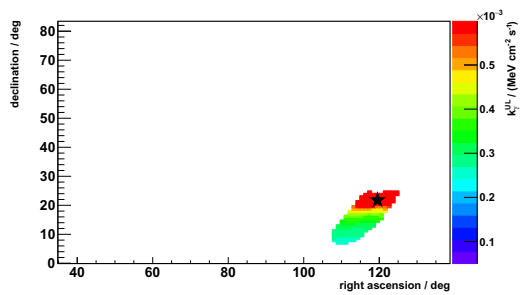
(b) GW151012



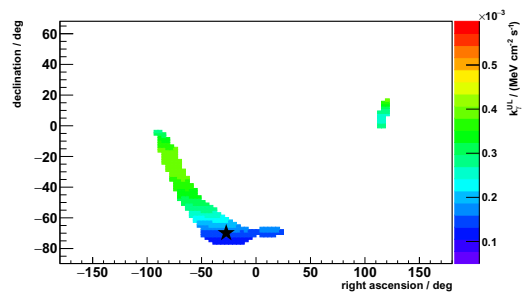
(c) GW151226



(d) GW170104



(e) GW170608



(f) GW170729

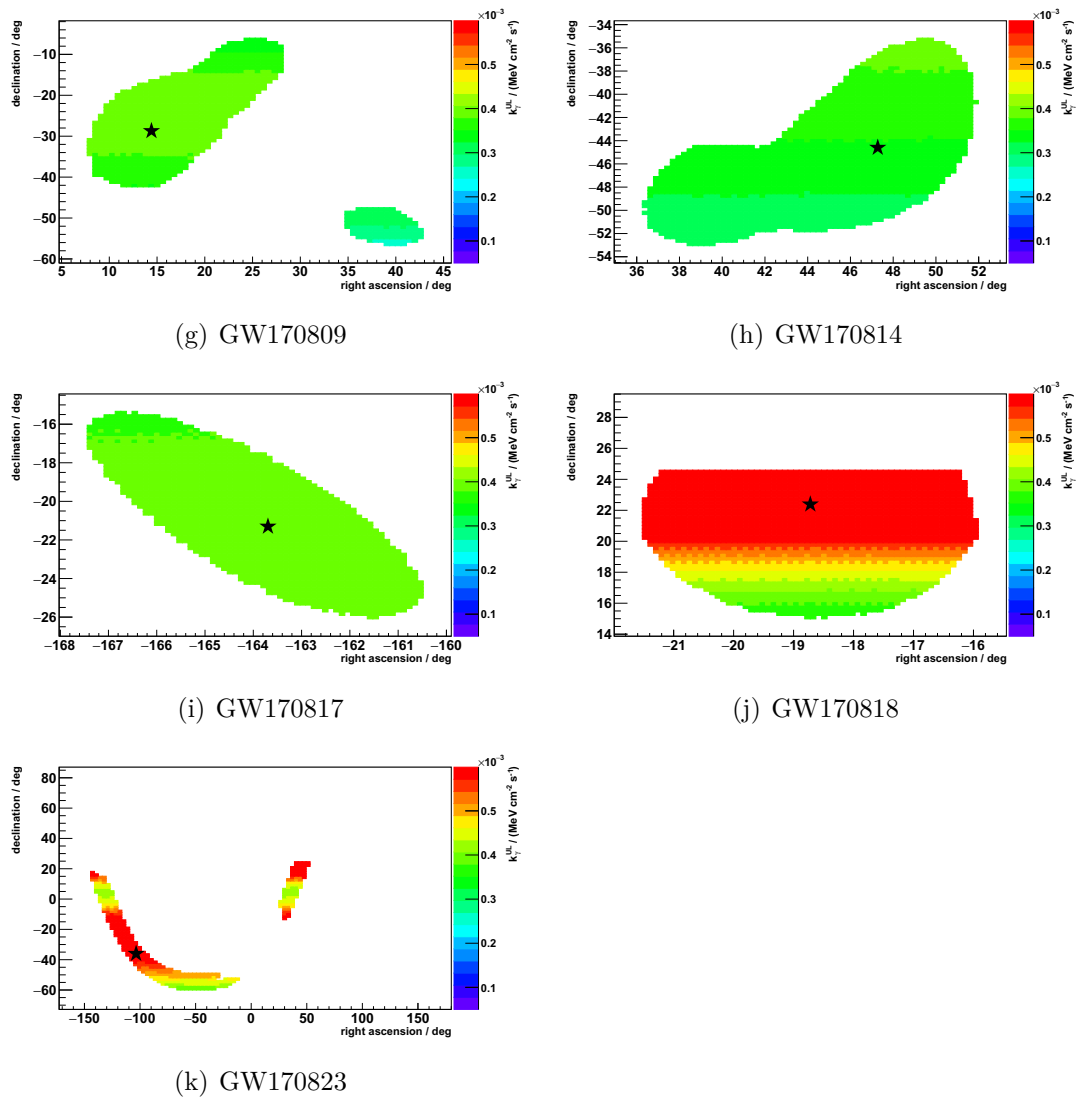


Figure 13.16: The upper limits on the flux normalization factor k_γ for source directions inside the 90% contours for all eleven GW events during the 1 d time window. The black stars mark the directions with the highest probabilities to contain the source.

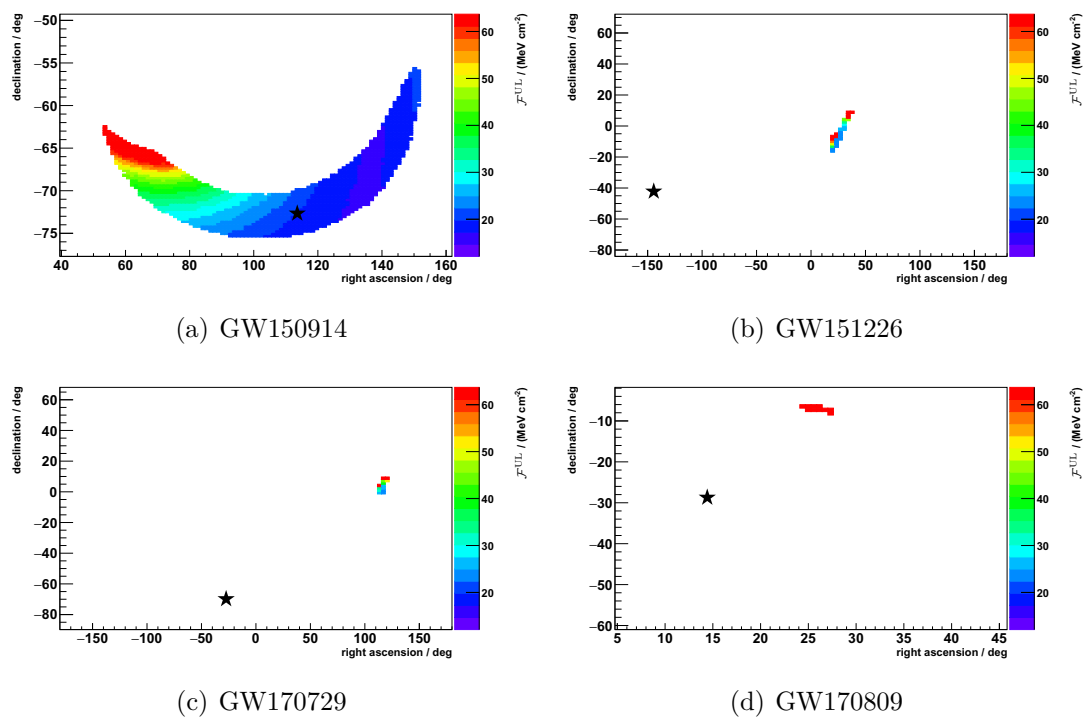
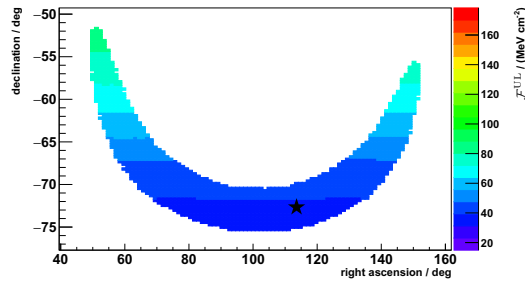
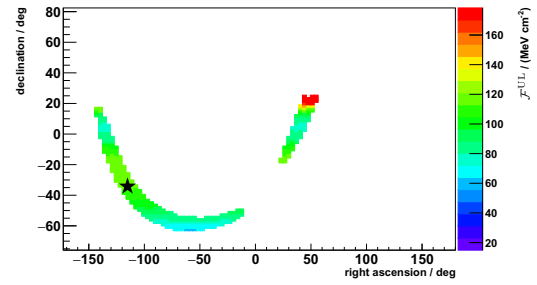


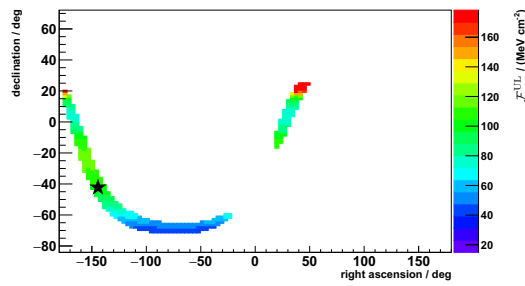
Figure 13.17: The upper limits on the spectral fluence \mathcal{F} for source directions inside the 90% contours for all GW events with a non-zero overlap between their 90% contour region and the field of view of the photon search during the 1000 s time window. The black stars mark the directions with the highest probabilities to contain the source.



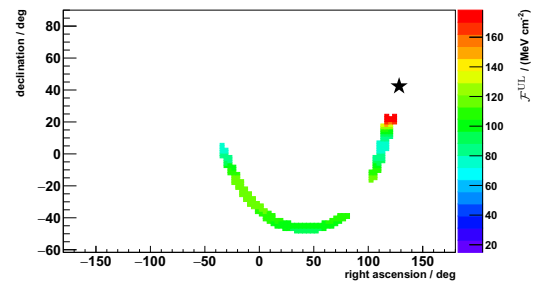
(a) GW150914



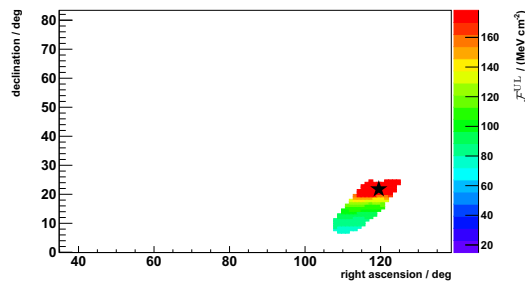
(b) GW151012



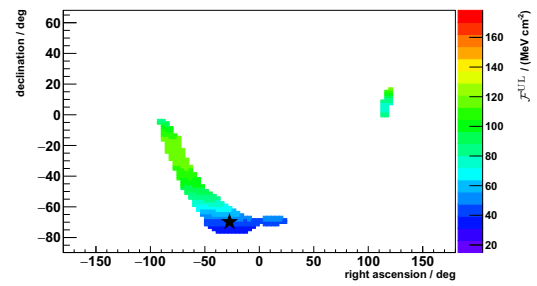
(c) GW151226



(d) GW170104



(e) GW170608



(f) GW170729

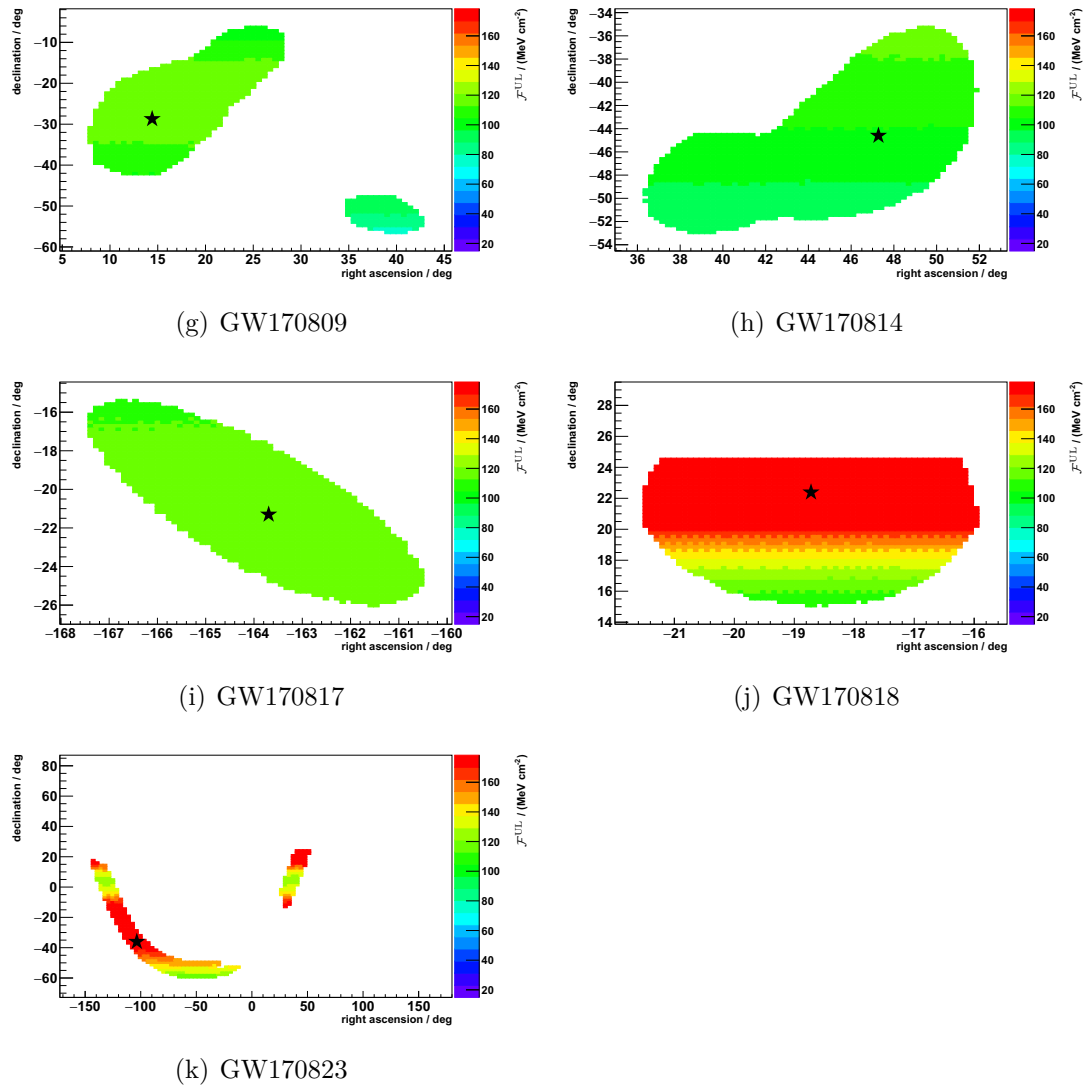


Figure 13.18: The upper limits on the spectral fluence \mathcal{F} for source directions inside the 90% contours for all eleven GW events during the 1 d time window. The black stars mark the directions with the highest probabilities to contain the source.

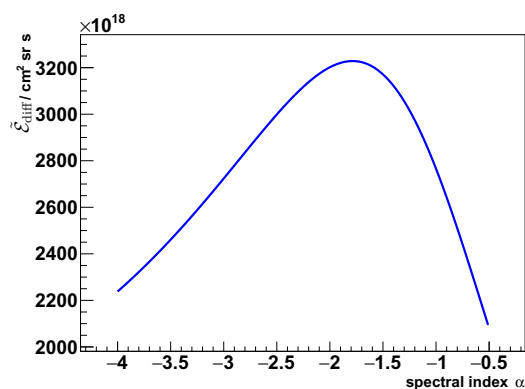
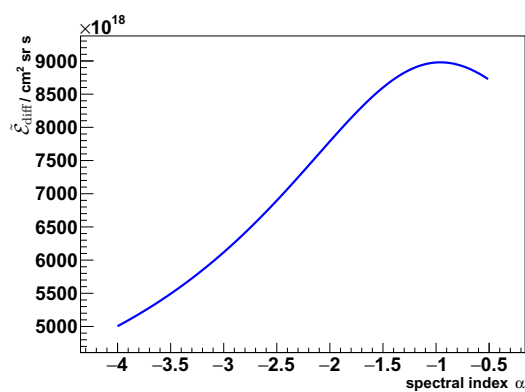
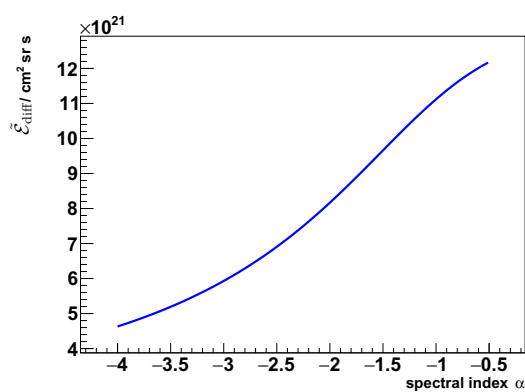
(a) $30^\circ \leq \theta < 40^\circ$ (b) $40^\circ \leq \theta < 50^\circ$ (c) $50^\circ \leq \theta < 60^\circ$

Figure 13.19: The dependence of the spectrum-averaged photon exposure $\tilde{\mathcal{E}}_{\text{diff}}$ in the search period from January 2004 to June 2018 on the spectral index α . The curves of $\tilde{\mathcal{E}}_{\text{diff}}(\alpha)$ are shown here separately in three different zenith angle bins.

13.4. Appendix of Chapter 9

GW event	$b_i(\Omega_{90\%})$	GW event	$b_i(\Omega_{90\%})$
GW150914	3.957×10^{-5}	GW190828a	1.715×10^{-5}
GW151012	9.573×10^{-5}	GW190828b	3.649×10^{-5}
GW151226	8.428×10^{-5}	GW190901	1.042×10^{-3}
GW170104	4.499×10^{-5}	GW190910a	2.125×10^{-4}
GW170608	8.594×10^{-6}	GW190910b	1.889×10^{-4}
GW170729	9.212×10^{-5}	GW190915	1.440×10^{-8}
GW170809	2.583×10^{-5}	GW190923	1.719×10^{-4}
GW170814	8.333×10^{-6}	GW190924	2.596×10^{-5}
GW170817	2.413×10^{-6}	GW190930a	5.535×10^{-5}
GW170818	1.724×10^{-6}	GW190930b	1.722×10^{-3}
GW170823	6.502×10^{-5}	GW191105	4.246×10^{-5}
GW190408	6.374×10^{-6}	GW191109	1.080×10^{-4}
GW190412	8.264×10^{-6}	GW191129	9.545×10^{-5}
GW190421	2.254×10^{-4}	GW191204	1.062×10^{-5}
GW190425	5.477×10^{-4}	GW191105	4.783×10^{-4}
GW190426	2.257×10^{-5}	GW191113	2.982×10^{-4}
GW190503	4.239×10^{-5}	GW191115	2.485×10^{-5}
GW190510	1.001×10^{-4}	GW191116	1.112×10^{-5}
GW190512	2.240×10^{-5}	GW191122	1.539×10^{-4}
GW190513	2.177×10^{-5}	GW200105	4.416×10^{-4}
GW190517	1.134×10^{-4}	GW200112	2.022×10^{-4}
GW190519	4.336×10^{-5}	GW200114	3.138×10^{-5}
GW190521a	2.166×10^{-6}	GW200115	4.908×10^{-5}
GW190521b	8.028×10^{-6}	GW200128	1.388×10^{-4}
GW190602	9.064×10^{-5}	GW200129	4.916×10^{-6}
GW190630	1.372×10^{-4}	GW200208	2.746×10^{-6}
GW190701	5.786×10^{-6}	GW200213	1.153×10^{-4}
GW190706	3.228×10^{-5}	GW200219	3.308×10^{-5}
GW190707	7.640×10^{-5}	GW200224	8.661×10^{-6}
GW190718	3.985×10^{-4}	GW200225	0
GW190720	3.637×10^{-5}	GW200302	2.694×10^{-4}
GW190727	1.837×10^{-5}	GW200311	4.206×10^{-6}
GW190728	1.042×10^{-5}	GW200316	3.168×10^{-5}
GW190814	2.627×10^{-6}		

Table 13.7: The background contributions b_i during the 1 d time windows from the 90% contours of the convolved localization maps of all GW events until the end of O3 as they are plotted in Fig. 9.3. The information about the preliminary GW events measured during O3 were taken from the publicly accessible database GraceDB [URL8]. In order to reduce the computation time of the convolution with the directional resolution of the Auger SD, the HEALPix resolution (see Sec. 6.3) has been reduced to $k \leq 7$. The numerical uncertainties that are introduced by that reduction are of the order $\lesssim 2\%$. In this table, the GW naming scheme used in [AB19b] for the events from O1 and O2 has been adopted for convenience to label the preliminary events of O3.

13.5. Appendix of Chapter 11

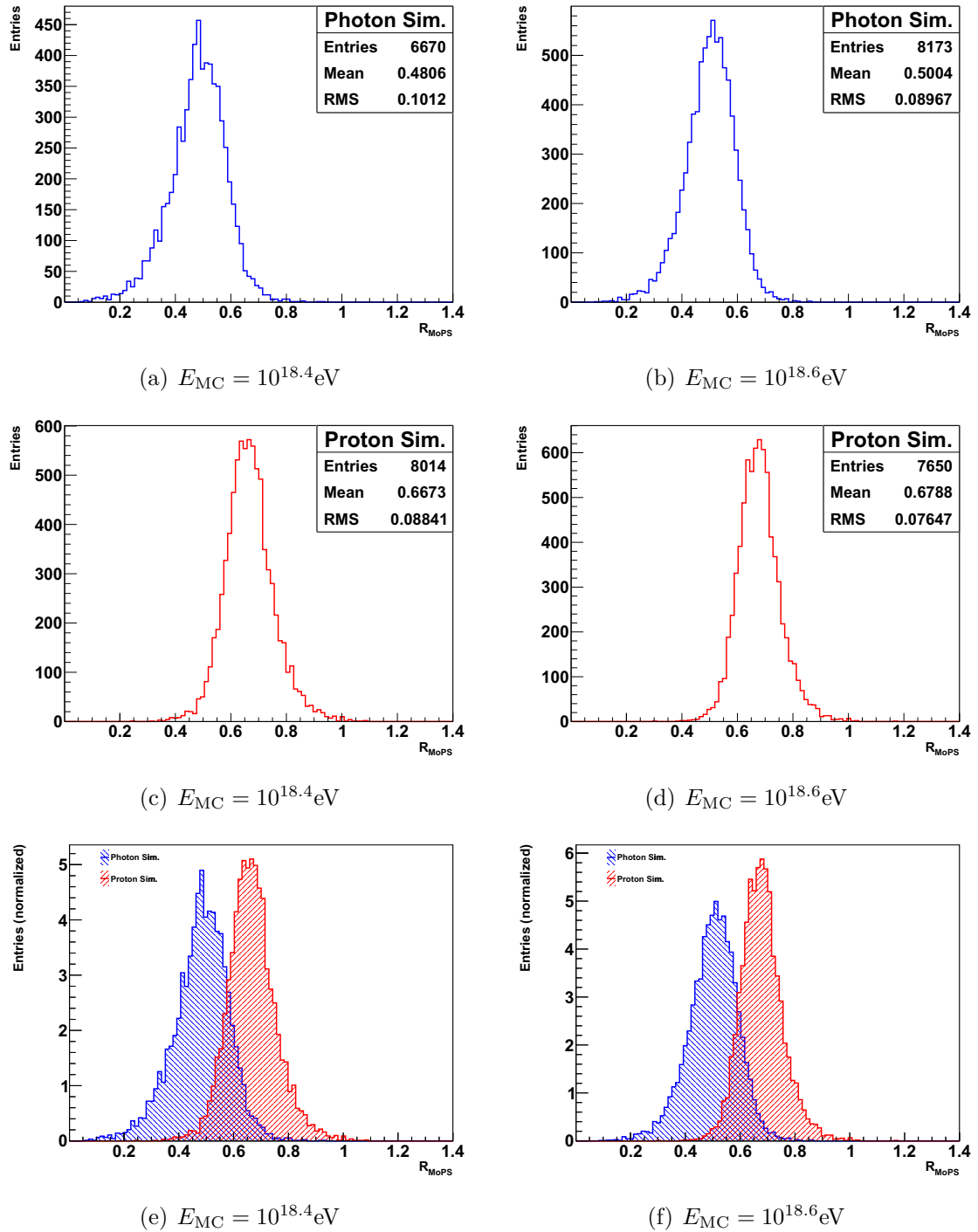


Figure 13.20: The distributions of R_{MoPS} from simulated sets of photon events (top row) and proton events (middle row) at $10^{18.4} \text{ eV}$ (left column) and $10^{18.6} \text{ eV}$ (right column). The bottom row shows the normalized overlays of the distributions. The simulation sets (B_γ and B_p) are described in Sec. 6.1.2.

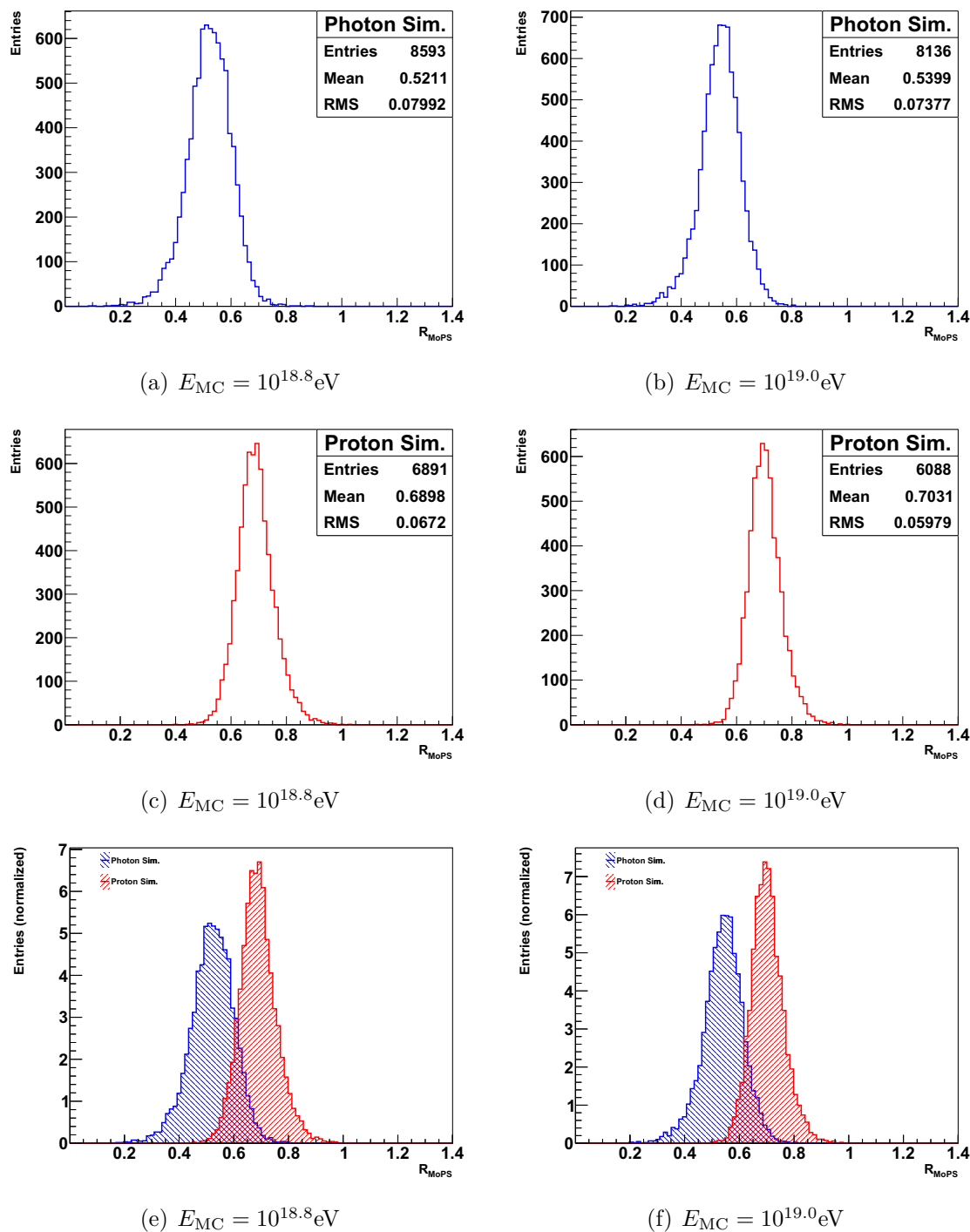


Figure 13.21: The distributions of R_{MoPS} from simulated sets of photon events (top row) and proton events (middle row) at $10^{18.8} \text{eV}$ (left column) and $10^{19.0} \text{eV}$ (right column). The bottom row shows the normalized overlays of the distributions. The simulation sets (B_γ and B_p) are described in Sec. 6.1.2.

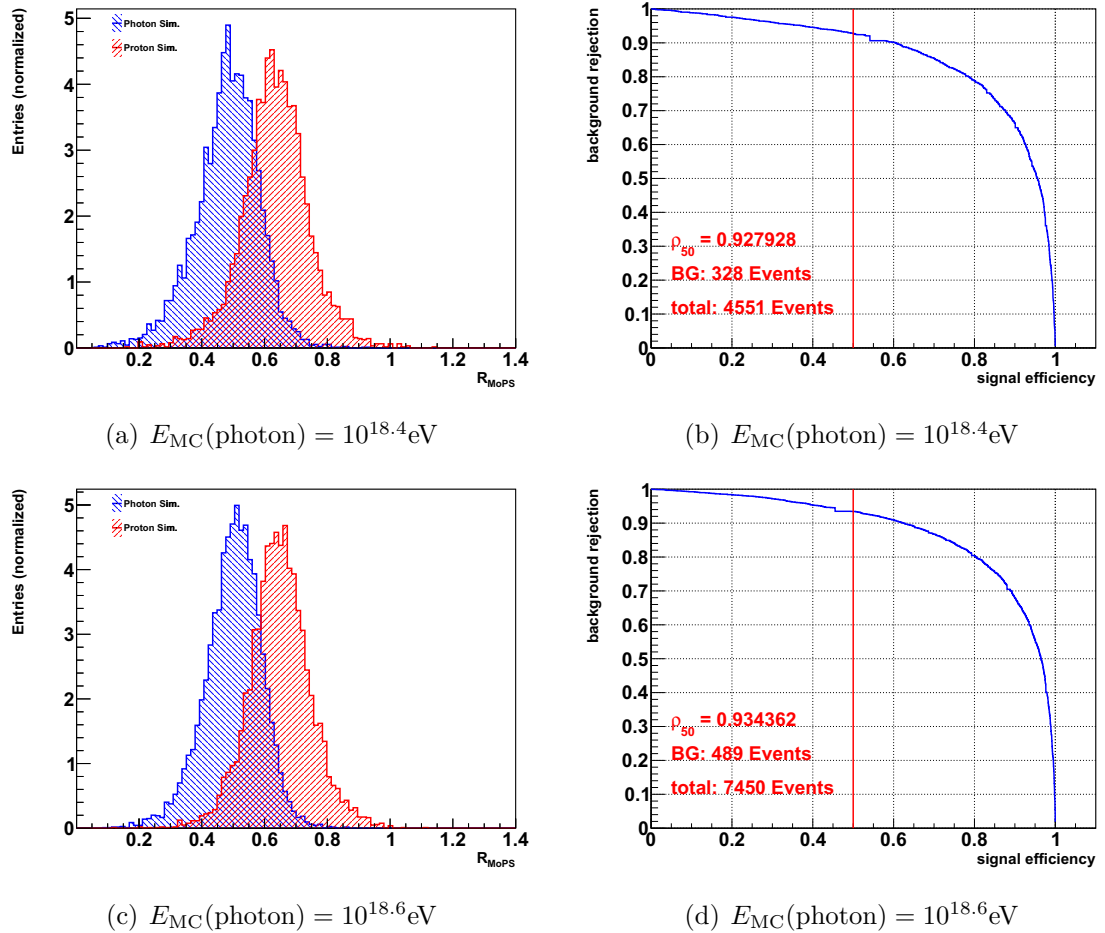


Figure 13.22: The R_{MoPS} distributions (left column) and the corresponding ROC curves (right column) of a set of photon events simulated at (a) $10^{18.4} \text{eV}$ and (c) $10^{18.6} \text{eV}$. The proton sets to which the photon distributions are compared have simulated energies that are by a factor of $10^{-0.4}$ lower which leads to comparable photon energies E_γ . The reconstructed photon energies E_γ are $10^{18.319 \pm 0.002} \text{eV}$ ($10^{18.290 \pm 0.002} \text{eV}$) for the photon (proton) set of (a) and $10^{18.526 \pm 0.002} \text{eV}$ ($10^{18.499 \pm 0.002} \text{eV}$) for the photon (proton) set of (c). The simulation sets (B_γ and B_p) are described in Sec. 6.1.2.

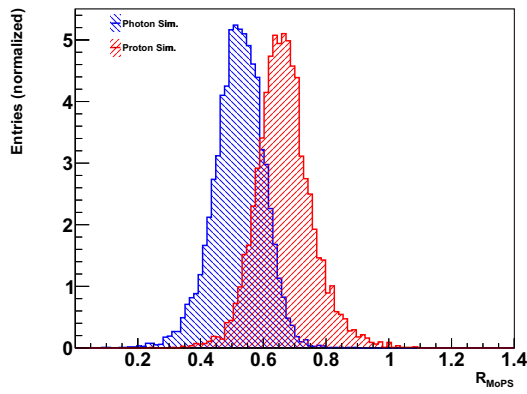
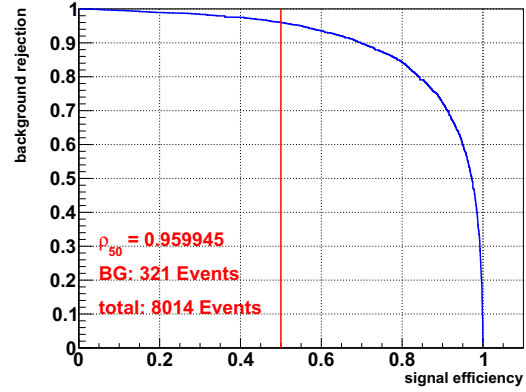
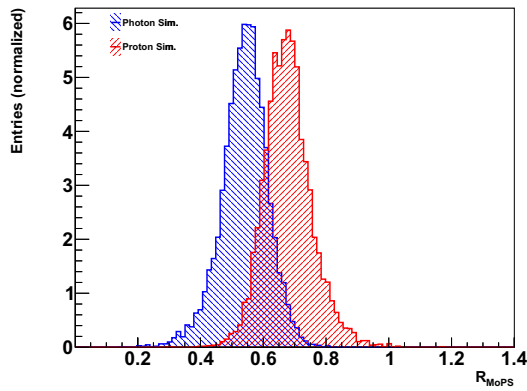
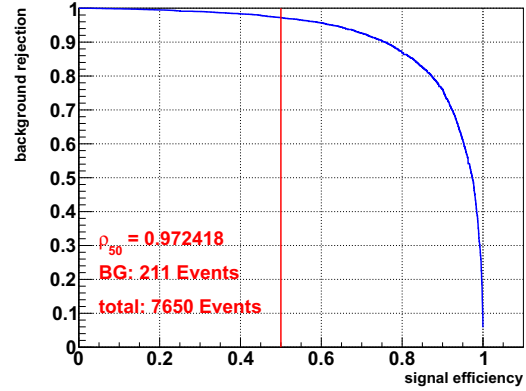
(a) $E_{\text{MC}}(\text{photon}) = 10^{18.8}\text{eV}$ (b) $E_{\text{MC}}(\text{photon}) = 10^{18.8}\text{eV}$ (c) $E_{\text{MC}}(\text{photon}) = 10^{19.0}\text{eV}$ (d) $E_{\text{MC}}(\text{photon}) = 10^{19.0}\text{eV}$

Figure 13.23: The R_{MoPS} distributions (left column) and the corresponding ROC curves (right column) of a set of photon events simulated at (a) $10^{18.8}\text{eV}$ and (c) $10^{19.0}\text{eV}$. The proton sets to which the photon distributions are compared have simulated energies that are by a factor of $10^{-0.4}$ lower which leads to comparable photon energies E_γ . The reconstructed photon energies E_γ are $10^{18.722 \pm 0.002}\text{eV}$ ($10^{18.711 \pm 0.002}\text{eV}$) for the photon (proton) set of (a) and $10^{18.915 \pm 0.002}\text{eV}$ ($10^{18.9096 \pm 0.0015}\text{eV}$) for the photon (proton) set of (c). The simulation sets (B_γ and B_p) are described in Sec. 6.1.2.

Bibliography

- [AA12] DE ANGELIS, A., GUAITA, C., from the collection of R. Fricke, distributed under the Creative Commons: Attribution-Share Alike 3.0 Unported (CC BY-SA 3.0) license.
- [AA14] AAB ET AL., THE PIERRE AUGER COLLABORATION, *Depth of Maximum of Air-Shower Profiles at the Pierre Auger Observatory: Composition Implications*, The Physical Review D **90**, 2014.
- [AA15a] AAB, A. ET AL., THE PIERRE AUGER COLLABORATION, *The Pierre Auger Cosmic Ray Observatory*, Nuclear Instruments and Methods in Physics Research A **798**, 172-213, 2015.
- [AA15b] AAB, A. ET AL., THE PIERRE AUGER COLLABORATION, *The Pierre Auger Collaboration: Contributions to the 34th International Cosmic Ray Conference (ICRC 2015)*, Proceedings of Science (ICRC2015) 420.
- [AA15c] AAB, A. ET AL., THE PIERRE AUGER COLLABORATION, *The Pierre Auger Observatory Upgrade “AugerPrime” – Preliminary Design Report*, arXiv:1604.03637 [astro-ph.IM], 2015.
- [AA15d] AASI, A. ET AL., THE LIGO SCIENTIFIC COLLABORATION, *Advanced LIGO*, Classical and Quantum Gravity **32**, 2015.
- [AA16a] AAB, A. ET AL., THE PIERRE AUGER COLLABORATION, *A targeted search for point sources of EeV photons with the Pierre Auger Observatory*, The Astrophysical Journal Letters **837**, L25, 2016.
- [AA16b] AAB, A. ET AL., THE PIERRE AUGER COLLABORATION, *Ultrahigh-energy neutrino follow-up of Gravitational Wave events GW150914 and GW151226 with the Pierre Auger Observatory*, Physical Review D **94**, 122007, 2016.
- [AA16c] AAB, A. ET AL., THE PIERRE AUGER COLLABORATION, *Prototype muon detectors for the AMIGA component of the Pierre Auger Observatory*, Journal of Instrumentation **11**, 2, 2016.
- [AA16d] AAB, A. ET AL., THE PIERRE AUGER COLLABORATION, *Evidence for a mixed mass composition at the ‘ankle’ in the cosmic-ray spectrum*, Physical Letter B **762**, 2016.
- [AA17a] AAB, A. ET AL., THE PIERRE AUGER COLLABORATION, *Search for photons above 10^{18} eV using the hybrid detector of the Pierre Auger*

- Observatory*, Journal of Cosmology and Astroparticle Physics **04**, 009, 2017.
- [AA17b] ANTARES COLLABORATION AND OTHER COLLABORATIONS, *Search for High-energy Neutrinos from Binary Neutron Star Merger GW170817 with ANTARES, IceCube, and the Pierre Auger Observatory*, The Astrophysical Journal Letters **850**, L35, 2017.
- [AA17d] AAB, A. ET AL., THE PIERRE AUGER COLLABORATION, *Combined fit of spectrum and composition data as measured by the Pierre Auger Observatory*, Journal of Cosmology and Astroparticle Physics **4**, 038, 2017.
- [AA18] AAB, A. ET AL., THE PIERRE AUGER COLLABORATION, *Large-scale Cosmic-Ray Anisotropies above 4 EeV Measured by the Pierre Auger Observatory*, The Astrophysical Journal **868**, 4, 2018.
- [AA20a] AAB, A. ET AL., THE PIERRE AUGER COLLABORATION, *A search for Ultra-High Energy neutrinos from TXS0506+056 using the Pierre Auger Observatory*, The Astrophysical Journal **902**, 105, 2020.
- [AA20b] Aab, A. et al., The Pierre Auger Collaboration, *Features of the energy spectrum of cosmic rays above 2.5×10^{18} eV using the Pierre Auger Observatory*, The Physical Review Letters **125**, 121106, 2020.
- [AB09] ABBOTT, B. P. ET AL., THE LIGO SCIENTIFIC COLLABORATION, *LIGO: The Laser Interferometer Gravitational-Wave Observatory*, Reports on Progress in Physics **72**, 7, 2009.
- [AB13] ACHARYA, B. S. ET AL., *Introducing the CTA concept*, Astroparticle Physics **43**, 2013.
- [AB16] ABBOT, B. P. ET AL., THE LIGO SCIENTIFIC COLLABORATION, THE VIRGO COLLABORATION, *Observation of Gravitational Waves from a Binary Black Hole Merger*, The Physical Review Letters **116**, 2016.
- [AB17a] ABBOTT, B. P. ET AL., THE LIGO, VIRGO AND OTHER COLLABORATIONS, *Multi-messenger Observations of a Binary Neutron Star Merger*, The Astrophysical Journal Letters **848**, L2, 2017.
- [AB17b] ABBOTT, B. P. ET AL., THE LIGO, VIRGO AND OTHER COLLABORATIONS, *Gravitational Waves and Gamma-Rays from a Binary Neutron Star Merger: GW170817 and GRB 170817A*, The Astrophysical Journal Letters **848**, L13, 2017.

-
- [AB18b] ABBOTT, B. P. ET AL., THE KAGRA COLLABORATION, THE LIGO SCIENTIFIC COLLABORATION AND THE VIRGO COLLABORATION, *Prospects for observing and localizing gravitational-wave transients with Advanced LIGO, Advanced Virgo and KAGRA*, Living Reviews in Relativity (2018) 21: 3.
- [AB19a] ABBOTT, B. P. ET AL., THE LIGO SCIENTIFIC COLLABORATION AND THE VIRGO COLLABORATION, *A gravitational-wave measurement of the Hubble constant following the second observing run of Advanced LIGO and Virgo*, arXiv:1908.06060 [astro-ph.CO], 2019.
- [AB19b] ABBOTT, B. P. ET AL., THE LIGO SCIENTIFIC COLLABORATION AND THE VIRGO COLLABORATION, *GWTC-1: A Gravitational-Wave Transient Catalog of Compact Binary Mergers Observed by LIGO and Virgo during the First and Second Observing Runs*, The Physical Review X **9**, 031040, 2019.
- [AB20a] ABBOTT, B. P. ET AL., THE KAGRA COLLABORATION, THE LIGO SCIENTIFIC COLLABORATION AND THE VIRGO COLLABORATION, *Prospects for Observing and Localizing Gravitational-Wave Transients with Advanced LIGO, Advanced Virgo and KAGRA*, arXiv:1304.0670v10 (updated version of [AB18b]), 2020.
- [AB20b] ABBOTT, B. P. ET AL., THE LIGO SCIENTIFIC COLLABORATION AND THE VIRGO COLLABORATION, *GW190425: Observation of a Compact Binary Coalescence with Total Mass $\sim 3.4 M_{\odot}$* , The Astrophysical Journal Letters **892**, L3, 2020.
- [AB20c] ABBOTT, B. P. ET AL., THE LIGO SCIENTIFIC COLLABORATION AND OTHER COLLABORATIONS, *Optically targeted search for gravitational waves emitted by core-collapse supernovae during the first and second observing runs of advanced LIGO and advanced Virgo*, The Physical Review D **101**, 084002, 2020.
- [AC32] ANDERSON, C. D., *The Apparent Existence of Easily Deflectable Positives*, Science **76**, 1967, 1932.
- [AC33] ANDERSON, C. D., *The Positive Electron*, The Physical Review **43**, 491, 1933.
- [AC36] ANDERSON, C. D., NEDDERMEYER, S. H. *Cloud Chamber Observations of Cosmic Rays at 4300 Meters Elevation and Near Sea-Level*, The Physical Review **50**, 163, 1936.
- [AD02] ALTSCHULER, D. R., *The National Astronomy and Ionosphere Center's (NAIC) Arecibo Observatory in Puerto Rico*, Single-Dish Radio Astronomy: Techniques and Applications, ASP Conference Series, Vol. 278, 2002.

- [AE08] ARIK, E. ET AL., THE CAST COLLABORATION, *Solar axion search with the CAST experiment*, Proceedings of the 34th International Conference on High Energy Physics, arXiv:0810.1874v1 [hep-ex], 2008.
- [AF15] ACERNESE, F. ET AL., THE VIRGO COLLABORATION, *Advanced Virgo: a second-generation interferometric gravitational wave detector*, Classical and Quantum Gravity **32**, 2015.
- [AH07] AHN, H. S. ET AL., *The Cosmic Ray Energetics and Mass (CREAM) instrument*, Nuclear Instruments and Methods in Physics Research A **579**, 3, 2007.
- [AI08] ALLEKOTTE, I. ET AL., THE PIERRE AUGER COLLABORATION, *The Surface Detector System of the Pierre Auger Observatory*, Nuclear Instruments and Methods in Physics Research A **586**, 409, 2008.
- [AJ10a] ABRAHAM, J. ET AL., THE PIERRE AUGER COLLABORATION, *Trigger and aperture of the surface detector array of the Pierre Auger Observatory*, Nuclear Instruments and Methods in Physics Research A **613**, 29-39, 2010.
- [AJ10b] ABRAHAM, J. ET AL., *The Fluorescence Detector of the Pierre Auger Observatory*, Nuclear Instruments and Methods in Physics Research A **620**, 227, 2010.
- [AM07a] AVE, M. ET AL., THE AIRFLY COLLABORATION, *Measurement of the pressure dependence of air fluorescence emission induced by electrons*, Astroparticle Physics **28**, 1, 2007.
- [AM07b] AVE, M. ET AL., THE PIERRE AUGER COLLABORATION *Reconstruction accuracy of the surface detector array of the Pierre Auger Observatory*, Contribution to the 30th International Cosmic Ray Conference (ICRC 2007), arXiv:0709.2125v1 [astro-ph], 2007.
- [AM13] AVE, M. ET AL., *Precise measurement of the absolute fluorescence yield of the 337nm band in atmospheric gases*, Astroparticle Physics **42**, 2013.
- [AM18a] THE ICECUBE COLLABORATION AND OTHER COLLABORATIONS, *Multimessenger observations of a flaring blazar coincident with high-energy neutrino IceCube-170922A*, Science **361**, 6398, 2018.
- [AM18b] AARTSEN, M. G. ET AL., THE ICECUBE COLLABORATION, *Neutrino emissions from the direction of the blazar TXS 0506+056 prior to the IceCube-170922A alert*, Science **361**, 147-151, 2018.
- [AM19] AMENOMORI, M. ET AL., THE TIBET AS γ COLLABORATION, *First Detection of Photons with Energy Beyond 100 TeV from an Astrophysical Source*, The Physical Review Letters **123**, 5, 2019.

-
- [AP11] ABREU, P., ET AL., *The exposure of the hybrid detector of the Pierre Auger Observatory*, *Astroparticle Physics* **34**, 6, 2011.
- [AP38a] AUGER, P. V., GRIVET-MEYER, T., MAZE, R., *Grandes gerbes cosmiques atmosphériques contenant des corpuscules ultra-pénétrantes*, *Comptes Rendus, Académie des Sciences* **206**, 1938.
- [AP38b] AUGER, P. V., MAZE, R., *Les grandes gerbes cosmiques de l'atmosphère*, *Comptes Rendus, Académie des Sciences* **207**, 1938.
- [AP39] AUGER, P. V. ET AL. *Extensive Cosmic-Ray Showers*, *Reviews of Modern Physics* **11**, 1939.
- [AR13] ABBASI, R. U. ET AL., THE ICECUBE COLLABORATION, *IceTop: The surface component of IceCube*, *Nuclear Instruments and Methods in Physics Research A* **700**, 1, 2013.
- [AR19] ABBASI, R. U. ET AL., *Constraints on the diffuse photon flux with energies above 10^{18} eV using the surface detector of the Telescope Array experiment*, *Astroparticle Physics* **110**, 2019.
- [AS02] ARGIRO, S. ET AL., *Proposed Design for Auger DPA Software*, Pierre Auger Collaboration internal note GAP 2002_21, 2002. The Auger Offline Software Wiki <https://www.auger.unam.mx/AugerWiki/OfflineSoftware>, state July 2020.
- [AS03] AGOSTINELLI, S. ET AL., *Geant4—a simulation toolkit*, *Nuclear Instruments and Methods in Physics Research A* **506**, 3, 2003.
- [AS16a] ADRIÁN-MARTÍNEZ, S. ET AL., ANTARES COLLABORATION AND ICECUBE COLLABORATION, *First combined search for neutrino point-sources in the Southern Hemisphere with the ANTARES and IceCube neutrino telescopes*, *The Astrophysical Journal* **823**, 65, 2016.
- [AS16b] ADRIÁN-MARTÍNEZ, S. ET AL., ANTARES COLLABORATION, ICECUBE COLLABORATION, LIGO SCIENTIFIC COLLABORATION AND VIRGO COLLABORATION, *High-energy neutrino follow-up search of gravitational wave event GW150914 with ANTARES and IceCube*, *Physical Review D* **93**, 122010, 2016.
- [AT01] ANTONI, T. ET AL., THE KASCADE COLLABORATION, *Electron, Muon and Hadron Lateral Distributions Measured in Air-Showers by the KASCADE Experiment*, *Astroparticle Physics* **14**, 4, 2001.
- [AT03] ANTONI, T. ET AL., THE KASCADE COLLABORATION, *The Cosmic-Ray Experiment KASCADE*, *Nuclear Instruments and Methods in Physics Research A* **513**, 3, 2003.

- [AT12] ABU-ZAYYAD, T. ET AL., *The surface detector array of the Telescope Array experiment*, Nuclear Instruments and Methods in Physics Research A **689**, 2012.
- [AT18a] AKUTSU, T. ET AL., KAGRA COLLABORATION, *Construction of KAGRA: an Underground Gravitational Wave Observatory*, Progress of Experimental and Theoretical Physics **2018**, 1, 2018.
- [AW10] APEL, W. D. ET AL., THE KASCADE COLLABORATION, *The KASCADE-Grande experiment*, Nuclear Instruments and Methods in Physics Research A **620**, 2-3, 2010.
- [AW17] APEL, W. D. ET AL., THE KASCADE-GRANDE COLLABORATION, *KASCADE-Grande Limits on the Isotropic Diffuse Gamma-Ray Flux between 100 TeV and 1 EeV*, The Astrophysical Journal **848**, 1, 2017.
- [BA78] BELL, A. R., *The acceleration of cosmic rays in shock fronts – I*, Monthly Notices of the Royal Astronomical Society **182**, 2, 1978.
- [BC09] BONIFAZI, C. FOR THE PIERRE AUGER COLLABORATION, *The angular resolution of the Pierre Auger Observatory*, Nuclear Physics Proceedings Supplements **190**, 20, 2009.
- [BD95] BIRD, D. ET AL., *Detection of a cosmic ray with measured energy well beyond the expected spectral cutoff due to cosmic microwave radiation*, The Astrophysical Journal **441**, 144, 1995.
- [BH96] BECQUEREL, H., *Sur les radiations émises par phosphorescence*, Comptes Rendus, Académie des Sciences **122**, 1896.
- [BI17] BARTOS, I., KOKALSKI, M., *Multimessenger Astronomy*, Bristol: IOP Publishing, 2017.
- [BP00] BHATTACHARJEE, P., SIGL, G. *Origin and Propagation of Extremely High Energy Cosmic Rays*, Physics Reports **327**, 3–4, 2000.
- [BP08] BILLOIR, P., BLANCH BIGAS, O., BONIFAZI, C., *Can we recover events with a less strict T5?*, Pierre Auger Collaboration internal note GAP 2008_163, 2008.
- [BP09] BILLOIR, P., *Proposition to improve the local trigger of Surface Detector for low energy showers*, Pierre Auger Collaboration internal note GAP 2009_179, 2009.
- [BP11] BILLOIR, P., *New Proposal to improve the local trigger of the Surface Detector*, Pierre Auger Collaboration internal note GAP 2011_89, 2011.

-
- [BP15] BEZYAZEEKOV, P.A. ET AL., *Measurement of cosmic-ray air showers with the Tunka Radio Extension (Tunka-Rex)*, Nuclear Instruments and Methods in Physics Research A **802**, 1, 2015.
- [BR16] BATISTA, R. A. ET AL., *CRPropa 3 - a Public Astrophysical Simulation Framework for Propagating Extraterrestrial Ultra-High Energy Particles*, Journal of Cosmology and Astroparticle Physics **05**, 038, 2016.
- [BR50] BJORKLUND, R. ET AL., *High Energy Photons from Proton-Nucleon Collisions*, The Physical Review **77**, 2, 1950.
- [BR97] BRUN, R., RADEMAKERS, F., *ROOT - An object oriented data analysis framework*, Nuclear Instruments and Methods in Physics Research A **389**, 1997.
- [BR98] BATTISTON, R., *The Alpha Magnetic Spectrometer (AMS): search for antimatter and dark matter on the International Space Station*, Nuclear Physics Proceedings Supplements **65**, 1998.
- [BS07] BENZVI, S. Y., ET AL., *The lidar system of the Pierre Auger Observatory*, Nuclear Instruments and Methods in Physics Research A **574**, 1, 2007.
- [BS19a] BRITZEN, S. ET AL., *A cosmic collider: Was the IceCube neutrino generated in a precessing jet-jet interaction in TXS 0506+056?*, Astrophysics & Astronomy **630**, 2019.
- [BS19b] BRITZEN, S. ET AL., *A cosmic collider: Was the IceCube neutrino generated in a precessing jet-jet interaction in TXS 0506+056? (Corrigendum)*, Astrophysics & Astronomy **632**, C3, 2019.
- [BW29] BOTHE, W., KOLHÖRSTER, W., *Das Wesen der Höhenstrahlung*, Zeitschrift für Physik **56**, 1929.
- [BX06] BERTOU, X. ET AL. FOR THE PIERRE AUGER COLLABORATION, *Calibration of the surface array of the Pierre Auger Observatory*, Nuclear Instruments and Methods in Physics Research A **568**, 839, 2006.
- [BX09] BERTOU, X., *Looking for correlation between lightning and UHECR*, Pierre Auger Collaboration internal note GAP 2009_99, 2009.
- [CA17] CASTELLINA, A. FOR THE PIERRE AUGER COLLABORATION, *The dynamic range of the AugerPrime Surface Detector: technical solution and physics reach*, The Pierre Auger Observatory: Contributions to the 35th International Cosmic Ray Conference (ICRC 2017), 2017.

- [CA19] CASTELLINA, A. FOR THE PIERRE AUGER COLLABORATION, *Auger-Prime: The Pierre Auger Observatory Upgrade*, EPJ Web of Conferences (UHECR 2018) **210**, 06002, 2019.
- [CA32] COMPTON, A. H., *Progress of cosmic-ray survey*, The Physical Review **41**, 1932.
- [CA33] COMPTON, A. H., *A geographic study of cosmic-rays*, The Physical Review **43**, 1933.
- [CC34] CLOPPER, C, PEARSON, E., *The use of confidence or fiducial limits illustrated in the case of the binomial*, Biometrika **26**, 4, 1934.
- [CC85] DE COULOMB, C. A., *Troisieme memoire sur l'Electricite et le Magnetisme. Histoire de l'Academie Royale des Sciences*, Paris: 1785.
- [CC94] CUTLER, C., FLANAGAN, É. E., *Gravitational Waves from Merging Compact Binaries: How Accurately Can One Extract the Binary's Parameters from the Inspiral Wave Form?*, The Physical Review D **49**, 1994.
- [CE74] CATMULL, E., ROM, R., *A class of local interpolating splines*, New York: Academic Press, Computer Aided Geometric Design, 1974.
- [CJ27] CLAY, J., *Penetrating radiation*, Proceedings of the Royal Academy of Sciences at Amsterdam **30**, 1927.
- [CJ28] CLAY, J., *Penetrating radiation II*, Proceedings of the Royal Academy of Sciences at Amsterdam **31**, 1928.
- [CJ32] CHADWICK, J., *Possible Existence of a Neutron*, Nature **129**, 1932.
- [CP11] CARLSON, P., DE ANGELIS, A., *Nationalism and internationalism in science: the case of the discovery of cosmic rays*, The European Physical Journal H **35**, 309, 2011.
- [CP98] CURIE, P, SKŁODOWSKA CURIE, M., BÉMONT, G., *Sur une nouvelle substance fortement radio-active, contenue dans la pechblende*, Comptes Rendus, Académie des Sciences **127**, 1898.
- [CT98] CAO, T. Y., *Conceptual Developments of 20th Century Field Theories*, Cambridge: Cambridge University Press, 1998.
- [DB07] DAWSON, B. FOR THE PIERRE AUGER COLLABORATION, *Hybrid Performance of the Pierre Auger Observatory*, Proceedings of the 30th International Cosmic Ray Conference (ICRC 2007), 2007.
- [DB96] DAWSON, B. ET AL., *Simulations of a giant hybrid air shower detector*, Astroparticle Physics **5**, 3-4, 1996.

-
- [DJ20] DEBATIN, J. F., *Preparation of the Operation and Calibration of the Fluorescence Detector of AugerPrime*, Karlsruher Institut für Technologie, Ph.D. thesis Joachim Friedemann Debatin, 2020.
- [DJ96] DOUGLAS, J. N. ET AL., *The Texas survey of radio sources covering $-35^{\circ}5 < \delta < 71^{\circ}5$ at 365 MHz*, The Astronomical Journal, Vol. 111, Nr. 5, 1996.
- [DK05] DOLAG, K. ET AL., *Constrained Simulations of the Magnetic Field in the Local Universe and the Propagation of UHECRs*, Journal of Cosmology and Astroparticle Physics **1**, 009, 2005.
- [DK17] DANZMANN, K. ET AL., *LISA: Laser Interferometer Space Antenna*, LISA Consortium, 2017 https://www.elisascience.org/files/publications/LISA_L3_20170120.pdf, August 2020.
- [DP28] DIRAC, P. A. M., *The Quantum Theory of the Electron.*, Proceedings of the Royal Society of London A **778**, 1928.
- [DV19a] DECOENE, V. ET AL., *High-energy neutrinos from fallback accretion of binary neutron star merger remnants*, Journal of Cosmology and Astroparticle Physics **2020**, 004, 2020.
- [EA11a] EVE, A. S., *On the ionization of the atmosphere due to radioactive matter*, Philosophical Magazine **21**, 1911.
- [EA11b] ECKART, A. ET AL., *Coordinated Multi-Wavelength Observations of Variable Emission from the Galactic Center*, Astronomical Society of the Pacific Conference Series **439**, 2011.
- [EA15] EINSTEIN A., *Die Feldgleichungen der Gravitation*, Sitzungsberichte der Königlich Preussischen Akademie der Wissenschaften zu Berlin, 1915.
- [EA16] EINSTEIN A., *Näherungsweise Integration der Feldgleichungen der Gravitation*, Sitzungsberichte der Königlich Preussischen Akademie der Wissenschaften zu Berlin, 1916.
- [EA18] EINSTEIN A., *Über Gravitationswellen*, Sitzungsberichte der Königlich Preussischen Akademie der Wissenschaften zu Berlin, 1918.
- [EJ06] ELLIS, J., MAYES, V. E., NANOPOULOS, D. V., *UHECR Particle Spectra from Crypton Decays*, The Physical Review D **74**, 2006.
- [ES09] ESO/WF, MPIFR/ESO/APEX/A.WEISS ET AL., NASA/CXC/CFA/R.KRAFT ET AL., <https://www.eso.org/public/images/eso0903a/>, European Southern Observatory, 2009.

- [FA05] FERRARI, A. ET AL., *FLUKA: A Multi-Particle Transport Code*, Report SLAC-R-773, 2005. <http://www.fluka.org/>. Further references given in [HD16].
- [FD09] FIXEN, D. J., *The Temperature of the Cosmic Microwave Background*, The Astrophysical Journal **707**, 2, 2009.
- [FE49] FERMI, E., *On the Origin of the Cosmic Radiation*, The Physical Review **75**, 1169, 1949.
- [FG98] FELDMAN, G. J., COUSINS, R. D., *A Unified Approach to the Classical Statistical Analysis of Small Signals*, Physical Review D **57**, 3873, 1998.
- [FJ17] FRAUNHOFER, J., *Denkschriften der königlichen Akademie der Wissenschaften zu München für 1814 und 1815*, 1817.
- [FM11] FAIRBAIRN, M, RASHBA, T., TROITSKY, S, *Photon-axion mixing and ultra-high-energy cosmic rays from BL Lac type objects – Shining light through the Universe*, The Physical Review D **84**, 2011.
- [FS04] FUNK, S. ET AL., *The Trigger System of the H.E.S.S. Telescope Array*, Astroparticle Physics **22**, 2004.
- [FW11] FARR, W. M. ET AL., *The mass distribution of stellar-mass black holes*, The Astrophysical Journal **741**, 103, 2011.
- [FY17] FOMIN, YU. A. ET AL., *Constraints on the flux of $\sim (10^{16} - 10^{17.5})$ eV cosmic photons from the EAS-MSU muon data*, The Physical Review D **95**, 2017.
- [GB33] GROSS, B., *Zur Absorption der Ultrastrahlung*, Zeitschrift für Physik **83**, 1933.
- [GC05] GRUPEN, C., *Astroparticle Physics*, Berlin, Heidelberg: Springer-Verlag, 2005.
- [GD01] GORBUNOV, D. S., RAFFELT, G. G., SEMIKOZ, D. V., *Axionlike particles as ultrahigh energy cosmic rays?*, The Physical Review D **64**, 2001.
- [GD08] GRIFFITHS, D., *Introduction to Elementary Particles*, Weinheim: Wiley-VCH Verlag GmbH, 2008.
- [GG07] GELMINI, G. B., KALASHEV, O., SEMIKOZ, D. V., *GZK Photons in the Minimal Ultra High Energy Cosmic Rays Model*, Astroparticle Physics **28**, 4-5, 2007.

-
- [GG08] GELMINI, G. B., KALASHEV, O., SEMIKOZ, D. V., *GZK photons as ultra-high-energy cosmic rays*, Journal of Experimental and Theoretical Physics **106**, 1061, 2008.
- [GK05] GORSKI, K. M. ET AL., *HEALPix: A Framework for High-Resolution Discretization and Fast Analysis of Data Distributed on the Sphere*, The Astrophysical Journal **622**, 2, 2005.
- [GK56] GREISEN, K., *Cosmic Ray Showers*, Annual Review of Nuclear Science **10**, 1960.
- [GK66] GREISEN, K., *End to the Cosmic-Ray Spectrum?*, The Physical Review Letters **16**, 748, 1966.
- [GM19] GOTTOWIK, M. FOR THE PIERRE AUGER COLLABORATION, *Measurements of Inclined Air Showers with the Auger Engineering Radio Array at the Pierre Auger Observatory*, 36th International Cosmic Ray Conference (ICRC 2019), Proceedings of Science, 274, 2019.
- [GP10] GRIEDER, P. K. F., *Extensive Air Showers: High Energy Phenomena and Astrophysical Aspects: A Tutorial, Reference Manual and Data Book*, Berlin, Heidelberg: Springer-Verlag, 2010.
- [GP13] GRINGER, P. R., https://commons.wikimedia.org/wiki/File:EM_spectrumrevised.png, April 2020, distributed under the Creative Commons: Attribution-Share Alike 3.0 Unported (CC BY-SA 3.0) license, 2013.
- [GT77] GAISSER, T., HILLAS, A. M., *Reliability of the Method of Constant Intensity Cuts for Reconstructing the Average Development of Vertical Showers*, Proceedings of the 15th International Cosmic Ray Conference (ICRC 1977), 1977.
- [HA51] HEIDEL, A., *The Babylonian Genesis*, 2nd edition, Chicago: University of Chicago Press, 1951.
- [HA84] HILLAS, A. M., *The origin of ultra-high-energy cosmic rays*, Annual Review of Astronomy and Astrophysics **22**, 1984.
- [HC18a] HEITER, C. ET AL., *Production and propagation of ultra-high-energy photons using CRPropa 3*, Astroparticle Physics **102**, 39-50, 2018.
- [HD16] HECK, D., PIEROG, T., *Extensive Air Shower Simulations with CORSIKA: A User's Guide (Version 7.5600 from August 17, 2016)*, Karlsruhe Institut für Technologie, Institut für Kernphysik, 2016.
- [HD98] HECK, D, ET AL., *CORSIKA: A Monte Carlo Code to Simulate Extensive Air Showers*, Forschungszentrum Karlsruhe, Technik und Umwelt, Wissenschaftliche Berichte FZKA 6019, 1989.

- [HG10] HOBBS, G. ET AL., *The international pulsar timing array project: using pulsars as a gravitational wave detector*, Classical and Quantum Gravity **27**, 2010.
- [HH17] HJORTH, H. ET AL., *The distance to NGC 4993: The host galaxy of gravitational-wave event GW170817*, The Astrophysical Journal Letters **848**, 2, 2017.
- [HJ61] HERSIL, J. ET AL., *Observations of Extensive Air Showers near the Maximum of Their Longitudinal Development*, The Physical Review Letters **6**, 22, 1961.
- [HR75] HULSE, R. A., TAYLOR, J. H., *Discovery of a pulsar in a binary system*, The Astrophysical Journal **195**, 1975.
- [HS77] HEININGER, S. K., *The Cosmographical Glass: Renaissance Diagrams of the Universe*, San Marino California: Huntington Library, 1977.
- [HT13] HUEGE, T., *Theory and simulations of air shower radio emission*, American Institute of Physics Conference Proceedings **1535**, 1, 2013.
- [HV12] HESS, F. V., *Über Beobachtungen der durchdringenden Strahlung bei sieben Freiballonfahrten*, Physikalische Zeitschrift **13**, 1912.
- [HV13] HESS, F. V., *Über den Ursprung der durchdringenden Strahlung*, Physikalische Zeitschrift **14**, 1913.
- [HV18] HESS, F. V., *Die Frage der durchdringenden Strahlung außerterrestrischen Ursprunges.*, Fachtechnische Sektion des Vereins der Beamten und Beamtinnen der deutsch-österreichischen Staatsdruckerei, 1918; redistributed by Verein zur Verbreitung naturwissenschaftlicher Kenntnisse.
- [HW70] HEITLER, W., *The quantum theory of radiation*, Oxford: Clarendon Press, 1970.
- [IAU12] IAU DIVISION I WORKING GROUP NUMERICAL STANDARDS, *Resolution B2: on the re-definition of the astronomical unit of length*, Beijing: International Astronomical Union, 2012.
- [II11] IRASTORZA, I. G. ET AL., *Towards a new generation axion helioscope*, Journal of Cosmology and Astroparticle Physics **6**, 013, 2011.
- [IJ95] ISBERT, J. ET AL. *Advanced Thin Ionization Calorimeter (ATIC)*, Proceedings of the 24th International Cosmic Ray Conference (ICRC 1995), 1995.
- [JR12] JANSSON, R., FARRAR, G. R., *A new model of the galactic magnetic field*, The Astrophysical Journal **757**, 14, 2012.

-
- [KB04] KEILHAUER, B., *Investigation of Atmospheric Effects on the Development of Extensive Air Showers and their Detection with the Pierre Auger Observatory*, Karlsruher Institut für Technologie, Ph.D. thesis Bianca Keilhauer, 2004.
- [KE20] KRAUSE, E., HOKKARÖMEROGLU, O., RUEHL, P., *AirShower3D: Visualization of an extensive air shower (CORSIKA simulation) in OpenGL*, <https://github.com/EeveeHuntress/AirShower3D>, April 2020.
- [KJ11] KELLEY, J. FOR THE PIERRE AUGER COLLABORATION, *AERA: the Auger Engineering Radio Array*, Proceedings of the 32nd International Cosmic Ray Conference (ICRC 2011), 2011.
- [KK02] KOKKOTAS K. D., *Gravitational Wave Physics*, Encyclopedia of Physical Science and Technology 3rd Edition **7**, Academic Press, 2002.
- [KK16] KOTERA, K., SILK, J., *Ultrahigh Energy Cosmic Rays and Black Hole Mergers*, The Astrophysical Journal Letters **823**, L29, 2016.
- [KK58] KAMATA, K., NISHIMURA, J., *The Lateral and the Angular Structure Functions of Electron Showers*, Progress of Theoretical Physics Supplement **6**, 93, 1958.
- [KN17] KROHM, N., *Search for Ultra-High Energy Photons with the Surface Detector of the Pierre Auger Observatory*, Bergische Universität Wuppertal, Ph.D. thesis Nicole Krohm, 2017.
- [KS19a] KIMURA, S. S., *High-energy emissions from neutron star mergers*, EPJ Web of Conferences (UHECR 2018) **210**, 03001, 2019.
- [KT82] KENT, J. T., *The Fisher-Bingham distribution on the sphere*, Journal of the Royal Statistical Society **44**, 1982.
- [KV17] KASPI, V., BELOBORODOV, V. M., *Magnetars*, Annual Review of Astronomy and Astrophysics **55**, 2017.
- [KW13] KOLHÖRSTER, W., *Messungen der durchdringenden Strahlung im Freiballon in größeren Höhen*, Physikalische Zeitschrift **14**, 1913.
- [KW14] KOLHÖRSTER, W., *Messung der durchdringenden Strahlung bis in Höhen von 9300 m*, Verhandlungen der Deutschen Physikalischen Gesellschaft **16**, 719, 1914.
- [LC83] LAWRENCE, C. ET AL., *5 GHz observations of sources in the Arecibo 611 MHz survey*, The Astrophysical Journal Supplement Series **51**:67-114, 1983.

- [LF07] LEEUWEN, F., *Validation of the new Hipparcos reduction*, Astronomy and Physics **474**, 2, 2007.
- [LJ63] LINSLEY, J., *Evidence for a Primary Cosmic-Ray Particle with Energy 10^{20} eV*, The Physical Review Letters **10**, 146, 1963.
- [LK03] LODDERS, K., *Solar System Abundances and Condensation Temperatures of the Elements*, The Astrophysical Journal **591**, 2003.
- [LK13] LAVE, K. ET AL., THE CRIS COLLABORATION, *Elemental GCR Observations during the 2009-2010*, Proceedings of the 33rd International Cosmic Ray Conference (IRCRC 2013), 2013.
- [LL32] LANDAU, L. D., *On the theory of stars*, Physikalische Zeitschrift der Sowjetunion **1**, 1932.
- [LL53] LANDAU, L. D., POMERANCHUK, I., *Limits of applicability of the theory of bremsstrahlung electrons and pair production at high-energies*, Doklady Akademii Nauk Seriya Fizicheskaya **92**, 1953.
- [LM01] LEMOINE, M., SIGL, G., *Physics and Astrophysics of Ultra-High-Energy Cosmic Rays*, Berlin, Heidelberg: Springer-Verlag, 2001.
- [LM91] LAWRENCE, M., REID, R., WATSON, A., *The cosmic ray energy spectrum above 4×10^{17} eV as measured by the Haverah Park array*, Journal of Physics G **17** (1991) 733, 1991.
- [LO93] LODGE, O., *Pioneers of Science*, London: Macmillan, 1893; New York: Dover Publications, 1960.
- [MA09] MELLINGER, A., *Axel Mellinger's Milky Way Panorama 2.0*, <http://www.milkywaysky.com/>, May 2020, image dated to 2009.
- [MA56] MIGDAL, A. B., *Bremsstrahlung and pair production in condensed media at high-energies*, The Physical Review D **103**, 6, 1956.
- [MB81] MCBREEN, B., LAMBERT, C. J., *Interactions of high-energy ($E > 5 \times 10^{19}$ eV) photons in the Earth's magnetic field*, The Physical Review D **24**, 1981.
- [MC14] MOORE, C. J., COLE, R. H., BERRY, C. P. L., *Gravitational-wave sensitivity curves*, Classical and Quantum Gravity **32**, 2015.
- [MC19] MOORE, C. J., COLE, R. H., BERRY, C. P. L., *Gravitational Wave Detectors and Sources*, <http://rhcole.com/apps/GWplotter/> (latest update February 27th 2019), August 2020.
- [MD07] MULLER, D., *The TRACER Project: Instrument Concept, Ballon Flights, and Analysis Procedures*, Proceedings of the 30th International Cosmic Ray Conference (ICRC 2007), 2007.

-
- [MH11] MATHES, H. FOR THE PIERRE AUGER COLLABORATION, *The HEAT Telescopes of the Pierre Auger Observatory Status and First Data*, 32nd International Cosmic Ray Conference (ICRC 2011), 2011.
- [MJ05] MATTHEWS, J., *A Heitler model of extensive air showers*, *Astroparticle Physics* **22**, 5-6, 2005.
- [MK18] MOOLEY, K. P. ET AL., *Superluminal motion of a relativistic jet in the neutron star merger GW170817*, *Nature* **561**, 2018.
- [MM06] MEDINA, M. C. ET AL., *Enhancing the Pierre Auger Observatory to the 10^{17} to $10^{18.5}$ eV Range: Capabilities of an Infill Surface Array*, *Nuclear Instruments and Methods in Physics Research A* **566**, 302, 2006.
- [MM11] DE MARIA, M., DE ANGELIS, A., *Domenico Pacini: La radiation p entrante sur la mer*, *Le Radium VIII (1910) 307*. Translation of [PD10] in French (with minor modifications). Translated in English and commented by Michela de Maria and Alessandro de Angelis, *Penetrating radiation on the sea*. (arXiv:1101.3015 [physics.hist-ph]), 2011.
- [MPI19] MAX-PLANCK-INSTITUT FÜR EXTRATERRESTRISCHE PHYSIK, *Max-Planck-Gesellschaft - Der Satellit mit Röntgenblick*, <https://www.mpg.de/13536066/rueckblende-rosat>, May 2020, article dated to June 2019.
- [MR17] MIRZOYAN, R. FOR THE MAGIC COLLABORATION, *First-time detection of VHE gamma rays by MAGIC from a direction constant with the recent EHE neutrino event IceCube-170922A*, *Astronomer's Telegram* 10817, <http://www.astronomerstelegam.org/?read=10817>, 2017.
- [MR26a] MILLIKAN, R. A., BOW, I. S., *High frequency rays of cosmic origin I: Sounding Balloon Observations at Extreme Altitudes*, *The Physical Review* **27**, 4, 1926.
- [MR26b] MILLIKAN, R. A., ORIS, R. M., *High frequency rays of cosmic origin II: Mountain Peak and Airplane*, *The Physical Review* **27**, 6, 1926.
- [MR26c] MILLIKAN, R. A., CAMERON, G. H., *High frequency rays of cosmic origin III. Measurements in snow-fed lakes at high altitudes*, *The Physical Review* **12**, 1926.
- [MR28] MAZE, R., *Etude d'un appareil à grand pouvoir de résolution pour rayons cosmiques*, *Journal de Physique et le Radium* **9**, 1938.
- [MS07] MEI, S. ET AL., *The ACS Virgo Cluster Survey. XIII. SBF Distance Catalog and the Three-dimensional Structure of the Virgo Cluster*, *The Astrophysical Journal* **655**, 1, 2007.

- [MS18] MOLLERACH, S., ROULET, E. *Progress in high-energy cosmic ray physics*, Progress in Particle and Nuclear Physics **98**, 2018.
- [NA05] NASA, ESA, HESTER, J., LOLL, A., *HubbleSite: Resource Gallery*, Arizona State University, 2005.
- [NA19] NASA/IPAC, *NED NASA/IPAC Extragalactic Database*, June 3rd 2019.
- [NA20a] WMAP SCIENCE TEAM, *WMAP Internal Linear Combination Map*, https://lambda.gsfc.nasa.gov/product/map/current/m_images.cfm, state May 2020.
- [NA20b] NASA/DOE/FERMI LAT COLLABORATION, *Fermi's Five-year View of the Gamma-ray Sky*, <https://svs.gsfc.nasa.gov/11342>, May 2020, article dated to August 2013.
- [ND07] NEWTON, D., KNAPP, J., WATSON, A., *The Optimum Distance at which to Determine the Size of a Giant Air Shower*, Astroparticle Physics **26**, 414, 2007.
- [NM04] NAGANO, M. ET AL., *New measurement on photon yields from air and the application to the energy estimation of primary cosmic rays*, Astroparticle Physics **22**, 3-4, 2004.
- [NM15] NIECHCIOL, M., *A New Window to the Universe? Searching for Ultra-High-Energy Photons at the Pierre Auger Observatory*, Universität Siegen, Ph.D. thesis Marcus Niechciol, 2015.
- [NW85] NELSON, W. R., HIRAYAMA, H., ROGERS, D. W. O., *The EGS4 code system*, Stanford Linear Accelerator Center, Report **SLAC 265**, 1985, <https://www.slac.stanford.edu/cgi-bin/getdoc/slac-r-265.pdf>, state July 2020.
- [OG47] OCCHIALINI, G. P., POWELL, C. F., *Nuclear disintegration produced by slow charged particles of small mass.*, Nature **159**, 1947.
- [PA16] PIRO, A. L., KOLLMEIER, J. A., *Ultrahigh-Energy Cosmic Rays from the "En Caul" Birth of Magnetars*, The Astrophysical Journal **826**, 97, 2016.
- [PB19] PONT, B. FOR THE PIERRE AUGER COLLABORATION, *A Large Radio Detector at the Pierre Auger Observatory – Measuring the Properties of Cosmic Rays up to the Highest Energies*, 36th International Cosmic Ray Conference, Proceedings of Science (ICRC 2019) 398, 2019.
- [PB61] PETERS, B., *Primary cosmic radiation and extensive air showers*, Il Nuovo Cimento **22**, 1961.

-
- [PD09] PACINI, D., *Sulle radiazioni penetranti*, Rendiconti Accademia dei Lincei **18**, 1909.
- [PD10] PACINI, D., *La radiazione penetrante sul mare*, Ann. Uff. Centr. Meteor. **XXXII**, parte I, 1910.
- [PD12] PACINI, D., *La radiazione penetrante alla superficie ed in seno alle acque*, Nuovo Cimento **VI/3**, 93, 2019.
- [PE05] PARIZOT, E. FOR THE PIERRE AUGER COLLABORATION, *Aperture calculation for the Pierre Auger Observatory surface detector*, 29th International Cosmic Ray Conference (ICRC 2005), Pune **00**, 101-106, 2005.
- [PP07] PICOZZA, P. ET AL., *Pamela – A Payload For Antimatter Matter Exploration And Light-Nuclei Astrophysics*, Astroparticle Physics **27**, 4, 2007.
- [PP15] PAPANBREER, P., RAUTENBERG, J., *Afterpulse structure in single muon PMT traces simulated at 120 MHz*, Pierre Auger Collaboration internal note GAP2015_10, 2015.
- [PP18a] PADOVANI, P. ET AL., *Dissecting the region around IceCube-170922A: the blazar TXS 0506+056 as the first cosmic neutrino source*, Monthly Notices of the Royal Astronomical Society **480**, 1, 2018.
- [PP18b] PAPANBREER, P., LHENRY-YVON, I., *Bad PMTs: the third levels of quality cuts, tuned for PMT traces analysis.*, Pierre Auger Collaboration internal note GAP2018_029, 2018.
- [PR14] POGGE, R. W., *Essay: The Folly of Giordano Bruno*, <http://www.astronomy.ohio-state.edu/~pogge/Essays/Bruno.html>, 2014.
- [PS18] PAIANO, S. ET AL., *The Redshift of the BL Lac Object TXS 0506+056*, The Astrophysical Journal Letters **854**, L32, 2018.
- [PT15] PIEROG, T. ET AL., *EPOS LHC: Test of collective hadronization with data measured at the CERN Large Hadron Collider*, The Physical Review C **92**, 2015.
- [PV93] PTUSKIN, V. S. ET AL., *Diffusion and drift of very high energy cosmic rays in galactic magnetic fields*, Astronomy and Astrophysics **268**, 2, 1993.
- [PW25] PAULI, W. E., *Über den Zusammenhang des Abschlusses der Elektronengruppen im Atom mit der Komplexstruktur der Spektren*, Zeitschrift für Physik **31**, 1925.

- [PW30] PAULI, W. E., Offener Brief an die Gruppe der Radioaktiven bei der Gauvereins-Tagung zu Tübingen, 1930.
- [RA05] ROCKE, A., *In Search of El Dorado: John Dalton and the Origins of the Atomic Theory*, Social Research **72**, 1, 2005.
- [RB33] ROSSI, B. B., *Interaction between Cosmic Rays and Matter*, Nature **132**, 1933.
- [RE19] ROULET, E. FOR PIERRE AUGER COLLABORATION, *Large-scale anisotropies above 0.03 EeV measured by the Pierre Auger Observatory*, 36th International Cosmic Ray Conference, Proceedings of Science (ICRC 2019) 408, 2019.
- [RE33] REGENER, E., *New Results in Cosmic Ray Measurements*, Nature **132**, 1933.
- [RE35] REGENER, E., PFOTZER, J. G. *Vertical Intensity of Cosmic Rays by Threefold Coincidences in the Stratosphere*, Nature **136**, 1935.
- [RF56] REINES, F., COWAN, C. L. *Detection of the Free Neutrino: a Confirmation.*, Science **124**, 1956.
- [RJ19] RAUTENBERG, J. ET AL., THE PIERRE AUGER COLLABORATION, *Limits on ultra-high energy photons with the Pierre Auger Observatory*, 36th International Cosmic Ray Conference, Proceedings of Science (ICRC 2019) 398, 2019.
- [RM07] RISSE, M., HOMOLA, P., *Search for ultra-high energy photons using air showers*, Modern Physics Letter A **22**, 2007.
- [RM85] ROWAN-ROBINSON, M. *The cosmological distance ladder*, New York: W.H. Freeman and Company, 1985.
- [RP16] RUEHL, P., *Studies of Air Shower Observables for the Search of Ultra High Energy Photons*, Universität Siegen, Master thesis Philip Ruehl, 2016.
- [RW95] RÖNTGEN, W. C., *Über eine neue Art von Strahlen (Vorläufige Mitteilung.)*, Sonderabdruck aus den Sitzungsberichten der Würzburger Physik.-medic. Gesellschaft, 1895.
- [SB11] SARKAR, B. ET AL., *Ultra-High Energy Photon and Neutrino Fluxes in Realistic Astrophysical Scenarios*, Proceedings of the 32nd International Cosmic Ray Conference (ICRC 2011), 2011.
- [SD20] STEINIGER, D., *Analyse einer neuen Luftschauberobservablen zur Identifikation primärer Photonen in der kosmischen Strahlung*, Universität Siegen, Bachelor thesis Daniel Steiniger, 2020.

-
- [SD85] SMART, D. F., SHEA, M. A., *Handbook of geophysics and space environment – Chapter 6: Galactic cosmic radiation and solar energetic particles*, Air Force Geophysics Laboratory, United States Air Force, 1985.
- [SE14] SEO, E. S. ET AL., *Cosmic Ray Energetics and Mass for the International Space Station (ISS-CREAM)*, Advances in Space Research **53**, 2014.
- [SH01] SALAZAR, H., NELLEN, L., VILLASEÑOR, L. FOR THE PIERRE AUGER COLLABORATION *Surface detector calibration for the Auger Observatory*, Proceedings of the 27th International Cosmic Ray Conference (ICRC 2001), Hamburg, 2001.
- [SH88] STEPHANI, H., *Allgemeine Relativitätstheorie - Eine Einführung in die Theorie des Gravitationsfeldes*, Berlin: VEB Deutscher Verlag der Wissenschaften, 1988.
- [SL16a] SINGER, L. P., ET AL., *Going the distance: mapping host galaxies of ligo and virgo sources in three dimensions using local cosmography and targeted follow-up*, The Astrophysical Journal Letters **829**, 1, 2016.
- [SL16b] SINGER, L. P., ET AL., *Supplement: “Going the distance: mapping host galaxies of ligo and virgo sources in three dimensions using local cosmography and targeted follow-up”*, The Astrophysical Journal Supplement Series **226**, 1, 2016.
- [SM04] SKŁOWSKA CURIE, M., *Recherches sur les substances radioactives*, Paris: Gauthier-Villars, Imprimeur-Libraire, Du bureau des longitudes de l'école polytechnique, Quai des Grands-Augustins, 55, 1904.
- [SM13] SETTIMO, M. ET AL., *Trigger probability for single stations and air-showers with the TOTd and MoPS algorithms*, Pierre Auger Collaboration internal note GAP 2013_114, 2013.
- [SM19] SCHIMP, M. FOR THE PIERRE AUGER COLLABORATION, *Follow-up searches for ultra-high energy neutrinos from transient astrophysical sources with the Pierre Auger Observatory*, 36th International Cosmic Ray Conference, Proceedings of Science (ICRC 2019) 415, 2019.
- [SM41] SCHEIN, M., JESSE, W. P., WOLLAN, E. O., *The nature of primary cosmic radiation and the origin of the mesotron*, The Physical Review **56**, 1941.
- [SP95] SOMMERS, P., *Capabilities of a giant hybrid air shower detector*, Astroparticle Physics **3**, 4, 1995.

- [SR17] ŠMÍDA, R. FOR THE PIERRE AUGER COLLABORATION, *Scintillator detectors of AugerPrime*, The Pierre Auger Observatory: Contributions to the 35th International Cosmic Ray Conference (ICRC 2017), 2017.
- [SS01] SWORDY, S. P., *The Energy Spectra and Anisotropies of Cosmic Rays*, Space Science Reviews **99**, 2001.
- [ST85] STENEV, T., VANKOV, C. P., HALSEN, F., *Muons in gamma showers*, Proceedings from the 19th International Cosmic Ray Conference (ICRC 1985), Vol. 7, 1985.
- [TJ04] TASSOUL, J., TASSOUL M., *A Concise History of Solar and Stellar Physics*, Princeton and Oxford: Princeton University Press, 2004.
- [TJ97] THOMSON, J. J., *XL. Cathode Rays*, The London, Edinburgh and Dublin Philosophical Magazine and Journal of Science, 44:269, 1897.
- [TM03] TAKEDA, M. ET AL., *Energy determination in the Akeno Giant Air-Shower Array experiment*, Astroparticle Physics **19**, 447, 2003.
- [TM18] TANABASHI, M. ET AL., THE PARTICLE DATA GROUP, *Particle Physics Booklet*, The Physical Review D **98**, 030001, 2018.
- [TM86] TESHIMA, M. ET AL., *Expanded array for giant air shower observation at Akeno*, Nuclear Instruments and Methods in Physics Research A **247**, 2, 1986.
- [TR67] TENNENT, R. M., *The Haverah Park extensive air shower array*, Proceedings of the Physical Society **92**, 3, 1967.
- [TY17] TANAKA, Y. T. FOR THE FERMI-LAT COLLABORATION, *Fermi-LAT detection of increased gamma-ray activity of TXS 0506+056, located inside the IceCube-170922A error region*, Astronomer's Telegram 1079, <http://www.astronomerstelegam.org/?read=10791>, 2017.
- [UC13] UNNIKRISHNAN, C., *IndIGO and LIGO-India: scope and plans for gravitational wave research and precision metrology in India*, International Journal of Modern Physics D **22**, 1, 2013.
- [UG25] UHLENBECK, G. E., GOUDSMIT, S. A., *Ersetzung der Hypothese vom unmechanischen Zwang durch eine Forderung bezüglich des inneren Verhaltens jedes einzelnen Elektrons*, Die Naturwissenschaften **13**, 1925.
- [UG26] UHLENBECK, G. E., GOUDSMIT, S. A., *Spinning Electrons and the Structure of Spectra*, Nature **117**, 1926.

-
- [UM08] UNGER, M. ET AL., *Reconstruction of longitudinal profiles of ultra-high energy cosmic ray showers from fluorescence and Cherenkov light measurements*, Nuclear Instruments and Methods in Physics Research A **588**, 433, 2008.
- [URL1] THE PIERRE AUGER COLLABORATION, *The PhotonsDiffuseSD Wiki page* <https://www.auger.unam.mx/AugerWiki/PhotonsDiffuseSD>, January 2020.
- [URL2] THE LIGO SCIENTIFIC COLLABORATION, *Observing Plans and Public Alerts*, <https://ligo.org/scientists/GWEMalerts.php>, January 2020.
- [URL3] <http://www.schott.com> Schott Glaswerke, Mainz, Germany, January 2020.
- [URL4] THE PIERRE AUGER COLLABORATION, *The Pierre Auger Observatory @ flickr*, <https://www.flickr.com/people/134252569@N07>, February 2020.
- [URL5] MISSMJ, CUSH, *Standard model of elementary particles: the 12 fundamental fermions and 5 fundamental bosons*. <https://commons.wikimedia.org/w/index.php?curid=4286964> (Own work by uploaders), March 2020.
- [URL6] THE LIGO SCIENTIFIC COLLABORATION, *Caltech/MIT/LIGO Lab*, <https://www.ligo.caltech.edu/>, May 2020.
- [URL7] THE VIRGO COLLABORATION, *The Virgo homepage*, <http://www.virgo-gw.eu/>, May 2020.
- [URL8] CERN, *CERN Accelerating science*, <https://home.cern/>, state July 2020.
- [URL9] THE LIGO SCIENTIFIC COLLABORATION, *GraceDB – Gravitational-Wave Candidate Event Database* <https://gracedb.ligo.org>, state October 2019.
- [VD13] VERBERIC, D., *Maps of the Pierre Auger Observatory*, https://web.ikp.kit.edu/darko/auger/auger-array/auger_array-pdf/, 2020, image dated to 2013.
- [VF15] VAN DE VOORT, F ET AL., *Galactic r-process enrichment by neutron star mergers in cosmological simulations of a Milky Way-mass galaxy*, Monthly Notices of the Royal Astronomical Society **447**, 1, 15.

- [VI15] VALIÑO, I. FOR THE PIERRE AUGER COLLABORATION, *The flux of ultra-high energy cosmic rays after ten years of operation of the Pierre Auger Observatory*, 34th International Cosmic Ray Conference (ICRC 2015), Proceedings of Science, 271, 2015.
- [VL13] VALORE, L. FOR THE PIERRE AUGER COLLABORATION, *Measuring Atmospheric Aerosol Attenuation at the Pierre Auger Observatory*, The Pierre Auger Observatory: Contributions to the 33rd International Cosmic Ray Conference (ICRC 2013), Rio de Janeiro 2013.
- [VV13] VERZI, V. FOR THE PIERRE AUGER COLLABORATION, *The Energy Scale of the Pierre Auger Observatory*, The Pierre Auger Observatory: Contributions to the 33rd International Cosmic Ray Conference (ICRC 2013), Rio de Janeiro 2013.
- [VV19] VERZI, V. FOR THE PIERRE AUGER COLLABORATION, *Measurement of the energy spectrum of ultra-high energy cosmic rays using the Pierre Auger Observatory*, 36th International Cosmic Ray Conference (ICRC 2019), Proceedings of Science, 450, 2019.
- [WC01] WILSON, C. T. R., *On the Ionisation of Atmospheric Air*, Proceedings of the Royal Society of London A **68**, 1901.
- [WC12] WILSON, C. T. R., *On an expansion apparatus for making visible the tracks of ionising particles in gases and some results obtained by its use*, Proceedings of the Royal Society of London A **87**, 595, 1912.
- [WE79] WELLS, E. W., GREISEN, E. W., HARTEN, R. H., *FITS: A Flexible Image Transport System*, International Workshop on Image Processing in Astronomy. Proceedings of the 5th Colloquium on Astrophysics, 1979.
- [WG13] WANG, G., WEI-TOU, N., *Numerical simulation of time delay interferometry for eLISA/NGO*, Classical and Quantum Gravity **30**, 2013.
- [WJ81] WEISBERG, J., TAYLOR, J. H., FOWLER, L. A., *Gravitational Waves from an Orbiting Pulsar*, Scientific American **245**, 4, 1981.
- [WR20] WILLIAMS, R., NASA, *Earth Fact Sheet*, <https://nssdc.gsfc.nasa.gov/planetary/factsheet/earthfact.html>, April 2020.
- [WT09] WULF, T., *Über die in der Atmosphäre vorhandene Strahlung von hoher Durchdringungsfähigkeit*, Physikalische Zeitschrift **10**, 1909.
- [WW19] WINTER, W. ET AL., *Multi-messenger interpretation of the neutrinos from TXS 0506+056*, 36th International Cosmic Ray Conference (ICRC 2019), Proceedings of Science 1032, 2019.

-
- [YA19] YUSHKOV, A. FOR THE PIERRE AUGER COLLABORATION, *Mass composition of cosmic rays with energies above $10^{17.2}$ eV from the hybrid data of the Pierre Auger Observatory*, 36th International Cosmic Ray Conference (ICRC 2019), Proceedings of Science, 482, 2019.
- [YH35] YUKAWA, H., *On the Interaction of Elementary Particles*, Proceedings of the Physico-Mathematical Society of Japan **17**, 48, 1935.
- [YY19] YUAN, Y., SHI, X., *Collision of ultra-relativistic proton with strong magnetic field: Production of ultra-high energy photons and neutrinos*, Physics Letters B **795**, 2019.
- [ZG66] ZATSEPIN, G. T., KUZMIN, V. A., *Upper limit of the spectrum of cosmic rays*, Journal of Experimental and Theoretical Physics Letters **4**, 1966.
- [ZV14] ZAKHARENKO, V. ET AL., *Solar system radio emission studies with the largest low-frequency radio telescopes*, European Planetary Science Congress Abstracts **9**, 114, 2014

List of abbreviations

2MASS	Two Micron All-Sky Survey
2MRS	2MASS Redshift Survey
ADST	Advanced Data Summary Tree
AERA	Auger Engineering Radio Array
AGASA	Akeno Giant Air Shower Array
AGN	active galactic nucleus (or active galactic nuclei)
AMIGA	Auger Muons and Infill for the Ground Array
AMS	Alpha Magnetic Spectrometer
APE	Auger Package Environment
ASCII	American Standard Code for Information Interchange
a.s.l.	above sea level
ATIC	Advanced Thin Ionization Calorimeter
ALP	axion-like particle
BBH	binary black hole
BCE	before common era
BH	black hole
BHNS	black hole-neutron star
BLS	balloon launching station
BNS	binary neutron star
CAST	CERN Axion Solar Telescope
CBM	compact binary merger
CDAS	central data acquisition system
CE	common era
CERN	Organisation européenne pour la recherche nucléaire
CIC	constant intensity cut
CL	confidence level
CLF	Central Laser Facility
CNO	carbon, nitrogen, oxygen
CMB	cosmic microwave background
CORSIKA	Cosmic Ray Simulations for KASCADE
CREAM	Cosmic Ray Energetics and Mass
EGS	Electron-Gamma Shower
EPOS	Energy conserving quantum mechanical multiple scattering approach, based on Partons (parton ladders) Off-shell remnants and Splitting of parton ladders
EPTA	European Pulsar Timing Array
FADC	flash analog-to-digital converter
FC	Feldman-Cousins
FD	fluorescence detector

FITS	Flexible Image Transport System
FLUKA	Fluktuierende Kaskade
FoV	field of view
GBM	Gamma-ray Burst Monitor
GDAS	Global Data Assimilation System
GCC	GNU Compiler Collection
GNU	GNU's Not Unix!
GPS	Global Positioning System
GraceDB	Gravitational-Wave Candidate Event Database
GRB	gamma-ray burst
GUT	grand unified theory
GW	gravitational wave
GZK	Greizen-Zatsepin-Kuzmin
HEAO	High Energy Astrophysics Observatory
HEAT	High Elevation Auger Telescopes
HEALPix	Hierarchical Equal Area isoLatitude Pixelisation
HECO	an acronym for the combination of HEAT and Coihueco
H.E.S.S.	High Energy Stereoscopic System
HG	high-gain
HPC	High Performance Computing
ICRC	International Cosmic Ray Conference
ID	identification (number)
INTEGRAL	INTErnational Gamma-Ray Astrophysics Laboratory
IPN	Interplanetary Network
IPTA	International Pulsar Timing Array
IR	infrared
IRB	infrared background light
ISS	International Space Station
KAGRA	Kamioka Gravitational Wave Detector
KASCADE	Karlsruhe Shower Core and Array Detector
LAT	Large Area Telescope
LDF	lateral distribution function
LED	light emitting diode
LG	low-gain
LHC	Large Hadron Collider
LIGO	Laser Interferometer Gravitational-Wave Observatory
LISA	Laser Interferometer Space Antenna
LPM	Landau-Pomeranchuk-Migdal
MAGIC	Major Atmospheric Gamma Imaging Cherenkov Telescopes
MC	Monte Carlo
MMA	Multimessenger Astronomy
MoPS	Multiplicity of Positive Steps
MVA	multivariate analysis
NANOGrav	North American Nanohertz Observatory for Gravitational Waves
NASA	National Aeronautics and Space Administration
NASU	National Academy of Sciences of Ukraine

ndf	number of degrees of freedom
NGC	New General Catalogue
NKG	Nishimura-Kamata-Greisen
NS	neutron star
PAMELA	Payload for Antimatter Matter Exploration and Light-nuclei Astrophysics
PC	principal component
PCA	principal component analysis
PMT	photomultiplier tube
PPTA	Parkes Pulsar Timing Array
QGSJET	Quark Gluon String model with Jets
RD	radio detector
RG	radio galaxy
RMS	root-mean-square
ROC	receiver operating characteristic
SALLA	short aperiodic loaded loop antenna
SHDM	super heavy dark matter
SD	surface detector
SDP	shower-detector plane
SiMPLE	Siegen MultiProcessor Linux Environment
SNR	supernova remnant
sPMT	small PMT
SSD	surface scintillation detector
TA	Telescope Array
TD	topological defect
ToT	Time over Threshold
ToTd	Time over Threshold deconvolved
TRACER	Tracking Aerosol Convection Interactions
TXS	Texas survey of radio sources
UHE	ultra-high-energy (or ultra-high energy)
URAN	Ukrainian Radio Interferometer of NASU
URB	universal radio background
UTC	Coordinated Universal Time
UTR	Ukrainian T-Shaped Radio Telescope
UV	ultraviolet
VEM	vertical equivalent muon
WCD	water Cherenkov detector
XLF	eXtreme Laser Facility
XML	Extensible Markup Language

Danksagung

An dieser Stelle möchte ich all jenen danken, die mich während meines Studiums und meiner anschließenden Promotion begleitet und unterstützt haben. Ohne sie wäre diese Arbeit kaum möglich gewesen.

Allen voran möchte ich meinem Doktorvater Prof. Dr. Markus Risse dafür danken, mir die Möglichkeit gegeben zu haben unter seiner Betreuung zu promovieren. Die vielen lehrreichen und ungezwungenen Diskussionen mit ihm haben nicht nur dazu beigetragen diese Arbeit voranzubringen, sondern auch meine eigenen fachlichen und wissenschaftlichen Fähigkeiten stetig zu verbessern. Außerdem möchte ich mich bei ihm dafür bedanken, dass er stets ein Arbeitsumfeld ermöglicht hat, in dem ich mich in meiner Arbeit wissenschaftlich frei entfalten konnte und niemals den Spaß an der Forschung verloren habe.

Bei Prof. Dr. Ivor Fleck bedanke ich mich vielmals für seine Zusage, als Zweitgutachter dieser Arbeit zur Verfügung zu stehen und weiterhin bei Prof. Dr. Karl-Heinz Kampert und Dr. Michael Johanning für ihre Bereitschaft bei meiner Promotionskommission mitzuwirken.

Ebenso möchte ich einen besonderen Dank gegenüber Dr. Markus Niechciol aussprechen, der einen signifikanten Teil meiner Einarbeitung während meiner Masterarbeit und in der Anfangszeit meiner Promotion übernommen hat. Darüber hinaus stand er mir jederzeit für Gespräche, Ratschläge und Kritik zur Verfügung und hat dadurch einen wichtigen Beitrag zu dieser Arbeit geleistet.

Besonders betonen möchte ich auch die enorme Wichtigkeit der Arbeit der Kolleginnen und Kollegen vom Pierre Auger Observatorium, die dafür sorgen, dass der pausenlose Betrieb des Detektors und die Datennahme zu jeder Zeit so reibungsfrei wie möglich funktionieren. Ohne die Bereitstellung dieser Daten wäre diese Arbeit nicht in dieser Form möglich gewesen. Ebenso danke ich allen Kolleginnen und Kollegen der Pierre Auger Collaboration und auch den vielen Menschen von anderen Institutionen, mit denen ich mich auf gemeinsamen Meetings, Schulungen und Konferenzen austauschen durfte, für die vielen wertvollen Erfahrungen die ich mit ihnen gesammelt habe.

Weiterhin möchte ich mich bei allen Mitgliedern der Arbeitsgruppe für Experimentelle Teilchen- und Astroteilchenphysik der Universität Siegen für eine jederzeit angenehme und freundliche Arbeitsatmosphäre bedanken. Hierbei möchte ich mich vor allem für das Engagement von Dr. Wolfgang Walkowiak bedanken, der mit der Administration des lokalen HPC Clusters "SiMPLE" zu jeder Zeit bemüht ist eine voll funktionsfähige Computing-Infrastruktur für die gesamte Arbeitsgruppe bereitzustellen. Und auch für seine Geduld und das Vertrauen, das er mir entgegengebracht hat bei meiner Einarbeitung als Co-Admin.

Darüber hinaus möchte ich mich noch bei allen Kommilitoninnen und Kommilitonen erkenntlich zeigen, die für mich das Hochschulleben zu mehr als nur

Studium und Arbeit gemacht haben. Besonders aber bei den beiden Personen, die mich während meines gesamten Studiums am längsten begleitet haben und trotz der fachlichen Divergenz nach dem Bachelorstudium in engem Kontakt geblieben sind: Patrick Huber und Moritz Porst. Ein weiterer persönlicher Dank gebührt Dr. Alexander Aab für die herzliche Aufnahme in der Siegener Arbeitsgruppe für Astroteilchenphysik und die Gemeinschaft der Doktoranden in der Pierre Auger Collaboration.

Der größte Dank gilt jedoch meiner Familie. Insbesondere meinen Eltern, die es mir ermöglicht haben, den von mir gewählten Bildungsweg einzuschlagen und mich zu jeder Zeit in jeder Entscheidung stets unterstützt und ermutigt haben. Und Evelyn Krause, die mich fast sechs Jahre lang durch Studium und Promotion begleitet hat. Ihr danke ich an dieser Stelle vor allem für ihre aktive Unterstützung durch das Lesen und Diskutieren meiner Arbeit und ihren Beitrag zu dieser mit dem Luftschauervisualisierungsprogramm AirShower3D, und dafür, mir in jeder Situation den nötigen Rückhalt gegeben zu haben.

